Kinetics, Structure and Dynamics of Block Copolymer Nanoparticles Prepared via RAFT Dispersion Polymerisation

Erik Jan Cornel

Under Supervision of Professor Steven P. Armes FRS

Department of Chemistry

The University of Sheffield

Submitted to the University of Sheffield

In Fulfilment of the Requirements for the Award of

Doctor of Philosophy

July 2019

For my mother Tineke Karsten-Cornel, my father John Cornel

and my brother Arnoud Cornel

Declaration

The work described in this report was carried out at the University of Sheffield under the supervision of Professor Steven P. Armes FRS between October 2015 and March 2019 and has not been submitted, either wholly or in part, for this or any other degree. All the work is the original work of the author, except where acknowledged by references.

Signature: _____

Erik Jan Cornel 29-03-2019

Acknowledgements

First of all I would like to thank Professor S. P. Armes for offering me a fully-funded PhD position in his research group and for his continuous support during the course of my studies. I would also like to thank my industrial sponsor Lubrizol for funding this PhD project, and my industrial contacts Dr. Tim Smith, Dr. Paul O'Hora and Dr. David Growney for their technical advice and support.

I would also like to acknowledge all the current members of the Armes research group for their help and assistance: Dr. Adam Czajka, Andrew Leigh, Craig Jesson, Csilla Gyorgy, Deborah Beattie, Derek Chan, Emma Brotherton, Isabella Dorsman, Dr. James Jennings, Dr. Matt Derry, Dr. Matt Rymaruk, Dr. Nick Penfold, Oliver Deane, Paul Grainger, Rebecca Gibson, Rory McBride, Sarah Byard, Saul Hunter, Shannon North, Aikaterini Tatani, Yide Han and Dr. Yin Ning. Additionally, I would also like to thank all the previous Armes group members for their help and support.

For their help with small-angle scattering analysis, I would like to thank the following people: Dr. Adam Czajka, Deborah Beattie, Dr. Fiona Hatton, Dr. Gregory Smith, Dr. James Jennings, Dr. Matt Derry, Dr. Oleksandr Mykhaylyk, Dr. Sarah Rogers, Thomas Neal and Dr. Thomas Zinn. I would like to thank Dr. Sandra van Meurs, Dr. Craig Robertson and Sue Bradshaw for their help with NMR analysis. I would like to acknowledge Dr. Svetomir Tzokov and Dr. Chris Hill for their assistance with TEM analysis. For their help and support with various instruments, I would like to thank Robert Hanson, Keith Owen, Stephen Atkin and Dan Jackson. For all their hard work, I would like to thank Denise Richards and Louis Brown-Leng in the finance office and Nick Smith in the department of chemistry stores.

Furthermore, I would like to thank various people who live (or used to live) in Sheffield: Andreas Koeppel, Dr Devanshi Singh, Dylan George, Iklima Oral, Dr Lucia Romero Azogil, Dr Mattia Sponchoni, Meng Fan and Dr Oliver Zirimwabagabo.

Finally, I am very grateful to my mother Tineke Karsten-Cornel, my brother Arnoud Cornel and Qingxuan Lin for their continuous support during the course of my PhD.

Abstract

This thesis reports the facile synthesis and analysis of poly(stearyl methacrylate)-poly(2,2,2-trifulroethyl methacrylate) (PSMA-PTFEMA), poly(lauryl methacrylate)-poly(methyl methacrylate) (PLMA-PMMA), poly(lauryl methacrylate)-poly(d_8-methyl methacrylate) (PLMA-d_8PMMA) and poly(lauryl methacrylate)-poly(benzyl methacrylate) (PLMA-PBzMA) spherical nanoparticles via reversible addition-fragmentation chain-transfer (RAFT) dispersion polymerisation in non-polar media. Such a synthetic approach is also known as polymerisation-induced-self-assembly (PISA), whereby growing block copolymer chains self-assemble during the polymerisation to form sterically stabilised nanoparticles. PLMA-PMMA and PLMA-PBzMA nanoparticles are used as friction modifiers in engine oils by the sponsor of this work (Lubrizol). Insight into nanoparticle properties at elevated temperatures (e.g. thermally-induced particle disassociation) is required to further improve this technology. In contrast, the relatively low refractive index of the semi-fluorinated core-forming PTFEMA block was utilised for the preparation of highly transparent nanoparticle dispersions. This feature allowed extraordinary opportunity to study general characteristics of non-polar RAFT PISA (such as RAFT chain-end stability and removal). The isorefractive character of these dispersions allowed *in situ* visible absorption spectra to be recorded during RAFT-mediated PISA, which allows assessment of the fate of the RAFT chain-ends. Much to our surprise, the trithiocarbonate RAFT end-groups were remarkably stable under monomer starved conditions. Moreover, the polymerisation kinetics can be monitored by dilatometry. The same spectroscopic technique was employed to investigate the kinetics of RAFT chain-end removal from nanoparticle cores using excess initiator. Visible absorption spectroscopy and GPC studies confirmed the complete removal of RAFT chain-ends using this approach. Small-angle X-ray scattering (SAXS) studies confirmed no change in the spherical nanoparticle diameter after this derivatisation. Furthermore, this RAFT PISA formulation allowed reaction kinetics to be conveniently monitored using *in situ* ^{19}F NMR spectroscopy. The second study in this Thesis describes copolymer chain exchange between hydrogenous and core-deuterated PLMA-PMMA spheres. This was investigated using time-resolved small-angle neutron scattering. A faster copolymer exchange rate was observed when using higher temperatures and shorter core-forming PMMA degrees of polymerisations (DPs). Since these experiments were performed on binary mixtures of dilute dispersions (1.0% w/w), it is likely that copolymer exchange between spherical nanoparticles proceeds via the chain insertion/expulsion mechanism. Copolymer exchange was even observed at 80 °C, which is below the T_g of the core-forming PMMA block and also below the reaction temperature for the synthesis of such nanoparticles via RAFT PISA. This suggests that the chain expulsion/insertion mechanism is likely to play a dominant role during RAFT dispersion polymerisation in non-polar media. The third study in this thesis involves copolymer chain exchange between PLMA-PBzMA spheres of differing particle diameters. Block copolymer chain exchange was confirmed using a binary mixture of such nanoparticles. Two distinct particle diameters were prepared by adjusting the PBzMA nanoparticle core DP with longer core DPs leading to larger spheres. Copolymer chain exchange between small and large nanoparticles led to the formation of hybrid nanoparticles with intermediate diameters. Time-resolved SAXS was used to examine particle fusion between such binary mixtures *in situ*. These data suggest that the fusion mechanism proceeds via weakly anisotropic intermediate morphologies. Variable temperature SAXS analysis of the initial nanoparticles and SAXS analysis of the hybrid nanoparticles obtained from binary mixtures of small and large nanoparticles mixed in various ratios suggests that the shorter block copolymer chains aid the thermally activated dissociation of the larger spherical nanoparticles.

Publications

Cornel, E. J.; van Meurs, S.; Smith, T.; O'Hora, P. S.; Armes, S. P. In situ spectroscopic studies of highly transparent nanoparticle dispersions enable assessment of trithiocarbonate chain-end fidelity during RAFT dispersion polymerization in nonpolar media, *Journal of the American Chemical Society* **2018**, *140*, 12980-12988.

Cornel, E. J.; Smith, G. N.; Rogers, S. E.; Hallett J. E.; Growney, D. J.; Smith, T.; O'Hora, P. S.; Sandra van Meurs, Mykhaylyk, O. O.; and Armes, S. P. Time-resolved small-angle neutron scattering studies of the thermally-induced exchange of copolymer chains between spherical diblock copolymer nanoparticles prepared via polymerization-induced self-assembly, *Manuscript to be submitted to Macromolecules*

Cornel, E. J.; O'Hora, P. S.; Smith, T.; Mykhaylyk, O. O.; and Armes, S. P. Thermally-Induced Sphere-Sphere Fusion Enables the Formation of Hybrid Spherical Diblock Copolymer Nanoparticles of Intermediate Size, *Manuscript to be submitted*

Cornel, E. J.; Derry, M.J.; O'Hora, P. S.; Smith, T.; Growney, D. J.; and Armes, S. P. Robust Synthesis of Cross-linked Diblock Copolymer Nanoparticles via RAFT Dispersion Polymerization of Methyl Methacrylate in Mineral Oil, *Manuscript to be submitted to ACS Applied Materials & Interfaces*

Conferences and Courses

2017	APME, Ghent, Belgium (Contribution: Poster presentation)
2017	YRM Edinburgh, United kingdom (Contribution: Poster presentation)
2017	ACS Washington, United States (Contribution: Poster presentation)
2018	ACS New Orleans, United States, (Contribution: Oral presentation)
2018	SAS Summer school, Bombannes, France (Contribution: Oral presentation)
2018	Early Career Colloid Meeting, ECColloid18, Sheffield, United Kingdom

Nomenclature

A_c	Surface area per corona chain at the core/corona interface
AIBN	Azobisisobutyronitril
ARGET	Activators regenerated by electron transfer
ATRP	Atom transfer radical polymerisation
BCC	Body-centred cubic lattice
BHT	Butylated hydroxytoluene
BPO	Benzoyl peroxide
C	Hexagonally-packed cylinders
CGT	Critical gelation temperature
CLRP	Controlled/living radical polymerisation
CMC	Critical micelle concentration
CPS	Closely packed sphere
CTA	Chain transfer agent
CWC	Critical water content
Đ	Dispersity
DCC	*N*,*N*'-Dicyclohexylcarbodiimide
DLS	Dynamic light scattering
DMAP	4-dimethylaminopyridine
DMF	Dimethylformamide
DP	Degree of polymerisation
DTB	Dithiobenzoate
eATRP	Electrochemical ATRP
FRP	Free radical polymerisation
G	Bicontinieous gyroid phase

G’	Storage modulus
G”	Loss modulus
GPC	Gel permeation chromatography
HHH	Hexagonally packed hollow hoops
ICAR	Initiators for continuous activator regeneration
IR	Infrared (spectroscopy)
k_B	Boltzmann constant
L	Lamellae structure
LAM	Less-activated monomers
LAP	Living anionic polymerisation
LCM	Large compound micelles
MA	Methyl acrylate
macro-CTA	Macromolecular chain transfer agent
MAM	More-activated monomers
M_n	Number-average molecular weight
M_w	Weight-average molecular weight
MWD	Molecular weight distribution
N_{agg}	Aggregation number
n-BuLi	*n*-Butyllithium
NMP	Nitroxide-mediated polymerisation
NMR	Nuclear magnetic resonance
ODT	Order-disorder temperature
P	Packing parameter
$P^{\bullet}$	Active radical chain-end
P2EHA	Poly(2-ethylhexyl acrylate)
PAA	Poly(acrylic acid)

PBuMA	Poly(*n*-butyl methacrylate)
PBzMA	Poly(benzyl methacrylate)
PCEA	Poly(2-cinnamoyloxyethyl acrylate)
PDMA	Polydimethylsiloxane
PEP	Polypropylene
PETTC	4-cyano-4-((2-phenylethanesulfonyl)thiocarbonylsulfanyl)pentanoic
PEXA	Poly(2-ethylhexyl acrylate)
PGMA	Poly(glycerol monomethacrylate)
PHEA	Poly(2-hydroxyethyl acrylate
PHPMA	Poly(2-hydroxypropyl methacrylate)
PI	Polyisoprene
PISA	Polymerisation-induced self-assembly
PLMA	Poly(lauryl methacrylate)
PMMA	Poly(methyl methacrylate)
PNAEP	Poly 2-(N-acryloyloxyethyl) pyrrolidone
PPFPMA	Poly(pentafluorophenyl methacrylate)
ppm	Parts per million
PPPMA	Poly(3-phenylpropyl methacrylate)
PPPMA	Poly(3-phenylpropyl methacrylate)
PS	Polystyrene
PSMA	Poly(stearyl methacrylate)
P*t*BA	Poly(tert-butyl acrylate)
PTFEMA	Poly(2,2,2-trifulroethyl methacrylate)
R(t)	Extent of copolymer exchange
RAFT	Reversible addition-fragmentation chain-transfer
R_g	Radius of gyration

RI	Refractive index
R_p	Rate of propagation
R_t	Rate of termination
S	Body-centred cubic sphere phase
St	Styrene
SANS	Small-angle neutron scattering
SAXS	Small-angle X-ray scattering
SLD	Scattering length density
T21s	Tert-butyl peroxy-2-ethylhexanoate
TEM	Transmission electron microscopy
T_g	Glass transition temperature
THF	Tetrahydrofuran
T_m	Melting temperature
TR	Time-resolved
TTC	Trithiocarbonate
UV	Ultra violet
WLF	Williams-Landel-Ferry (Equation)
X_{sol}	Volume fraction of solvent within the core domain
α_T	Shift factor
χ_{AB}	Flory-Huggins parameter
χN	Segregation product

Contents

Chapter 1

Introduction

1.1. Polymer Science

Polymer molecules consist of long chains of repeating units. In the last two decades, polymers have gained increasing attention owing to their wide range of applications in medicine[1-4], cosmetics[5], paints[6], coatings[6] and food manufacture.[5,7] The usefulness of these polymer materials originates from the tunability of their molecular structure; for example, molecular weight and polymer architecture can be varied to obtain the desired material properties.

An important characteristic of polymers is their relatively high molecular weight compared to small molecules. Additionally, polymers do not exhibit a single molecular weight, but a molecular weight distribution (MWD). Two important moments of the MWD are number-average molecular weight (M_n) and the weight-average molecular weight (M_w). M_n is defined as the sum of the molecular weight of all chains (M_i) divided by the number of chains (n_i) (**Equation 1.1**). M_w is based on the weight fraction (W_i) of polymer chains and can be calculated using **Equation 1.2**.[8] M_n is always smaller than (or equal to) M_w (**Figure 1.1**). The dispersity ($Đ$) (formally known as polydispersity index), is a crude way to define the monodispersity of the polymer molecular weight, and can be determined by dividing M_w by M_n (**Equation 1.3**) An M_w/M_n value of unity represents an ideal polymer where all chains have precisely the same molecular weight.[8] In practice, such ideal polymers are not synthetically accessible. However, certain naturally-occurring proteins can exhibit a unique molecular weight.

$$\boldsymbol{M_n = \frac{\Sigma n_i \cdot M_i}{\Sigma n_i}} \quad (\mathbf{1.1})$$

$$\boldsymbol{M_w = \frac{\Sigma W_i \cdot M_i}{\Sigma W_i} = \frac{\Sigma n_i \cdot M_i^2}{\Sigma n_i \cdot M_i}} \quad (\mathbf{1.2})$$

$$\boldsymbol{PDI}\ (Đ) = \boldsymbol{\frac{M_w}{M_n}} \quad (\mathbf{1.3})$$

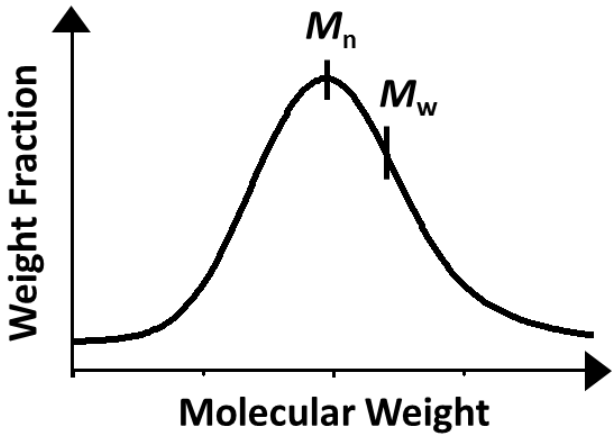

Figure 1.1. Schematic representation of a polymer molecular weight distribution (MWD). Two important moments of this MWD are the number-average molecular weight (M_n) and the weight-average molecular weight (M_w); the former value is always smaller than the latter.

The degree of polymerisation (DP) can be defined as the mean number of repeat units per polymer chain. By definition, the DP is always an integer and it can be calculated from the M_n of the polymer, as shown in **Equation 1.4**.[8]

$$DP = \frac{M_n \text{ of polymer chain}}{\text{Molecular weight of repeat unit}} \quad (1.4)$$

Polymer chains can exhibit various architectures (**Figure 1.2**). The simplest architecture is a homopolymer, which consists of a chain of identical repeat units. In contrast, a statistical copolymer has a random distribution of at least two repeat units along the polymer chain. On the other hand, an alternating copolymer has a more regular structure where the repeat units are strictly alternating in sequence. Block copolymers have spatially separated sequences of repeat units, while a graft polymer has branches emanating from a backbone. A star polymer consists of multiple polymer chains emanating from a centre. Polymer gels (or networks) are obtained when individual polymer chains are chemically crosslinked together to form a macroscopic network.

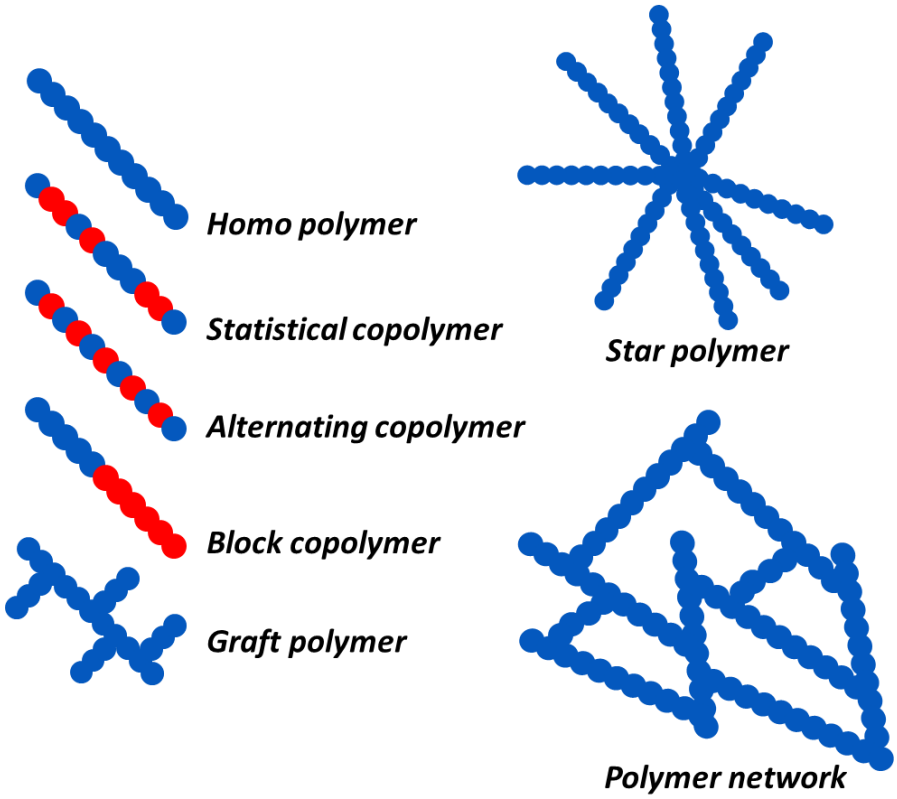

Figure 1.2. Schematic representation of various well-known polymer architectures: homopolymer, statistical copolymer, alternating copolymer, block copolymer, graft copolymer, star polymer and a polymer network (or gel).

1.1.1. Free Radical Polymerisation

One of the most widely used techniques to synthesise polymers in industry is free radical polymerisation (FRP). This technique offers the ability to polymerise a wide range of vinyl monomers with tolerance of both monomer functionality and solvent. Unfortunately, conventional FRP is, like all radical polymerisations, sensitive to oxygen and offers only rather limited control over molecular weight and copolymer architectures. Additionally, polymers prepared by FRP have a broad MWD as a result of uncontrolled termination, side reactions and relative slow initiation. Generally speaking, only limited control over the molecular weight can be achieved when the FRP technique is employed. [8,9]

Conventional FRP consists of three stages: initiation, propagation and termination. Typically, FRP comprises an initiator, a vinyl monomer and an optional suitable solvent depending on

whether the polymerisation proceeds under solution or bulk conditions. During the initiation step, an initiator radical reacts with a vinyl monomer. Examples of commonly used initiators are azobisisobutyronitril (AIBN) and benzoyl peroxide (BPO). These initiators are activated by thermal decomposition, resulting in the formation of two radical species that can initiate polymerisation (**Figure 1.3**).[8,10,11] An active centre is generated when an initiator radical reacts with a monomer. This species is capable of further chain growth (or propagation) by the subsequent addition of multiple monomer units (**Figure 1.4**). In FRP, the rate of initiation is relatively slow to the rate of propagation, which leads to broadening of the MWD. The evolution of molecular weight with conversion is strongly non-linear (**Figure 1.6**).[8]

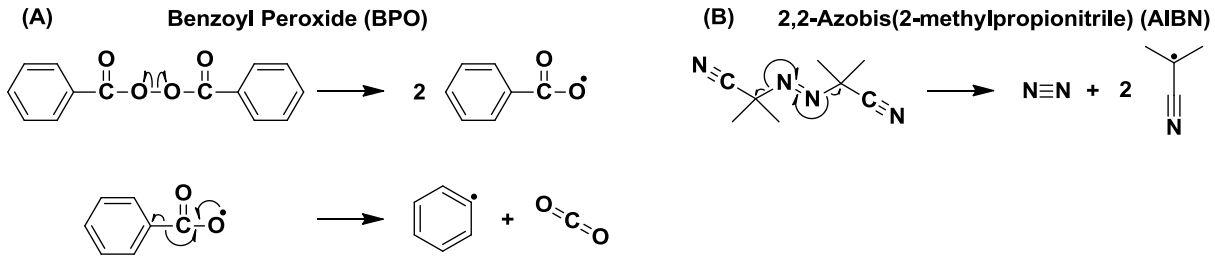

Figure 1.3. Decomposition mechanisms for two thermal initiators; (A) benzoyl peroxide (BPO) generates two radicals and CO_2 as a by-product. (B) azobisisobutyronitril (AIBN) forms two radicals and nitrogen gas.[11]

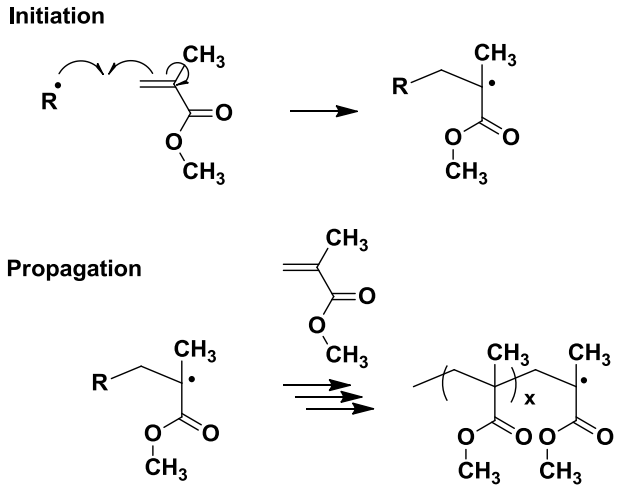

Figure 1.4. Initiation and propagation mechanisms for the free radical polymerisation (FRP) of methyl methacrylate. A radical starts a chain polymerisation by reacting with a vinyl monomer, further monomer addition generates a polymer chain.[8]

Two common termination mechanisms are combination and disproportionation. Termination by combination involves reaction between two active polymer radicals to produce a single 'dead' chain comprising the sum of the molecular weights of the two precursor chains. Termination by disproportionation occurs when an active chain-end abstracts a hydrogen atom from a second growing polymer chain to form a dormant species and a macromonomer; the latter species can participate in further polymerisation (**Figure 1.5**).[8,12] Various chain transfer events can occur during FRP. The most important of these side-reactions is chain transfer to polymer, which readily occurs with acrylic monomers (leading to main chain branching) but is much less common for methacrylic monomers.[13]

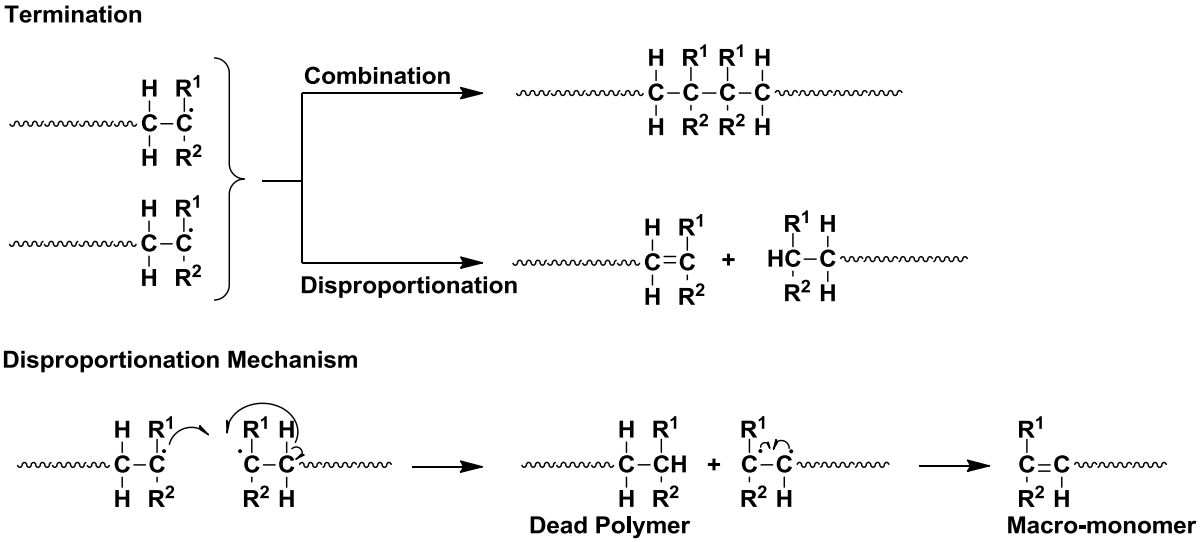

Figure 1.5. Termination by either combination or disproportionation during FRP. When two polymer chains terminate by combination, the final molecular weight becomes the sum of the molecular weights of the two precursor polymer chains. Termination by disproportionation leads to a dead polymer chain-end and a macro-monomer.[8,12]

1.1.2. Living Anionic Polymerisation

When specific molecular weights with narrow MWD polymers are required, living polymerisation techniques can be utilised for the synthesis of certain polymers. In an ideal

living polymerisation, initiation occurs at the start of the reaction, then all polymer chains propagate at a similar rate, and no termination or irreversible chain transfer occurs. This means that a linear increase in molecular weight against conversion is expected for a living polymerisation (**Figure 1.6**). A relatively rapid rate of initiation compared to the rate of propagation results in narrow MWDs.[9] Living polymerisations enable the synthesis of more complex polymer architectures such as block copolymers. In this particular case, a chemically different block is generated by simply adding a second monomer to a 'living polymer' after full consumption of the first monomer.[8]

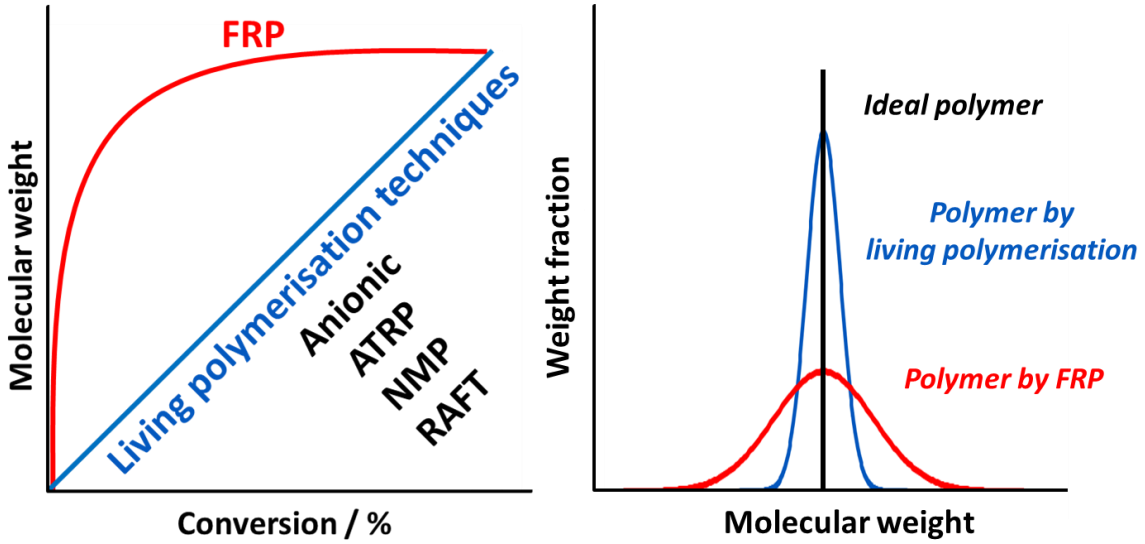

Figure 1.6. (left) Schematic representation of the evolution of molecular weight with conversion for FRP and various types of living polymerisations (e.g. anionic, ATRP, NMP and RAFT). (right) Schematic representation of GPC curves from an ideal polymer, a polymer via a living polymerisation techniques and a polymer prepared via FRP. A larger MWD is observed for a polymer compared by FRP in comparison to a polymer via living polymerisation.

A classical example of living polymerisation is living anionic polymerisation (LAP). A strong base, such as *n*-butyllithium (*n*-BuLi), is used to initiate the anionic polymerisation of a vinyl monomer such as styrene (**Figure 1.7).**[8] The living character is conferred by the anionic chain-ends which cannot react with one another, thus preventing termination by

combination. Since narrow MWDs are observed and termination is absent in anionic polymerisations, a specific DP can be targeted using **Equation 1.5**, assuming full monomer conversion and 100% initiator efficiency, where [M] and [I] are the monomer and initiator concentration, respectively.[8]

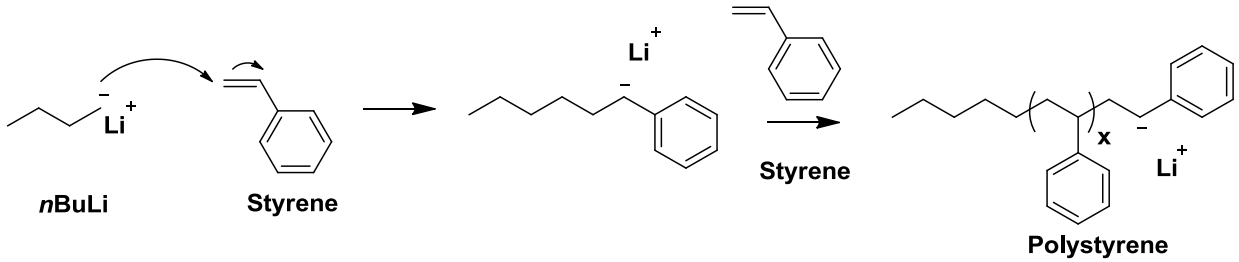

Figure 1.7. Anionic polymerisation mechanism of styrene. A strong base such as *n*-BuLi initiates the polymerisation by forming a carbanion on the polymer chain-end, which is capable of further propagation.

$$\mathbf{DP} = \frac{[\mathbf{M}]}{[\mathbf{I}]} \qquad (\mathbf{1.5})$$

LAP offers a useful synthetic route for the preparation of monodisperse polymers. Unfortunately, it suffers from several disadvantages. Since the growing chain-end is a carbanion, it can be readily protonated by protic solvents such as water, resulting in termination.[8] LAP is generally performed at or below room temperature. One important disadvantage is the limited choice of vinyl monomers that are suitable for LAP. Styrene is a suitable monomer for LAP (**Figure 1.8A**), because it is able to stabilise anionic charge due to its electron-withdrawing aromatic group. In contrast, propylene (**Figure 1.8B**) is not suitable because its methyl substituent donates electrons and destabilises the negative charge.[8] Other unsuitable vinyl monomers for LAP include those containing labile protons, which are easily abstracted by the basic initiator (or anionic chain-end). An example of one such monomer is acrylic acid (**Figure 1.8C**).[8]

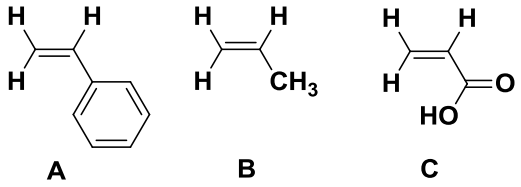

Figure 1.8. Chemical structures of (A) styrene, (B) propylene and (C) acrylic acid. Styrene is able to stabilise the negative charge during LAP, making this monomer suitable for this polymerisation technique. In contrast, the electron-donating methyl group on propylene makes this species unsuitable. The labile proton form acrylic acid makes this monomer unsuitable for LAP.

1.1.3. Controlled/Living Radical Polymerisation

Nitroxide-mediated polymerisation (NMP)[9,14], atom transfer radical polymerisation (ATRP)[15] and reversible addition-fragmentation chain-transfer (RAFT)[15] polymerisation, have been developed over the past 25 years. These polymerisation techniques are known as controlled/living radical polymerisation (CLRP) techniques. Like LAP, they offer good control over the MWD. Additionally, as a radical mechanism is employed, a wide range of functional vinyl monomers can be polymerised in various solvents.

1.1.3.1.1. Nitroxide Mediated Polymerisation

Growing polymer chains are reversibly deactivated through reactions with stable nitroxide radicals during NMP (**Figure 1.9**). The preferential reaction of polymer radicals with the stable nitroxide radical or with monomer units minimises termination by combination or disproportionation. Additionally, termination is suppressed owing to the persistent radical effect. Here, cleavage of the C-ON bond results in unstable transient radicals and stable persistent nitroxide radicals. Transient radicals can be source of initiation (together with optional addition of a thermal initiator, while persistent radicals act as capping agents and are responsible for the living character. The concentration of transient radicals reduces over time through self-termination, initiation and combination reactions of growing polymer chains in the early stages of the reaction. In contrast, the persistent radical concentration does not

change due to its inability to self-terminate. Self-termination of the transient radicals continues over time, causing nitroxide capped polymer chains to become the main reaction product. Rapid reversible capping lowers the effective polymer radical concentration, which reduces the probability of termination. Rate of termination $(R_t) \propto [P^\bullet]^2$, whereas the rate of propagation $(R_p) \propto [P^\bullet]$, where $[P^\bullet]$ corresponds to the concentration of active chain-ends.[14,16]

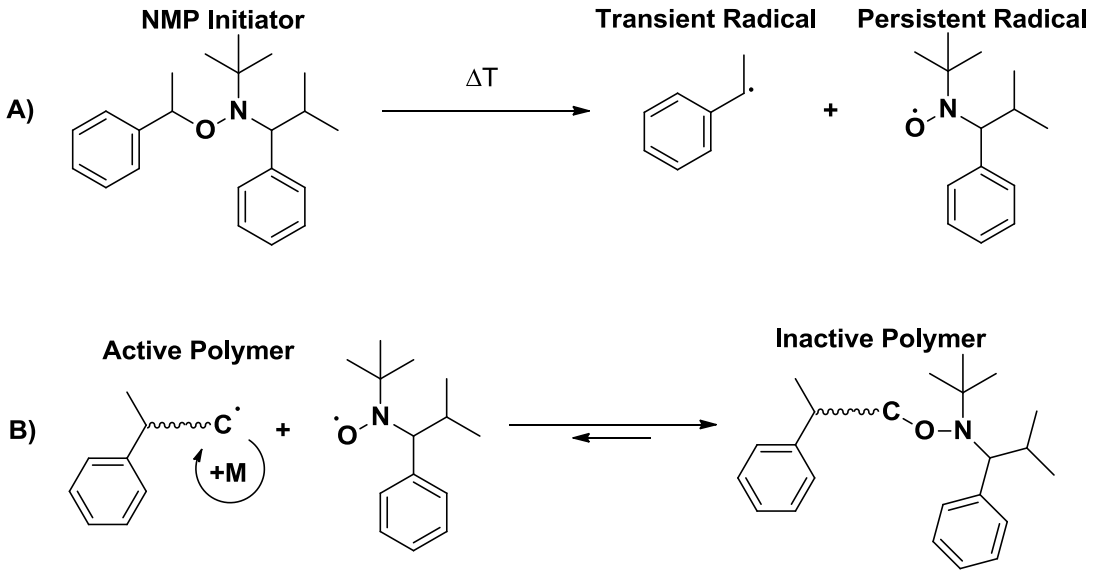

Figure 1.9. (A) Thermal initiation of an NMP initiator forms a stable persistent radical and an unstable transient radical. (B) Reversible deactivation/activation equilibrium for NMP. Active polymer chains can be reversibly capped with persistent radicals to form an inactive polymer species.[14,16,17]

The more widespread use of NMP has been prevented by its own intrinsic limitations and the concomitant development of the two other competing CLRP techniques (ATRP and RAFT polymerisation). NMP suffers from three main disadvantages compared to other CLRP techniques. It requires high reaction temperatures owing to the slow polymerisation kinetics. In addition, nitroxides are often not commercially available and need to be synthesised in-house. Moreover, nitroxides cannot be used to homopolymerise methacrylates because the relatively high reaction temperature leads to hydrogen abstraction from the methyl group on the monomer by the nitroxide, which leads to its deactivation. However, NMP can be

preferred in certain cases because alternative CLRP techniques suffer from their own disadvantages, as discussed in the following sections.

1.1.3.1.2. Atom Transfer Radical Polymerisation

ATRP is based on an activation/deactivation mechanism between an alkylhalide (ATRP initiator) and a transition metal (ATRP catalyst) (**Figure 1.10**). The ATRP initiator oxidises the ATRP catalyst and a halogen atom is transferred to the ATRP catalyst, simultaneously a radical is formed that is capable of initiating the polymerisation. Active polymer chain-ends can be reversibly deactivated by the transition metal complex. This converts the active polymer radical into a dormant halogen-capped polymer. ATRP can be mediated with various transition metal complexes such as Ru, Fe, Mo, Os; however, Cu is the most commonly used.[15,18]

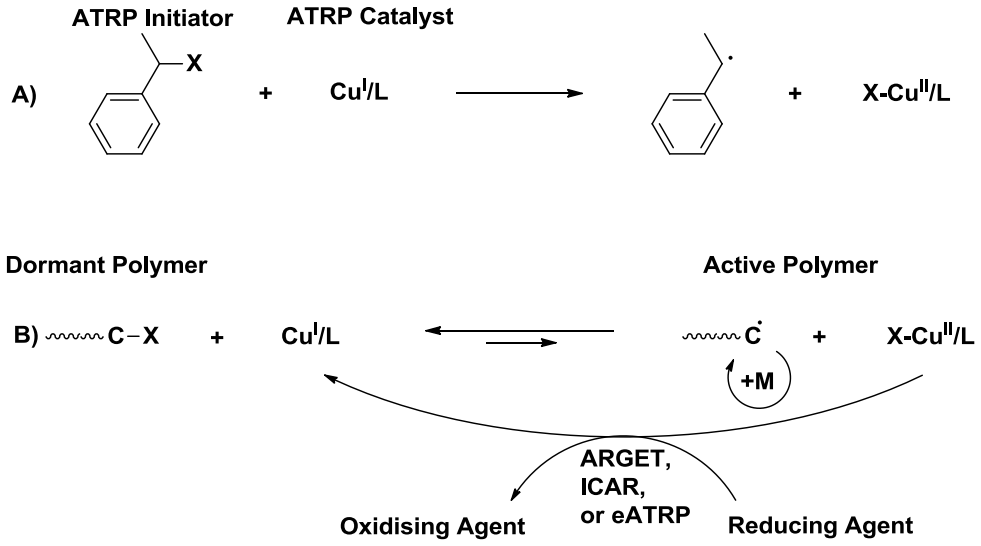

Figure 1.10. Cu-mediated ATRP mechanism, where X corresponds to a halogen atom. (A) An ATRP catalyst reacts with the ATRP initiator forming a radical species capable of initiating a polymerisation. (B) Dormant alkyl halide polymer is capable of reinitiation via reaction with a transition metal in its lower oxidation state.[18]

ATRP is a convenient technique for the production of many types of polymers with narrow MWDs. However, several important disadvantages have limited its industrial use. The

requirement for a transition metal catalyst introduces several problems. The ATRP catalyst concentration is often comparable to that of the ATRP initiator. This leads to post polymerisation purification steps which are both necessary and expensive. Another disadvantage of ATRP in terms of the production of block copolymers is the selection of a specific alkyl halide and transition metal catalyst for the monomer class of interest. Finally, most transition metals are mildly toxic, which can cause problems for potential biological applications.[15,18]

Fortunately, there are several ATRP methods developed to counter these problems. For example, so-called reverse ATRP is less oxygen-sensitive than some ATRP formulations. Instead of Cu^{I}, the more stable Cu^{II} species is used in combination with a thermal initiator, which generates the required Cu^{I} species *in situ*. In this approach, the initial starting materials are less prone to oxidation. Other methods can regenerate the inactive Cu^{II} species, generally by utilising a reducing agent. The so-called activators regenerated by electron transfer (ARGET) ATRP method uses reducing agents that do not produce radicals to regenerate inactive Cu^{II}. Examples of such reducing agents are trimethylamine or ascorbic acid. Another approach, named initiators for continuous activator regeneration (ICAR) ATRP utilises thermal initiators to regenerate the inactive Cu^{II} species. A general downside of these ATRP methods is the introduction of additional impurities to the polymer product. A technique which does not suffer from these disadvantages is electrochemical (eATRP). Here, potential current can be altered to obtain the desired concentration of redox-active catalytic species.[15,18,19]

1.1.3.2. Reversible Addition-Fragmentation Chain Transfer (RAFT) Polymerisation

RAFT polymerisation is a CLRP where initiation and propagation are conform to a FRP. Additionally, a chain transfer agent (CTA) is added to the reaction solution. This molecule induces a rapid equilibrium between active and dormant polymer chain-ends by a two-step addition-fragmentation mechanism (**Figure 1.11**). This equilibrium ensures equal probability for all polymer chains to grow, which results in a narrow molecular weight distribution.

Many CTAs are now commercially available. They possess the same three features which should be varied accordingly based on the kind of monomer (**Figure 1.12**). The first feature

is the C=S double bound where active polymer radicals are able to add to the CTA. Secondly, CTAs contain a Z group, which stabilises to the intermediate species and determines the reactivity of the C=S bond. The CTA reactivity can be tuned by modification of this Z group; electron-donating groups confer stabilisation by conjugation with the C=S bond. This lowers the addition rate of active chain-ends to the sulfur atom, and so affects the overall rate of chain transfer. In contrast, electron-withdrawing Z groups lead to an increase in addition rate. The final component of the CTA is the R group, which is a radical leaving group that is capable of re-initiating polymerisation. This R group should be a better leaving group compared to the propagating radical. In most cases a cyanoalkyl or cumyl group is preferred.[9,20-23]

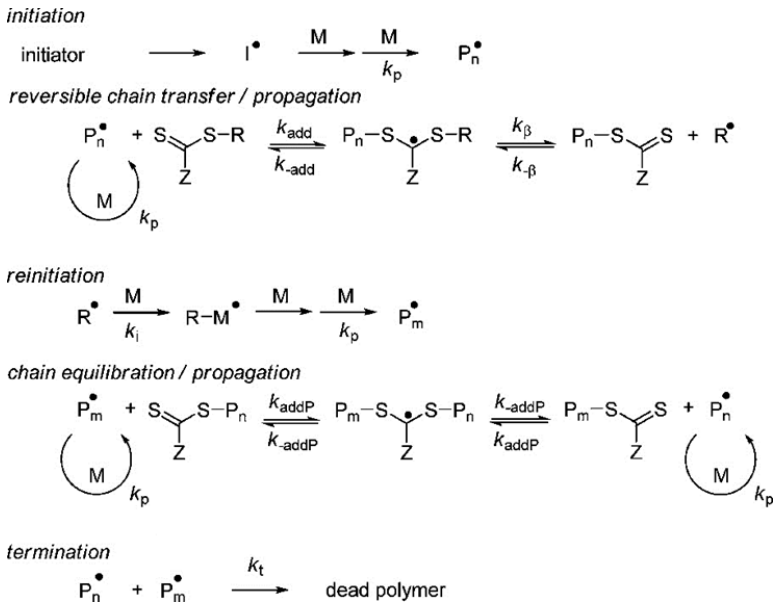

Figure 1.11. The RAFT reaction mechanism according to Rizzardo and co-workers. Initiation proceeds similar to the conventional radical polymerisation mechanism. Active polymer chain-ends can reversibly react with the chain transfer agent (CTA), which results in a dormant polymer chain. During this process fragmentation of the leaving group (R) occurs, which initiates a new polymer chain. The rapid equilibrium between the active and dormant chain-ends ensures the living character of the polymerisation. Termination follows the same mechanism as in conventional radical polymerisation. However, this is suppressed due to the relatively low radical concentration compared to the total amount of active and dormant polymer chains. Here, $I^{\bullet}$, $P_n^{\bullet}$ and $P_m^{\bullet}$ correspond to the radical initiator fragments and active polymer chain ends; K_p, K_{add} , K_{addP} and K_β correspond to the reaction rate; K_i and K_t correspond to the rate of initiation and termination, respectively.[21]

The appropriate choice of CTA strongly depends on the corresponding monomer species (**Figure 1.12**). Generally, vinyl monomers can be divided into two categories: More-activated monomers (MAMs) are less reactive towards propagation owing to their conjugation, hence they are more reactive towards deactivation via interaction with the CTA. Examples of such monomers are vinyl aromatics (e.g. styrene), methacrylics and acrylics. In contrast less-activated monomers (LAMs) are not conjugated, which makes these monomers highly reactive towards propagation, and less susceptible to react with the CTA. Vinyl esters and vinyl amides are examples of such monomers. Dithiobenzoate CTAs (and other dithioester) are well suited for the polymerisation of MAMs. Here, the Z group leads to a high addition rate due to the electron-withdrawing groups that makes the C=S bond more electrophilic.[24] Living radical polymerisation of LAMs is more challenging since the more active CTAs inhibit polymerisation of these species.[9]

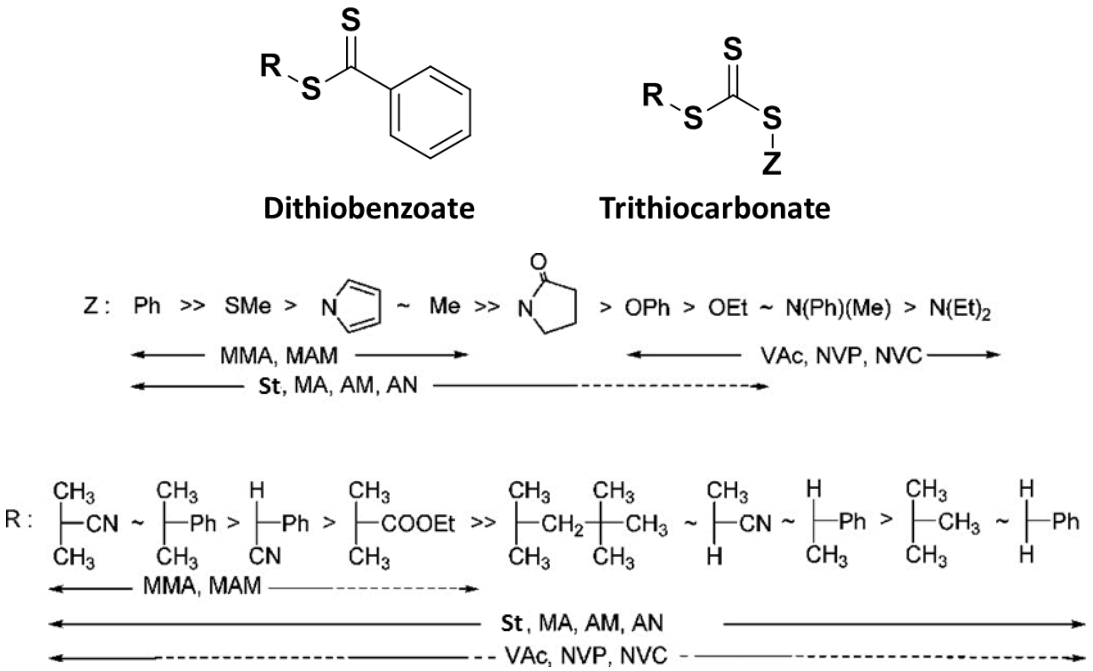

Figure 1.12. CTA selection guidelines. For the Z group, fragmentation rates increase from left to right (and addition rates decrease). For the R group, fragmentation rates reduce from left to right. The dashed line is an indication of limited control. The following abbriviations are used in this figure: phenyl (Ph), methyl (Me), ethyl (Et), methyl methacrylate (MMA), methyl acryl amide (MAM), styrene (St), vinyl acetate (VAc), *N*-vinylpyrrolidone (NVP), *N*-vinylcarbazole (NVC), methyl acrylate (MA), acrylamide (AM), acrylonitrile (AN).[9] (N.B. this Figure has been slightly modified from that reported in ref. 9)

Another characteristic of a well-controlled RAFT polymerisation is the CTA/initiator molar ratio. This is always greater than unity, typically ratios between five and hundred are used. This means that most of the polymer chains are initiated by the R-group of the CTA ('R' RAFT end) instead of the initiator fragments. The amount of active polymer chains is much smaller than the amount of dormant polymer chains ('ZCS_2' RAFT end), which results in minimal termination (dead chains) (**Figure 1.13**).[9] Due to the linear relation between molecular weight and conversions for all living polymerisations, and because almost all polymer chains are initiated by the CTA, the target DP can be determined from the ratio between the monomer and the CTA concentrations (**Equation 1.6**).

$$\mathbf{DP} = \frac{[\mathbf{M}]}{[\mathbf{CTA}]} \quad (\mathbf{1.6})$$

Here, [M] and [CTA] represent the monomer and CTA concentration, respectively. A typical dispersity for a RAFT polymerisation is 1.2-1.3. RAFT polymerisation usually produces a slightly broader molecular weight distribution compared to anionic polymerisation, but the former technique requires much less stringent polymerisation conditions and is applicable to a far wider range of functional vinyl monomers.

One disadvantage of RAFT polymerisation is that the thiocarbonylthio compound species remains as an end-group on most of the polymer chains, which leads to intrinsically coloured polymers.[9] This malodorous reagent also has a certain degree of toxicity, which is problematic for applications such as drug delivery.[1,25] Fortunately, several strategies for the removal of these RAFT end-groups, such as oxidation[26] or reduction[27] have been identified. Resent research has shown that trithio carbonate RAFT agents are more robust than dithio benzoates, and are more difficult to remove from diblock copolymer nanoparticles.[28] Chain-end stability needs to be considered when preparing high molecular weight monomers, longer reaction times increase the change of termination by combination, and chain-end degradation is detrimental for RAFT polymerisation. In general, RAFT polymerisation is more suitable for the preparation of polymers of intermediate molecular weight.

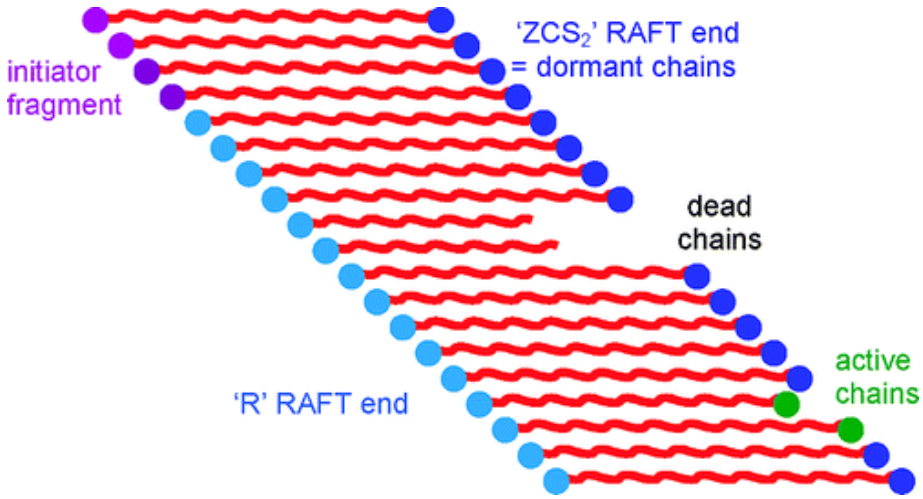

Figure 1.13. General schematic of a RAFT polymerisation. A rapid equilibrium, with respect to propagation, between dormant ('ZCS_2' RAFT end) and active chain-ends allows all chains to grow with a similar rate, resulting in a narrow MWD. Most polymer chains are initiated by 'R' RAFT ends (CTA leaving groups [R]), not by initiator fragments. Hence, the proportion of 'ZCS_2' RAFT ends is much larger than that of the active propagating chains. The low active chain-end concentration leads to a low chance of termination via combination, hence only a few (ideally none) dead polymer chains are present during the RAFT polymerisation.[9]

1.2. Block Copolymer Self-Assembly

Molecular self-assembly is an important natural phenomenon; phospholipids form cell membranes and surfactants form micelles above their critical micelle concentration (CMC).[29] Apart from phospholipids and surfactants, amphiphilic AB diblock copolymers can also self-assemble in solution. Such polymer micelles can be more stable than small-molecule surfactant micelles.[30] The principle of block copolymer self-assembly is based on enthalphic incompatibility, either between the two blocks in the solids or between the hydrophobic block and the aqueous solution. Block copolymer micelles can also be formed in organic solvents if the solvent is a selective solvent for one of the blocks.[31-33]

1.2.1. Block Copolymer Self-Assembly in the Solid State

Interfacial reduction between immiscible block copolymer chains is the driving force for block copolymer self-assembly in the bulk (also known as micro-phase separation). This process can lead to a range of copolymer morphologies. Specific morphologies can be targeted by varying the relative volume fraction of each block, the total DP and the block copolymer types. The degree of incompatibility between the two blocks can be tuned by careful selection of the monomer repeat unit. This aspect is captured by the Flory-Huggins parameter (χ_{AB}) (**Equation 1.7**).

$$\chi_{AB} = \left(\frac{z}{k_B T}\right)\left[\varepsilon_{AB} - \frac{1}{2}(\varepsilon_{AA} + \varepsilon_{BB})\right] \quad (1.7)$$

Here z is the number of nearest neighbours per repeat unit, k_B is the Boltzmann constant, T is the absolute temperature in °K and ε_{AA}, ε_{BB} and ε_{AB} are the respective interaction energies between the two types of repeat units.[34,35]

The degree of micro-phase separation depends on the segregation product (χN) (**Equation 1.8**). This parameter is obtained by multiplying the Flory-Huggins interaction parameter by the total DP of the copolymer. The higher the segregation product, the more incompatible the two blocks, which makes micro-phase separation more likely to occur at a given temperature.

$$\chi N = \chi_{AB} \times DP \quad (1.8)$$

Temperature plays an important role with respect to the degree of incompatibility between the two blocks. **Equation 1.7** shows that higher temperatures reduce the mutual incompatibility between blocks. Hence, thermal annealing can lead to a reversible order-

disorder transition. The temperature at which this occurs is known as the order-disorder temperature (ODT).[35,36]

A range of block copolymer morphologies in the bulk were predicted by Förster and Bates based on varying the segregation product and volume fraction of each segment, and summarised in a phase diagram (**Figure 1.14A and 1.14B**).[35] This shows an increase in volume fraction for one block, at a certain χN value, results in the formation of various ordered structures. The first morphology is closely packed sphere (CPS) phase. A slight increase in volume fraction of the minor block produces a body-centred cubic sphere phase (S). Hexagonally-packed cylinders (C) and a bicontinieous gyroid phase (G) were predicted at higher volume fractions. Finally, a lamellae structure (L) was predicted for approximately equal fractions. A further increase in volume fraction leads to a series of identical morphologies with inverted compositions. This phase diagram also predicted disordered blends below $\chi N \sim 10$. This suggests that lower molecular weight block copolymers do not undergo microphase separation.[34-36]

These predicted block copolymer morphologies were experimentally verified for a series of polyisoprene-polystyrene (PI-PS) diblock copolymers prepared by anionic polymerisation. Bulk morphologies and phase transitions were confirmed using dynamic mechanical spectroscopy, TEM, small-angle X-ray and neutron scattering (SAXS and SANS). An experimental phase diagram was constructed that closely resembled the theoretical predication (**Figure 1.14C**).[35,37]

(Although, classically, a phase diagrams represent the reversible physical distinct states (solid, liquid and gas) of substances under various temperatures and pressure in equilibrium; block copolymer phase diagrams are different, and can therefore be more accurately classified as morphology maps. However, since the block copolymer literature describes these morphology maps as 'phase diagrams',[35,37-40] this work uses same term to describe these figures, out of consistency [despite of the Author's preference]).

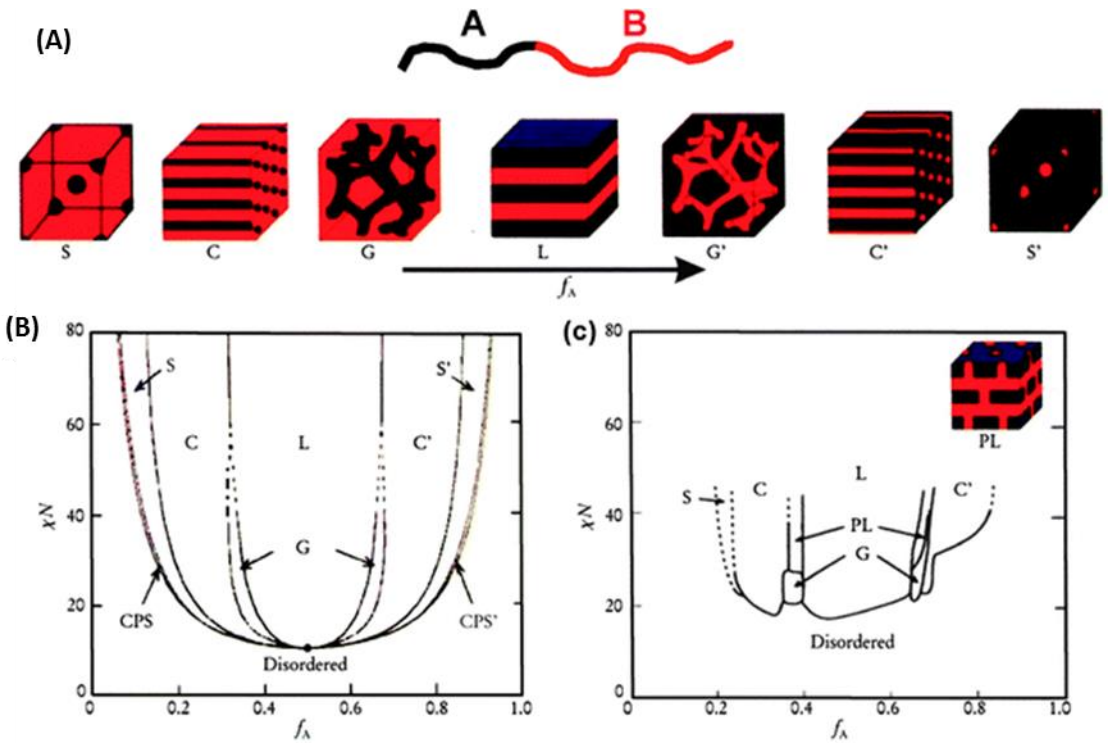

Figure 1.14. (A) Schematic representation of block copolymer morphologies in the bulk. A change in volume fraction leads to the evolution of various copolymer morphologies: body-centered-cubic spheres (S), hexagonally-packed cylinders (C), bicontinuous gyroids (G) and lamellae (L). Inverted morphologies (denoted by S', C', G' and L') are predicted for a further increase in volume fraction. (B) Theoretical phase diagram for a linear block copolymer, various morphologies were predicted for certain volume fractions and segregation products (χN). (c) Experimental phase diagram determined for polyisoprene-polystyrene (PI-PS) block copolymers in the bulk, for which an additional perforated lamellae phase was observed (PL).[35,37]

1.2.2. Block Copolymer Self-Assembly in Solution

Block copolymers can self-assemble in the bulk and also in solution, with sterically-stabilised nanoparticles being obtained in the latter case. Self-assembly in solution is more complex compared to that in solid state. The introduction of a single solvent (or solvent mixtures) introduces additional interaction parameters. Six interaction parameters are involved for a block copolymer in a binary mixture of two solvents, which consists of a good solvent for both blocks and a selective solvent (i.e. good solvent for one block, but a bad solvent for the

other block). One striking difference between self-assembled block copolymer micelles compared to the bulk morphologies is the wider range of accessible morphologies. For example, eight ordered structures were observed for polystyrene-poly(acrylic acid) block copolymers in water (**Figure 1.15**).[30,41]

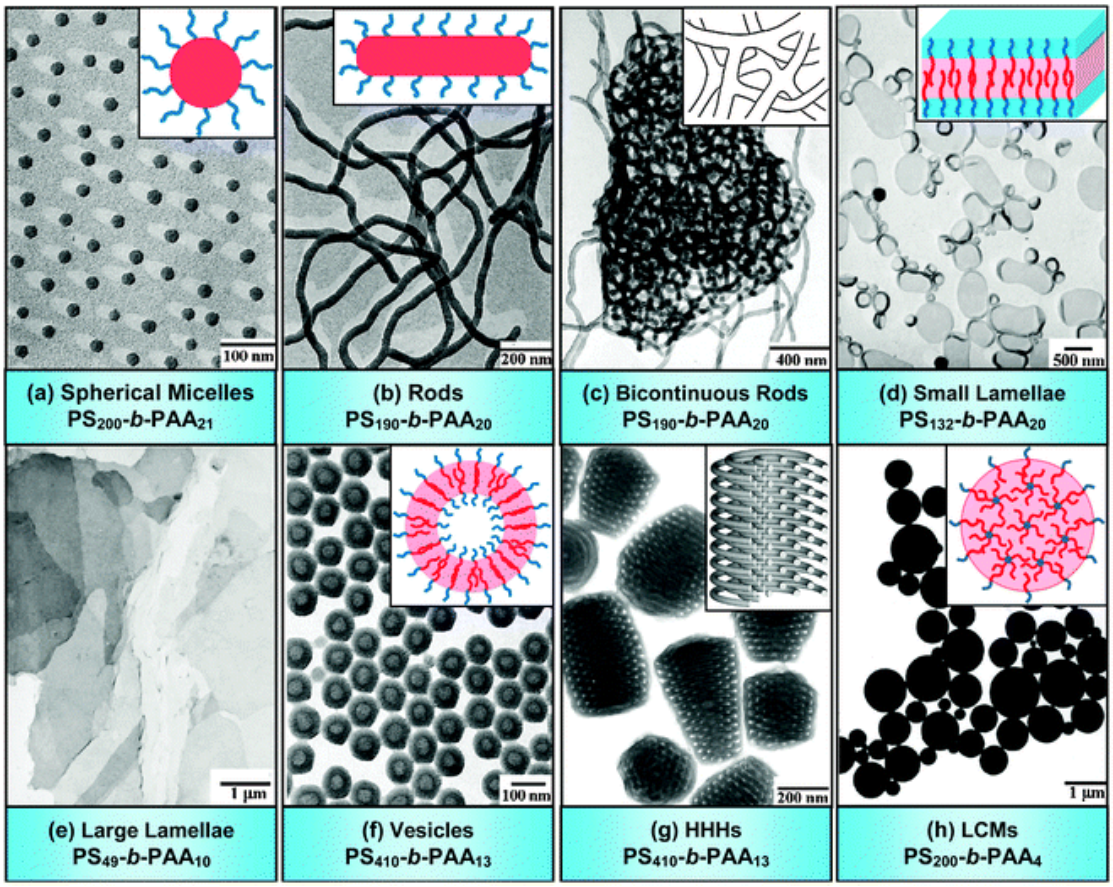

Figure 1.15. Transmission electron microscopy (TEM) images from various polystyrene-poly(acrylic acid) (PS-PAA) diblock copolymer nanostructures in water. Where, blue is the hydrophilic PAA and red the hydrophobic PS block. HHHs are hexagonally packed hollow hoops and LCMs are large compound micelles.[41]

Colloidal dispersions of block copolymer nanoparticles are traditionally prepared via post-polymerisation self-assembly. For example a 'solvent-switch' method is commonly used.[30,42,43] Here, the block copolymer is dissolved in a good solvent prior to slow addition of a selective solvent. The latter component induces block copolymer self-assembly as the solvent mixture becomes less favourable for one of the two blocks. This block forms the micelle cores, while the other block acts as steric stabiliser. Particles are formed on addition

of sufficient selective solvent. Finally, the good solvent can be removed if desired by dialysis or heating *in vacuo*.[42-45]

The block copolymer morphology is dictated by the relative block copolymer volume fractions.[30] A large mismatch between block volume fractions results in a high curvature (**Figure 1.16**). Desired block copolymer morphologies can be achieved by adjusting the degree of polymerisation of the individual blocks. A higher curvature results in spherical nanoparticles, while lower curvature leads to the formation of higher order morphologies.[44,45] For example, spheres, rods, vesicles and lamellae were observed by varying the poly(acrylic acid) (PAA) DP for a series of PS-PAA block copolymers in a DMF-water binary solutions (**Table 1.1**). Here, the hydrophilic PAA sterically stabilises the PS cores. Reducing the volume fraction of the PAA block results in a reduction in surface area per corona chain (A_c), and less stretched core-forming PS segments (S_c). This leads to a reduction in curvature, and hence evolution from spheres to higher order morphologies.[30]

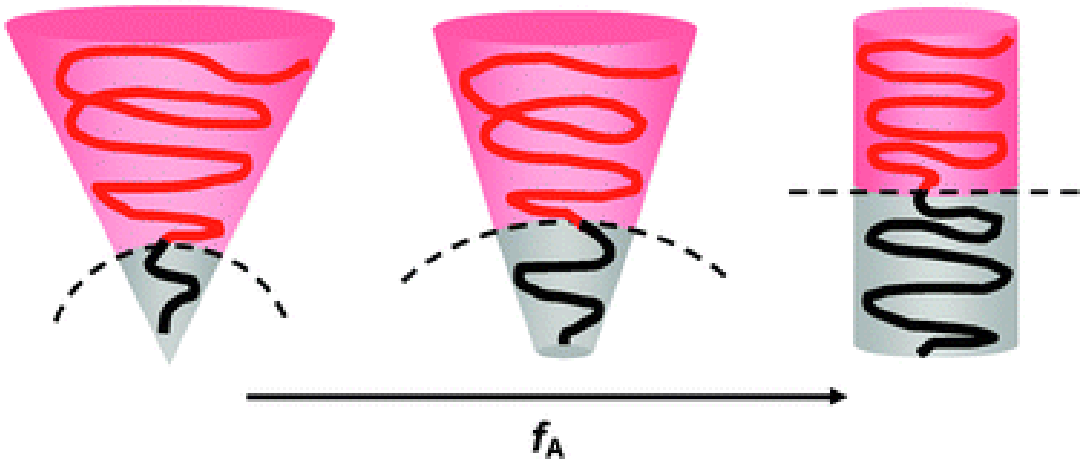

Figure 1.16. Relative block volume fractions in a diblock copolymer dictate the copolymer morphology. A relatively long stabiliser block favours spheres, whereas a relatively long insoluble block favours bilayers or vesicles. Worms are obtained at intermediate volume fractions.[46]

Table 1.1. Summary of a series of four polystyrene-poly(acrylic acid) (PS-PAA) block copolymers where a systematic reduction in PAA molar fraction leads to an evolution in copolymer morphology. PS dimension is the average diameter of spherical nanoparticles, mean rod thickness or vesicular membrane thickness. S_c refers to the degree of stretching of the core-forming PS blocks, and A_c refers to the surface area of the PAA corona chains at the core/corona interface.[30]

Composition	PAA (mol%)	Morphology	PS dimension (nm)	S_c	A_c (nm^2)
PS_{200}-PAA_{21}	9.5	Spheres	26	1.41	8
PS_{200}-PAA_{15}	7	Rods	23	1.26	5.8
PS_{200}-PAA_{8}	3.8	Vesicles	18	0.99	4.2
PS_{200}-PAA_{4}	2	LCMs	—[a]	—[a]	—[a]

[a]Not applicable because LCMs consist of a large number of reverse micelles with polar PAA cores in a PS matrix.

Copolymer concentration is another important parameter with regard to the morphology. For example, PS_{190}-PAA_{20} block copolymers can form spheres, rod or vesicles in DMF-water mixtures on varying the copolymer concentration from 1.0 to 3.5% w/w.[40,47,48] This observation was explained in terms of the relationship between copolymer concentrations and aggregation number, **Equation 1.9.**

$$\boldsymbol{N_{agg} = 2(C/CMC)^{1/2}} \quad (\mathbf{1.9})$$

Here, N_{agg} represents the aggregation number (mean number of polymer chains per nano-object), C is the copolymer concentration and CMC is the critical micelle concentration for this specific formulation in a particular solvent composition. This equation indicates simultaneous increase in copolymer concentration with N_{agg}, which leads to larger spheres or speculatively more efficient packing into higher order morphologies. However, it should be mentioned that this equation was originally derived for small molecule surfactants.[49,50]

The concentration of selective solvent affects the CMC and hence the N_{agg}. For example, an increase in water content for the previously discussed PS-PAA copolymer dispersions results in a reduction in CMC due to unfavourable interaction with the hydrophobic PS block.[49] This allows convenient tuning of the N_{agg} and copolymer morphology by careful addition of water, as shown in **Figure 1.17**. Insufficient water does not induce self-assembly. Once the critical water content (CWC) is reached, nucleation occurs to form spherical micelles. Further addition of water causes a reduction in the number of particles via particle fusion. As a result, both N_{agg} and the core diameter increase, since the interfacial area between the core and the selective solvent (water) is reduced. Eventually, the addition of water results in a morphological transition from spheres to rods and eventually to vesicles.[30,40,49]

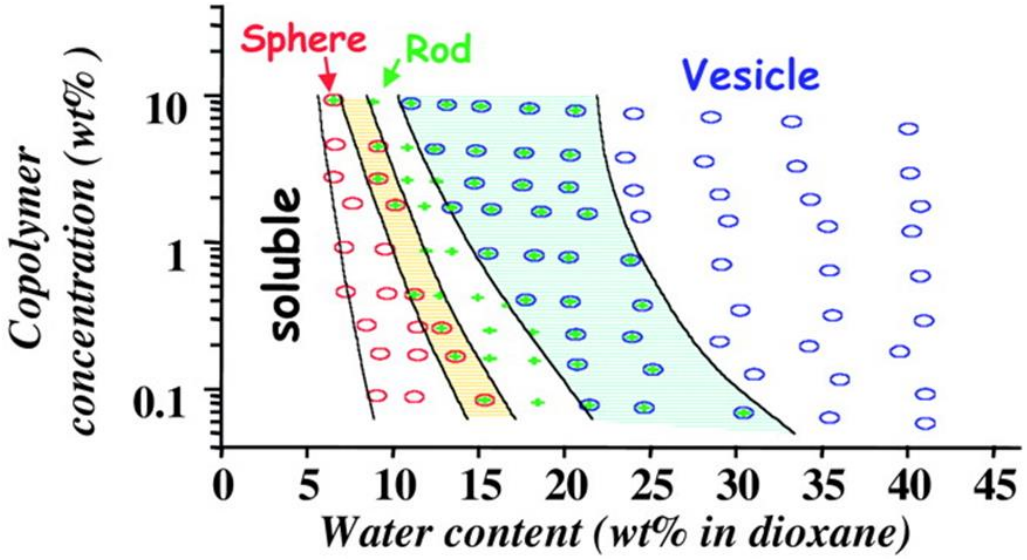

Figure 1.17. Phase diagram constructed for a polystyrene-poly(acrylic acid) (PS_{310}-PAA_{52}) block copolymer where the copolymer concentration and the dioxane-water solvent ratio is systematically altered. Low water contents result in homogeneous mixtures and spherical nanoparticles, whereas higher water concentrations result in higher order morphologies, such as rods and vesicles. Mixed phases are observed in the coloured intermediate regions between the sphere and rod phase.[40]

The choice of good solvent for both blocks can also affect the nanoparticle morphology because it affects the dimensions of both the hydrophobic core-forming block and the hydrophilic corona. For example, a PS_{200}-PAA_{18} block copolymer forms spherical particles

when DMF is used as a common solvent but large compound micelles (LCM) are observed when THF is used instead under the same conditions. This difference can be attributed to the core-block solubility in the solvent. THF is a better solvent for PS than DMF; core solvation in the former case leads to a reduction in copolymer curvature and hence higher order morphologies.[32,51,52]

1.2.3. Polymerisation-Induced Self-Assembly in Polar Media

Traditionally, block copolymer self-assembly in the bulk and in solution involves post-polymerisation methods. A more direct route for the preparation of nanoparticle dispersions is offered by polymerisation-induced self-assembly (PISA). This approach utilises the polymerisation to drive *in situ* block copolymer self-assembly, with the gradually depleting monomer effectively acting as a co-solvent for the insoluble block. RAFT polymerisation is commonly utilised for PISA synthesis. A two-step process is usually used for block copolymer nanoparticle syntheses via PISA. First, a homopolymer (macro-CTA) is prepared via RAFT *solution* polymerisation. Subsequently, this soluble homopolymer is chain-extended with a second monomer to form a diblock copolymer. This second polymerisation can be performed under either *dispersion* or *emulsion* polymerisation conditions, where the second monomer is either miscible or immiscible, respectively. In each case the second monomer is chosen to produce an insoluble block under the reaction conditions. Once a sufficiently high DP is attained, nucleation occurs and polymerisation continues within the nanoparticle cores. The most common morphologies are spheres worms and vesicles, each of which can be readily targeted by adjusting the DP of each block and the overall copolymer concentration. Moreover, PISA can be performed as a "one-pot synthesis" whereby the second monomer is added to the reaction mixture once high conversion is attained for the first monomer. PISA typically offers faster kinetics in comparison to the equivalent solution polymerisation in a good solvent. An increase in reaction rate is almost invariably observed immediately after nucleation owing to a higher local monomer concentration within the monomer-swollen nanoparticle cores.[31,53-57]

A well-established RAFT PISA formulation is the synthesis of poly(glycerol monomethacrylate)-poly(2-hydroxypropyl methacrylate) (PGMA-PHPMA) nano-objects in water. Here, a water-soluble $PGMA_{47}$ macro-CTA is chain-extended with the water-miscible HPMA monomer. $PGMA_{47}$-$PHPMA_x$ diblock copolymers undergo self-assembly once the

insoluble core-forming PHPMA block reaches a critical DP (i.e. critical insoluble block volume), to reduce the interfacial area between the polymer block and the solvent. Spheres, worms and vesicles can be readily targeted by adjusting the core-forming PHPMA DP when using a fixed PGMA DP (**Figure 1.18**).

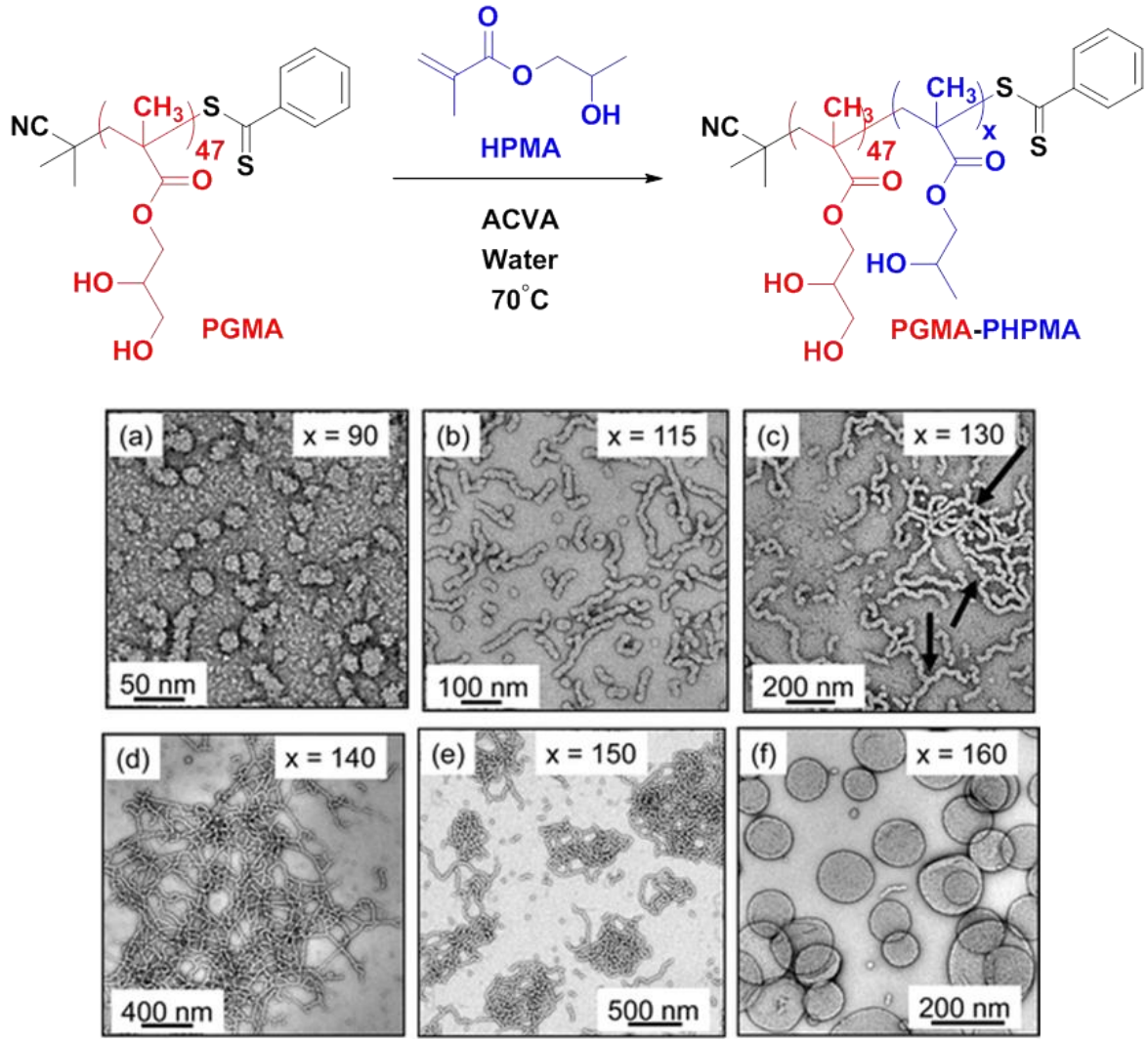

Figure 1.18. TEM images obtained for $PGMA_{47}$-$PHPMA_x$ block copolymer nanoparticles prepared via RAFT PISA in water (10 % w/v copolymer concentration), where x corresponds to (a) 90, (b) 115, (c) 130, (d) 140, (e) 150 and (f) 160. The black arrows in (c) indicate branching points within the worms.

The $PGMA_{47}$-$PHPMA_{200}$ composition forms vesicles in water at 10% w/v. A morphological evolution is observed during the preparation of these block copolymers via RAFT-mediated PISA (**Figure 1.19**). Spherical nanoparticles appear after nucleation once a critical HPMA DP is attained at around 40% HPMA conversion. Subsequently, worms are generated by the multiple 1D fusion of spherical particles at around 55% conversion.[58] When the DP of the core-forming block is increased further, branched worms are formed and eventually bilayer octopus structures are observed. These octopus structures then 'wrap up' to form jellyfish and well-defined vesicles are obtained at full HPMA conversion. The crucial step for the morphological evolution towards higher order morphologies is the initial *fusion* of spherical particles. Worm-like particles cannot be formed without this first essential step, hence higher order morphologies would become inaccessible and the copolymer morphology is restricted to kinetically-trapped spheres.[31,53-56]

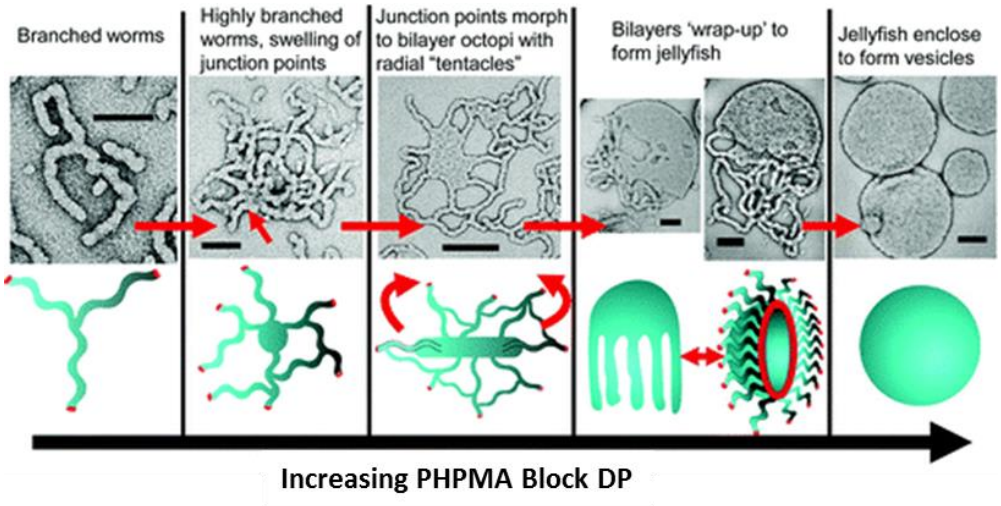

Figure 1.19. Morphological evolution observed during the preparation of $PGMA_{47}$-$PHPMA_{200}$ vesicles via RAFT-mediated PISA in water at 10 w/v %. Worm, octopi and jellyfish morphologies are observed at intermediate conversions. Finally, well-defined vesicles are observed at >99% HPMA conversion. All scale bars are 100 nm.[53]

The final copolymer morphology obtained via RAFT PISA depends on the copolymer concentration in addition to the relative volume fractions of the two blocks.[59] At relatively low concentrations, 1D fusion of multiple spherical nanoparticles is less favourable. Particle-

particle fusion is more likely at higher solids. The effect of the copolymer concentration is clearly visible when this parameter is plotted against the final PHPMA DP for a fixed PGMA DP to construct phase diagrams for the PGMA-PHPMA formulation when using a $PGMA_{78}$ and a longer $PGMA_{47}$ stabiliser block (**Figure 1.20**). For the former block, solely spherical particles are produced at low block copolymer concentrations (10 % w/w) but higher order morphologies could be obtained at higher copolymer concentrations (up to 25% w/w).[53]

Another important parameter during PISA is the DP of the stabiliser block. A relatively long stabiliser block promotes the formation of kinetically-trapped spheres owing to more efficient steric stabilisation.[53] In comparison, shorter stabiliser blocks promote 1D fusion of multiple spherical particles because steric stabilisation is less effective in this case. This allows higher order morphologies at lower copolymer concentrations. This effect is clearly visible for the two PGMA-PHPMA phase diagrams shown in **Figure 1.20**. A longer stabiliser block, $PGMA_{78}$, forms solely spherical particles at 10%, whereas a shorter $PGMA_{47}$ block can produce spherical, worm-like or vesicular particles increasing the DP of the core-forming PHPMA block.[53]

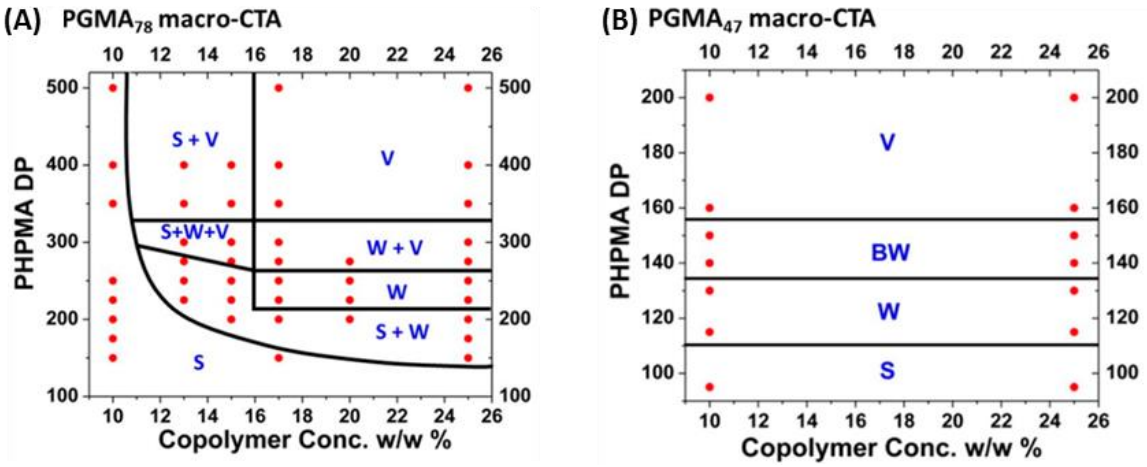

Figure 1.20. Phase diagrams (or morphology map) constructed for PGMA-PHPMA block copolymer dispersions, prepared via RAFT PISA in water. Core-forming PHPMA DP and copolymer concentrations were varied for a fixed PGMA DP of either (A) 78 or (B) 47. (S = spheres, W = worms, BW = branched worms, V = vesicles).[53]

The morphological evolution can be explained by the relative volume fractions of each block, as this dictates the curvature of the block copolymer when self-assembled into nanoparticles (**Figure 1.21**). The packing parameter (P) describes the curvature of the block copolymer and in principle can be calculated using **Equation 1.10**. Here, v is the volume of the hydrophobic block, a_o is the optimal area of the stabiliser block and l_c is the length of the core-forming block.[59]

$$\mathbf{P} = \frac{\mathbf{v}}{\boldsymbol{a_0} \times \boldsymbol{l_c}} \quad (\mathbf{1.10})$$

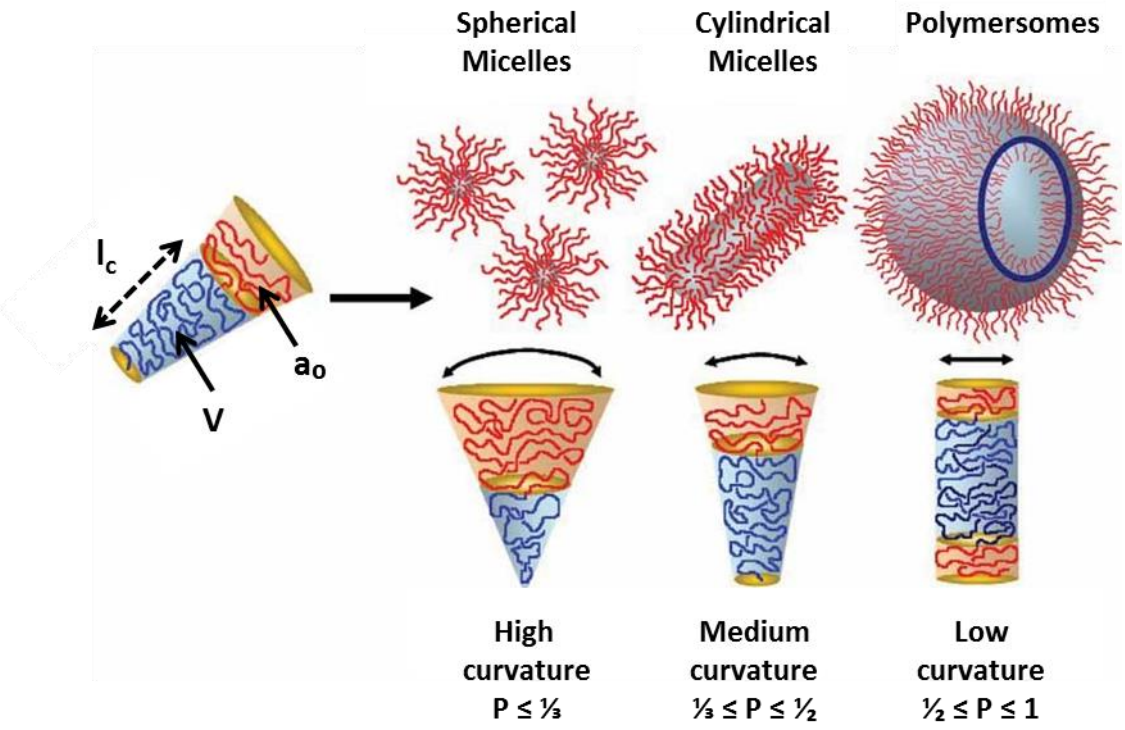

Figure 1.21. The relative block volume fractions dictate the copolymer morphology as described by the packing parameter (P), **Equation 1.10.** High curvature (P ≤ ⅓) favour spheres, while medium (⅓ ≤ P ≤ ½) and low curvature (½ ≤ P ≤ 1) favour cylindrical micelles and vesicles, respectively.[59]

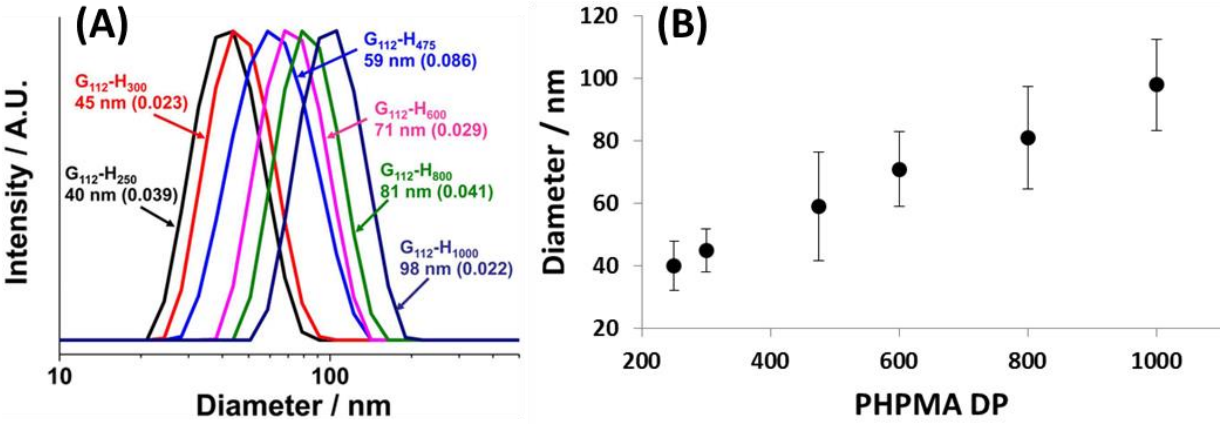

Figure 1.22. (A) DLS size distributions obtained for $PGMA_{112}$-$PHPMA_x$ block copolymer dispersions in water, where x ranges from 250 to 1000. (B) As the PHPMA DP increases, larger spherical particles are obtained.[60]

The copolymer chains pervade cones when longer corona blocks are used, according to **Equation 1.10**. This means that RAFT PISA formulations with longer macro-CTAs have a strong tendency to form spherical particles. This is apparent for the $PGMA_{112}$-$PHPMA_x$ series. Solely spherical particles were obtained for a PHPMA DP range of between 250 and 1000. DLS analysis of these dispersions shows that the spherical particle diameter increases when larger core DPs are targeted (**Figure 1.22**). When plotting this DLS diameter against PHPMA DP there is a clear relation between these two parameters. This highlights the versatility of RAFT PISA: it enables accurate control over the mean spherical particle diameter in addition to the *in situ* preparation of higher order morphologies.[60]

1.2.4. Polymerisation-Induced Self-Assembly in Non-Polar Media

PISA mediated by RAFT dispersion polymerisation is well reported in polar media.[38,53,60-62] In contrast, non-polar media has received far less attention.[32,39,57,63-71] The first PISA formulations in non-polar solvents were reported by Charleux and co-workers in 2007.[63-65] In these studies a poly(2-ethylhexyl acrylate) (P2EHA) macromolecular chain transfer agent was chain-extended with methyl acrylate (MA) in isododecane. This all-acrylic formulation

was used to compare a dithiobenzoate (DTB) with a trithiocarbonate-based RAFT agent (TTC) (**Figure 1.23**). Conversions of 83% and 89% were achieved when using DTB and TTC, respectively. The purified macro-CTAs were then chain-extended with methyl acrylate in isododecane (**Table 1.2**). The TTC was a bifunctional CTA: polymerisation from each active TTC produced an ABA-triblock copolymer, whereas the monofunctional DTB yielded a diblock copolymer. Higher monomer conversions, narrower molecular weight distributions, and more well-defined spherical particles were obtained when the TTC CTA was used. The main reason for the loss of control, in the case of DTB, was suggested to be due to irreversible termination between intermediate radicals at the interface of the dispersed particles.[63-65] However, in the light of more recent PISA syntheses conducted in non-polar media[32,57,72] this explanation appears to be unlikely.

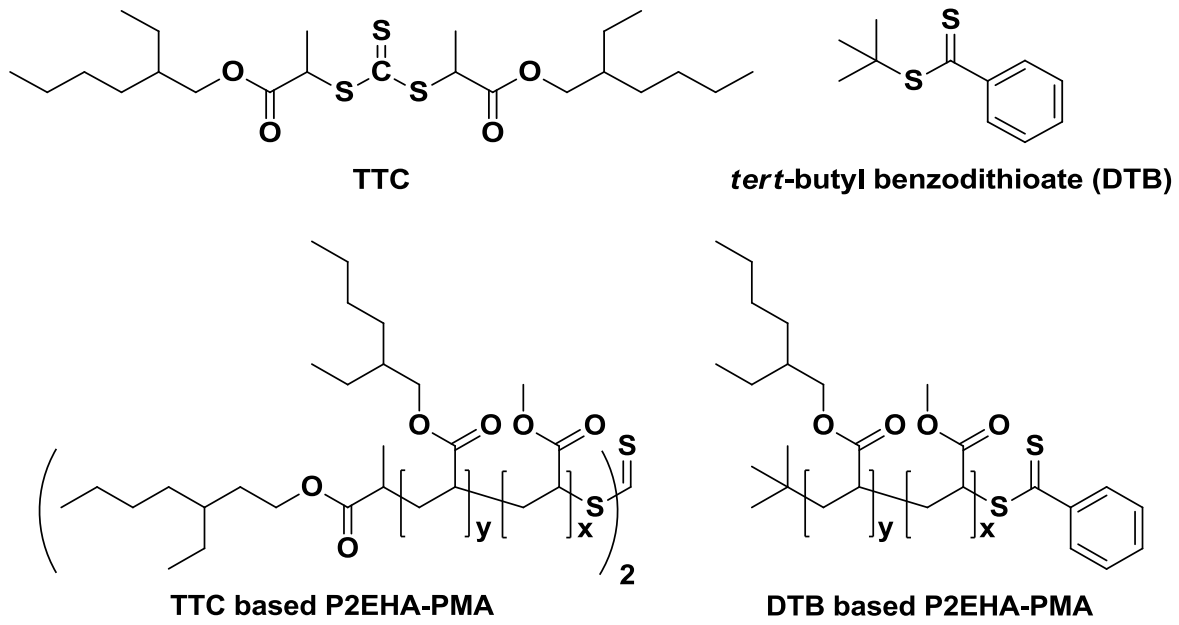

Figure 1.23. Chemical structures of the TTC and DTB chain transfer agents (CTAs) and the resulting diblock and triblock copolymers after chain extension of poly(2-ethyl hexylacrylate) (P2EHA) macro-CTAs with methyl acrylate.[63-65]

Table 1.2. Synthesis of spherical P(2-EHA)-PMA nanoparticles via RAFT dispersion polymerisation in isodecane. [We should note that the reported diameters seem inconsistent with the M_n in Entry 6][63]

Entry	CTA	P(2-EHA) DP	PMA DP[a]	Solids / %	Conversion / %	M_n	M_w/M_n	Diameter (nm)[b]	σ
1	DTB	114		25	100	56 100	18	93	0.09
2	DTB	114		28	85	46 400	6	51	0.22
3	DTB	114		30	48	28 900	1.8	39	0.18
4	TTC	102	936	23	91	99 700	2.7	50	0.03
5	TTC	102	389	29	92	52 600	1.6	30	0.03
6	TTC	102	241	39	100	40 000	1.2	54	0.1

[a]PMA DPs were not reported in the original publication. [b]Diameters were determined by DLS, a bimodal peak was observed for experiments 2 and 3.

Armes and co-workers reported a PISA formulation in *n*-heptane for which higher order morphologies could be obtained in 2013. A poly(lauryl methacrylate) (PLMA) macro-CTA was chain-extended with benzyl methacrylate (BzMA), using cumyl dithiobanzoate (CDB) as RAFT agent.[66,67] This was the first PISA formulation which enabled access to worms and vesicles in non-polar media. A phase diagram was constructed that enabled the reproducible targeting of spherical and higher order morphologies (**Figure 1.24**). Like the PGMA-PHPMA phase diagram reported by Blanazs *et.al.*, spherical particles were observed when targeting relatively low core-forming block DPs (PBzMA block DPs below 40). A narrow worm phase was observed for $PLMA_{17}$-$PBzMA_{60}$ at a minimum copolymer concentration of 17.5% w/w. Vesicles were observed over the whole copolymer concentration range for PBzMA DPs greater than 80. In addition, a master phase diagram was generated by varying both the stabiliser and core-forming block DPs at a fixed 20% w/w solids (**Figure 1.24**). A stabiliser PLMA block DP of 21 resulted in solely spherical particles. Shorter stabiliser block DPs of 16 and 18 provided access to spheres, worms and vesicles.[66,67]

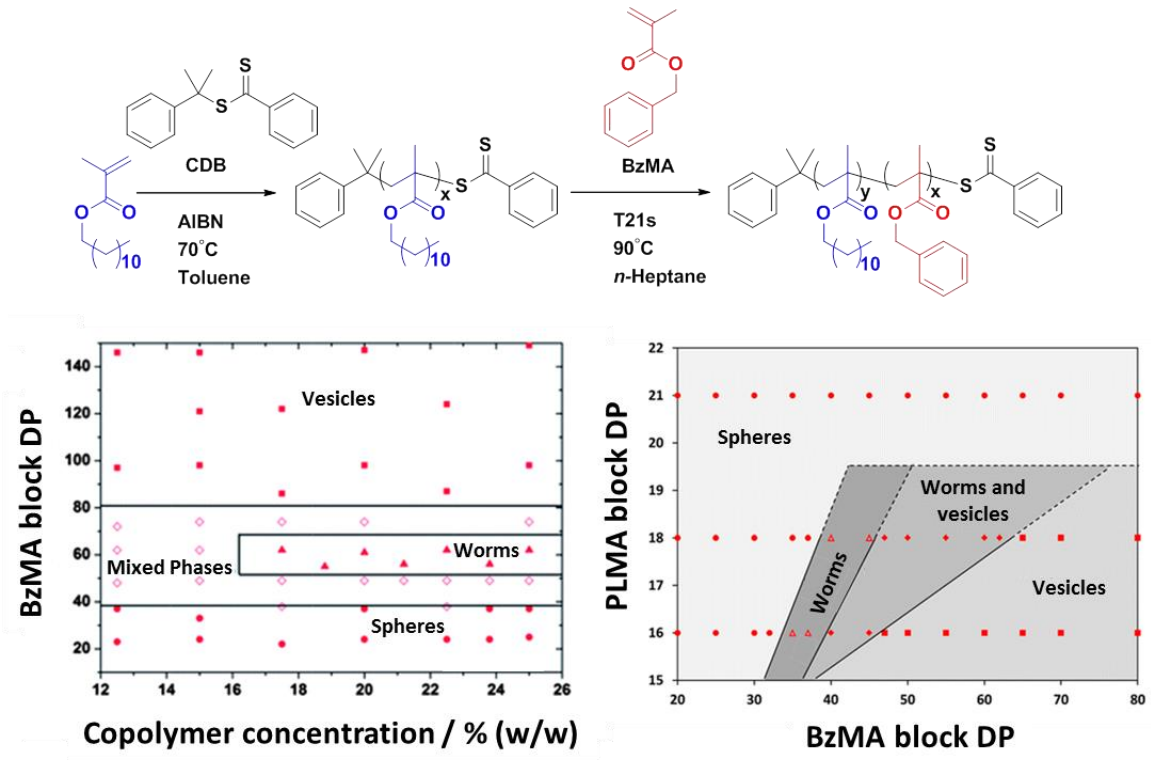

Figure 1.24. (Left) Phase diagram constructed for $PLMA_{17}$-$PBzMA_x$ nano-objects in *n*-heptane. Here, the DP of the core forming-block PBzMA is varied with the copolymer concentration (or solids content). (Right) Master phase diagram for PLMA-PBzMA formulations in *n*-dodecane, both stabiliser and core-forming block DPs were varied at a fixed solids content of 20% w/w.[66,67]

Further studies confirmed the versatility of this formulation in various non-polar solvents; spheres, worms and vesicles were observed when *n*-dodecane and mineral oil were used instead of *n*-heptane. Further proof of the robust nature of this PISA formulation was obtained with a one-pot synthesis of spherical PLMA-PBzMA nanoparticles, where a mixture of BzMA, initiator and solvent was added after the RAFT solution polymerisation of PLMA was taken to 95% conversion.[57,66,67] The Armes group has also used benzyl methacrylate for the core-forming block to produce nano-objects using a polydimethylsiloxane (PDMA) macro-CTA.[39] In contrast to the previous discussed formulations, an acid functional RAFT agent was converted into a macro-CTA via DCC/DMAP-catalysed esterification with PDMS (**Figure 1.25**).

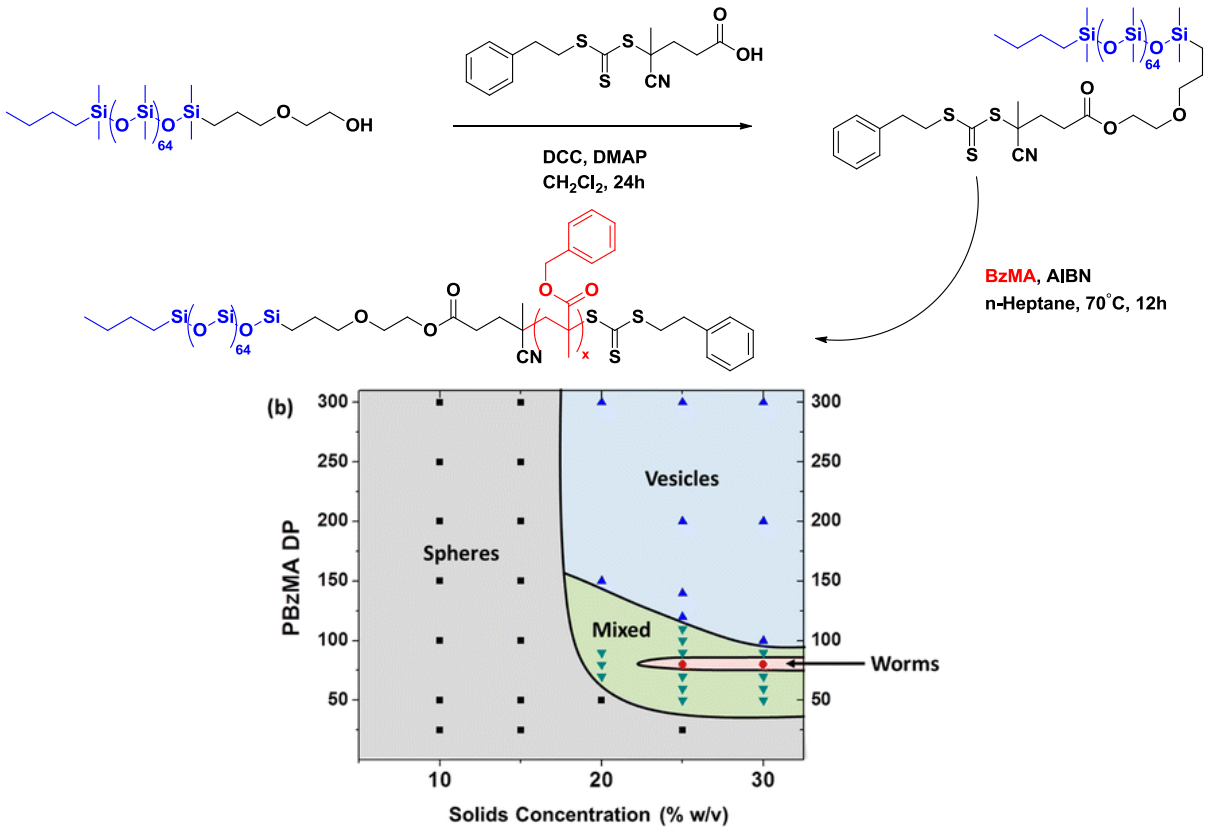

Figure 1.25. $PDMS_{66}$-$PBzMA_x$ phase diagram for which the DP of the core-forming PBzMA block and the solids content were systematically varied. Spheres, worms or vesicles were observed, with very narrow worm phase for this particular PISA formulation.[39]

An important advantage of this approach is that the same molecular weight for the macro-CTA can be obtained reproducibly. This is challenging for the previously discussed $PLMA_x$ macro-CTA formulations. A kinetic experiment prior to the macro-CTA synthesis was required to quench the polymerisation at an appropriate intermediate monomer conversion to prevent RAFT chain-end degradation. RAFT chain-end degradation was minimised, but reproducibility is lost in this approach as the polymer DP depends on the precise reaction time. However, both methods require a purification step, either precipitation in methanol for PLMA or column chromatography for PDMS macro-CTA. After purification of the PDMS macro-CTA, RAFT dispersion polymerisation was conducted with BzMA in *n*-hexane. Varying the PBzMA DP and solids concentration led to the formation of spheres, worms or vesicles. This PISA formulation led to the construction of a phase diagram (**Figure 1.25**). In this case, the cylindrical worm phase has a particularly narrow phase region, making this morphology somewhat elusive.[39]

Table 1.3. Summary of data obtained for a series of PSMA-PPPMA (S-P) block copolymer dispersions via PISA in *n*-tetradecane. High PPMA conversions and low dispersities (*Đ*) were obtained. An increase in core-forming block DP results in larger spherical particle (S) diameters, followed by the appearance of worms (W) and vesicles (V). An increase in solids content for a $PSMA_{17}$-$PPPMA_{60}$ target composition results in an evolution from spheres to worms.[69]

Entry	Composition	Concentration / %	Conversion / %	M_n	M_w/M_n	DLS diameter / nm	TEM Morphology
1	S_{19}-P_{33}	20	98	9 500	1.15	18 ± 1.1	S
2	S_{19}-P_{47}	20	98	10 900	1.17	22 ± 1.2	S
3	S_{19}-P_{68}	20	96	16 000	1.16	243 ± 124	S+W
4	S_{19}-P_{85}	20	96	16 800	1.17	217 ± 121	W
5	S_{19}-P_{87}	20	94	17 000	1.16	345 ± 169	W+V
6	S_{19}-P_{98}	20	96	20 400	1.16	498 ± 259	V
7	S_{19}-P_{165}	20	92	28 500	1.17	1121 ± 372	V
8	S_{17}-P_{49}	10	93	12 100	1.15	23 ± 3.9	S
9	S_{17}-P_{50}	20	96	13 200	1.15	59 ± 23.9	S+W
10	S_{17}-P_{54}	30	98	13 400	1.16	71 ± 26.8	S+W
11	S_{17}-P_{57}	40	99	14 300	1.15	120 ± 48.1	W

Another example of a RAFT dispersion polymerisation in non-polar media was reported by the Lowe group[69]: a poly(stearyl methacrylate) (PSMA) macro-CTA was prepared and chain-extended with 3-phenylpropyl methacrylate (PPMA) in *n*-tetradecane. These formulations resulted in high conversions and narrow molecular weight distributions (**Table 1.3**) and provided access to higher order morphologies. An increase in core-forming PPPMA DP for a fixed PSMA stabiliser block DP, results in the formation of spheres, worms or vesicles. As observed for previous polar and non-polar examples, a higher copolymer concentration also resulted in a morphological transition. Spherical particles were observed at 10% w/w, whereas worms were obtained at 40% w/w.[68] Additionally, a longer stabiliser block prevented access to higher order morphologies. Like the spherical particles provided in polar[62] and non-polar media[66], a higher core-forming block DP results in larger spherical particle diameters.[69]

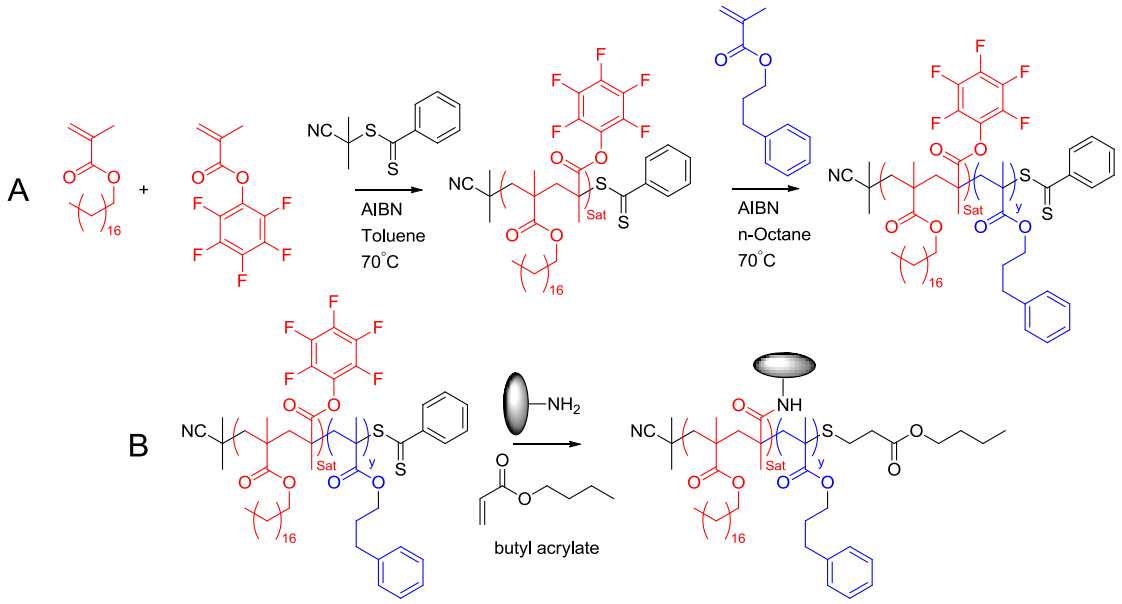

Figure 1.26. (a) PSMA and PFPMA are copolymerised to yield a statistical copolymer macro-CTA, which is chain-extended with $PPMA_x$, to produce spheres, worms or vesicles. (b) Post-polymerisation modification via nucleophilic aryl substitution enables functionalisation of these nanoparticles with various primary amines.[68]

The PSMA-PPPMA formulation was slightly modified by the same team by incorporating pentafluorophenyl methacrylate (PFPMA) within the stabiliser block. First, a macro-CTA was prepared by statistically copolymerising SMA and FPMA. Then, this macro-CTA was chain-extended with 3-phenylpropyl methacrylate (PPMA) in either *n*-octane or *n*-tetradecane (**Figure 1.26A**).[68] In a third step, post-polymerisation modification of nanoparticles was achieved via nucleophilic aryl substitution with various functional amines (**Figure 1.26B**). The success of this derivatisation chemistry was confirmed by ^{1}H NMR,^{19}F NMR and IR spectroscopy. However, GPC analysis indicated a high molecular weight shoulder for the post-polymerisation modified particles. This is most likely to be owing to the formulation of a polymeric disulfide as a result of the *in situ* aminolysis of the trithiocarbonate. To prevent this side-reaction, *n*-butyl acrylate was added to react with the thiol formed during aminolysis. However, this approach was not successful and it was suggested that disulfide formation is a direct result of the local high concentrations of free thiol groups within the nanoparticle cores.[68]

1.3. Industrial Applications of Block Copolymer Nanoparticles

Block copolymer nanoparticles have become much more easily accessible via RAFT PISA during the last decade. Their versatility in chemical composition and morphology makes such nanoparticles extremely interesting for industrial applications. Furthermore, the possibility to induce a morphological transition by varying the solution temperature or pH offers further scope for commercial exploration. Selected examples taken from the literature are discussed below.

1.3.1. Spherical nanoparticles as lubricants in engine oils

Spherical block copolymer nanoparticles can improve the lubricating performance of base oils, as demonstrated by Liu and co-workers. Such nanoparticles have the ability to reduce friction between moving metal surfaces. Block copolymer chains were prepared and purified, before addition to base oil to demonstrate this application.[73]

More specifically, poly(2-ethylhexyl acrylate)-*ran*-(*tert*-butyl acrylate) (P(EXA-*ran*-*t*BA)-PCEA)) was prepared via solution polymerisation in toluene using ATRP. Subsequently, this polymer was purified and chain-extended with 2-hydroxyethyl acrylate in 2-butanone to form block copolymers. Post-polymerisation modification involved reacting the pendent hydroxyl groups with cinnamoyl chloride in pyridine to form the final P(EXA-*ran*-*t*BA)-PCEA) block copolymer (**Figure 1.27**).[74] This block copolymer was selected because the PCEA block offers the possibility of photo-crosslinking after micellar self-assembly. The small fraction of *t*BA was incorporated into the corona because it can be readily hydrolysed to afford acrylic acid residues, which should enhance nanoparticle binding to metal surfaces.

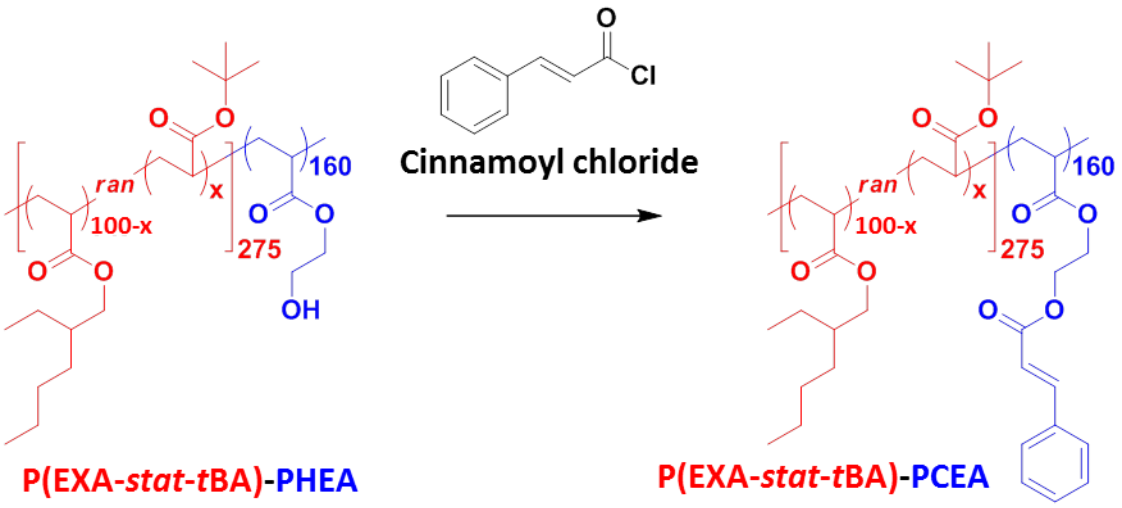

Figure 1.27. Poly[(2-ethylhexyl acrylate)-*ran*-(*tert*-butyl acrylate)]-poly(2-hydroxyethyl acrylate) (P(EXA-*ran*-*t*BA)-PHEA) (x = 1.5%) was prepared via solution copolymerisation in toluene using ATRP. The subsequent reaction with cinnamoyl chloride in pyridine transformed the PHEA block into a poly(2-cinnamoyloxyethyl acrylate) block (PCEA). GPC analysis for this specific composition indicated M_w = 98 000 and $Đ$ = 1.24.[73]

Micellar self-assembly was achieved via post-polymerisation processing using the solvent switch method[30] in a THF/cyclohexame mixture. P(EXA$_{1-x}$-*ran*-*t*BA$_x$)$_{275}$-PCEA$_{160}$ (x = 1.5%) was dissolved in THF and subsequent addition of cyclohexane let to the formation of PCEA-core micelles. This block copolymer dispersion had a final cyclohexane volume fraction of 80-95% and was subsequently photo-crosslinked using UV radiation. The core-crosslinked nanoparticles were then precipitated in methanol and finally dispersed in base oil for friction tests. TEM analysis of this final dispersion confirmed the spherical morphology of these nanoparticles with a mean diameter of 33 ± 4 nm **(Figure 1.28A)**. Solvent exchange was necessary because the base oil contained photosensitive compounds; photo-crosslinking in such media would otherwise turn the base oil yellow, which is undesirable in terms of product appearance.[73]

Lubrication tests were performed on a range of crosslinked spherical P(EXA-*ran*-*t*BA)-PCEA) nanoparticles dispersed in base oil. These experiments were performed using a mini-traction machine (**Figure 1.28B**). Here, the friction of a metal ball against a metal plate is assessed when both are immersed in base oil. The rotation speed of the ball and plate can be

controlled separately, which allows the determination of the friction coefficient over a range of entrainment speeds for a fixed slide to rolling ratio. A commonly used lubricating oil additive is glyceryl monooleate. This mini-traction analysis showed that modest addition of this surfactant drastically reduced the friction coefficient of the base oil over a whole range of entrainment speeds. Interestingly, the addition of crosslinked spheres produced a remarkable reduction of friction coefficient at low entrainment speeds which corresponds to the boundary lubrication regime (**Figure 1.28C**). In principle, this performance makes these nanoparticles an excellent friction modifier additive. The mechanism to obtain enhanced lubricating properties from such oil additives originates from the capability of the spherical nanoparticles to prevent direct contact between moving metal surfaces.[73]

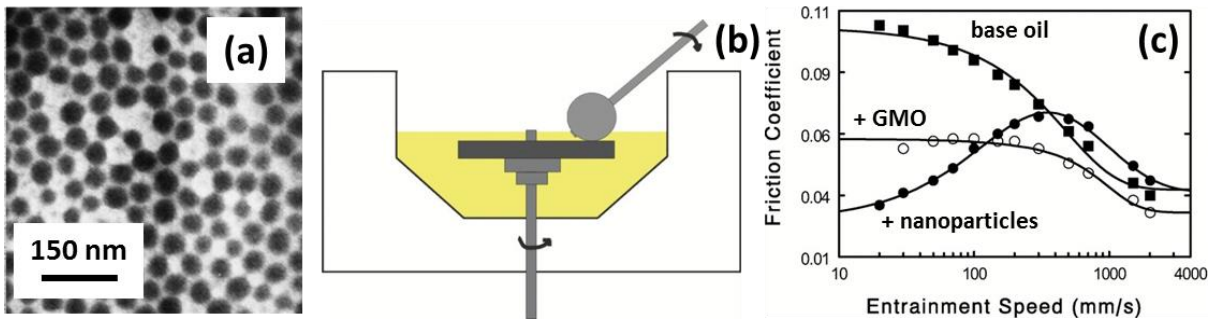

Figure 1.28. (A) TEM image of crosslinked spherical P(EXA_{1-x}-*ran*-*t*BA_x)$_{275}$-$PCEA_{160}$ (x = 1.5%) block copolymer nanoparticles with a mean diameter of 33 ± 4 nm. (B) Schematic representation of a mini-traction machine, whereby friction of a metal ball against a metal surface determines the lubrication properties of a base oils with two different additives. (C) Lubrication data for base oil alone (■), base oil with 1% glyceryl monooleate (o), base oil containing 0.5% w/w core-crosslinked P(EXA_{1-x}-*ran*-*t*BA_x)$_{275}$-$PCEA_{160}$ (x = 1.5%) spherical nanoparticles (●).[73]

The friction modifying ability of these crosslinked P(EXA-*ran*-*t*BA)-PCEA) block copolymer nanoparticles is certainly impressive, but their complex synthesis prohibits cost-effective scale up. This problem can be circumvented by RAFT-mediated PISA as described by Armes and co-workers, making this technology much cheaper and more accessible. This

approach utilises RAFT dispersion polymerisation of BzMA to drive block copolymer self-assembly directly in suitable base oils. This work covers the preparation of PLMA-PBzMA block copolymer nanoparticles directly in *n*-dodecane, mineral oil or a poly(α-olefin).[57] This PISA formulation had previously proven to be effective for the preparation of a range of nanoparticles in *n*-heptane by the same group in 2013.[66] The ability to perform this reaction directly in base oil clearly demonstrates that RAFT PISA in non-polar media is a robust protocol. Similar phase diagrams with well-defined sphere, worm and vesicular phases were obtained for all four solvents (**Figure 1.24 and Figure 1.29**).[66]

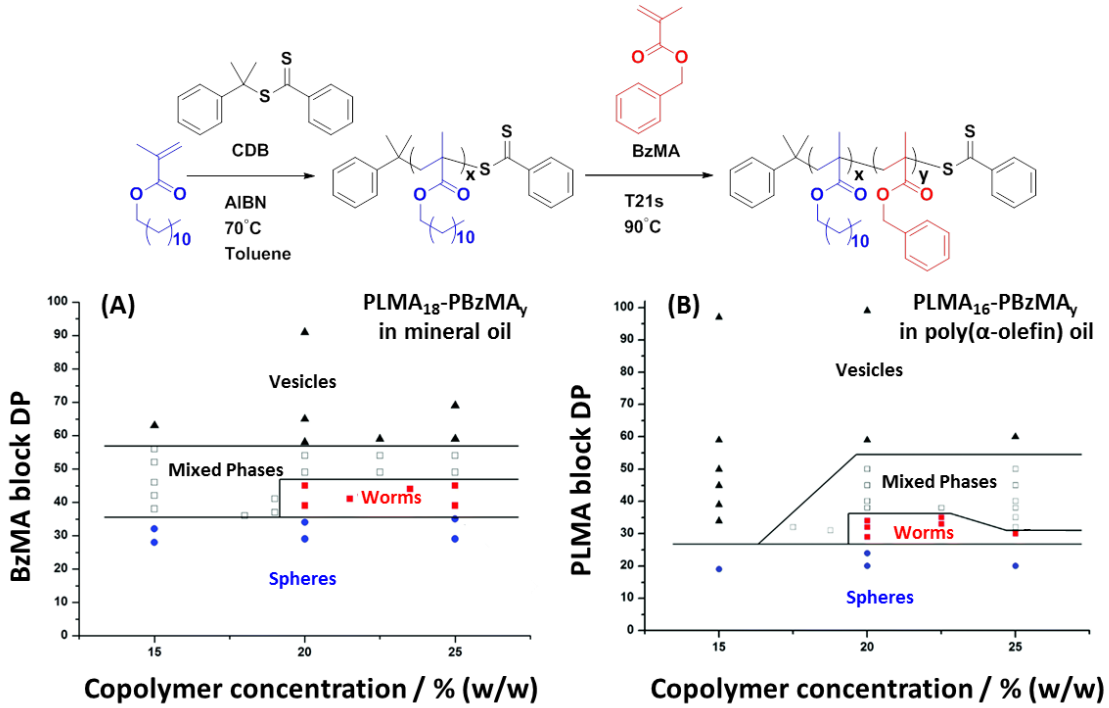

Figure 1.29. Phase diagrams of $PLMA_x$-$PBzMA_y$ block copolymer nanoparticles via RAFT PISA in (A) mineral oil, and (B) a poly(α-olefin). Variation of the core-forming PBzMA DP and copolymer concentration allows spheres, worms and vesicles to be targeted reproducibly.[57]

Apart from the convenience and efficiency of a one-pot RAFT PISA, an all-methacrylic formulation is also more likely to produce more robust block copolymers in comparison to the previously discussed P(EXA-*ran*-*t*BA)-PCEA) formulation. This is because acrylic polymers are more prone to undergo ester hydrolysis at elevated temperatures. Another

downside of the formulation reported by Liu and co-workers is that ATRP requires CuBr, which requires post-polymerisation removal prior to application. In contrast, RAFT-synthesised polymers can be used directly but suffer from other disadvantages such as intrinsic colour and sulfur-based end-groups. Fortunately, RAFT chain-ends can be readily removed in both aqueous[28] and non-polar media[71]. However, for engine oil applications neither of the latter problems is considered to be particularly detrimental.

1.3.2. Worm Gels for Oil Thickening

PISA enables the convenient preparation of PLMA-PBzMA spheres, worms or vesicles reproducibly in various non-polar solvents, as shown in **Figure 1.29**. The latter two morphologies may also offer potential industrial applications. Sufficiently long worms are able to form free-standing physical gels. Initially, it was believed that inter-worm entanglements are responsible for gelation, with longer worms resulting in stronger gels.[75] However, recent research has shown that this gelation behaviour can be explained by percolation theory, for worms prepared in both aqueous and non-polar media.[76] These PLMA-PBzMA worms are industrially relevant as viscosity modifiers. Interestingly, heating the worm gels causes degelation. TEM analysis of these dispersions suggests that a worm-to-sphere morphological transition is responsible for this behaviour (**Figure 1.30**). Subsequent cooling of this dispersion caused regelation via a regenerated worm phase, demonstrating the thermoreversibility of this transition. However, the worm-to-sphere transition becomes irreversible for dilute worm dispersions. This suggests that the sphere-to-worm transition is a 1D particle-particle *fusion* process. TEM analysis of the diluted block copolymer morphologies supports this hypothesis since the spherical particle diameter is comparable to the worm cross-sectional diameter. For this experiment, worms were heated to induce the morphological transition to spherical particles and subsequently diluted in hot *n*-dodecane to the concentration required for TEM analysis; this approach trapped the spherical morphology.

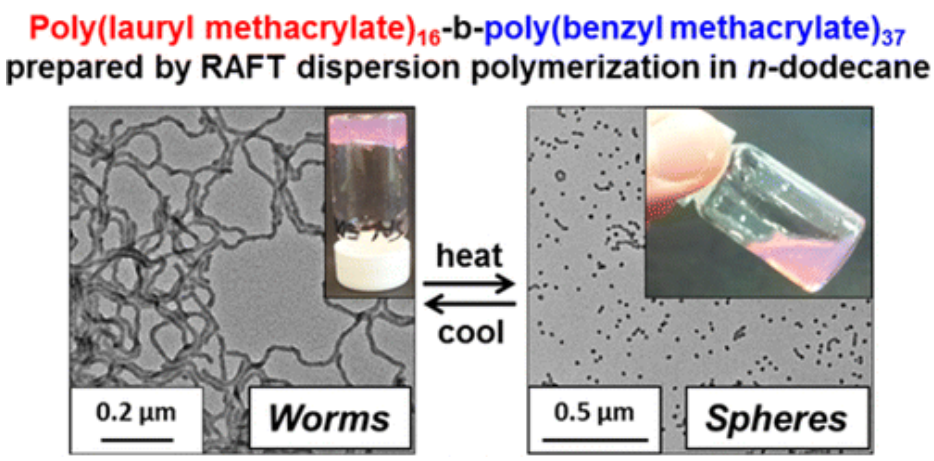

Figure 1.30. Heating a $PLMA_{16}$-$PBzMA_{37}$ worm gel in *n*-dodecane induces reversible degelation which can be attributed to the morphological change from worms to spherical nanoparticles. Surface plasticisation is believed to drive this transition, with the PBzMA core-forming block becoming more solvated at higher temperatures. This leads to a suitable increase in the molecular packing parameter[67]

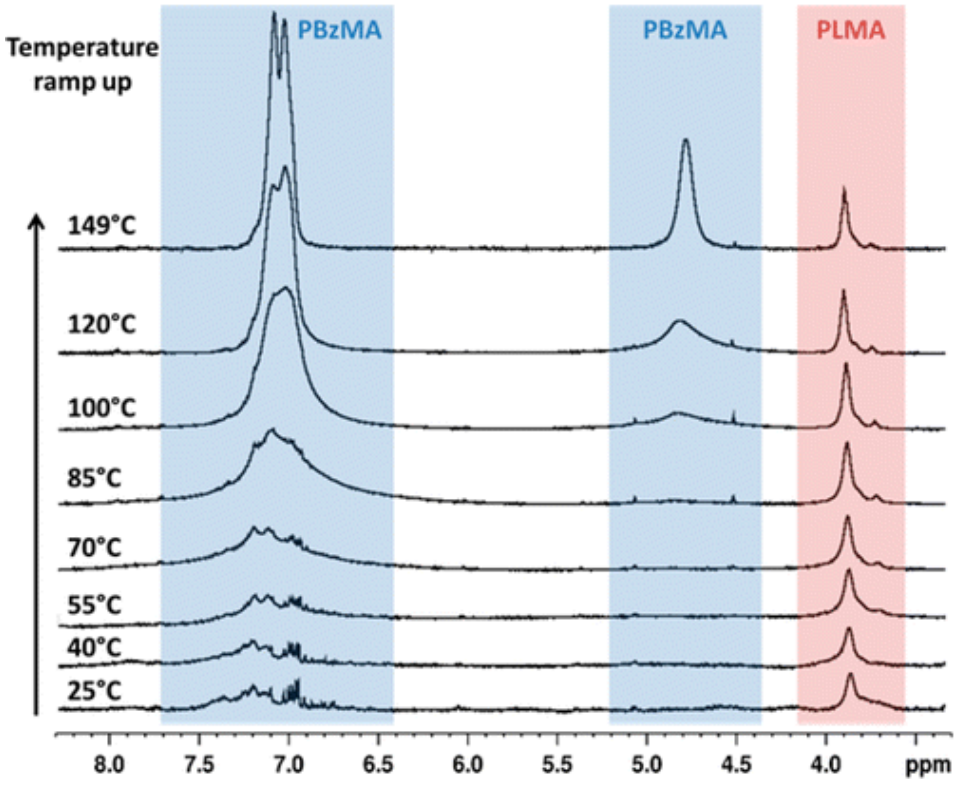

Figure 1.31. Variable temperature ^{1}H NMR studies of $PLMA_{16}$-$PBzMA_{37}$ diblock copolymer nano-objects in d_{26}-dodecane indicate more intense PBzMA signals on heating. This provides direct spectroscopic evidence for progressively more solvated core-forming chains at elevated temperature.[67]

This change in morphology is believed to be caused by a reduction in the molecular packing parameter (**Figure 1.21**), as a result of surface plasticisation of the core-forming PBzMA block. This leads to an effective increase in volume fraction of the stabiliser block. This hypothesis was supported by variable temperature ^{1}H NMR studies of these nanoparticles in d_{26}-dodecane (**Figure 1.31**). The nanoparticle dispersion was analysed from 25 to 149 °C. The benzylic and aromatic proton signals from the PBzMA core became more prominent at higher temperatures. The increase in intensity of the aromatic signals at around 7.1 ppm and the benzylic protons at around 4.8 ppm clearly indicates more solvated core at higher temperatures.[67]

1.3.3. Vesicles for Oil Thickening

The most common morphologies obtained via RAFT PISA in polar and non-polar solvent are spheres worms and vesicles.[38,57] The latter nanoparticles consist of a block copolymer membrane and its lumen is filled with solvent. It has been shown that this morphology has interesting properties in aqueous formulations where they can act as drug delivery vehicles.[2] Vesicles prepared in oil offer some potential in terms of viscosity modifiers. As shows in **Figure 1.24 and Figure 1.29**, PLMA-PBzMA block copolymer vesicles are accessible via RAFT PISA when selecting appropriate block DPs at a suitable copolymer concentration. Like the spherical PLMA-PBzMA particles, these vesicles form a free-flowing dispersion. Armes and co-workers have shown that PSMA-PBzMA vesicles can be prepared in mineral oil. The subtle change from PLMA to PSMA stabiliser block, shows the versatility of RAFT PISA. Heating such PSMA-PBzMA vesicles up to 150 °C induces a vesicle-to-worm transition, as was confirmed by TEM (**Figure 1.32.**) and SAXS studies. Thus this dispersion exhibits oil-thickening properties upon heating. In contrast, the previously discussed worm-to-sphere transition leads to oil-thinning properties at elevated temperatures.[77]

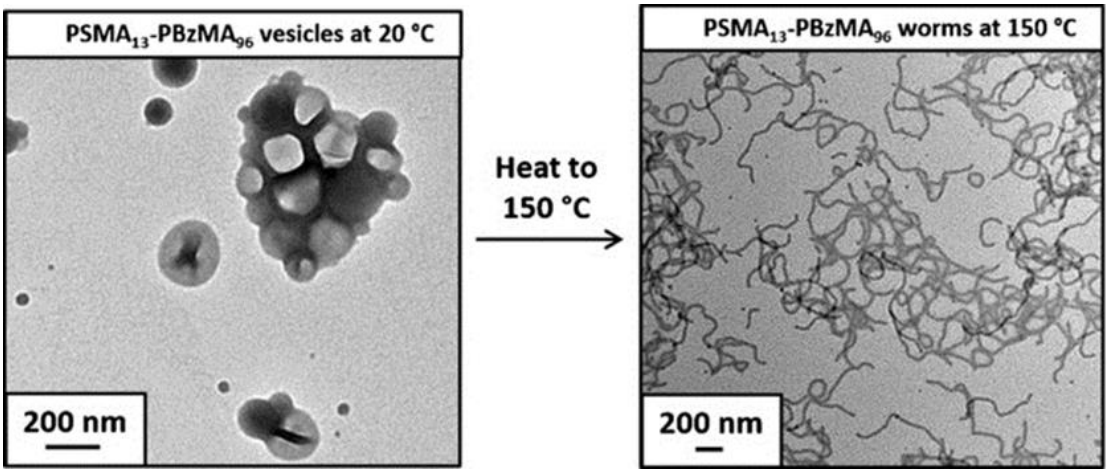

Figure 1.32. Heating a dispersion of $PSMA_{13}$-$PBzMA_{96}$ vesicles, prepared via RAFT PISA in mineral oil up to 150 °C induces a vesicle-to-worm morphological transition.[77]

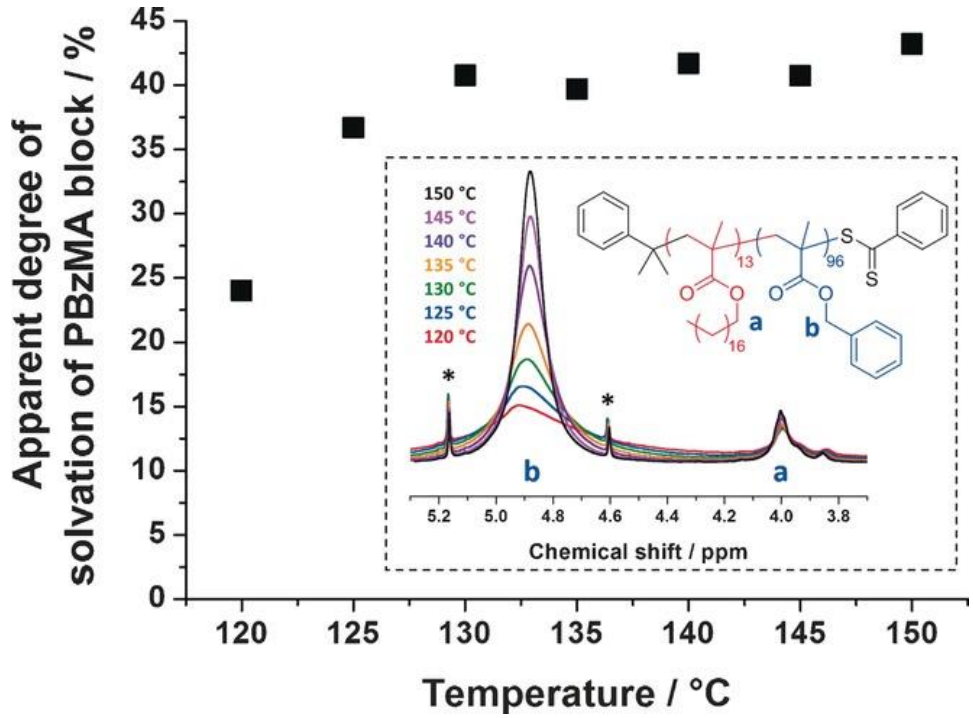

Figure 1.33. ^{1}H NMR analysis of $PSMA_{13}$-$PBzMA_{96}$ nano-objects in d_{26}-dodecane from 120 to 150 °C. The degree of solvation of the core-forming PBzMA chains remained constant at around 40% above 130 °C.[77]

Like the previously discussed reversible worm-to-sphere transition observed for PLMA-PBzMA worms in *n*-dodecane, the vesicle-to-worm transition was expected to be the result of surface plasticisation of the vesicular nanoparticle membrane (a larger block copolymer curvature should prefer the formation of worms above vesicles). This was confirmed by variable temperature ^{1}H NMR studies conducted in d_{26}-dodecane (**Figure 1.33**). The original vesicles were transferred from mineral oil to d_{26}-dodecane via centrifugation-redispersion. (TEM and SAXS analysis shows that this did not affect the vesicular morphology.) This variable temperature ^{1}H NMR study was performed between 120 °C and 150 °C. Heating this vesicle dispersion led to an increase in the normalised benzylic proton signals of the PBzMA block at around 4.9 ppm. Like the previously discussed worm-to sphere transition (**Figure 1.31**), this suggests that the PBzMA chains become more plasticised at elevated temperature. Higher degrees of solvation were observed up to 130 °C, with no further change occurring up to 150 °C.[77]

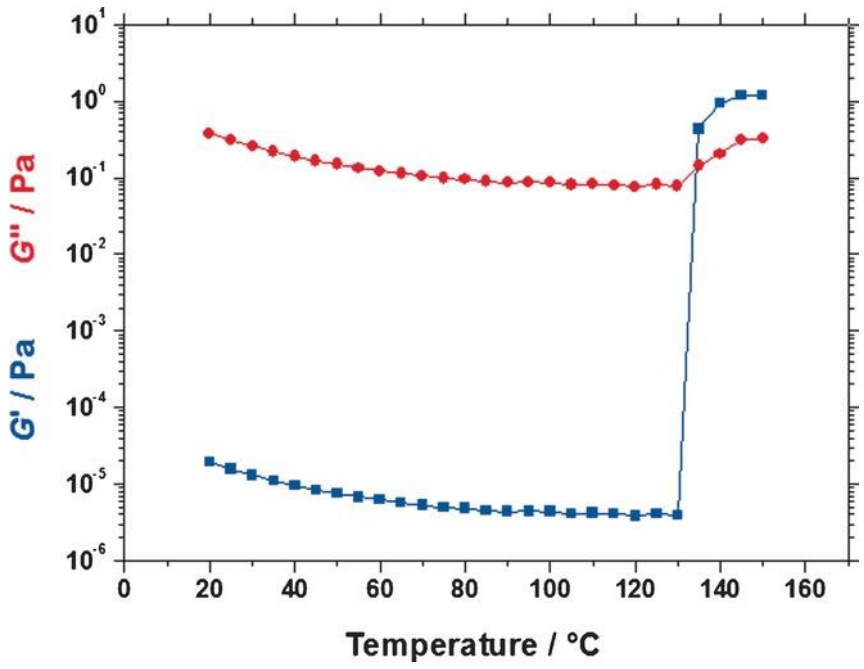

Figure 1.34. Rheology studies of $PSMA_{13}$-$PBzMA_{96}$ nano-objects block copolymer particles in mineral oil. Gradual heating from 20 °C to 150 °C shows a noticeable increase in storage modulus (G') at 130 °C. This indicates a sudden increase in viscosity at this temperature as it exceeds the loss modulus (G''); the change in this physical characteristic is attributed to a vesicle-to-worm morphological transition.[77]

The thermally-induced vesicle-to-worm transition was also investigated by rheology (**Figure 1.34**). This analysis initially showed a gradual reduction in both the storage (G') and loss moduli (G") upon heating, which indicates that the dispersion becomes progressively less viscous. This behaviour is well-known for most fluids.[78] However, further heating from 130 °C to 135 °C caused an abrupt increase in G'. This suggests that the initial free-flowing dispersion is transformed into a viscoelastic gel at the latter temperature, which is also known as the critical gelation temperature (CGT).

1.3.4. Aqueous Formulations With Inverted Thermal Behaviour

The previously discussed thermally-induced morphological changes covers dispersions prepared via RAFT PISA in non-polar media. However, similar behaviour is also observed for aqueous formulations. For example, thermally-induced degelation was also observed for aqueous worm-gel formulations. However, in contrast to the non-polar PISA formulations, degelation for these aqueous dispersions is observed upon cooling, rather than heating. Thus, $PGMA_{54}$-$PHPMA_{140}$ block copolymer worms form a free-standing gel at 21 °C, but cooling to 4 °C results in degelation. Like the non-polar PISA formulations, this was caused by a worm-to-sphere transition according to TEM studies. Heating the dispersion back to its original temperature (21 °C) resulted in regeneration of the worm gel (**Figure 1.35**).[60]

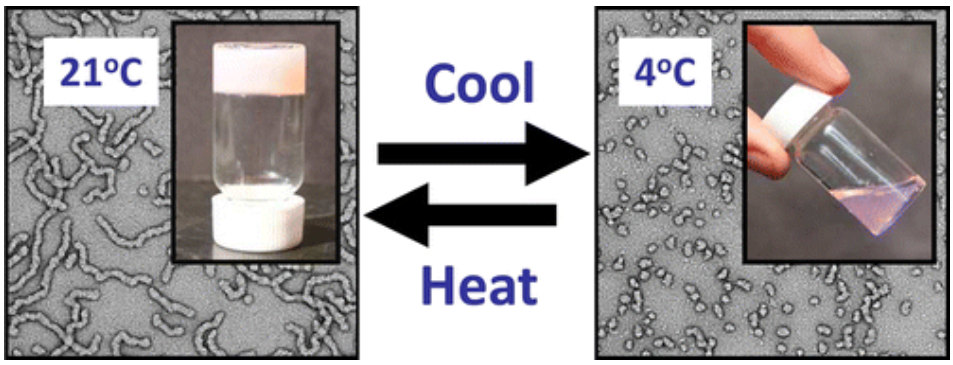

Figure 1.35. A $PGMA_{54}$-$PHPMA_{140}$ worm gel undergoes a phase transition from a free-standing gel to a free-flowing liquid when cooled to 4 °C. This physical change is the result of a worm-to-sphere transition. Heating the dispersion back to its initial temperature causes reformation of the worm gel.[60]

This thermal response is akin to the lower critical solution temperature (LCST) behaviour that is well-known for certain water-soluble polymers such as poly(*N*-isopropylacrylamide).[32,67,79] This specific formulation can be utilised for biological applications because of its unusual temperature-induced degelation behaviour. Temperature-responsive worm gels can be readily ultra-filtrated when they are in the cold free-flowing sphere form; regeneration of the worm gel by heating to room temperature results in a sterile gel. Such worm gels are biocompatible and can be used for certain biological applications such as the long-term storage of human stem cells and embryos.[60,80]

1.4. Copolymer Chain Exchange between Block Copolymer Nanoparticles

A common characteristic of block copolymer micelles is their ability to exchange copolymer chains between nanoparticles.[81] Two main mechanisms have been suggested for this process: (i) chain expulsion/insertion and (ii) micelle fusion/fission (**Figure 1.36**).[81] Micelle fusion/fission is expected to be more significant for weakly repulsive nanoparticles, such as non-ionic micelles.[82] The copolymer exchange rate for micelle fusion/fission is expected to decrease with concentration owing to the lower probability of inter-particle collision under these conditions.[83] It is generally accepted that block copolymer micelles normally exhibit the chain expulsion/insertion mechanism.[81,84] However, the micelle fusion/fission mechanism should not be neglected for at least some block copolymer nano-objects prepared via PISA. For example, the previously discussed worm-to-sphere transition observed for block copolymer nanoparticles prepared via RAFT PISA in aqueous and non-polar media is likely to involve the latter mechanism (**Figure 1.30 and 1.35**). In this section, we focus on diblock copolymer nanoparticles prepared in non-polar media. We briefly examine theoretical aspects of the two main mechanisms, and their relative likelihood with respect to block copolymer nanoparticles. In addition, the concept of a small-angle neutron scattering (SANS) contrast-matching experiment to probe copolymer exchange between nano-objects is also discussed.

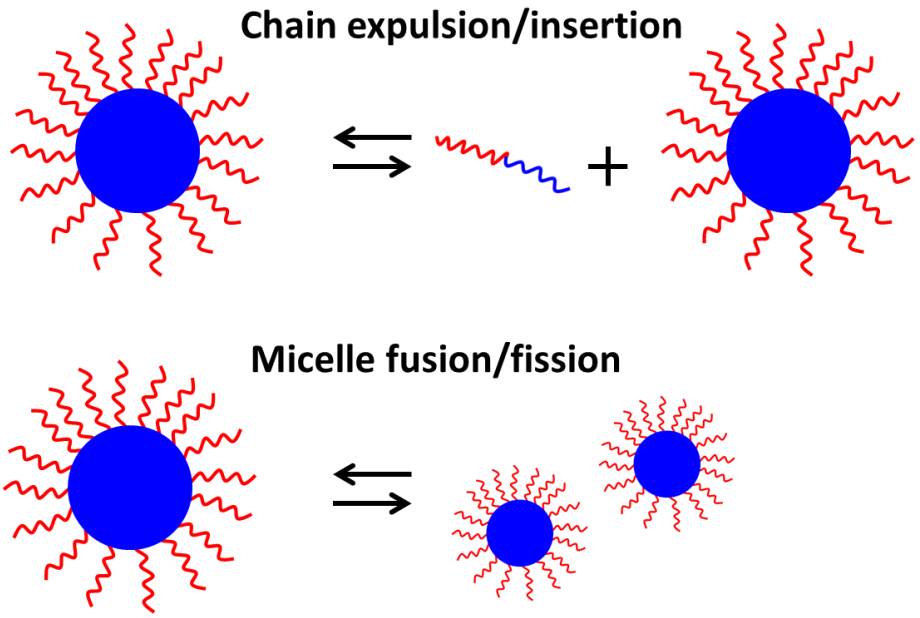

Figure 1.36. Two possible copolymer exchange mechanisms for block copolymer micelles. (top) Chain expulsion/insertion involves the expulsion of individual block copolymer chains from nanoparticles, which subsequently diffuse towards and then insert into another nanoparticle. (bottom) Micelle fusion/fission involves nanoparticle break-up (fission) to form smaller particles, which can thereafter fuse together to form either smaller, larger or similar-sized nanoparticles.[81]

1.4.1. Chain Expulsion/Insertion Mechanism

Block copolymer micelles have the tendency to redistribute copolymer chains to maintain their global equilibrium. Chain expulsion/insertion is believed to be the predominant mechanism for this process. For this mechanism, we need to consider both copolymer chain diffusion between micelles and chain expulsion/insertion. Generally, the diffusion of polymer chains in a low molecular weight solvent is fast.[81] For a diffusion coefficient of 10^{-11} m^2/s a distance of 10 nm would be traversed within microseconds.[81] This suggests that the rate of chain exchange is governed by the expulsion rate constant, which is a significantly slower process. Halperin and Alexander suggest that this rate-limiting step can be described in terms of a two-step process: (i) ejection of the solphophobic part of the block to form a bud at the interface of the micelle core and (ii) diffusion of the whole copolymer chain through the

micelle corona.[81,85] Here, the radius of the collapsed core-forming block (bud) should determine the ejection rate. This theory is valid for copolymers with relatively large cores, but diffusion through the corona layer needs to be considered for star-like micelles.

1.4.2. Micelle Fusion/Fission Mechanism

The activation energy for the micelle fusion/fission mechanism is more energetically demanding than that for the chain expulsion/insertion mechanism. Alexander determined the activation energies for such a process.[81] The activation energy for micelle fusion becomes unrealistically high for larger particle diameters. However, fusion of micelles of dissimilar size is more probable. The route with the lowest energy barrier corresponds to the insertion of a particle of minimal size with a larger particle. Indeed, this means insertion of an individual copolymer chain into a particle. Thus, the most favourable pathway for particle fission would result in a micelle and a dissolved copolymer chain; which corresponds to the previously discussed chain expulsion/insertion mechanism. This indicates that the micelle fusion/fission mechanism is not important for copolymer micelles owing to unreasonably high activation energies, especially when the corona layer is rather dense and/or extended. However, work by Dormidontova challenged this idea.[86] She proposed that micellar fusion/fission is not negligible, and may play an important role in the formation kinetics of polymer micelles. Additionally, Armes and co-workers have suggested that micelle fusion/fission may be the dominant mechanism for the worm-to-sphere transition during RAFT PISA as previously discussed (**Figure 1.30 and 1.35**).

1.4.3. Monitoring Copolymer Chain Exchange Between Nanoparticles

Copolymer exchange between hydrogenous and deuterated core nanoparticles can be conveniently monitored by small-angle neutron scattering (SANS). This is because sufficient contrast can be readily introduced by using hydrogenated and deuterated species. Additionally, the neutron scattering length density (SLD) of the solvent can be conveniently adjusted to a desired value by using isotopic solvent mixtures.[42,43,84] A binary mixture of hydrogenous and deuterated block copolymer particles was prepared for which the core-

forming blocks are chemically identical but isotopically different. The SLD value of the solvent is chosen to lie between that of the hydrogenous and deuterated nanoparticles. When copolymer exchange occurs, hybrid particles with mixed cores are formed. The SLD of such hybrid particles should match the SLD of the binary solvent mixture (**Figure 1.37**). This means that the total scattering intensity of the hybrid particle dispersion is significantly reduced, because the total scattering intensity is related to the squared difference between the SLD of the solvent and because that of the nanoparticles. One advantage of this approach is that it is feasible when using only deuterated particle cores, as this component is generally responsible for most of the coherent scattering.[87]

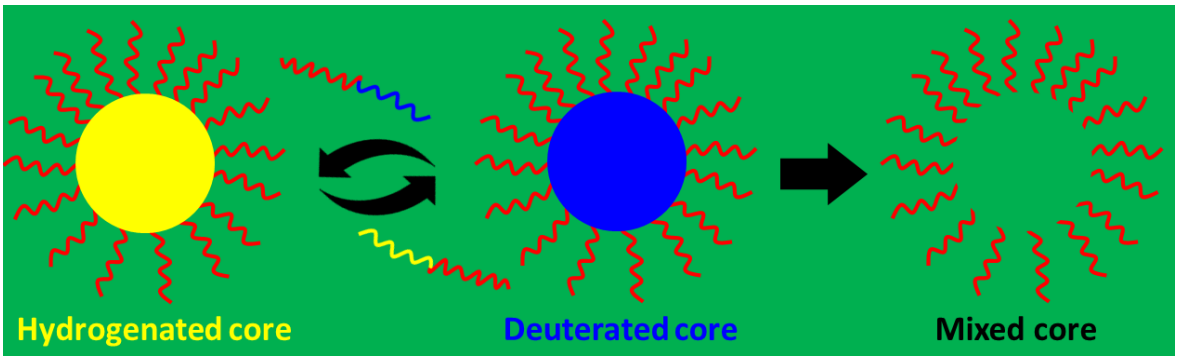

Figure 1.37. Schematic representation of a SANS experiment where copolymer exchange between micelles is monitored. The yellow particle cores are hydrogenous and the blue cores consist of deuterated polymers. The cores are chemically identical but isotopically different. As copolymer chain exchange occurs particles of intermediate colour (green) appear, which is similar to the solvent colour hence neutron contrast disappears. Hybrid particles with mixed cores have the same neutron SLD as that of the solvent, hence scattering of the core becomes negligible.

The hybrid nanoparticle cores gradually become more homogeneous during copolymer chain exchange, meaning that the scattering intensity gradually reduces. It is possible to monitor this process over time during a time-resolved neutron scattering (TR-SANS) experiment. The extent of copolymer exchange [R(t)] can be described by **Equation 1.11.**[42,43,84,88]

$$R(t) = \left[\frac{I(t) - I(\infty)}{I(0) - I(\infty)}\right]^{1/2} \qquad (\mathbf{1.11})$$

Here, I(0) and I(∞) are the integrated scattering intensities at the start of the experiment (isotopically heterogeneous mixture of nanoparticles) and the end of the experiment (fully isotopically homogeneous cores), respectively. I(t) is the integrated scattering intensity at various time points during the exchange process.

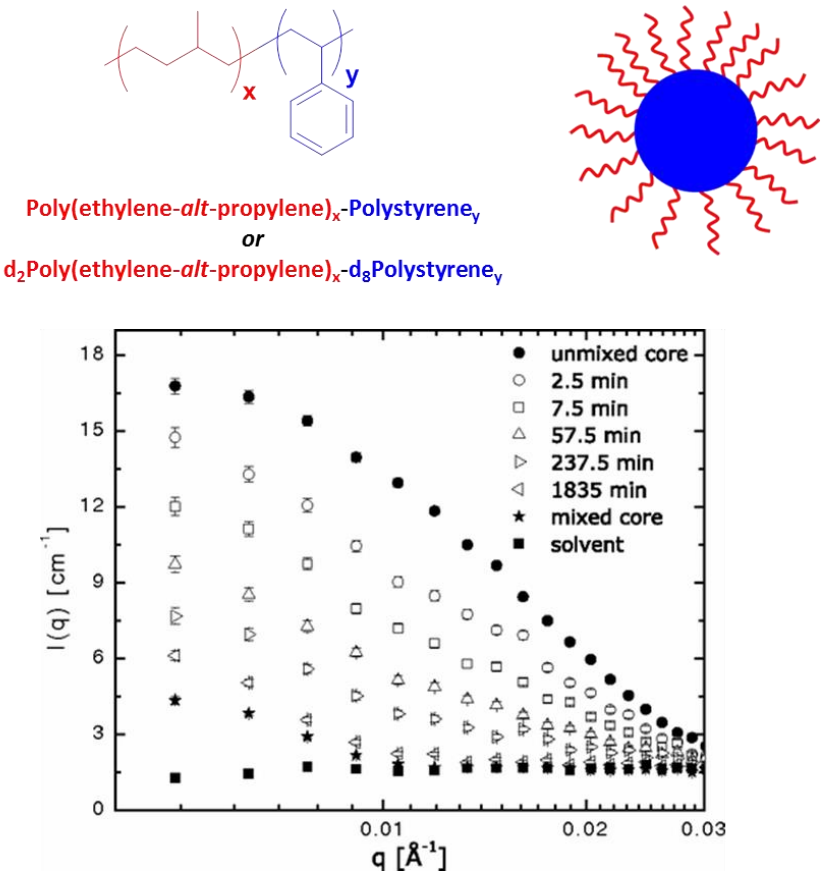

Figure 1.38. Spherical PS-PEP block copolymer nanoparticles were prepared in isotopic squalene mixtures with an intermediate neutron SLD lying between hydrogenous and deuterated nanoparticles. TR-SANS scattering patterns of 1:1 v/v mixtures of hPS_{400}-PEP_{880} and dPS_{423}-PEP_{926} at 135 °C at 1.0 % v/v. As copolymer exchange between the particles occurs, the scattering intensity is progressively reduced.[42]

A good example of such an experiment is reported by Bates and co-workers[42] Fully deuterated and hydrogenated polystyrene-poly(ethylene-*alt*-propylene) (PS-PEP) polymers were prepared via sequential anionic polymerisation of styrene and isoprene, followed by selective hydrogenation of the isoprene repeat units with deuterium or hydrogen. Post-polymerisation self-assembly was achieved via a dichloromethane-based solvent switch into isotopical squalene mixtures. The volume ratio between hydrogenated and deuterated squalene was chosen to have a neutron SLD halfway between the SLD values of hydrogenous and deuterated particles. The hydrogenous and deuterated dispersions were mixed (at 1.0 % v/v) prior to the TR-SANS experiment. Subsequent heating to 135 °C stimulated copolymer exchange and resulted in a gradual reduction in the intensity of the SANS pattern over time (**Figure 1.38**).[42] This work assessed the effect of different temperatures and PS core DPs on the rate of copolymer exchange. Spherical hPS_{250}-PEP_{970} and dPS_{260}-PEP_{985} block copolymer particles were annealed at 100, 110 and 115 °C. Additionally, hPS_{400}-PEP_{880} and dPS_{423}-PEP_{926} were analysed at 135, 140 and 145 °C. Both dispersions were prepared at 1.0 % v/v prior to thermal annealing; neutron scattering patterns were collected during this process. The extent of copolymer exchange over a certain amount of time was calculated from the integrated scattering patterns using **Equation 1.11**. These experiments showed that higher temperatures resulted in faster exchange kinetics for both block copolymer species (**Figure 1.39**). Higher PS core DPs required higher temperatures to achieve similar copolymer exchange rates in comparison to the lower PS core DPs. All the data sets were summarised in a master curve (**Figure 1.39**). These master curves were generated using shift factors obtained via the Williams-Landel-Ferry (WLF) **Equation 1.12**.[89] Clearly, the larger PS cores require higher temperatures for copolymer exchange. The master curve was fitted to a model where the rate-limiting step was assumed to be extraction of the core-forming block from the nanoparticles. This work highlights the hypersensitivity of the exchange kinetics towards both the core-forming block DP and temperature. We should note that a vertical shift was not employed for the generation of these master curves; ideally, this would be required to correct for the density change of the material at various temperatures.

$$\log \alpha_{\mathrm{T}} = \frac{-\mathrm{C}_1(T - T_0)}{\mathrm{C}_2 + (T - T_0)} \quad (\mathbf{1.12})$$

Here, α_T is the shift factor and C1 and C2 are positive constants that depend on the material and reference temperature. T is the absolute temperature of interest (measured temperature) and T_0 the reference temperature (often chosen to be the T_g). Each data set has its own individual shift factor depending on the measured temperature.

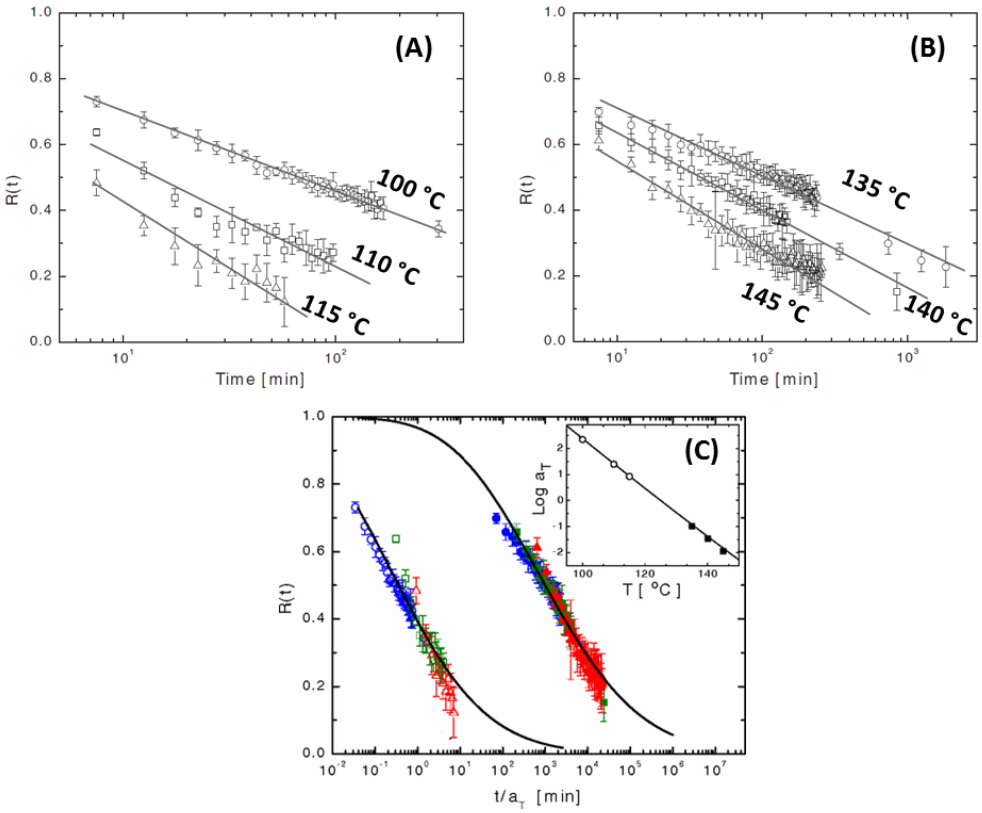

Figure 1.39. Extent of copolymer exchange [R(t)] as a function of time for (A) 1:1 v/v mixtures of hPS_{250}-PEP_{970} and dPS_{260}-PEP_{985} nanoparticles at 100, 110 and 115 °C, and (B) hPS_{400}-PEP_{880} and dPS_{423}-PEP_{926} nanoparticles at 135, 140 and 145 °C at 1 % v/v. (C) Time-temperature superimposed SANS results: open symbols correspond to hPS_{250}-PEP_{970} and dPS_{260}-PEP_{985} while the filled symbols refer to hPS_{400}-PEP_{880} and dPS_{423}-PEP_{926}. a_T shift factors were determined from the WLF equation (**Equation 1.12**) as shown in the inset (with T_{ref} = 125 °C). Higher temperatures yield faster exchange kinetics. Larger PS core DPs require higher temperatures to yield comparable exchange rates. The solid curves were the best fits to the data using a model that assumes copolymer chain expulsion from the nanoparticles to be rate-limiting.[42] (N.B. This Figure has been slightly modified from that reported in ref. 42).

The same experiment was repeated at 15 % v/v to assess the effect of concentration on the extent of copolymer exchange.[43] Apart from simply more concentrated dispersions, another factor was introduced by this process. A dispersion of 15 % v/v was sufficiently concentrated to pack into a body-centred cubic (bcc) lattice, according to SAXS analysis. The experiment was performed on both the previously discussed PS-PEP polymers, having PS core DPs of around 250 and 400. Again, higher temperatures were required for polymers with higher PS core DPs. Remarkably, the more concentrated dispersions required more intense heating in comparison to the non-ordered dispersions at 1.0 % v/v. This is clearly evident in the time–temperature superimposed plots (**Figure 1.40**). Here, the filled symbols correspond to the data at 15 % v/v, whereas the open symbols correspond to the previously discussed data at 1.0 % v/v. This result was unexpected because it was assumed that the exchange rate should be independent of the copolymer concentration. The tentative conclusion drawn by Bates and co-workers is that a higher concentration of corona chains may constitute an extra barrier to the rate-limiting polymer expulsion step.

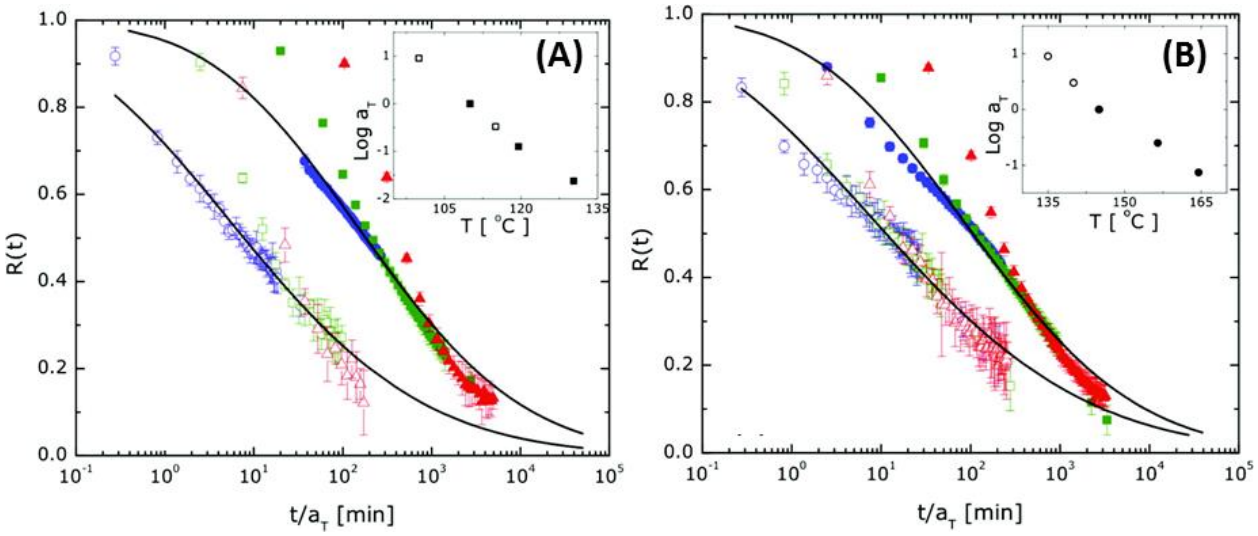

Figure 1.40. Time-temperature TR-SANS results for (A) hPS_{250}-PEP_{970} and dPS_{260}-PEP_{985} and (B) hPS_{400}-PEP_{880} and dPS_{423}-PEP_{926}. Open symbols corresponds to the data from **Figure 1.39** at 1.0 % v/v, while filled symbols correspond to copolymer exchange for the same particles at 15 % v/v, where they form an ordered bcc structure. Copolymer chain exchange for the ordered structure at 15 % v/v is an order of magnitude slower. Reference temperatures were: (A) T_{ref} = 110 °C (filled circles), 119.5 °C (filled squares) and 130.3 °C (filled triangles); and (B) PS T_{ref} = 145 °C (filled squares), 156.5 °C (filled circles), and 164.5 °C (filled triangles).[43]

Furthermore, the effect of polydispersity on copolymer chain exchange at 1.0 % v/v was assessed for the same set of block copolymers.[84] Block copolymer dispersions with small and large PS core-forming blocks (hPS_{250}-PEP_{970} and hPS_{400}-PEP_{880}) were prepared by co-dissolving them in dichloromethane before self-assembly in an isotopical squalene mixture. The same approach was used for the deuterated PS-PEP species. Finally, both species were combined prior to SANS analysis over a range of temperatures between 87 and 146 °C. A time-temperature superimposed master curve was generated from the data (**Figure 1.41**). The open and filled grey symbols in this graph correspond to the previously obtained master curves for the individual PS-PEP copolymer exchange experiments performed at 1.0 % v/v. The data obtained for the nano-objects comprising of two copolymers falls in the middle of this graph. This demonstrates that the use of bimodal mixtures of copolymer chains allows turning of the exchange rate between particles. Moreover, this work also supports the single chain exchange dynamics model as the master curve can be well-fitted to the corresponding model if the exchange rate of the individual particles is considered.[84]

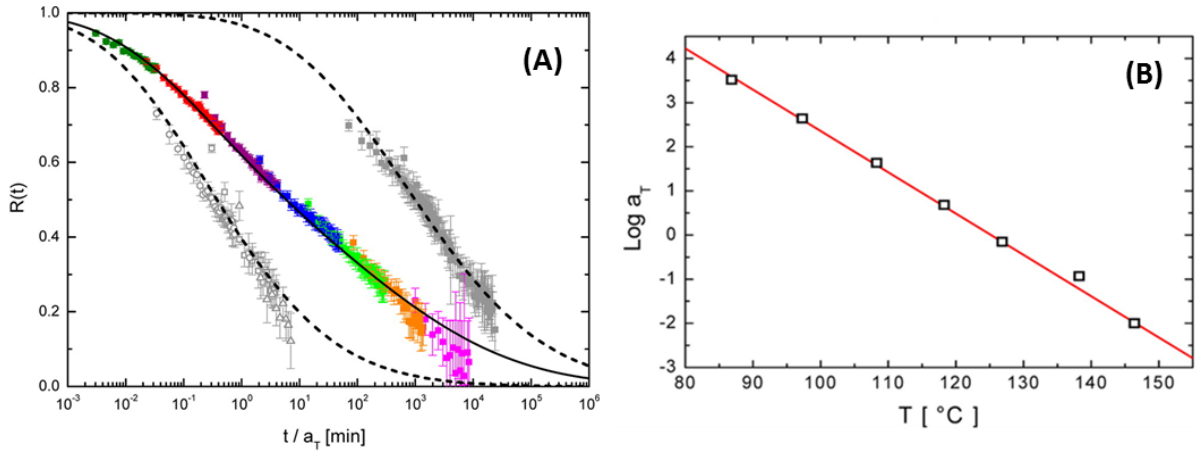

Figure 1.41. (A) Time-temperature TR-SANS master curve obtained for copolymer chain exchange between binary blends of hydrogenous hPS_{250}-PEP_{970} and hPS_{400}-PEP_{880} particles, and deuterated particles consisting of a blend of dPS_{260}-PEP_{985} and dPS_{423}-PEP_{926} particles. (B) Individual data sets were shifted using temperature-dependent shift factors as determined via the WLF equation with T_{ref} = 125 °C (**Equation 1.12**) [84]

The same block copolymer micelles comprising binary mixtures of two different sizes of core-forming block DPs were further utilised in a subsequent study. Contrast-matching enabled copolymer chain exchange of the long and short PS core-forming blocks to be investigated individually. Copolymer chain exchange for the longer core-forming block was slower that for the shorter PS core-forming block, but exchange of both species occurred simultaneously.[90]

In a subsequent study, copolymer chain exchange between triblock copolymer micelles was investigated.[88] Block copolymer micelles were prepared from PEP-PS-PEP and PS-PEP-PS in squalane. Like the PEP-PS diblock copolymer micelles, higher temperatures led to faster copolymer exchange rates. As expected, the PS-PEP-PS exchange rate was slower than that for PEP-PS-PEP. This was rationalised in terms of a higher enthalpic barrier owing to the extra PS block in the former case. Unexpectedly, PEP-PS-PEP underwent copolymer exchange faster than the corresponding PEP-PS. It was originally assumed that expulsion of the PS core-forming block would be the rate-limiting step, meaning that copolymer exchange would be independent of the stabiliser block DP. These results suggest that the corona block plays a crucial role in the copolymer chain exchange kinetics.

Subsequently the Minnesota team investigated copolymer exchange on addition of excess PEP homopolymer to the previously discussed PEP-PS micelles at 1.0% v/v.[91] This work shows a reduction in the chain exchange rate with an increased amount of added PEP homopolymer. However, these results suggest that this addition only retards copolymer exchange above a critical PEP homopolymer concentration where the PEP chains are able to penetrate into the corona region of the nanoparticle. This hypothesis was further supported by an earlier study where the same diblock copolymer chains were exchanged at higher concentrations (15% v/v).[43] The authors proposed that the addition of PEP homopolymer and higher copolymer concentrations led to a slower copolymer exchange rate. According to Halperin, this slower copolymer exchange kinetics is the result of the increase in osmotic pressure owing to an increase in the effective concentration of corona chains.[92]

As copolymer exchange is thermally-assisted one might assume that copolymer exchange does not occur below the T_g, or T_m of the core-forming copolymer block. However, recent research from Lund and co-workers shows that this assumptions may not be valid.[93] In contrast to the previously-discussed block copolymer dispersions, an aqueous formulation

highlights the possibility of block copolymer exchange below the T_m of the core-forming C_{28} block. The T_m of C_{28}-PEO_5 block copolymer was 56 °C according to DSC analysis. In this example, the copolymer exchange between hydrogenated and deuterated C_{28}-PEO_5 at 1.0 % v/v occurred below the T_m of the core-forming block. Like the previously discussed formulations, a higher temperature increases the rate of copolymer exchange (**Figure 1.42**). This study shows that core crystallisation led to significant enthalpic and entropic contributions to the exchange process, but did not make it impossible. Clearly, further studies are warranted to unravel the precise nature of this process.[93]

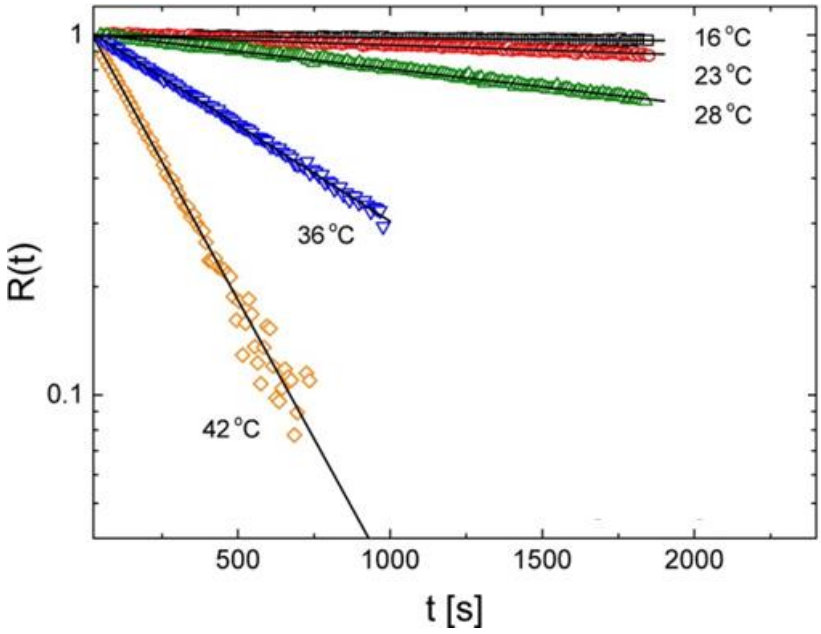

Figure 1.42. Relaxation function of chain exchange kinetics of C_{28}-PEO_5 micelles in aqueous solution. Solid lines represent linear fit curves indicating a single exponent decay. It is noteworthy that the T_m of C_{28}-PEO_5 is 56 °C according to DSC studies. [93] (N.B. This Figure has been slightly modified from that reported in ref. 93).

More recently, Lodge reported copolymer exchange between poly(methyl methacrylate)$_x$-poly(*n*-butyl methacrylate)$_y$ (PMMA-PBuMA) block copolymer nanoparticles in an ionic liquid, in which the PBuMA forms the nanoparticle cores.[94,95] Two post-polymerisation self-assembly approaches were used: the traditional solvent switch method (conform to the previous examples) and a thin film approach whereby ionic liquid was added to a block

copolymer film (deposited on the glass walls of the vial by casting from dichloromethane). The latter approach yielded larger block copolymer micelles. This allowed assessment of the effect of varying the particle diameter on the rate of copolymer exchange for identical copolymers. This experiment showed that copolymer chain exchange from the larger particles was slower than that for the smaller particles prepared using the solvent switch method.

1.5. Thesis Outline

In this Thesis we report the efficient preparation of four types of spherical diblock copolymer nanoparticles via RAFT-mediated PISA in non-polar media. In principle, careful selection of monomer and solvent should provide new insights into PISA and diblock copolymer chain exchange between sterically stabilised nanoparticles. In **Chapter 2**, we examine poly(stearyl methacrylate)-poly(2,2,2-trifluoroethyl methacrylate) (PSMA-PTFEMA) spherical nanoparticles. PTFEMA has a relatively low RI, which allows the preparation of highly transparent nanoparticles when using a suitable *n*-alkane at an appropriate temperature. Such isorefractive dispersions allow *in situ* visible absorption spectroscopy studies to be performed to assess the fate of the RAFT end-groups during PISA. Moreover, this technique allows RAFT chain-end removal to be monitored *in situ* when treating this dispersion with excess initiator. Furthermore, the semi-fluorinated nature of TFEMA enabled the polymerisation kinetics to be conveniently monitored using *in situ* ^{19}F NMR spectroscopy. This provided insights into core solvation by monomer and solvent during RAFT PISA. **Chapter 3** is dedicated to copolymer chain exchange between spherical nanoparticles at elevated temperatures. Fully hydrogenous and core-deuterated poly(lauryl methacrylate)-poly(methyl methacrylate) (PLMA-PMMA) spherical nanoparticles were prepared via RAFT PISA. These nanoparticles allowed a well-designed TR-SANS experiment; a contrast-matching approach was used to examine the effect of core DP and temperature on the extent of copolymer chain exchange. In **Chapter 4**, we show that copolymer chain exchange between binary mixtures of poly(lauryl methacrylate)-poly(benzyl methacrylate) (PLMA-PBzMA) spherical nanoparticles of differing particle diameters yields *intermediate* nanoparticle diameters. Nanoparticle fusion was further investigated using TR-SAXS, to establish the characteristic time scale for this process. Concluding remarks and suggestions for future work are discussed in **Chapter 5**.

1.6. References

(1) Ahmed, F.; Pakunlu, R. I.; Srinivas, G.; Brannan, A.; Bates, F.; Klein, M. L.; Minko, T.; Discher, D. E. Shrinkage of a rapidly growing tumor by drug-loaded polymersomes: pH-triggered release through copolymer degradation, *Molecular Pharmaceutics*, **2006**, *3*, 340-350.

(2) Chen, W.; Du, J. Ultrasound and pH Dually Responsive Polymer Vesicles for Anticancer Drug Delivery, *Scientific Reports*, **2013**, *3*, 2162.

(3) Galaev, I. Y.; Mattiasson, B. 'Smart' polymers and what they could do in biotechnology and medicine, *Trends in Biotechnology*, **1999**, *17*, 335-340.

(4) Kazunori, K.; Glenn S, K.; Masayuki, Y.; Teruo, O.; Yasuhisa, S. Block copolymer micelles as vehicles for drug delivery, *Journal of Controlled Release*, **1993**, *24*, 119-132.

(5) Tang, J.; Quinlan, P. J.; Tam, K. C. Stimuli-responsive Pickering emulsions: recent advances and potential applications, *Soft Matter*, **2015**, *11*, 3512-3529.

(6) Joshi, Y. M. Dynamics of Colloidal Glasses and Gels, *Annual Review of Chemical and Biomolecular Engineering*, **2014**, *5*, 181-202.

(7) Saha, D.; Bhattacharya, S. Hydrocolloids as thickening and gelling agents in food: a critical review, *Journal of Food Science and Technology-Mysore*, **2010**, *47*, 587-597.

(8) Krause, S. Polymer Chemistry: An Introduction, 3rd Edition (Stevens, Malcolm P.), *Journal of Chemical Education*, **2000**, *77*, 35.

(9) Moad, G.; Rizzardo, E.; Thang, S. H. Toward living radical polymerization, *Accounts of Chemical Research*, **2008**, *41*, 1133-1142.

(10) Buback, M.; Frauendorf, H.; Guenzler, F.; Huff, F.; Vana, P. Determining Initiator Efficiency in Radical Polymerization by Electrospray-Ionization Mass Spectrometry, *Macromolecular Chemistry and Physics*, **2009**, *210*, 1591-1599.

(11) Clayden, J.; Greeves, N.; Warren, S. G. *Organic chemistry*; Oxford University Press: Oxford; New YorK, **2012**, p1041.

(12) Kamigaito, M.; Ando, T.; Sawamoto, M. Metal-catalyzed living radical polymerization, *Chemical Reviews*, **2001**, *101*, 3689-3745.

(13) Ahmad, N. M.; Charleux, B.; Farcet, C.; Ferguson, C. J.; Gaynor, S. G.; Hawkett, B. S.; Heatley, F.; Klumperman, B.; Konkolewicz, D.; Lovell, P. A.; Matyjaszewski, K.; Venkatesh, R. Chain Transfer to Polymer and Branching in Controlled Radical Polymerizations of n-Butyl Acrylate, *Macromolecular Rapid Communications*, **2009**, *30*, 2002-2021.

(14) Nicolas, J.; Guillaneuf, Y.; Lefay, C.; Bertin, D.; Gigmes, D.; Charleux, B. Nitroxide-mediated polymerization, *Progress in Polymer Science*, **2013**, *38*, 63-235.

(15) Braunecker, W. A.; Matyjaszewski, K. Controlled/living radical polymerization: Features, developments, and perspectives, *Progress in Polymer Science*, **2007**, *32*, 93-146.

(16) Grubbs, R. B. Nitroxide-Mediated Radical Polymerization: Limitations and Versatility, *Polymer Reviews*, **2011**, *51*, 104-137.

(17) Chang, C.-C.; Studer, A. Acceleration of the Styryl-TEMPO-Mediated Controlled Radical Styrene Polymerization by Addition of an Efficient Alkoxyamine, *Macromolecules*, **2006**, *39*, 4062-4068.

(18) Matyjaszewski, K. Atom Transfer Radical Polymerization (ATRP): Current Status and Future Perspectives, *Macromolecules*, **2012**, *45*, 4015-4039.

(19) Chmielarz, P.; Krys, P.; Park, S.; Matyjaszewski, K. PEO-b-PNIPAM copolymers via SARA ATRP and eATRP in aqueous media, *Polymer*, **2015**, *71*, 143-147.

(20) Moad, G.; Rizzardo, E.; Thang, S. H. Living radical polymerization by the RAFT process - A first update, *Australian Journal of Chemistry*, **2006**, *59*, 669-692.

(21) Moad, G.; Rizzardo, E.; Thang, S. H. Living Radical Polymerization by the RAFT Process - A Second Update, *Australian Journal of Chemistry*, **2009**, *62*, 1402-1472.

(22) Moad, G.; Rizzardo, E.; Thang, S. H. Living Radical Polymerization by the RAFT Process - A Third Update, *Australian Journal of Chemistry*, **2012**, *65*, 985-1076.

(23) Nakabayashi, K.; Mori, H. Recent progress in controlled radical polymerization of N-vinyl monomers, *European Polymer Journal*, **2013**, *49*, 2808-2838.

(24) Benaglia, M.; Rizzardo, E.; Alberti, A.; Guerra, M. Searching for more effective agents and conditions for the RAFT polymerization of MMA: Influence of dithioester substituents, solvent, and temperature, *Macromolecules*, **2005**, *38*, 3129-3140.

(25) Barner-Kowollik, C. *Handbook of RAFT polymerization*; Wiley-VCH, **2008**, p438.

(26) Chen, B. C.; Bednarz, M. S.; Kocy, O. R.; Sundeen, J. E. A new highly enantioselective synthesis of both (R)- and (S)-2-mercaptosuccinic acids, *Tetrahedron-Asymmetry*, **1998**, *9*, 1641-1644.

(27) Liard, A.; QuicletSire, B.; Zard, S. Z. A practical method for the reductive cleavage of the sulfide bond in xanthates, *Tetrahedron Letters*, **1996**, *37*, 5877-5880.

(28) Jesson, C. P.; Pearce, C. M.; Simon, H.; Werner, A.; Cunningham, V. J.; Lovett, J. R.; Smallridge, M. J.; Warren, N. J.; Armes, S. P. H2O2 Enables Convenient Removal of RAFT End-Groups from Block Copolymer Nano-Objects Prepared via Polymerization-Induced Self-Assembly in Water, *Macromolecules*, **2017**, *50*, 182-191.

(29) Pichot, R.; Watson, R. L.; Norton, I. T. Phospholipids at the interface: current trends and challenges, *International Journal of Molecular Science*, **2013**, *14*, 11767-11794.

(30) Mai, Y.; Eisenberg, A. Self-assembly of block copolymers, *Chemical Society Reviews*, **2012**, *41*, 5969-5985.

(31) Warren, N. J.; Armes, S. P. Polymerization-Induced Self-Assembly of Block Copolymer Nano-objects via RAFT Aqueous Dispersion Polymerization, *Journal of the American Chemical Society*, **2014**, *136*, 10174-10185.

(32) Derry, M. J.; Fielding, L. A.; Armes, S. P. Polymerization-induced self-assembly of block copolymer nanoparticles via RAFT non-aqueous dispersion polymerization, *Progress in Polymer Science*, **2016**, *52*, 1-18.

(33) Canning, S. L.; Smith, G. N.; Armes, S. P. A Critical Appraisal of RAFT-Mediated Polymerization-Induced Self-Assembly, *Macromolecules*, **2016**, 49, 1985-2001

(34) Bates, F. S. Polymer-polymer phase-behavior, *Science*, **1991**, *251*, 898-905.

(35) Bates, F. S.; Fredrickson, G. H. Block copolymers - Designer soft materials, *Physics Today*, **1999**, *52*, 32-38.

(36) Forster, S.; Plantenberg, T. From self-organizing polymers to nanohybrid and biomaterials, *Angewandte Chemie-International Edition*, **2002**, *41*, 689-714.

(37) Khandpur, A. K.; Forster, S.; Bates, F. S.; Hamley, I. W.; Ryan, A. J.; Bras, W.; Almdal, K.; Mortensen, K. Polyisoprene-polystyrene diblock copolymer phase diagram near the order-disorder transition, *Macromolecules*, **1995**, *28*, 8796-8806.

(38) Blanazs, A.; Ryan, A. J.; Armes, S. P. Predictive Phase Diagrams for RAFT Aqueous Dispersion Polymerization: Effect of Block Copolymer Composition, Molecular Weight, and Copolymer Concentration, *Macromolecules*, **2012**, *45*, 5099-5107.

(39) Lopez-Oliva, A. P.; Warren, N. J.; Rajkumar, A.; Mykhaylyk, O. O.; Derry, M. J.; Doncom, K. E. B.; Rymaruk, M. J.; Armes, S. P. Polydimethylsiloxane-Based Diblock Copolymer Nano-objects Prepared in Nonpolar Media via RAFT-Mediated Polymerization-Induced Self-Assembly, *Macromolecules*, **2015**, *48*, 3547-3555.

(40) Discher, D. E.; Eisenberg, A. Polymer vesicles, *Science*, **2002**, *297*, 967-973.

(41) Cameron, N. S.; Corbierre, M. K.; Eisenberg, A. 1998 E.W.R. Steacie Award Lecture Asymmetric amphiphilic block copolymers in solution: a morphological wonderland, *Canadian Journal of Chemistry-Revue Canadienne De Chimie*, **1999**, *77*, 1311-1326.

(42) Choi, S. H.; Lodge, T. P.; Bates, F. S. Mechanism of Molecular Exchange in Diblock Copolymer Micelles: Hypersensitivity to Core Chain Length, *Physical Review Letters*, **2010**, *104*, 047802.

(43) Choi, S.-H.; Bates, F. S.; Lodge, T. P. Molecular Exchange in Ordered Diblock Copolymer Micelles, *Macromolecules*, **2011**, *44*, 3594-3604.

(44) Zhang, L. F.; Eisenberg, A. Multiple morphologies and characteristics of "crew-cut" micelle-like aggregates of polystyrene-b-poly(acrylic acid) diblock copolymers in aqueous solutions, *Journal of the American Chemical Society*, **1996**, *118*, 3168-3181.

(45) Zhang, L. F.; Eisenberg, A. Formation of crew-cut aggregates of various morphologies from amphiphilic block copolymers in solution, *Polymers for Advanced Technologies*, **1998**, *9*, 677-699.

(46) Discher, D. E.; Ahmed, F. In Annual Review of Biomedical Engineering **2006**, *8*, p323-341.

(47) Zhang, L. F.; Eisenberg, A. Thermodynamic vs kinetic aspects in the formation and morphological transitions of crew-cut aggregates produced by self-assembly of polystyrene-b-poly(acrylic acid) block copolymers in dilute solution, *Macromolecules*, **1999**, *32*, 2239-2249.

(48) Shen, H. W.; Eisenberg, A. Morphological phase diagram for a ternary system of block copolymer PS310-b-PAA(52)/dioxane/H2O, *Journal of Physical Chemistry B*, **1999**, *103*, 9473-9487.

(49) Zhang, L. F.; Shen, H. W.; Eisenberg, A. Phase separation behavior and crew-cut micelle formation of polystyrene-b-poly(acrylic acid) copolymers in solutions, *Macromolecules*, **1997**, *30*, 1001-1011.

(50) Israelachvili, J. N. Intermolecular and Surface Forces, 3rd Edition **2011**, p1.

(51) Yu, Y. S.; Zhang, L. F.; Eisenberg, A. Morphogenic effect of solvent on crew-cut aggregates of apmphiphilic diblock copolymers, *Macromolecules*, **1998**, *31*, 1144-1154.

(52) Bhargava, P.; Zheng, J. X.; Li, P.; Quirk, R. P.; Harris, F. W.; Cheng, S. Z. D. Self-assembled polystyrene-block-poly(ethylene oxide) micelle morphologies in solution, *Macromolecules*, **2006**, *39*, 4880-4888.

(53) Blanazs, A.; Madsen, J.; Battaglia, G.; Ryan, A. J.; Armes, S. P. Mechanistic Insights for Block Copolymer Morphologies: How Do Worms Form Vesicles?, *Journal of the American Chemical Society*, **2011**, *133*, 16581-16587.

(54) Warren, N. J.; Mykhaylyk, O. O.; Mahmood, D.; Ryan, A. J.; Armes, S. P. RAFT Aqueous Dispersion Polymerization Yields Poly(ethylene glycol)-Based Diblock Copolymer Nano-Objects with Predictable Single Phase Morphologies, *Journal of the American Chemical Society*, **2014**, *136*, 1023-1033.

(55) Ratcliffe, L. P. D.; Ryan, A. J.; Armes, S. P. From a Water-Immiscible Monomer to Block Copolymer Nano-Objects via a One-Pot RAFT Aqueous Dispersion Polymerization Formulation, *Macromolecules*, **2013**, *46*, 769-777.

(56) Chambon, P.; Blanazs, A.; Battaglia, G.; Armes, S. P. Facile Synthesis of Methacrylic ABC Triblock Copolymer Vesicles by RAFT Aqueous Dispersion Polymerization, *Macromolecules*, **2012**, *45*, 5081-5090.

(57) Derry, M. J.; Fielding, L. A.; Armes, S. P. Industrially-relevant polymerization-induced self-assembly formulations in non-polar solvents: RAFT dispersion polymerization of benzyl methacrylate, *Polymer Chemistry*, **2015**, *6*, 3054-3062.

(58) Zehm, D.; Ratcliffe, L. P. D.; Armes, S. P. Synthesis of Diblock Copolymer Nanoparticles via RAFT Alcoholic Dispersion Polymerization: Effect of Block Copolymer Composition, Molecular Weight, Copolymer Concentration, and Solvent Type on the Final Particle Morphology, *Macromolecules*, **2013**, *46*, 128-139.

(59) Blanazs, A.; Armes, S. P.; Ryan, A. J. Self-Assembled Block Copolymer Aggregates: From Micelles to Vesicles and their Biological Applications, *Macromolecular Rapid Communications*, **2009**, *30*, 267-277.

(60) Blanazs, A.; Verber, R.; Mykhaylyk, O. O.; Ryan, A. J.; Heath, J. Z.; Douglas, C. W. I.; Armes, S. P. Sterilizable Gels from Thermoresponsive Block Copolymer Worms, *Journal of the American Chemical Society*, **2012**, *134*, 9741-9748.

(61) Cockram, A. A.; Neal, T. J.; Derry, M. J.; Mykhaylyk, O. O.; Williams, N. S. J.; Murray, M. W.; Emmett, S. N.; Armes, S. P. Effect of Monomer Solubility on the Evolution of Copolymer Morphology during Polymerization-Induced Self-Assembly in Aqueous Solution, *Macromolecules*, **2017**, *50*, 796-802.

(62) Cunningham, V. J.; Alswieleh, A. M.; Thompson, K. L.; Williams, M.; Leggett, G. J.; Armes, S. P.; Musa, O. M. Poly(glycerol monomethacrylate)-Poly(benzyl methacrylate) Diblock Copolymer Nanoparticles via RAFT Emulsion Polymerization: Synthesis, Characterization, and Interfacial Activity, *Macromolecules*, **2014**, *47*, 5613-5623.

(63) Houillot, L.; Bui, C.; Save, M.; Charleux, B.; Farcet, C.; Moire, C.; Raust, J.-A.; Rodriguez, I. Synthesis of well-defined polyacrylate particle dispersions in organic

medium using simultaneous RAFT polymerization and self-assembly of block copolymers. A strong influence of the selected thiocarbonylthio chain transfer agent, *Macromolecules*, **2007**, *40*, 6500-6509.

(64) Houillot, L.; Bui, C.; Farcet, C.; Moire, C.; Raust, J.-A.; Pasch, H.; Save, M.; Charleux, B. Dispersion Polymerization of Methyl Acrylate in Nonpolar Solvent Stabilized by Block Copolymers Formed In situ via the RAFT Process, *ACS Applied Materials & Interfaces*, **2010**, *2*, 434-442.

(65) Raust, J.-A.; Houillot, L.; Save, M.; Charleux, B.; Moire, C.; Farcet, C.; Pasch, H. Two Dimensional Chromatographic Characterization of Block Copolymers of 2-Ethylhexyl Acrylate and Methyl Acrylate, P2EHA-b-PMA, produced via RAFT-Mediated Polymerization in Organic Dispersion, *Macromolecules*, **2010**, *43*, 8755-8765.

(66) Fielding, L. A.; Derry, M. J.; Ladmiral, V.; Rosselgong, J.; Rodrigues, A. M.; Ratcliffe, L. P. D.; Sugihara, S.; Armes, S. P. RAFT dispersion polymerization in non-polar solvents: facile production of block copolymer spheres, worms and vesicles in n-alkanes, *Chemical Science*, **2013**, *4*, 2081-2087.

(67) Fielding, L. A.; Lane, J. A.; Derry, M. J.; Mykhaylyk, O. O.; Armes, S. P. Thermo-responsive Diblock Copolymer Worm Gels in Non-polar Solvents, *Journal of the American Chemical Society*, **2014**, *136*, 5790-5798.

(68) Pei, Y.; Thurairajah, L.; Sugita, O. R.; Lowe, A. B. RAFT Dispersion Polymerization in Nonpolar Media: Polymerization of 3-Phenylpropyl Methacrylate in n-Tetradecane with Poly(stearyl methacrylate) Homopolymers as Macro Chain Transfer Agents, *Macromolecules*, **2015**, *48*, 236-244.

(69) Pei, Y.; Sugita, O. R.; Thurairajah, L.; Lowe, A. B. Synthesis of poly(stearyl methacrylate-b-3-phenylpropyl methacrylate) nanoparticles in n-octane and associated thermoreversible polymorphism, *RSC Advances*, **2015**, *5*, 17636-17646.

(70) Pei, Y.; Noy, J.-M.; Roth, P. J.; Lowe, A. B. Soft Matter Nanoparticles with Reactive Coronal Pentafluorophenyl Methacrylate Residues via Non-Polar RAFT Dispersion Polymerization and Polymerization-Induced Self-Assembly, *Journal of Polymer Science Part A - Polymer Chemistry*, **2015**, *53*, 2326-2335.

(71) Cornel, E. J.; van Meurs, S.; Smith, T.; O'Hora, P. S.; Armes, S. P. In Situ Spectroscopic Studies of Highly Transparent Nanoparticle Dispersions Enable Assessment of Trithiocarbonate Chain-End Fidelity during RAFT Dispersion Polymerization in Nonpolar Media, *Journal of the American Chemical Society*, **2018**, *140*, 12980-12988.

(72) Derry, M. J.; Fielding, L. A.; Warren, N. J.; Mable, C. J.; Smith, A. J.; Mykhaylyk, O. O.; Armes, S. P. In situ small-angle X-ray scattering studies of sterically-stabilized diblock copolymer nanoparticles formed during polymerization-induced self-assembly in non-polar media, *Chemical Science*, **2016**, *7*, 5078-5090.

(73) Zheng, R.; Liu, G.; Devlin, M.; Hux, K.; Jao, T.-C. Friction Reduction of Lubricant Base Oil by Micelles and Crosslinked Micelles of Block Copolymers, *Tribology Transactions*, **2010**, *53*, 97-107.

(74) Zheng, R. H.; Liu, G. J.; Jao, T. C. Poly (2-ethylhexyl acrylate)-ran-(tert-butyl acrylate) -block-poly(2-cinnamoyloxyethyl acrylate) synthesis and properties, *Polymer*, **2007**, *48*, 7049-7057.

(75) Verber, R.; Blanazs, A.; Armes, S. P. Rheological studies of thermo-responsive diblock copolymer worm gels, *Soft Matter*, **2012**, *8*, 9915-9922.

(76) Lovett, J. R.; Derry, M. J.; Yang, P.; Hatton, F. L.; Warren, N. J.; Fowler, Patrick W.; Armes, S. P. Can percolation theory explain the gelation behavior of diblock copolymer worms?, *Chemical Science*, **2018**, *9*, 7138-7144.

(77) Derry, M. J.; Mykhaylyk, O. O.; Armes, S. P. A Vesicle-to-Worm Transition Provides a New High-Temperature Oil Thickening Mechanism, *Angewandte Chemie International Edition*, **2017**, *56*, 1746-1750.

(78) Andrade, E. N. D. C. The Viscosity of Liquids, *Nature*, **1930**, *125*, 309.

(79) Heskins, M.; Guillet, J. E. Solution Properties of Poly(N-isopropylacrylamide), *Journal of Macromolecular Science: Part A - Chemistry*, **1968**, *2*, 1441-1455.

(80) Canton, I.; Warren, N. J.; Chahal, A.; Amps, K.; Wood, A.; Weightman, R.; Wang, E.; Moore, H.; Armes, S. P. Mucin-Inspired Thermoresponsive Synthetic Hydrogels

Induce Stasis in Human Pluripotent Stem Cells and Human Embryos, *ACS Central Science*, **2016**, *2*, 65-74.

(81) Lund, R.; Willner, L.; Richter, D. In Controlled Polymerization and Polymeric Structures: Flow Microreactor Polymerization, Micelles Kinetics, Polypeptide Ordering, Light Emitting Nanostructures; Abe, A., Lee, K. S., Leibler, L., Kobayashi, S., **2013**, *259*, p51-158.

(82) Dautzenberq, H. Surfactant solutions. New methods of investigation, New York/Basel, **1988**, *39*, 470-470.

(83) Lessner, E.; Teubner, M.; Kahlweit, M. Relaxation experiments in aqueous solutions of ionic micelles. 2. Experiments on the system water-sodium dodecyl sulfate-sodium perchlorate and their theoretical interpretation, *The Journal of Physical Chemistry*, **1981**, *85*, 3167-3175.

(84) Lu, J.; Choi, S.; Bates, F. S.; Lodge, T. P. Molecular Exchange in Diblock Copolymer Micelles: Bimodal Distribution in Core-Block Molecular Weights, *ACS Macro Letters*, **2012**, *1*, 982-985.

(85) Halperin, A.; Alexander, S. Polymeric micelles: their relaxation kinetics, *Macromolecules*, **1989**, *22*, 2403-2412.

(86) Dormidontova, E. E. Micellization Kinetics in Block Copolymer Solutions: Scaling Model, *Macromolecules*, **1999**, *32*, 7630-7644.

(87) Pedersen, J. S. Form factors of block copolymer micelles with spherical, ellipsoidal and cylindrical cores, *Journal of Applied Crystallography*, **2000**, *33*, 637-640.

(88) Lu, J.; Bates, F. S.; Lodge, T. P. Remarkable Effect of Molecular Architecture on Chain Exchange in Triblock Copolymer Micelles, *Macromolecules*, **2015**, *48*, 2667-2676.

(89) Ferry, J. D. *Viscoelastic properties of polymers*; Wiley: New York, **1980**, p280.

(90) Lu, J.; Bates, F. S.; Lodge, T. P. Chain Exchange in Binary Copolymer Micelles at Equilibrium: Confirmation of the Independent Chain Hypothesis, *ACS Macro Letters*, **2013**, *2*, 451-455.

(91) Lu, J.; Bates, F. S.; Lodge, T. P. Addition of Corona Block Homopolymer Retards Chain Exchange in Solutions of Block Copolymer Micelles, *Macromolecules*, **2016**, *49*, 1405-1413.

(92) Halperin, A. On Micellar Exchange: The Role of the Insertion Penalty, *Macromolecules*, **2011**, *44*, 5072-5074.

(93) Zinn, T.; Willner, L.; Pipich, V.; Richter, D.; Lund, R. Effect of Core Crystallization and Conformational Entropy on the Molecular Exchange Kinetics of Polymeric Micelles, *ACS Macro Letters*, **2015**, *4*, 651-655.

(94) Zhao, D.; Ma, Y.; Lodge, T. P. Exchange Kinetics for a Single Block Copolymer in Micelles of Two Different Sizes, *Macromolecules*, **2018**, *51*, 2312-2320.

(95) Ma, Y.; Lodge, T. P. Chain Exchange Kinetics in Diblock Copolymer Micelles in Ionic Liquids: The Role of χ, *Macromolecules*, **2016**, *49*, 9542-9552.

Chapter 2

In Situ Spectroscopic Studies of Highly Transparent Nanoparticle Dispersions

2.1. Introduction

This first results Chapter is dedicated to the *in situ* analysis of spherical nanoparticle synthesis via RAFT PISA. In contrast to the following result chapters, nanoparticle behaviour is assessed after synthesis. All polymers prepared by RAFT polymerisation have a RAFT group located at the chain-end. As discussed in **Chapter 1**, RAFT chain transfer agents (CTAs) are organosulfur compounds that can be utilised for chain-end functionalisation.[1-4] For optimal control, RAFT chain-ends should remain stable during RAFT polymerisation but it is well-known that RAFT end-groups are gradually lost either under monomer-starved conditions[5-8] or in the presence of water.[9,10] Moreover, such CTAs are coloured, malodorous and potentially toxic, so their quantitative removal is often desired for potential applications.[11,12] Fortunately, RAFT chain-ends can be readily cleaved using reagents such as amines[13], ozone,[11] H_2O_2[14] or excess radical initiator[15].

Semsarilar *et al.* examined the stability of trithiocarbonate RAFT end-groups for the RAFT dispersion polymerisation of 2,2,2-trifluoroethyl methacrylate (TFEMA) in ethanol using either a poly(methacrylic acid) (PMAA) or a poly(2-(dimethylamino)ethyl methacrylate) (PDMA) CTA.[5] The growing PTFEMA block became insoluble in ethanol and hence formed the nanoparticle cores, with the PMAA or PDMA chains acting as the steric stabiliser. Semi-fluorinated polymers typically exhibit relatively low refractive indices.[16] In this particular example, the refractive index of PTFEMA (1.41) is reasonably close to that of ethanol (1.36), which results in a weakly scattering dispersion. Periodic sampling of the reaction solution for such a dispersion polymerisation followed by dilution enabled UV spectra to be recorded, and hence the RAFT chain-end fidelity to be assessed. A slow decay in RAFT chain-end fidelity was observed over 24 h at 70 °C by monitoring the absorption maximum corresponding to the trithiocarbonate end-groups at 305 nm. Approximately 43 % end-groups were lost during RAFT solution polymerisation of TFEMA in THF at 70 °C, whereas only 27% end-groups were degraded during the corresponding RAFT dispersion polymerisation of TFEMA in ethanol under the same conditions. Thus the latter *heterogeneous* polymerisation offers greater pseudo-living character (and a faster rate of polymerisation) than the equivalent *homogeneous* polymerisation.[17] However, *in situ* spectroscopic studies were not feasible for this PISA formulation, partly because the dispersions were not sufficiently isorefractive and

also because the UV signal arising from the RAFT CTA chain-ends was far too intense (molar extinction coefficient, $\varepsilon_{max} \sim 1.5 \times 10^4$ dm^3 mol^{-1} cm^{-1}).

Herein we report the RAFT dispersion polymerisation of TFEMA in *n*-tetradecane to afford poly(stearyl methacrylate)-poly(2,2,2-trifluoroethyl methacrylate) (PSMA-PTFEMA) spherical nanoparticles of 33 nm diameter. These nanoparticles are almost perfectly isorefractive with the solvent at the reaction temperature of 70 °C, which enables high-quality visible absorption spectra to be recorded *in situ* without any interference from particle scattering. This allows the RAFT chain-end fidelity to be conveniently monitored throughout the polymerisation, *even when preparing such nanoparticles at 30% w/w solids*. Subsequently, removal of the RAFT end-groups can be monitored *in situ* after addition of excess initiator at 70 °C. Moreover, *in situ* ^{19}F NMR spectroscopy studies provide useful insights with regard to both the PISA mechanism and the ingress of hot solvent within the nanoparticle cores at 70 °C. Finally, such highly transparent dispersions may offer new opportunities for further scientific studies in the field of colloid science.[18-20]

2.2. Experimental

2.2.1 Materials

Stearyl methacrylate (SMA), 2,2,2-trifluoroethyl methacrylate (TFEMA), *n*-dodecane, *n*-tetradecane, *n*-hexane, trimethylamine, butylhydroxytoluene (BHT) tetrahydrofuran (THF), toluene, 2,2-azobis(2-methylpropionitrile) (AIBN), lauroyl peroxide (Luperox®), ruthenium(IV) oxide hydrate and sodium periodate were all purchased from Sigma-Aldrich (UK). Monomers were passed through a basic alumina column prior to use to remove inhibitor. Tert-butyl peroxy-2-ethylhexanoate (Trigonox 21S or T21s) initiator was supplied by AkzoNobel (The Netherlands). d-Chloroform ($CDCl_3$) was purchased from VWR (UK), d_2-dichloromethane (CD_2Cl_2) and d_8-toluene were obtained from Cambridge Isotope Laboratory (USA). The 4-cyano-4-((2-phenylethanesulfonyl)thiocarbonylsulfanyl)pentanoic acid (PETTC) RAFT agent was prepared in-house according to a previously reported protocol.[1]

2.2.2. Methods

2.2.2.1. PSMA Macro-CTA Synthesis via RAFT Solution Polymerisation

A $PSMA_{12}$ macro-CTA was prepared via RAFT solution polymerisation of SMA in toluene. Briefly, SMA (19.95 g, 58.91 mmol), PETTC (2.00 g, 5.89 mmol; target DP = 10), AIBN (0.19 g, 1.18 mmol; PETTC/AIBN molar ratio = 5.0) and toluene (22.14 g) were added to a 100 ml round-bottomed flask. This reaction solution was heated by immersing the flask in an oil bath set at 70 °C and the resulting SMA polymerisation was quenched by exposure to air after 4 h. ^{1}H NMR analysis in $CDCl_3$ indicated 72% SMA conversion under these conditions (**Figure 2.1**).

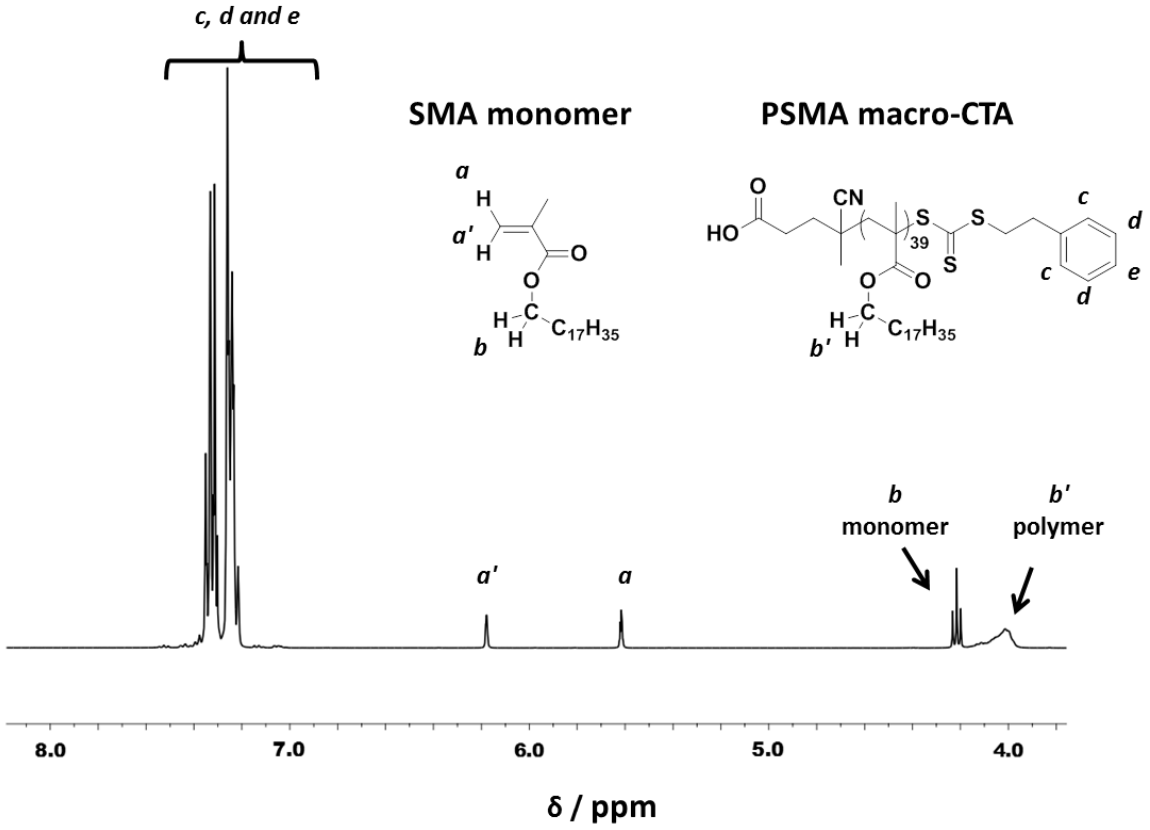

Figure 2.1. Representative proton NMR spectrum recorded in $CDCl_3$ for a sample of the reaction solution taken during the RAFT-mediated solution polymerization of stearyl methacrylate. After a reaction time of 4 h, a monomer conversion of 76% was calculated using **Equation 2.1** by comparing the integrated monomer vinyl protons (a and a') with the integrated oxymethylene signals (b_{monomer} and b'_{polymer}) assigned to SMA monomer and PSMA homopolymer.

The crude product was precipitated in excess ethanol and dried *in vacuo* at 30 °C. A mean DP of 12 was determined for the purified PSMA macro-CTA via ^{1}H NMR analysis in CD_2Cl_2; the integrated aromatic PETTC signals at 7.1–8.1 ppm were compared to that of the oxymethylene signal at 3.7–4.2 ppm. This analysis indicated a CTA efficiency of 61%. THF GPC studies (refractive index detector; using a series of eight polystyrene calibration standards) indicated a M_n of 5 400 g mol^{-1} and an M_w/M_n of 1.15. A $PSMA_{32}$ macro-CTA was prepared in a similar fashion. In this case, a DP of 40 was targeted and the CTA efficiency was determined to be 96%. End-group analysis using ^{1}H NMR spectroscopy indicated an M_n of 11 200 g mol^{-1}, which was comparable to that indicated by THF GPC analysis (M_n = 12 300 g mol^{-1}, M_w/M_n = 1.18).

$$\textbf{\textit{SMA conversion}}\ (\%) = \left[1 - \frac{\boldsymbol{a} + \boldsymbol{a}'}{\boldsymbol{b}_{\textbf{monomer}} + \boldsymbol{b}'_{\textbf{polymer}}}\right] \times 100\% \quad (\mathbf{2.1})$$

The mean DP of the PLMA precursor was determined via end-group analysis by analyzing a proton NMR spectrum recorded for the purified homopolymer in CD_2Cl_2. In this case, the proton signal assigned to the aromatic end-group at 7.18-7.38 ppm was compared to that of the oxymethylene (b'_{polymer}) signal of the PLMA homopolymer at 3.92–4.08 ppm. (**Equation 2.2**).

$$\textbf{\textit{PSMA DP}} = \frac{\left[(\boldsymbol{c} + \boldsymbol{d} + \boldsymbol{e}) \times \frac{\mathbf{2}}{\mathbf{5}}\right]}{\boldsymbol{b}'_{\textbf{polymer}}} \quad (\mathbf{2.2})$$

2.2.2.2. Synthesis of Spherical PSMA-PTFEMA Diblock Copolymer Nanoparticles via RAFT Dispersion Polymerisation

The synthesis of $PSMA_{12}$-$PTFEMA_{100}$ nanoparticles at 30% w/w solids was conducted as follows: a $PSMA_{12}$ macro-CTA (1.04 g, 0.24 mmol), lauroyl peroxide (38 mg, 0.096 mmol), and *n*-tetradecane (11.82 g, 15.5 ml) were added in turn to a glass vial and the resulting solution was degassed with N_2 gas for 30 min at 20 °C. TFEMA was degassed separately at

20 °C to minimise evaporation. This monomer (3.42 ml, 20.3 mmol; target DP = 100) was then added by syringe to the reaction mixture, which was subsequently heated to 70 °C for 16 h by immersing the vial in an oil bath. The synthesis of $PSMA_{32}$-$PTFEMA_{500}$ nanoparticles at 30% w/w solids was conducted as follows: a $PSMA_{32}$ macro-CTA (0.1 g, 0.0089 mmol), T21s initiator (8.6 µl of a 10 % v/v dispersion), and *n*-tetradecane (1.99 g, 1.52 ml) (or *n*-dodecane 1.99 g, 1.49 ml) were combined in a glass vial and degassed with N_2 for 30 min at 20 °C. TFEMA was degassed separately at 20 °C to minimise evaporation problems and this monomer (0.64 ml, 4.48 mmol; target DP = 500) was then added via syringe to the reaction mixture, which was subsequently heated to 90 °C for 16 h by immersing the vial in an oil bath.

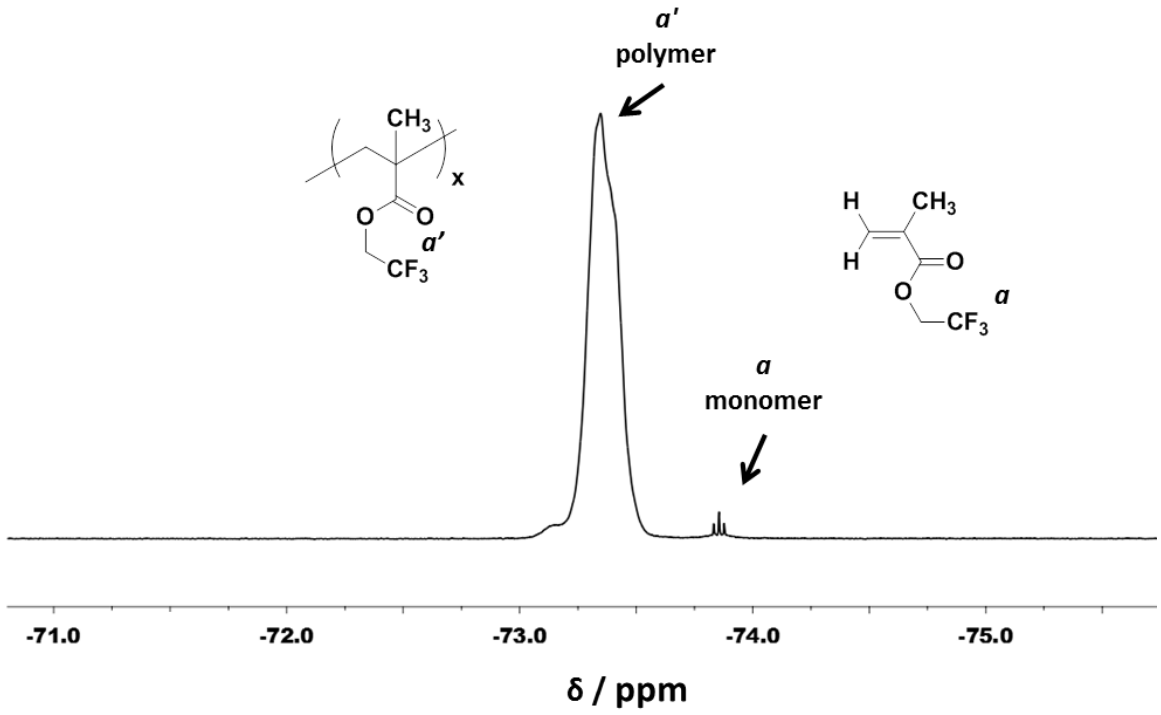

Figure 2.2. Representative ^{19}F NMR spectrum for a crude sample of $PSMA_{12}$-$PTFEMA_{100}$ recorded in $CDCl_3$. Monomer conversions were calculated according to **Equation 2.3** using the integrated monomer signals (a_{monomer}) and the methyl signals (a'_{polymer}) assigned to the TFEMA and PTFEMA.

$$\textbf{\textit{TFEMA conversions}}\ \% = \frac{\boldsymbol{a'}_{\textbf{polymer}}}{\boldsymbol{a'}_{\textbf{polymer}} + \boldsymbol{a}_{\textbf{monomer}}} \times \mathbf{100}\% \quad (\mathbf{2.3})$$

2.2.2.3. In Situ Visible Absorption Spectroscopy Studies During the Synthesis of $PSMA_{12}$-$PTFEMA_{98}$ Spherical Nanoparticles

Visible absorption spectra were recorded using an Agilent Cary 60 spectrometer equipped with a Hellma all-quartz UV/visible immersion probe, 1.8 m fibre-optic cables and SMA 905 connectors. This probe has a wavelength range of 190 to 1100 nm, a 10 mm path length, and its operating temperature range is from 5 to 150 °C. Prior to these *in situ* measurements a baseline for pure *n*-tetradecane was recorded at 70 °C. Spectra were recorded between 200 and 800 nm every 5 min for 15 h at a scan rate of 1800 nm min^{-1} during both the TFEMA polymerisation and the subsequent chain-end removal reaction.

2.2.2.4. In Situ ^{19}F NMR Spectroscopy Studies During the Synthesis of $PSMA_{12}$-$PTFEMA_{98}$ Spherical Nanoparticles

A $PSMA_{12}$ macro-CTA was chain-extended with TFEMA targeting a PTFEMA DP of 100 and a solids content of 30% w/w. The reaction mixture was prepared as described above and loaded into a degassed NMR tube equipped with a J-Young's tap. A capillary tube containing 1.20 mol dm^{-3} trifluorotoluene (used as an external standard; ^{19}F shift at -63.72 ppm) dissolved in d_8-toluene (lock solvent) was flame-sealed and inserted into the NMR tube under an N_2 atmosphere. This NMR tube assembly was inserted in a preheated Bruker AVANCE III HD spectrometer operating at 500.13 MHz (^1H frequency) at 70 °C. ^{19}F NMR spectra were recorded using a 90° pulse, eight transients and a relaxation delay of 15 s (the T_1 values for both the TFEMA monomer and the internal standard having previously been determined to be less than 2.5 s) with an acquisition window of 113.6 kHz and 227 k data points. Spectra were recorded every 5 min for 3 h. A reference spectrum at the beginning of the polymerisation was obtained by quenching the initial reaction mixture with oxygen, and analysed at 70 °C using the same parameters. All spectra were phase- and baseline-corrected using Bruker TopSpin 3.1 software. The PTFEMA signal was normalised relative to the d_8-trifluorotoluene lock solvent and TFEMA conversions were determined by comparing integrated monomer and polymer signals (using deconvolution, if required).

2.2.2.5. Variable temperature ^{19}F NMR studies of $PSMA_{12}$-$PTFEMA_{98}$ spherical nanoparticles

Variable temperature ^{19}F NMR spectra were recorded after the *in situ* ^{19}F NMR studies of the PISA synthesis of $PSMA_{12}$-$PTFEMA_{98}$ spherical nanoparticles. The final reaction mixture was heated up to 90 °C and a spectrum was recorded after allowing 15 min for thermal equilibration. Thereafter, this reaction mixture was cooled to 10 °C, with further spectra being recorded at 10 °C intervals (with 15 min thermal equilibration being allowed in each case).

2.2.2.6. Copolymer Characterisation

THF GPC. Molecular weight distributions were assessed by gel permeation chromatography (GPC) using THF as an eluent. The GPC set-up comprised an Agilent 1260 Infinity series degasser and pump, two Agilent PLgel 5 μm *Mixed C* columns in series and a refractive index detector. The mobile phase contained 2.0% v/v trimethylamine and 0.05% w/w butylhydroxytoluene (BHT) and the flow rate was fixed at 1.0 ml min^{-1}. Samples were dissolved in THF containing 0.50% v/v toluene as a flow-rate marker prior to GPC analysis. A series of eight near-monodisperse polystyrene standards (M_p values ranging from 580 to 552 500 g mol^{-1}) were used for calibration using either a refractive index detector or a UV detector operating at a fixed λ of 260 nm.

^{1}H NMR spectroscopy. Proton NMR spectra were recorded in $CDCl_3$ or CD_2Cl_2 using a Bruker AV3HD-400 or 500 MHz spectrometer. Spectra were analysed using TopSpin version 3.1 software. For the $PLMA_{39}$ synthesis, the final LMA monomer conversion was determined by dissolution of a small volume of the crude dispersion in $CDCl_3$ prior to analysis. The PLMA DP was acquired by dissolution of a small volume of purified PLMA in CD_2Cl_2, and calculated via end-group analysis as described in Section 2.2.2.1.

^{19}F NMR spectroscopy. ^{19}F NMR spectra were recorded in $CDCl_3$ using a Bruker AVANCE III HD spectrometer operating at 400.23 MHz (^{1}H frequency). Spectra were recorded using 16 transients with an acquisition window of 89.3 kHz, 128 points and a relaxation delay of 1 s. Spectra were analysed using TopSpin version 3.1 software. TFEMA conversions were determined by comparing the integrated intensities of signals assigned to monomer and polymer.

Transmission Electron Microscopy (TEM). TEM stain was prepared by dissolving ruthenium(IV) oxide hydrate (0.30 g) and sodium periodate (2.00 g) in 50 ml water.

Copolymer dispersions were diluted to 0.02% w/w in *n*-tetradecane and dispersed on carbon-coated copper TEM grids. Loaded grids were stained for 7 min by exposure to the TEM stain in a desiccator TEM images were recorded using a Tecnai Spirit T12 TEM instrument operating at 80 kV and equipped with an Orius SC1000B CCD camera (2672 x 4008 pixels; 9 μm each).

Small-angle X-ray scattering (SAXS). Measurements were performed using a Bruker Nanostar SAXS instrument modified with a GeniX3D microfocus Cu Kα X-ray tube and motorized scatterless slits for the beam collimation (Xenocs, France) and equipped with a 2D HiSTAR multiwire gas detector (Siemens/Bruker). Data were recorded over a q (scattering vector) range of 0.009 $Å^{-1} < q < 0.17$ $Å^{-1}$ using a sample-to-detector distance of 1.46 m. Data were collected using 2 mm diameter glass capillaries (WJM-Glass Muller GMBH, Germany). Water and a glassy carbon standard were used for absolute intensity calibration.[21] SAXS measurements were conducted on 1.0% w/w dispersions of either $PLMA_{39}$-$PMMA_x$ or $PLMA_{39}$-d_8PMMA_x nanoparticles in *n*-dodecane. Exposure times were 1800 s for the empty capillary and solvent background. Scattering data for the dilute copolymer dispersions (1.0% w/w) were collected for 300 s. SAXS patterns were fitted using either the Debye function[22] or a spherical micelle model[23-25] (Both models will be discussed later in **Chapter 3.2.3.**) after normalization and background subtraction using the Irena macros[26] for Igor Pro software. Scattering length densities (SLD) of each component and block volumes (**Table 2.1**) were calculated as described in **Chapter 3.2.3.**

Table 2.1. Scattering length densities and core volumes used to fit the SAXS scattering patterns.

Compound	**Block volume / Å^3**	**Density / g cm^{-3}**	**X-ray SLD (×10^{-6}) / Å^{-2}**
$PSMA_{12}$	6955	1.2	9.24
$PTFEMA_{100}$	18611	1.47	12.76
n-tetradecane	-	0.764	7.43

Mass Density measurements. Solution densities of the reaction mixture before polymerisation and of the final dispersion were determined using an Anton Paar DMA 5000 M densitometer at 70 °C.

Dynamic Light Scattering (DLS). Copolymer dispersions were diluted to approximately 0.02% w/w in *n*-hexane (to deliberately produce a mismatched refractive index) and then placed in a glass cuvette. A Malvern Zetasizer NanoZS instrument was used to determine intensity-average hydrodynamic diameters at 20 °C via the Stokes-Einstein equation using a fixed scattering angle of 173°.

2.3. Results and Discussion

2.3.1. Preparation of Isorefractive PSMA-PTFEMA Nanoparticle Dispersions

In initial scouting experiments, poly(stearyl methacrylate)-poly(2,2,2-trifluoroethyl methacrylate) (PSMA-PTFEMA) diblock copolymer nanoparticles were prepared via RAFT dispersion polymerisation in either *n*-tetradecane or *n*-dodecane. As expected, the PTFEMA block became insoluble at a certain critical degree of polymerisation (DP) as it grows from the soluble PSMA block; this leads to micellar nucleation and eventually the formation of sterically-stabilised spherical nanoparticles, as shown with TEM analysis (**Figure 2.3.**).

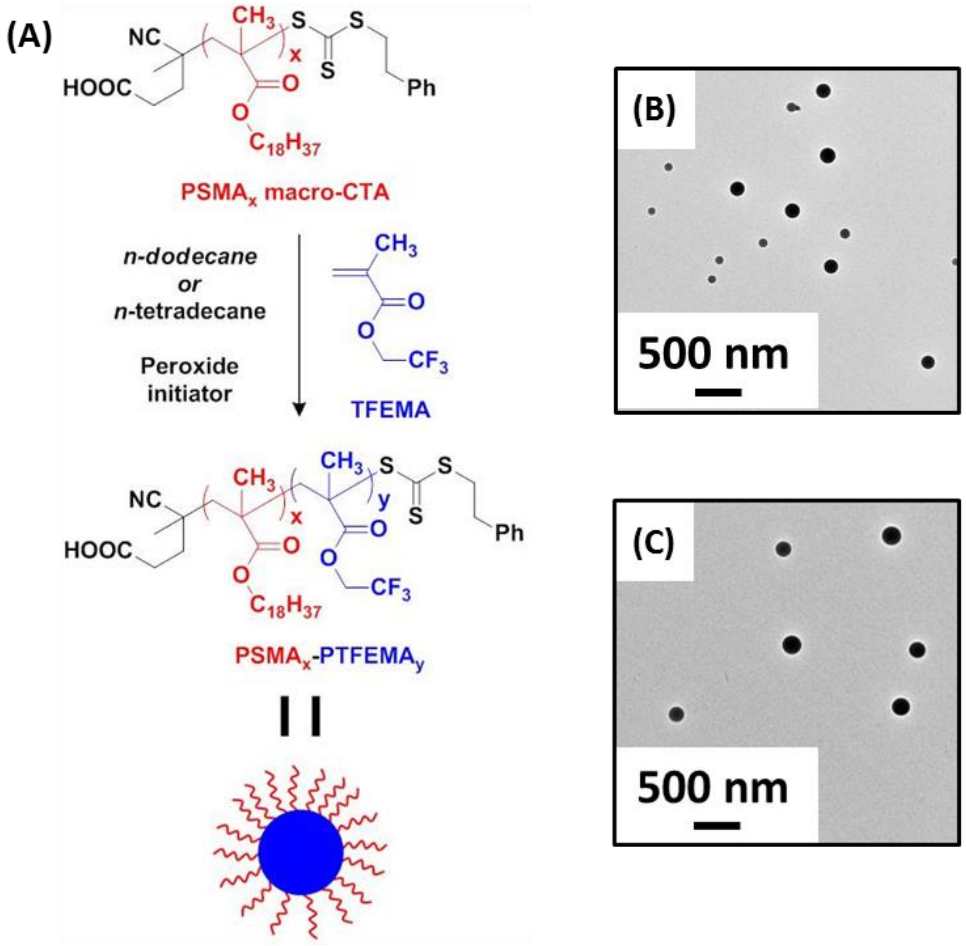

Figure 2.3. (A) Chain extension of a $PSMA_x$ homopolymer precursor via RAFT dispersion polymerisation of TFEMA in either *n*-dodecane or *n*-tetradecane at 70 or 90 °C. The growing PTFEMA block becomes insoluble at a certain critical DP, leading to *in situ* self-assembly to form spherical $PSMA_x$-$PTFEMA_y$ nanoparticles. (B) TEM image of spherical $PSMA_{32}$-$PTFEMA_{490}$ nanoparticles prepared via RAFT-mediated PISA in *n*-dodecane, (c) and *n*-tetradecane.

Such PISA syntheses enable high monomer conversions to be achieved (>98%) and can be performed at relatively high copolymer concentration (30% w/w in this particular case).[27] In the present study, we sought to identify suitable reaction conditions to produce highly transparent dispersions. This is because we wished to utilise *in situ* visible absorption spectroscopy to monitor the fidelity of the trithiocarbonate RAFT end-groups during RAFT dispersion polymerisation.

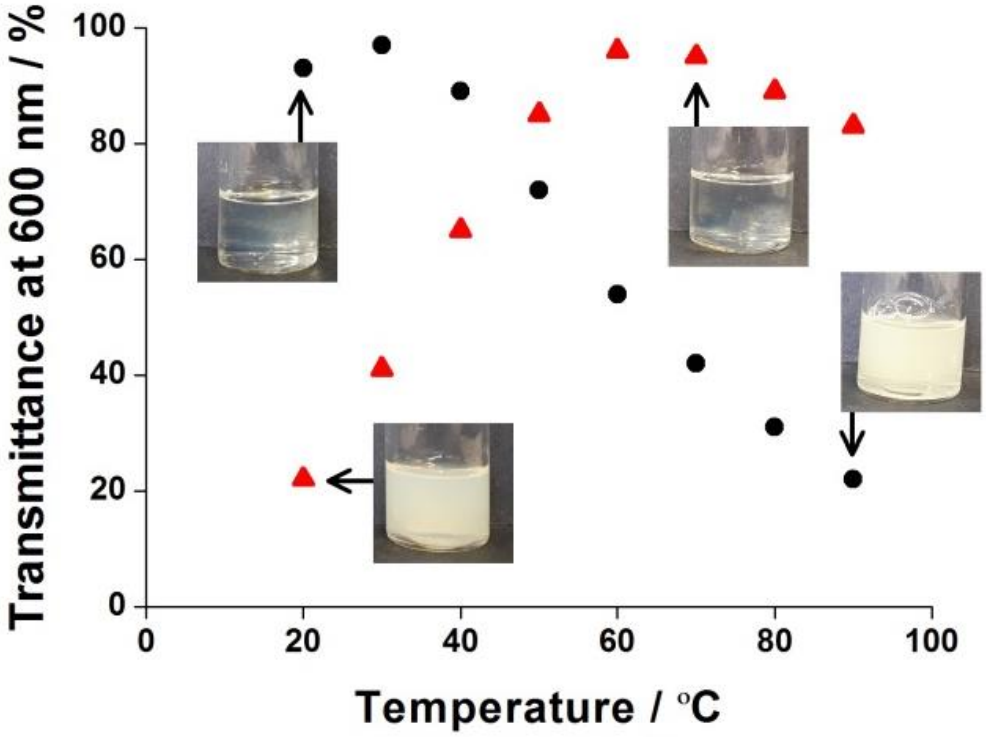

Figure 2.4. Transmittance (at λ = 600 nm) vs. temperature plots recorded for $PSMA_{32}$-$PTFEMA_{490}$ spherical nanoparticles prepared via RAFT dispersion polymerisation of TFEMA in either *n*-dodecane (●) or *n*-tetradecane (▲) at 30% w/w solids. For a given particle size and concentration, the refractive index difference between the PTFEMA nanoparticle cores and the solvent (either *n*-dodecane or *n*-tetradecane) determines the turbidity of the dispersion.

It is essential that particle scattering is eliminated for such studies. Otherwise, Tyndall scattering results in a rising baseline at shorter wavelengths which prevents reliable quantification of the spectra.[28] PTFEMA was selected as the core-forming block because this semifluorinated polymer has a relatively low refractive index (1.418 at 20 °C).[16] PTFEMA is insoluble in all linear *n*-alkanes, and this homologous series of solvents offers an appropriate range of refractive indices.[29] Thus, it should be feasible to obtain a reasonably good match to the PTFEMA refractive index by simply selecting an appropriate *n*-alkane as the solvent for the PISA synthesis.[30] However, this approach is complicated by the temperature dependence of the refractive index for both the PTFEMA and the *n*-alkane. Moreover, the refractive index of the PSMA (1.48 at 20 °C) nanoparticle corona block could also influence the isorefractive temperature of these dispersions. **Figure 2.4** shows the transmittance versus temperature

plots recorded for $PSMA_{32}$-$PTFEMA_{490}$ nanoparticles prepared via PISA in *n*-dodecane (1.420 at 20 °C) and *n*-tetradecane (1.429 at 20 °C), respectively. The former solvent (black circles) provides a highly transparent dispersion for $PSMA_{32}$-$PTFEMA_{490}$ nanoparticles of 235 ± 77 nm diameter at 30 °C (**Figure 2.3**), but a relatively turbid dispersion at higher temperatures (e.g. see the inset digital image recorded at 90 °C).

Because RAFT polymerisations are typically performed at 60-90 °C, such turbidity prevents *in situ* visible absorption spectroscopy studies from being performed during PISA syntheses conducted in this solvent. In contrast, similar-sized $PSMA_{32}$-$PTFEMA_{490}$ nanoparticles (240 ± 36 nm diameter) prepared in *n*-tetradecane are turbid at ambient temperature but become highly transparent at elevated temperature, with a minimum in turbidity being observed at around 60-70 °C. It is perhaps worth emphasising the remarkably subtle nature of this refractive index matching problem: the refractive indices of *n*-dodecane and *n*-tetradecane at 20 °C are 1.421 and 1.429, respectively. In view of these initial observations, we elected to perform PISA syntheses of PSMA-PTFEMA nanoparticles in *n*-tetradecane at 70 °C. For spherical nanoparticles, it is well-known that the scattered light intensity scales as the sixth power of the particle radius. Thus, shorter DPs were targeted for the PTFEMA block in order to reduce the nanoparticle core diameter and hence further minimise the dispersion turbidity. More specifically, $PSMA_{12}$-$PTFEMA_{100}$ nanoparticles were targeted at a copolymer concentration of 30% w/w and this PISA formulation forms the basis of the rest of this **Chapter**.

2.3.2. *In situ* Visible Absorbance Spectroscopy during RAFT PISA

The very high transmittance (>99%) observed for $PSMA_{12}$-$PTFEMA_{98}$ nanoparticles in *n*-tetradecane at 70 °C is sufficient to enable high-quality visible absorption spectra to be recorded with minimal interference from particle scattering. In principle, this can be achieved by using a commercial all-quartz UV-visible probe (**Figure 2.5**) and a dedicated UV-visible spectrometer. In practice, such *in situ* measurements also require a sufficiently weak absorption band to avoid signal saturation when monitoring PISA syntheses performed in concentrated solution (30% w/w). Fortunately, the well-known 'forbidden' absorption band at 446 nm associated with trithiocarbonate RAFT end-groups proved to be suitable for the

purpose of this study.[31] Shi and co-workers assigned this spectral feature to an n→π* transition and used it to monitor the stability of trithiocarbonate chain-ends during the visible light-mediated RAFT aqueous *solution* polymerisation of 2-(N-acryloyloxyethyl) pyrrolidone (NAEP) at 25 °C using a water-soluble photoinitiator.[31] However, as far as we are aware, this band has not been exploited to monitor the progress of any *heterogeneous* formulations such as RAFT dispersion polymerisation, for which isorefractivity is essential. A Beer-Lambert calibration plot for the trithiocarbonate-based $PSMA_{12}$ precursor block used in this study indicated that this weak 446 nm band had a molar extinction coefficient of 33.21 ± 0.14 dm^3 mol^{-1} cm^{-1} (**Figure 2.6**). For comparison, the well-known UV band at 305-310 nm associated with trithiocarbonates has a much higher molar extinction coefficient of ~ 1.5 x 10^4 dm^3 mol^{-1} cm^{-1}.[5,32]

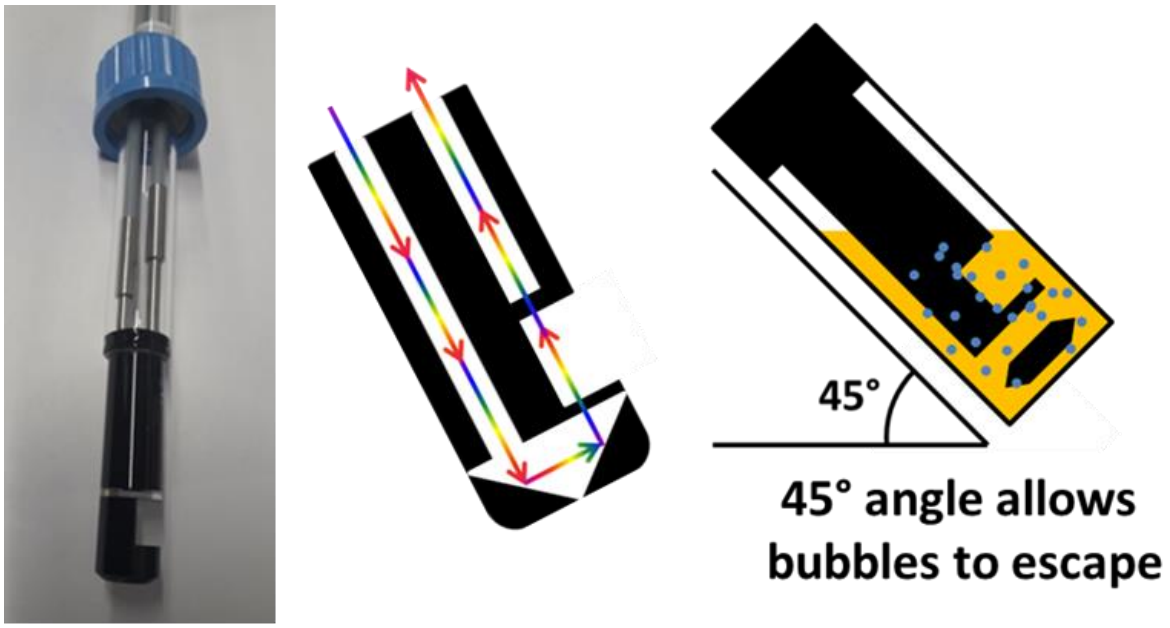

Figure 2.5. Digital photograph and schematic cartoons of the all-quartz UV/visible immersion probe used in this study. This 10 mm path length probe was tilted at 45° during in situ visible absorption spectroscopy studies in order to prevent gas bubbles from becoming trapped in the cell (which would otherwise cause unwanted light scattering).

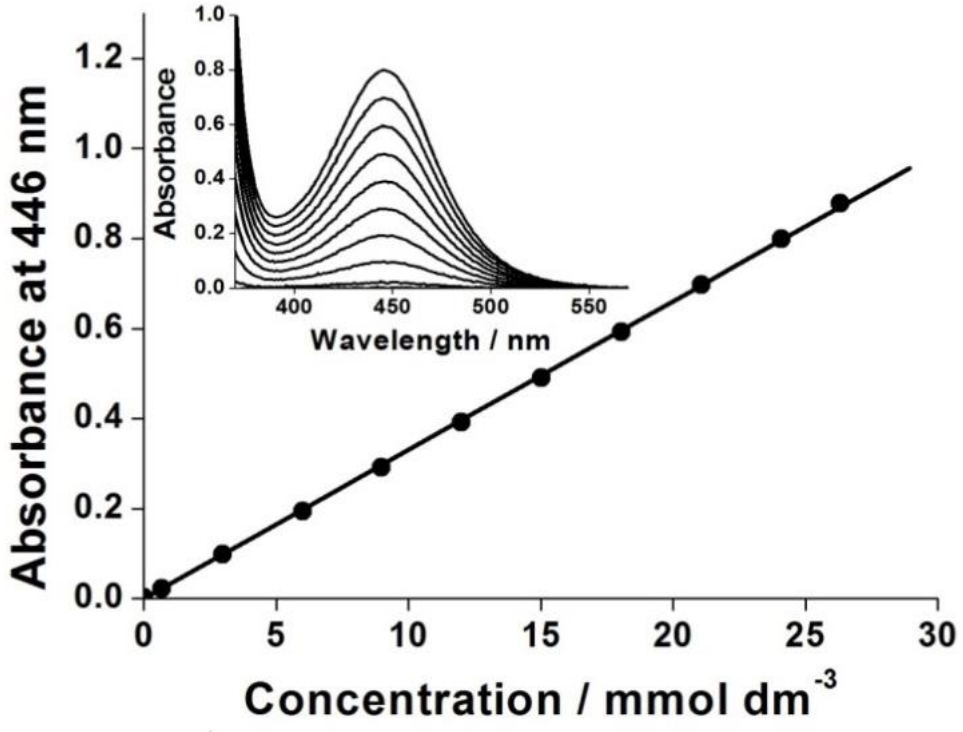

Figure 2.6. Beer-Lambert calibration curve constructed for the trithiocarbonate-based $PSMA_{12}$ precursor block (inset shows the associated visible absorption spectra) using its relatively weak n→π* band at λ_{max} = 446 nm, for which Ɛ is calculated to be 33.21 ± 0.14 dm^3 mol^{-1} cm^{-1}. This $PSMA_{12}$ RAFT agent also exhibits a much more intense band at 305 nm.[5] However, this latter spectral feature is too strong to allow *in situ* spectroscopic studies during RAFT dispersion Polymerisations performed at 30% w/w. Please note that the forbidden absorbance band is located on the tail of a stronger π→π* transition at lower wavelengths. However, this strong absorbance band should not influence the absorbance at 446 nm, as is visible from spectra in the insert of this figure. This is further supported by the linearity of the Beer-Lambert plot.

Spherical $PSMA_{12}$-$PTFEMA_{98}$ nanoparticles were prepared in *n*-tetradecane at 30% w/w and this isorefractive PISA formulation was studied using *in situ* visible absorption spectroscopy. Preliminary experiments yielded very noisy data, because gas bubbles associated with the thermal decomposition of the lauroyl peroxide initiator led to sporadic light scattering (and hence anomalous absorbance values). Fortunately, this technical problem was solved by inclining the UV-visible quartz probe at an angle of approximately 45° so that the rising gas bubbles were much less likely to interfere with the light beam (**Figure 2.5**).

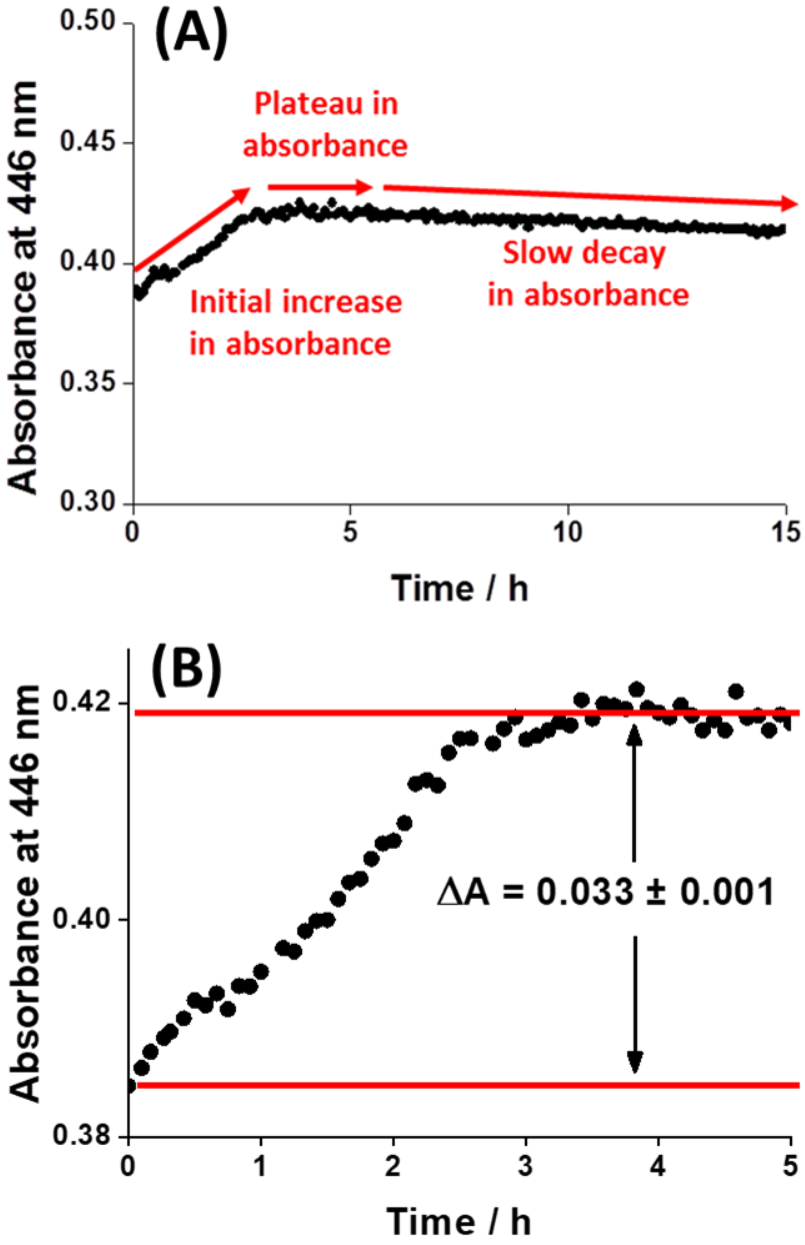

Figure 2.7. (A) Typical absorbance vs. time plot obtained via *in situ* visible absorption spectroscopy studies of the RAFT dispersion polymerisation of TFEMA using a $PSMA_{12}$ macro-CTA at 70°C, where the weak absorption band at 446 nm is assigned to the trithiocarbonate RAFT end-groups. The constant absorbance observed after approximately 3 h indicates excellent RAFT chain-end stability under monomer-starved conditions, with only a slow decay in absorbance observed between 5 and 15 h. (B) Expansion of [(A)] between 0 to 5 h, a significant volume contraction occurs on converting TFEMA (ρ = 1.18 g cm^{-3}) into PTFEMA (ρ = 1.47 g cm^{-3}), which leads to the observed increase in absorbance. These data can be used to conveniently monitor the polymerisation kinetics via dilatometry (**Figure 2.8**).

Originally, we had expected to see a gradual decay in the 446 nm absorption band during polymerisation due to the degradation of RAFT end-groups.[5-8] In fact, a significant *increase* in absorbance at 446 nm was observed over the first 3 h of the TFEMA polymerisation (**Figure 2.7**), followed by a plateau region where the absorbance of this band remained approximately constant for at least 2 h at 70 °C. Initially, we were puzzled by the unexpected increase in absorbance within the first 3 h.

Literature[32] suggests that the substituents of the CTA (in this particular case from PSMA-CTA to PSMA-PTFEMA-CTA) can drastically affect λ_{max} and Ɛ; however, we have seen in other unpublished studies that a change in λ_{max} (peak shift to lower wavelengths) is more prominent in the case of dithiobenzoate CTAs. Moreover, rapid formation of the low molecular weight polymer, after the first few monomer additions to the CTA would suppress further change in peak shift. Furthermore, a similar Ɛ was obtained for the $PSMA_{12}$ macro-CTA and a $PSMA_{12}$-$PTFEMA_{50}$ block copolymer; both measured in toluene to avoid nucleation artefacts. Eventually, we realised that the absorbance increase during RAFT PISA was directly related to the significant volume contraction that occurs during the conversion of TFEMA monomer (ρ = 1.18 g cm^{-3} at 20 °C)[33] into PTFEMA (ρ = 1.47 g cm^{-3} at 20 °C),[34] which leads to an increase in the RAFT end-group concentration. Solution density measurements were performed before and after the TFEMA polymerisation to confirm this interpretation. The theoretical change in absorbance owing to volumetric contraction, ΔA, is calculated to be 0.032 from the densities of the initial and final dispersions, see **Equation 2.4**.

$$\Delta \mathbf{A} = \boldsymbol{\varepsilon} \cdot \Delta \mathbf{V}(\mathbf{L}) = \boldsymbol{\varepsilon} \cdot \frac{\boldsymbol{\rho}_1}{\boldsymbol{\rho}_2 \cdot 1000} = 33.21 \cdot \frac{0.8089}{0.8365 \cdot 1000} = 0.032 \quad (\mathbf{2.4})$$

Here, ρ_1 and ρ_2 are the densities of the reaction mixture at 70 °C determined before (0.8089 g cm^{-3}) and after (0.8365 g cm^{-3}) the TFEMA polymerisation, respectively (with a final TFEMA conversion of 98% being achieved). $\mathcal{E}$ is the molar extinction coefficient calculated from the Beer-Lambert plot constructed for the $PSMA_{12}$ macro-CTA, using the weak absorption bond at 446 nm (**Figure 2.6**), and ΔV(L) is the change in volume expressed in litres. The experimentally observed increase in absorbance (0.033 ± 0.001) indicated in

Figure 2.7 is equal to this theoretical value within experimental error. Such a dilatometric effect is well-known in polymer science and has been previously utilised to monitor the kinetics of polymerisation.[35,36] Hence, we examined whether the RAFT end-group absorption band at 446 nm could be used to monitor the kinetics of a RAFT dispersion polymerisation for such an isorefractive formulation.

The raw absorbance data shown in **Figure 2.7** can be converted into fractional TFEMA conversions using **Equation 2.5**.

$$\textbf{TFEMA conversion}\ (\%) = \frac{\mathbf{A_t - A_0}}{\mathbf{A_f - A_0}} \times \textbf{final conversion}\ (\%) \quad (\mathbf{2.5})$$

Here, A_0 is the initial absorbance (obtained by extrapolating the linear region of the absorbance plot at the beginning of the reaction, see **Figure 2.7**), A_t is the absorbance at any given time (t) and A_f is the final absorbance of the reaction mixture at the end of the polymerisation, as calculated by averaging absorbance values recorded between 3 h and 5 h. The resulting conversion vs. time curve determined by *in situ* visible absorption spectroscopy (**Figure 2.8A**) is in good agreement with kinetic data obtained by ^{19}F NMR studies conducted in $CDCl_3$, which is a good solvent for both the PSMA and PTFEMA blocks and hence ensures molecular dissolution of the nanoparticles prior to their analysis (**Figure 2.8B**). Aliquots were periodically taken during the TFEMA polymerisation, with 96% TFEMA conversion being achieved within 3 h. The corresponding semi-logarithmic kinetic plots, calculated from the initial monomer concentration ($[M]_0$), and monomer concentration at intermediate time points during the polymerisation ($[M]_x$), revealed three distinct linear regimes in each case. A discernible change in the rate of polymerisation is observed after 1 h, which corresponds to the onset of micellar nucleation (**Figure 2.8**, see blue arrows). This occurs at approximately 20% TFEMA conversion, which suggests that the growing PTFEMA chains become insoluble in the polymerising mixture when they reach a critical DP of approximately 20, with further polymerisation occurring within monomer-swollen micelles. The higher local monomer concentration leads to an approximate two-fold increase in the rate of polymerisation, as judged by the change in gradient (**Figure 2.8**). Similar observations

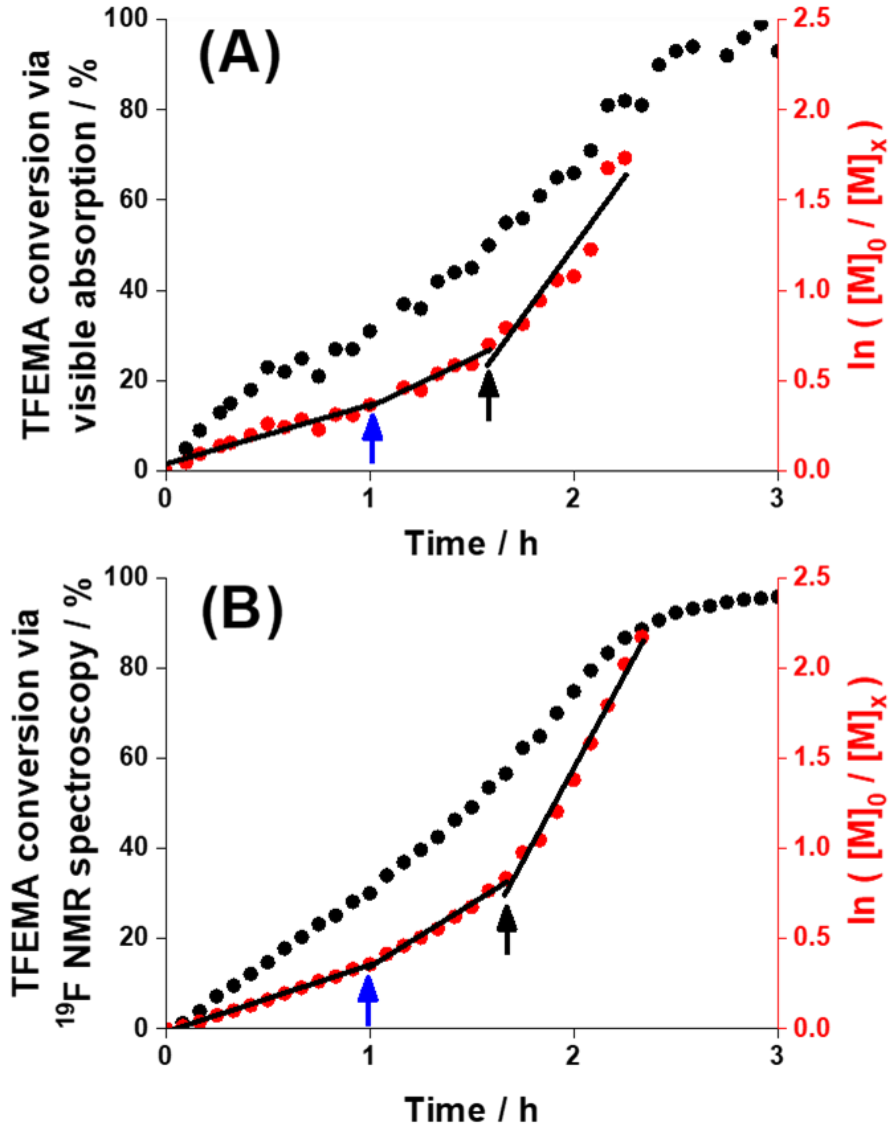

Figure 2.8. Conversion vs. time curves and associated semi-logarithmic plots for the RAFT dispersion polymerisation of TFEMA at 70 °C using a $PSMA_{12}$ precursor to produce a 30% w/w dispersion of sterically-stabilised spherical nanoparticles. Remarkably similar reaction kinetics were observed by (a) *in situ* visible absorption spectroscopy using the weak 446 nm band assigned to the trithiocarbonate end-groups and (b) periodic sampling of the polymerisation, followed by ^{19}F NMR spectroscopy analysis of the quenched aliquots. The TFEMA conversion was 98% after 3 h, indicating a final $PSMA_{12}$-$PTFEMA_{98}$ composition. Changes in reaction rate are indicated by blue and black arrows. The semi-logarithmic plots were calculated from the initial monomer concentration ($[M]_0$), and monomer concentration at intermediate time points during the polymerisation ($[M]_x$).

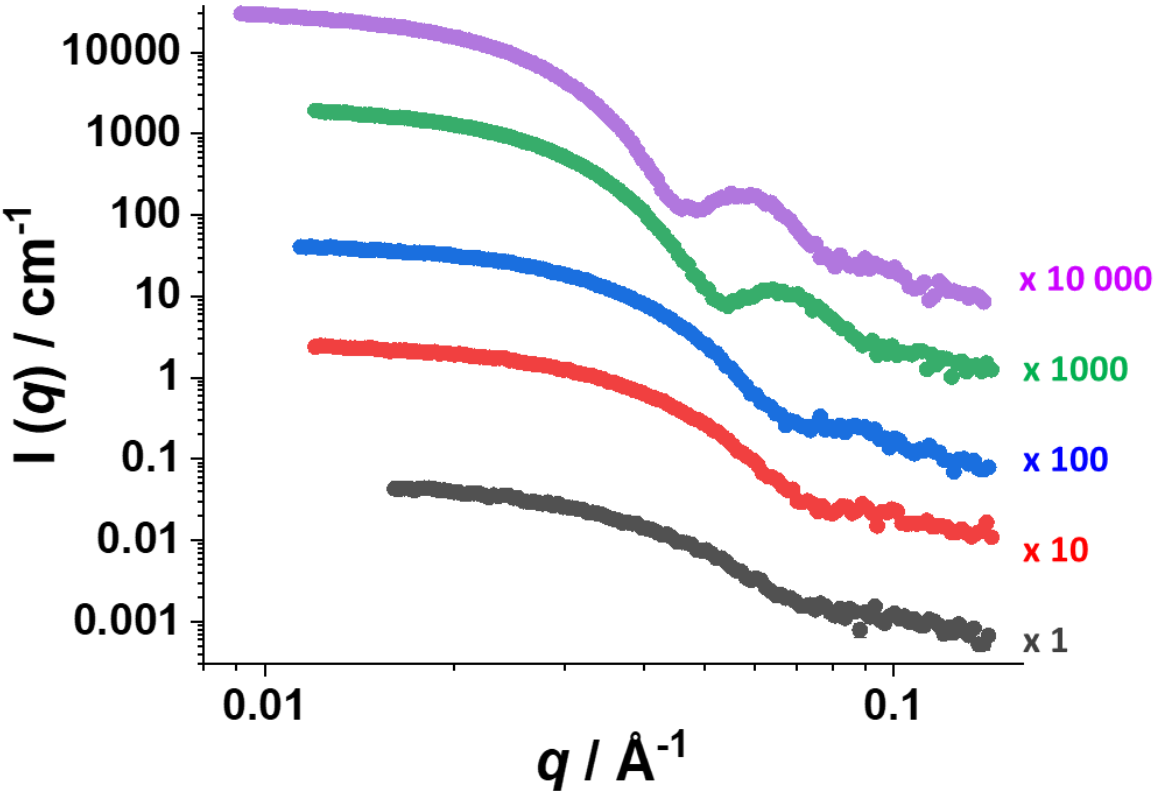

Figure 2.9. SAXS patterns recorded for quenched aliquots taken during the PISA synthesis of $PSMA_{12}$-$PTFEMA_{100}$ spherical nanoparticles at 70 °C in *n*-tetradecane at 30% w/w solids. Aliquots were diluted to 1.0% w/w prior to SAXS analysis at 70 °C so as to avoid reinitiation of the polymerisation. Moreover, no structure factor is observed at this low copolymer concentration. The black pattern corresponds to that recorded for the reaction mixture at 15% TFEMA conversion, which is prior to micellar nucleation. The red pattern was recorded at 30% TEFEMA conversion, which is just after the initial two-fold increase in reaction rate, and the blue pattern was recorded at 43% TFEMA conversion. The appearance of fringes in the scattering pattern indicates the formation of relatively loose nascent nanoparticles. The green pattern was collected after the subsequent three-fold increase in reaction rate observed at 62%, indicating the formation of more compact nanoparticles. The purple pattern represents the polymerisation at 75% TFEMA conversion. Here, we see the shift of the first minimum to lower q, which suggests that the nanoparticles increase as TFEMA monomer is consumed during the polymerisation. Scattering patterns were multiplied by arbitrary factors for clarification.

have been reported for other RAFT dispersion polymerisations.[27,37] Normally, such micellar nucleation is accompanied by solution turbidity but this cannot be observed for the *isorefractive* dispersions studied herein. Instead, small-angle X-ray scattering (SAXS) studies were performed at various time points to confirm the onset of micellisation after approximately 1 h (**Figure 2.9**).

Unexpectedly, both *in situ* visible absorption spectroscopy and ^{19}F NMR studies also indicate a second change in slope, with a further three-fold rate enhancement being observed after 115 min (**Figure 2.8**, see black arrows). This is tentatively interpreted as a switch from relatively loose nascent micelles to the formation of more compact micelles, for which the local monomer concentration is somewhat higher because the micelle cores contain less solvent.

Returning to **Figure 2.7**, the above explanation for the initial increase in absorbance has an important consequence: the constant absorbance observed in the 3-5 h interval implies minimal loss of RAFT chain-ends under monomer-starved conditions at 70 °C, at least for this 2 h time period. In contrast, 27% loss of RAFT chain-ends was reported by Semsarilar and co-workers for the RAFT dispersion polymerisation of TFEMA in ethanol using the same RAFT agent at the same temperature.[5] However, the rate of polymerisation of TFEMA was significantly slower for this latter PISA formulation, with 24 h being required for 91% conversion. Finally, it is perhaps worth emphasising that gradual loss of the RAFT chain-ends is observed when the present PISA formulation is monitored over significantly longer time scales (5-15 h).

2.3.3. In situ ^{19}F NMR Spectroscopy during RAFT PISA

To further investigate the polymerisation kinetics, *in situ* ^{19}F NMR spectroscopy studies were performed. An NMR tube was loaded with the degassed reaction solution along with an inner NMR tube containing a solution of trifluorotoluene in d_8-toluene, which served as an external standard. Typical ^{19}F NMR spectra recorded during the polymerisation of TFEMA when targeting $PSMA_{12}$- $PTFEMA_{100}$ nanoparticles at 70 °C are shown in **Figure 2.10.** The *in situ* ^{19}F NMR spectra exhibit three distinct features: a TFEMA monomer triplet at -75.3 ppm

(with satellite triplets at -75.1 and -75.7 ppm), a broad PTFEMA signal at -74.6 ppm and the trifluorotoluene signal used as an external standard at -63.7 ppm. As expected, there is a gradual reduction in the TFEMA signal during the course of the polymerisation while the PTFEMA signal intensity progressively increases (**Figure 2.11A**). After normalisation with respect to the external standard, the PTFEMA signal intensity is shown as a function of TFEMA conversion in **Figure 2.11C**. This latter signal increases initially before reaching a maximum after approximately 1 h, which corresponds to the onset of micellar nucleation. After nucleation, the growing nascent micelles become enriched with unreacted TFEMA monomer, which accounts for the two-fold rate enhancement observed in **Figure 2.11B**.

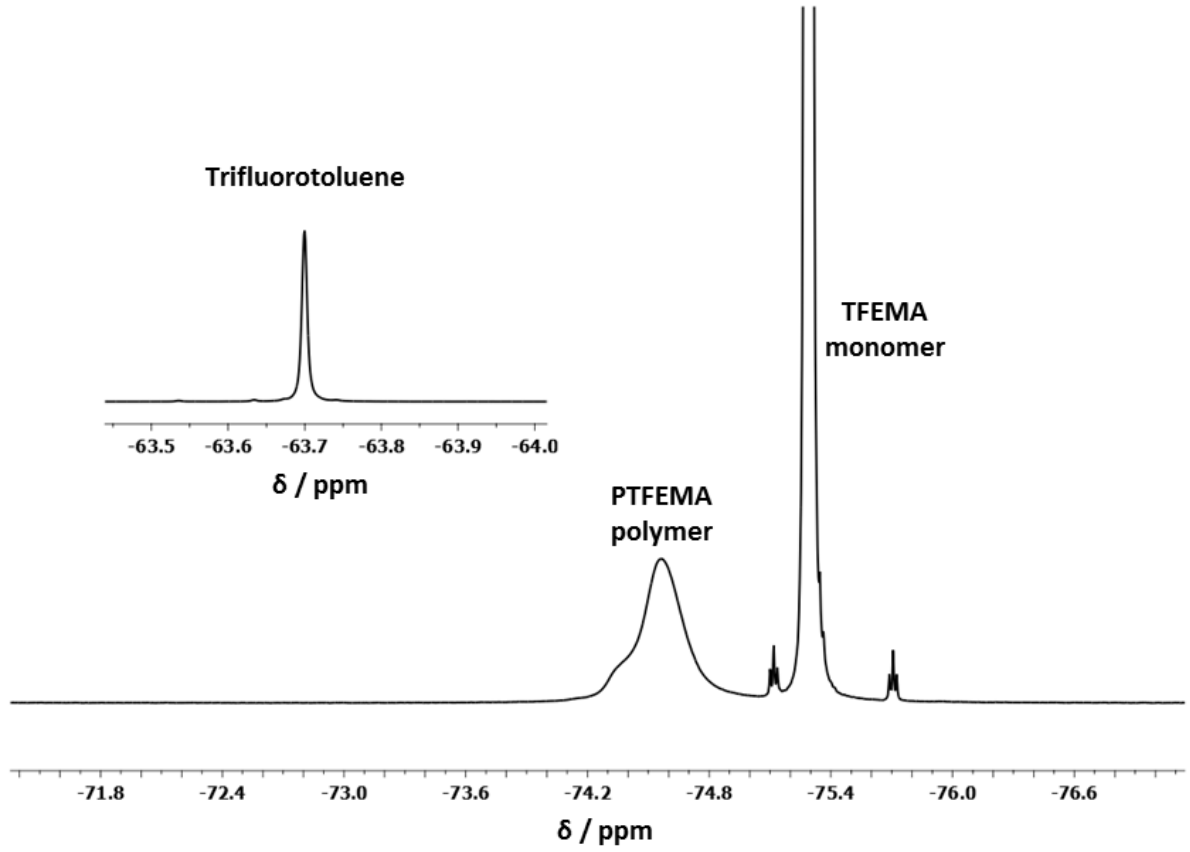

Figure 2.10. ^{19}F NMR spectrum recorded *in situ* after 18 % TFEMA monomer conversion during the RAFT polymerisation of TFEMA at 70 °C when targeting a $PSMA_{12}$-$PTFEMA_{100}$ composition at 30% w/w. The three signals correspond to a TFEMA monomer triplet at -75.3 ppm (with satellite triplets at -75.1 and -75.7 ppm), a broad PTFEMA signal at -74.6 ppm and an external standard (trifluorotoluene) signal at -63.7 ppm.

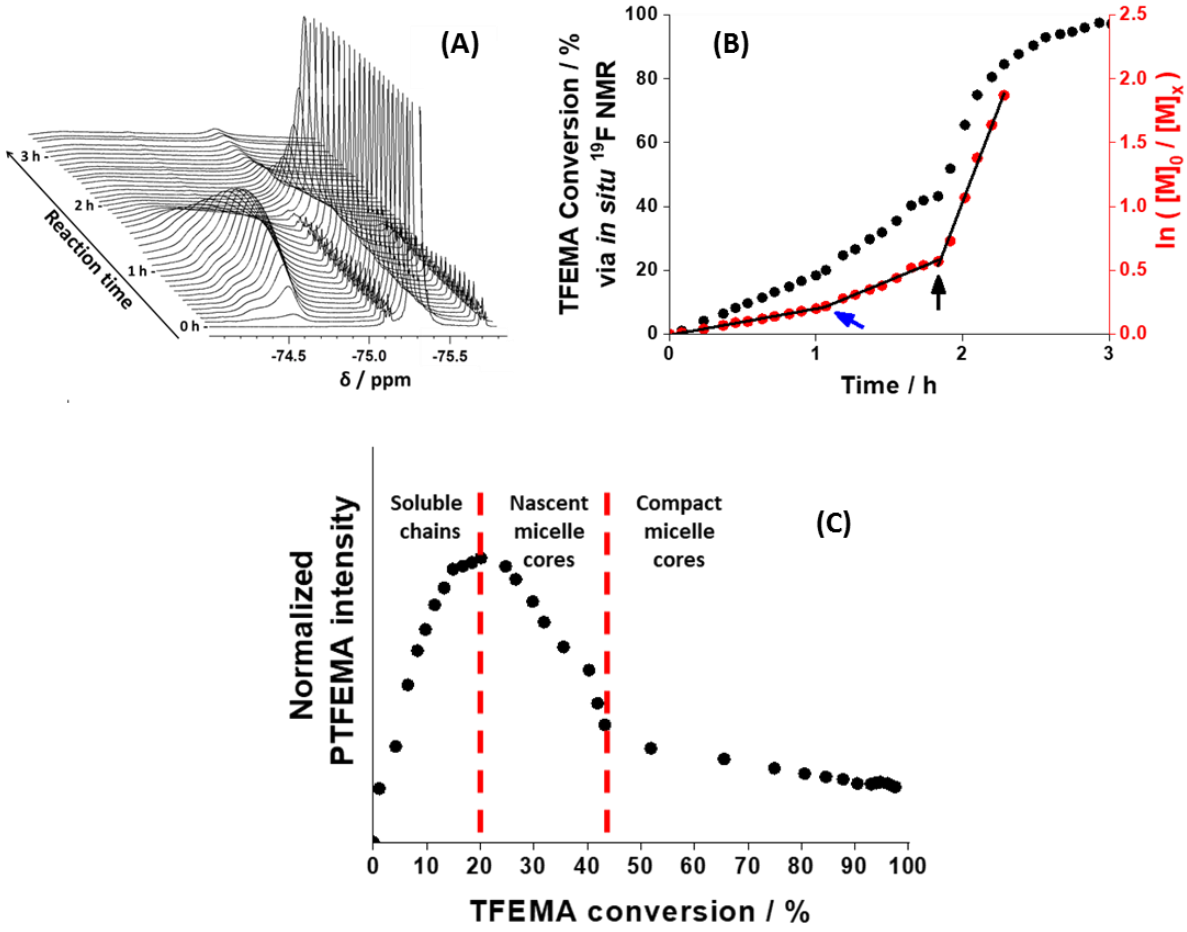

Figure 2.11. (A) ^{19}F NMR spectra recorded at 70 °C during the *in situ* polymerisation of TFEMA when targeting $PSMA_{12}$-$PTFEMA_{100}$ nanoparticles at 30% w/w. The intensity of the monomer triplet signal at -75.3 ppm decreases during polymerisation. (B) Kinetics data obtained from *in situ* ^{19}NMR studies of the RAFT polymerisation of TFEMA when targeting $PSMA_{12}$-$PTFEMA_{98}$ spherical nanoparticles at 30% w/w in *n*-tetradecane at 70 °C. A blue arrow indicated the first rate increase (at around 20% TFEMA conversion), while the second increase in reaction rate is indicated by the black arrow. (C) The corresponding polymer signal at -74.6 ppm initially increases before reaching a maximum after 1 h, which indicates the onset of micellar nucleation. This occurs at 20% TFEMA conversion, which suggests that the growing PTFEMA chains become insoluble at a critical DP of ~ 20 under these conditions.

The reduced mobility of the growing PTFEMA chains within the micelle cores accounts for the gradual broadening and apparent attenuation of the ^{19}F NMR signal at -74.6 ppm observed in **Figure 2.11**. However, the *integrated* peak *area* for this polymer signal continues to increase after nucleation, which enables determination of the TFEMA conversion. A third distinct kinetic regime is observed after approximately 43% TFEMA conversion (**Figure 2.11**), which indicates a PTFEMA DP of 43. Interestingly, this corresponds to a change in the rate of attenuation of the PTFEMA signal intensity, which thereafter proceeds relatively slowly up to 98% conversion (**Figure 2.11C**). This suggests that there is little or no further expulsion of *n*-tetradecane solvent from the growing nanoparticle cores from this point until the TFEMA polymerisation ceases. Although the same three step profile is observed, it should be noted that the kinetics plot in **Figure 2.11** looks significantly different to that from **Figure 2.8.** It might be that this difference arose from the absence of stirring and the small sample volume within the NMR tube.

To examine the extent of core solvation for the final $PSMA_{12}$-$PTFEMA_{98}$ nanoparticles, a series of ^{19}F NMR spectra were recorded from 10 to 90 °C (**Figure 2.12**). The increase in intensity for the broad polymer signal at -74.6 ppm indicates plasticisation of the PTFEMA nanoparticle cores by the hot *n*-tetradecane (note that the sharp signal at -75.3 ppm is assigned to approximately 2% residual TFEMA monomer). These results suggest that RAFT end-group removal should be feasible at elevated temperature, because such solvation should enhance the diffusion of reagent into the nanoparticle cores.

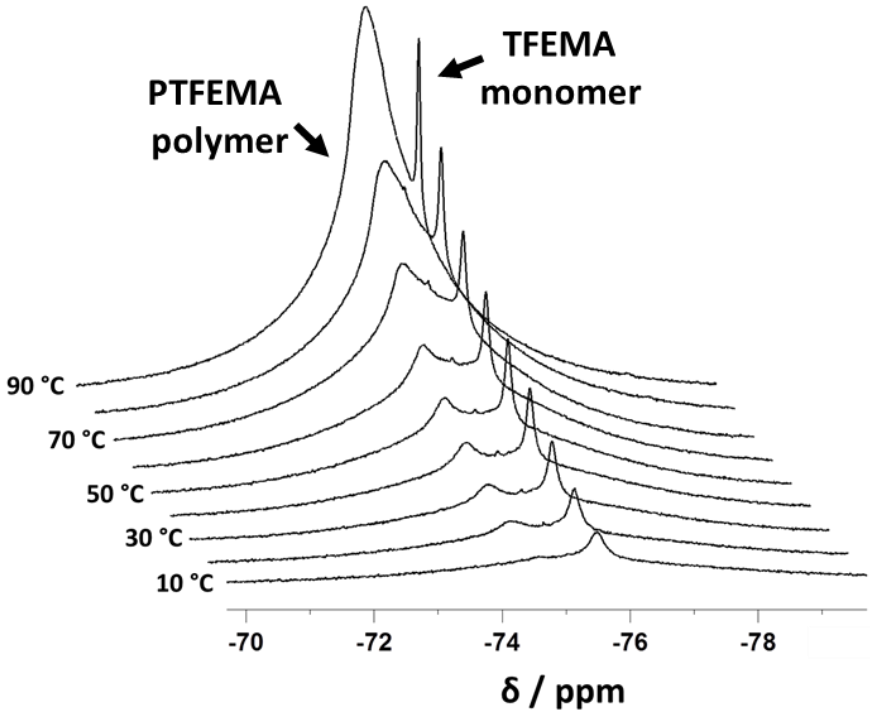

Figure 2.12. Variable temperature ^{19}F NMR spectra recorded from 10 to 90 °C for $PSMA_{12}$-$PTFEMA_{98}$ nanoparticles obtained after 98% TFEMA conversion. The broad PTFEMA signal at -74.6 ppm observed at elevated temperature indicates ingress of hot solvent into the nanoparticle cores (N.B. the sharp signal observed at -75.3 ppm is assigned to the 2% residual TFEMA monomer).

2.3.4. RAFT Chain-End Removal from Spherical Nanoparticle Cores

In principle, chemically stable RAFT chain-ends should offer enhanced control over the molecular weight distribution. However, RAFT chain-end removal is desirable for various potential applications.[3,38] In this context, Jesson and co-workers recently reported that dithiobenzoate chain-ends can be readily removed from a range of diblock copolymer nanoparticles in *aqueous* media by adding a five-fold excess of H_2O_2 at 70 °C.[14] However, we are not aware of any reports of the removal of RAFT chain-ends from diblock copolymer nanoparticles prepared in *non-polar* media. Thus we examined the effect of adding an excess of lauroyl peroxide initiator to a 30% w/w dispersion of $PSMA_{12}$-$PTFEMA_{98}$ nanoparticles in *n*-tetradecane at 70 °C. The highly transparent nature of this dispersion enabled the kinetics of RAFT chain-end removal to be conveniently monitored *in situ* using visible absorption spectroscopy (**Figure 2.13**).

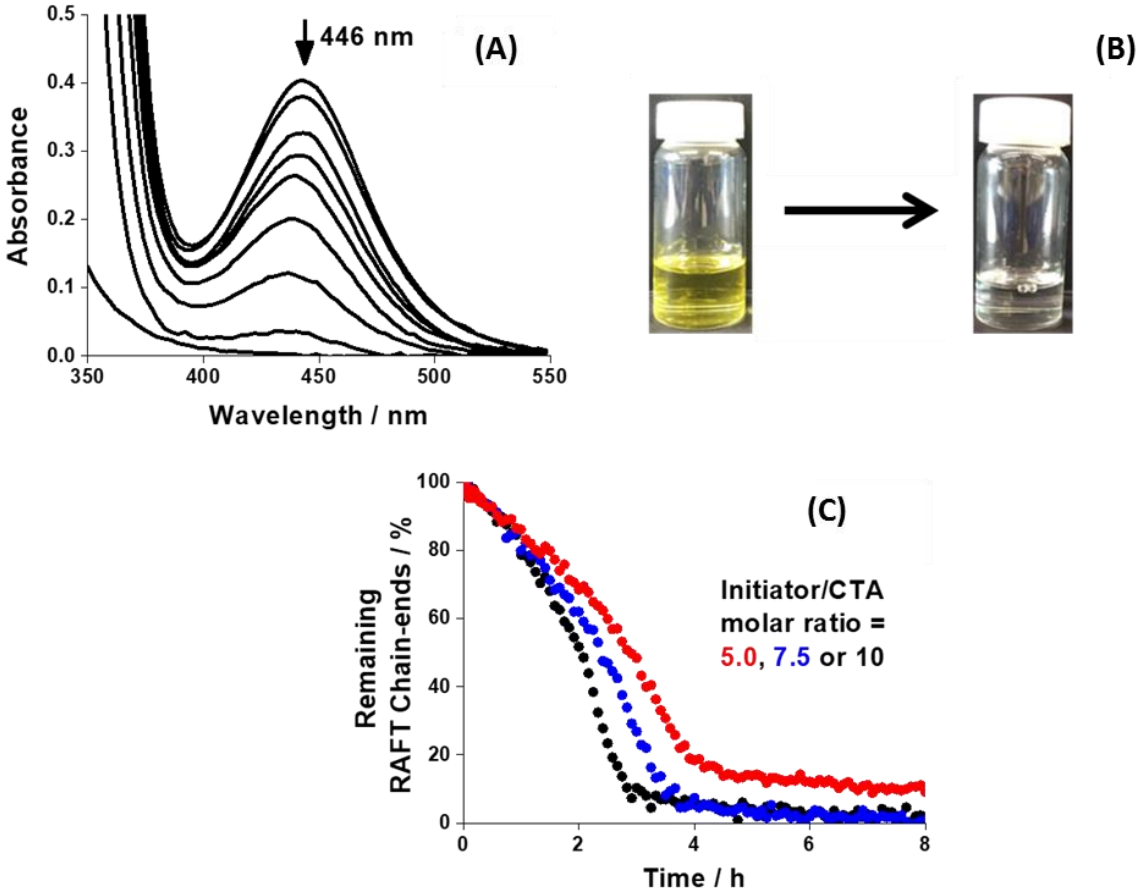

Figure 2.13. (A) *In situ* visible absorption spectra recorded for a 30% w/w dispersion of $PSMA_{12}$-$PTFEMA_{98}$ spherical nanoparticles in *n*-tetradecane at 70 °C using 7.5 equiv. of lauroyl peroxide (Luperox) initiator to remove the trithiocarbonate end-groups. The 446 nm absorption band assigned to this RAFT end-group disappeared within 8 h. (B) RAFT chain-end removal caused the dispersion to gradually lose its intense yellow colour. (C) Kinetics of RAFT chain-end removal at 70 °C for this PISA formulation under the same conditions using lauroyl peroxide/RAFT chain-end molar ratios of 5.0 (red), 7.5 (blue) and 10 (black).

The initial pale yellow dispersion gradually became colourless with essentially all (>98%) of the trithiocarbonate chain-ends being destroyed within 8 h at 70 °C when using initiator/trithiocarbonate molar ratios of either 7.5 or 10 (**Figure 2.13**). The colour change from yellow to colourless suggests destruction of the RAFT chain-end (or functionalisation - since substituents can drastically affect λ_{max} and ε)[32], but not necessarily the *removal* of the CTA end-group from the polymer. Therefore, UV-GPC was used to

examine if the latter phenomenon occurred in addition to the destruction of the RAFT end-group. Successful removal of the aromatic ring associated with each trithiocarbonate end-group was confirmed with this approach using a UV detector at a fixed wavelength of 260 nm in combination with a series of near-monodisperse polystyrene calibration standards (**Figure 2.14 and Table 2.2**). The $PSMA_{12}$-$PTFEMA_{98}$ diblock copolymer chains also absorb at this wavelength, but solely as a result of the *aromatic* character of their trithiocarbonate chain-ends. Hence complete removal of these RAFT chain-ends leads to no GPC signal being observed (see red curve in **Figure 2.12**). The chain-end removed species could, however, still be observed by GPC when employing an RI detector, this approach suggests a slight increase in M_n after chain-end removal, which might be within experimental error (**Table 2.2**). Finally, it would be interesting to purify and examine the by-products from this chain-end removal procedure (e.g. by ^{1}H NMR and mass spectroscopy) to gain insights into the RAFT chain-end removal mechanism. However, this is outside the scope of the research presented here were we look at the chain-end stability during RAFT PISA with respect to initiator concentration.

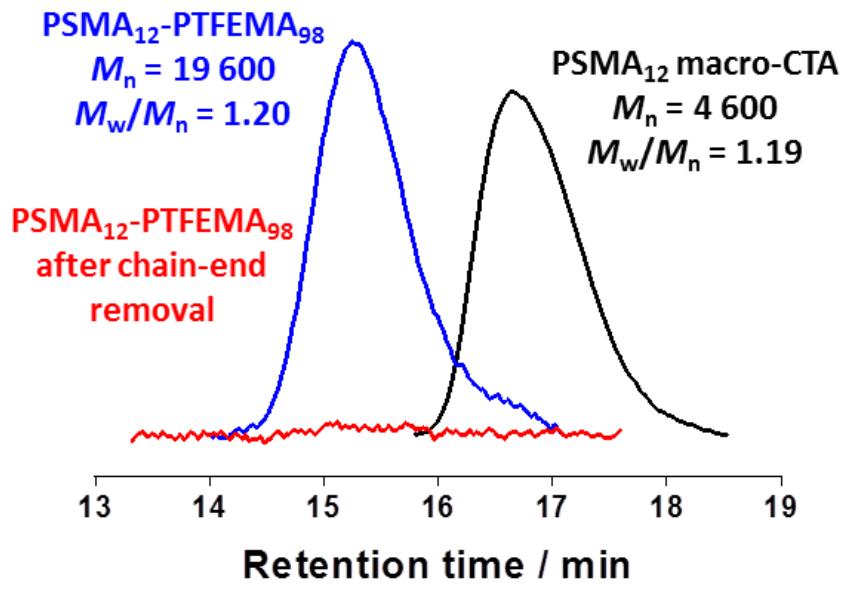

Figure 2.14. UV GPC traces recorded for a $PSMA_{12}$ macro-CTA (black trace), as-prepared $PSMA_{12}$-$PTFEMA_{98}$ diblock copolymer (blue trace) and a $PSMA_{12}$-$PTFEMA_{98}$ diblock copolymer after removal of its RAFT end-groups (red trace). The UV detector wavelength was set at 260 nm and a series of polystyrene standards were used for calibration. The $PSMA_{12}$-$PTFEMA_{98}$ diblock copolymer chains also absorb at this wavelength, but solely as a result of the *aromatic* character of their trithiocarbonate chain-ends. Hence complete removal of these RAFT chain-ends leads to loss of the original GPC (see red trace).

Table 2.2. Summary of GPC data recorded using a refractive index and a UV detector (at a fixed λ of 260 nm) for $PSMA_{12}$ homopolymer and $PSMA_{12}$-$PTFEMA_{98}$ diblock copolymer before and after RAFT chain-end removal. A flat UV baseline was observed in the latter case, indicating complete removal of the trithiocarbonate end-group.

Sample ID	RI M_n	RI M_w/M_n	UV (260 nm) M_n	UV (260 nm) M_w/M_n
$PSMA_{12}$ macro-CTA	5 400	1.15	4 600	1.19
$PSMA_{12}$-$PTFEMA_{98}$ (as-prepared)	17 700	1.29	19 600	1.20
$PSMA_{12}$-$PTFEMA_{98}$ (after chain-end removal)	18 800	1.27	-	-

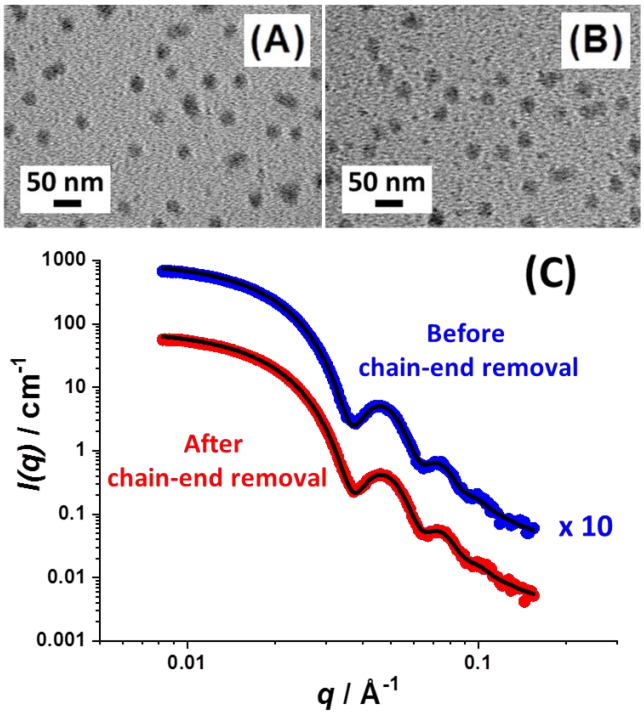

Figure 2.15. TEM images obtained for $PSMA_{12}$-$PTFEMA_{98}$ nanoparticles (A) before and (B) after RAFT chain-end removal at 70 °C using lauroyl peroxide (peroxide/trithiocarbonate molar ratio = 7.5). (C) SAXS patterns recorded for 1.0% w/w dispersions of $PSMA_{12}$-$PTFEMA_{98}$ nanoparticles in *n*-tetradecane before (blue) and after (red) RAFT chain-end removal under the same conditions. Fitting these patterns using a spherical micelle model yielded nanoparticle core diameters of 25.5 nm (before chain-end removal) and 24.9 nm (after chain-end removal). This confirms that RAFT chain-end removal does not affect the size or morphology of these sterically-stabilised nanoparticles.

Further experiments were performed to confirm that RAFT end-group removal had no significant effect on the nanoparticle morphology. TEM images confirmed that the original spherical morphology was retained (**Figures 2.15A and B**) while SAXS patterns (fitted using a spherical micelle model[23-25]) recorded for a 1.0% w/w $PSMA_{12}$-$PTFEMA_{98}$ dispersion in *n*-tetradecane indicated minimal change in the volume-average diameter of the overall nanoparticle diameter before (28.6 nm) and after (28.4 nm) RAFT chain-end removal (**Figure 2.15C and Table 2.3**).

Table 2.3. Summary of SAXS data obtained for $PSMA_{12}$-$PTFEMA_{98}$ spherical nanoparticles before and after the removal of their RAFT chain-ends using excess lauroyl peroxide initiator. Here the copolymer concentration (expressed in volume percent), core radius (nm), shell radius (R_g in nm, or radius of gyration) and the overall particle diameter (nm) are shown.

Sample ID	Copolymer concentration % v/v	Core Radius / nm	Shell R_g / nm	Overall nanoparticle diameter / nm
$PSMA_{12}$-$PTFEMA_{98}$ before chain-end removal	0.40	11.9 ± 1.1	1.2	28.6
$PSMA_{12}$-$PTFEMA_{98}$ after chain-end removal	0.33	11.8 ± 1.1	1.2	28.4

Finally, we note that the highly transparent dispersions described herein should offer new opportunities for further studies in the field of colloid science.[18-20] This is because such isorefractive nanoparticles should exhibit significantly weaker attractive van der Waals interactions compared to nanoparticles for which the refractive index difference is not negligible, which in principle should lead to enhanced colloidal stability.[39,40] Furthermore, isorefractive nanoparticles also enable tracer diffusion experiments to be performed at relatively high volume fractions. Moreover, there is the possibility of preparing new examples of highly transparent Pickering emulsions.[41]

2.4. Conclusions

RAFT dispersion polymerisation of TFEMA enables the PISA synthesis of sterically-stabilised PSMA-PTFEMA spherical nanoparticles in *n*-alkanes at 70 °C. In the case of *n*-tetradecane, the reaction solution is almost perfectly isorefractive at this temperature: this minimises the problem of nanoparticle scattering and enables visible absorption spectra to be recorded *in situ* using a commercial optical immersion probe at up to 30% w/w solids. Unexpectedly, the polymerisation kinetics can be conveniently monitored by examining the increase in absorbance of a relatively weak n→π* band at 446 nm. This is because the relatively large increase in density that occurs on converting TFEMA into PTFEMA leads to a significant volume contraction during the polymerisation. This 446 nm band is assigned to the trithiocarbonate chain-ends and remains constant for at least 2 h under monomer-starved conditions, which indicates remarkably good pseudo-living character for such heterogeneous polymerisations. Gradual loss of the RAFT chain-ends is observed over longer time scales, as expected. This degradation can be accelerated by the addition of excess initiator, which leads to the complete loss of RAFT chain-ends within 8 h at 70 °C, while preserving the original spherical morphology. This is consistent with ^{19}F NMR studies, which indicate solvent-plasticised PTFEMA cores at this temperature. Such solvation is essential to allow ingress of radicals derived from the lauroyl peroxide initiator into the nanoparticle cores to remove the RAFT chain-ends. ^{19}F NMR spectroscopy also enabled micellar nucleation to be monitored during the TFEMA polymerisation and remarkably good agreement is obtained for the kinetic data obtained with this latter technique compared to that determined using *in situ* visible absorption spectroscopy. This study has provided important new insights regarding the true nature of RAFT dispersion polymerisation, which is a powerful and versatile technique for the rational design of a wide range of organic nanoparticles.

2.5. References

(1) Roth, P. J.; Kessler, D.; Zentel, R.; Theato, P. Versatile omega-End Group Functionalization of RAFT Polymers Using Functional Methane Thiosulfonates, *Journal of Polymer Science Part a-Polymer Chemistry*, **2009**, *47*, 3118-3130.

(2) Roth, P. J.; Kessler, D.; Zentel, R.; Theato, P. A Method for Obtaining Defined End Groups of Polymethacrylates Prepared by the RAFT Process during Aminolysis, *Macromolecules*, **2008**, *41*, 8316-8319.

(3) Willcock, H.; O'Reilly, R. K. End group removal and modification of RAFT polymers, *Polymer Chemistry*, **2010**, *1*, 149-157.

(4) Discekici, E. H.; Shankel, S. L.; Anastasaki, A.; Oschmann, B.; Lee, I.-H.; Niu, J.; McGrath, A. J.; Clark, P. G.; Laitar, D. S.; de Alaniz, J. R.; Hawker, C. J.; Lunn, D. J. Dual-pathway chain-end modification of RAFT polymers using visible light and metal-free conditions, *Chemical Communications*, **2017**, *53*, 1888-1891.

(5) Semsarilar, M.; Jones, E. R.; Armes, S. P. Comparison of pseudo-living character of RAFT polymerizations conducted under homogeneous and heterogeneous conditions, *Polymer Chemistry*, **2014**, *5*, 195-203.

(6) Blackman, L. D.; Doncom, K. E. B.; Gibson, M. I.; O'Reilly, R. K. Comparison of photo- and thermally initiated polymerization-induced self-assembly: a lack of end group fidelity drives the formation of higher order morphologies, *Polymer Chemistry*, **2017**, *8*, 2860-2871.

(7) Zetterlund, P. B.; Gody, G.; Perrier, S. Sequence-Controlled Multiblock Copolymers via RAFT Polymerization: Modeling and Simulations, *Macromolecular Theory and Simulations*, **2014**, *23*, 331-339.

(8) Gody, G.; Maschmeyer, T.; Zetterlund, P. B.; Perrier, S. Exploitation of the Degenerative Transfer Mechanism in RAFT Polymerization for Synthesis of Polymer of High Livingness at Full Monomer Conversion, *Macromolecules*, **2014**, *47*, 639-649.

(9) Herfurth, C.; Malo de Molina, P.; Wieland, C.; Rogers, S.; Gradzielski, M.; Laschewsky, A. One-step RAFT synthesis of well-defined amphiphilic star polymers and their self-assembly in aqueous solution, *Polymer Chemistry*, **2012**, *3*, 1606-1617.

(10) McCormick, C. L.; Lowe, A. B. Aqueous RAFT Polymerization: Recent Developments in Synthesis of Functional Water-Soluble (Co)polymers with Controlled Structures, *Accounts of Chemical Research*, **2004**, *37*, 312-325.

(11) Matioszek, D.; Dufils, P.-E.; Vinas, J.; Destarac, M. Selective and Quantitative Oxidation of Xanthate End-Groups of RAFT Poly(n-butyl acrylate) Latexes by Ozonolysis, *Macromolecular Rapid Communications*, **2015**, *36*, 1354-1361.

(12) Fairbanks, B. D.; Gunatillake, P. A.; Meagher, L. Biomedical applications of polymers derived by reversible addition – fragmentation chain-transfer (RAFT), *Advanced Drug Delivery Reviews*, **2015**, *91*, 141-152.

(13) Wang, Z.; He, J.; Tao, Y.; Yang, L.; Jiang, H.; Yang, Y. Controlled Chain Branching by RAFT-Based Radical Polymerization, *Macromolecules*, **2003**, *36*, 7446-7452.

(14) Jesson, C. P.; Pearce, C. M.; Simon, H.; Werner, A.; Cunningham, V. J.; Lovett, J. R.; Smallridge, M. J.; Warren, N. J.; Armes, S. P. H2O2 Enables Convenient Removal of RAFT End-Groups from Block Copolymer Nano-Objects Prepared via Polymerization-Induced Self-Assembly in Water, *Macromolecules*, **2017**, *50*, 182-191.

(15) Chong, Y. K.; Moad, G.; Rizzardo, E.; Thang, S. H. Thiocarbonylthio end group removal from RAFT-synthesized polymers by radical-induced reduction, *Macromolecules*, **2007**, *40*, 4446-4455.

(16) Gaynor, J.; Schueneman, G.; Schuman, P.; Harmon, J. P. Effects of fluorinated substituents on the refractive-index and optical radiation-resistance of methacrylates, *J. Appl. Polym. Sci.*, **1993**, *50*, 1645-1653.

(17) Thomas, D. B.; Convertine, A. J.; Hester, R. D.; Lowe, A. B.; McCormick, C. L. Hydrolytic susceptibility of dithioester chain transfer agents and implications in aqueous RAFT polymerizations, *Macromolecules*, **2004**, *37*, 1735-1741.

(18) Sun, J. Z.; Erickson, M. C. E.; Parr, J. W. Refractive index matching and clear emulsions, *Journal of Cosmetic Science*, **2005**, *56*, 253-265.

(19) Hibberd, D. J.; Mackie, A. R.; Moates, G. K.; Penfold, R.; Watson, A. D.; Barker, G. C. Preparation and characterisation of a novel buoyancy and refractive index matched oil-in-water emulsion, *Colloids and Surfaces A: Physicochemical and Engineering Aspects*, **2007**, *301*, 453-461.

(20) Husband, F. A.; Garrood, M. J.; Mackie, A. R.; Burnett, G. R.; Wilde, P. J. Adsorbed Protein Secondary and Tertiary Structures by Circular Dichroism and Infrared Spectroscopy with Refractive Index Matched Emulsions, *Journal of Agricultural and Food Chemistry*, **2001**, *49*, 859-866.

(21) Fan, L. X.; Degen, M.; Bendle, S.; Grupido, N.; Ilavsky, J. The Absolute Calibration of a Small-Angle Scattering Instrument with a Laboratory X-ray Source, **2010**, *247*, 012005.

(22) Debye, P. Molecular-weight Determination by Light Scattering, *The Journal of Physical and Colloid Chemistry*, **1947**, *51*, 18-32.

(23) Pedersen, J. S.; Gerstenberg, M. C. Scattering Form Factor of Block Copolymer Micelles, *Macromolecules*, **1996**, *29*, 1363-1365.

(24) Pedersen, J. S.; Schurtenberger, P. Scattering Functions of Semiflexible Polymers with and without Excluded Volume Effects, *Macromolecules*, **1996**, *29*, 7602-7612.

(25) Pedersen, J. S. Form factors of block copolymer micelles with spherical, ellipsoidal and cylindrical cores, *Journal of Applied Crystallography*, **2000**, *33*, 637-640.

(26) Ilavsky, J.; Jemian, P. R. Irena: tool suite for modeling and analysis of small-angle scattering, *Journal of Applied Crystallography*, **2009**, *42*, 347-353.

(27) Derry, M. J.; Fielding, L. A.; Armes, S. P. Industrially-relevant polymerization-induced self-assembly formulations in non-polar solvents: RAFT dispersion polymerization of benzyl methacrylate, *Polymer Chemistry*, **2015**, *6*, 3054-3062.

(28) Mazurowski, M.; Gallei, M.; Rehahn, M. Convenient Quantification of Accessible Surface-Attached ATRP Initiators and RAFT Chain Transfer Agents on Cross-Linked Polystyrene Nanoparticles, *ACS Macro Letters*, **2012**, *1*, 1362-1366.

(29) Laib, J. P.; Mittleman, D. M. Temperature-Dependent Terahertz Spectroscopy of Liquid n-alkanes, *Journal of Infrared, Millimeter, and Terahertz Waves*, **2010**, *31*, 1015-1021.

(30) N.B. Isorefractivity is only required at some point after the onset of micellisation when the growing diblock copolymer nanoparticles are sufficiently large to scatter light. Thus, in the early (pre-nucleation) stage where is substantial unreacted TFEMA monomer (refractive index = 1.361 at 20 °C) present in the reaction solution, the mismatched refractive index under such conditions does not prevent *in situ* spectroscopic studies. However, isorefractivity is *essential* in the latter stages of the RAFT dispersion polymerisation of TFEMA for which there are nanoparticles present at up to 30% w/w solids.

(31) Shi, Y.; Liu, G.; Gao, H.; Lu, L.; Cai, Y. Effect of Mild Visible Light on Rapid Aqueous RAFT Polymerization of Water-Soluble Acrylic Monomers at Ambient Temperature: Initiation and Activation, *Macromolecules*, **2009**, *42*, 3917-3926.

(32) Skrabania, K.; Miasnikova, A.; Bivigou-Koumba, A. M.; Zehm, D.; Laschewsky, A. Examining the UV-vis absorption of RAFT chain transfer agents and their use for polymer analysis, *Polymer Chemistry*, **2011**, *2*, 2074-2083.

(33) Yaochen, Z.; Qingquan, X.; Lemin, Z.; Zhirong, X.; Yan, S.; Wanzhong, R. Copolymer architecture effects on the morphology and surface performance of epoxy thermosets containing fluorinated block copolymers, *Journal of Polymer Science Part B: Polymer Physics*, **2014**, *52*, 1037-1045.

(34) Akpinar, B.; Fielding, L. A.; Cunningham, V. J.; Ning, Y.; Mykhaylyk, O. O.; Fowler, P. W.; Armes, S. P. Determining the Effective Density and Stabilizer Layer Thickness of Sterically Stabilized Nanoparticles, *Macromolecules*, **2016**, *49*, 5160-5171.

(35) Pepper, D. C. Friedel-Crafts polymerizations. Part II. The kinetics of polymerization of styrene by stannic chloride, *Transactions of the Faraday Society*, **1949**, *45*, 404-411.

(36) Kwak, Y.; Goto, A.; Tsujii, Y.; Murata, Y.; Komatsu, K.; Fukuda, T. A Kinetic Study on the Rate Retardation in Radical Polymerization of Styrene with Addition−Fragmentation Chain Transfer, *Macromolecules*, **2002**, *35*, 3026-3029.

(37) Blanazs, A.; Madsen, J.; Battaglia, G.; Ryan, A. J.; Armes, S. P. Mechanistic Insights for Block Copolymer Morphologies: How Do Worms Form Vesicles?, *Journal of the American Chemical Society*, **2011**, *133*, 16581-16587.

(38) Pissuwan, D.; Boyer, C.; Gunasekaran, K.; Davis, T. P.; Bulmus, V. In Vitro Cytotoxicity of RAFT Polymers, *Biomacromolecules*, **2010**, *11*, 412-420.

(39) Bergstrom, L. Hamaker constants of inorganic materials, *Advances in Colloid and Interface Science*, **1997**, *70*, 125-169.

(40) Israelachvili, J. N. Intermolecular and Surface Forces, 3rd Edition 2011, p3.

(41) Rymaruk, M. J.; Thompson, K. L.; Derry, M. J.; Warren, N. J.; Ratcliffe, L. P. D.; Williams, C. N.; Brown, S. L.; Armes, S. P. Bespoke contrast-matched diblock copolymer nanoparticles enable the rational design of highly transparent Pickering double emulsions, *Nanoscale*, **2016**, *8*, 14497-14506.

Chapter 3

Time-Resolved SANS Studies of Copolymer Chain Exchange Between Spherical Diblock Copolymer Nanoparticles

3.1. Introduction

In contrast to **Chapter 2**, where nanoparticle synthesis by RAFT PISA is examined *in situ*, this **Chapter** focuses on the behaviour of nanoparticles prepared via RAFT PISA in non-polar media at elevated temperatures. Finally, the behaviour of the analysed nanoparticles is discussed with respect to nanoparticle growth mechanism during RAFT PISA.

As discussed in **Chapter 1**, the RAFT-mediated PISA of methacrylic monomers enables the rational synthesis of diblock copolymer spheres, worms or vesicles by careful selection of the target block composition and copolymer concentration.[1-3] Although kinetically-trapped spheres are commonly observed, it is well-known that spheres can evolve to form highly anisotropic worms during PISA under certain conditions.[4-8] Moreover, worm formation is generally favoured at higher copolymer concentration, which perhaps suggests that the sphere-to-worm transition is likely to proceed via the 1D fusion of multiple spheres.[1-4,9]

There is good precedent for copolymer chain exchange between diblock copolymer micelles (i.e. sterically-stabilised nanoparticles).[10-20] Two principal mechanisms have been suggested for this process in the literature: (i) chain expulsion/insertion and (ii) micelle fusion/fission.[11,21-25] It appears to be generally accepted that the latter mechanism is energetically demanding, and hence most likely not applicable for diblock copolymer micelles under normal experimental conditions. Moreover, dynamic light scattering studies provide direct evidence for a population of molecularly-dissolved copolymer chains on heating polystyrene-core micelles in *n*-heptane to 90 °C, which is consistent with the former mechanism.[26] In the context of PISA, it is interesting to consider whether copolymer chain exchange occurs between monomer-swollen diblock copolymer nano-objects either during the growth of kinetically-trapped spheres[27-30] or during the evolution in copolymer morphology from spheres to worms to vesicles.[2,4,9,30,31]

Copolymer chain exchange between diblock copolymer micelles prepared in non-polar media was studied by Choi and co-workers at elevated temperature.[11] More specifically, both hydrogenous and partially deuterated poly(ethylene-*alt*-propylene)-polystyrene (PEP-PS) diblock copolymers were prepared by anionic polymerisation and dispersed in turn in a mixture of hydrogenous and deuterated squalane to produce 1.0% v/v dispersions of

polystyrene-core micelles (**Figure 3.1**). These two dispersions were then combined in a 1:1 ratio by volume and analysed by time-resolved small-angle neutron scattering (TR-SANS). A distinct scattering pattern was obtained for the initial dispersion, since this comprised a binary mixture of two distinct types of micelles containing either deuterated or hydrogenous polystyrene cores, with the binary solvent composition being chosen to produce a neutron SLD lying halfway between that of the two types of micelle cores.

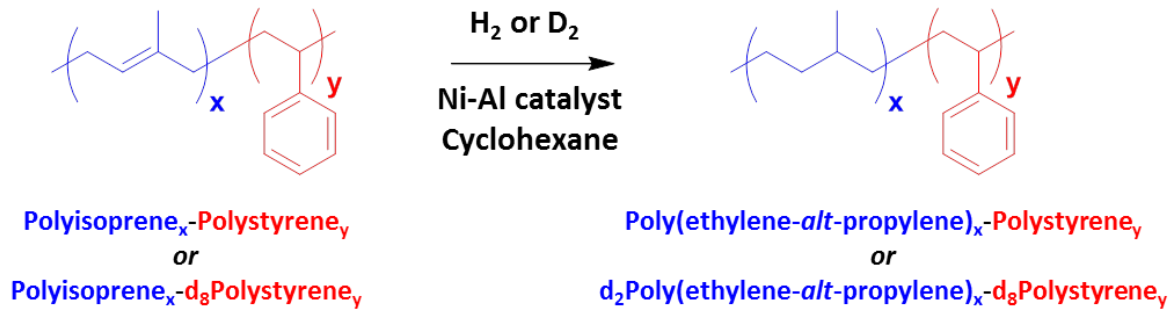

Figure 3.1. Polyisoprene$_x$-polystyrene$_y$ and polyisoprene$_x$-d$_8$polystyrene$_y$ block copolymers were prepared via anionic polymerisation. The polyisoprene blocks were either hydrogenated or deuterated for the preparation of poly(ethylene-*alt*-propylene)-polystyrene or d$_2$poly(ethylene-*alt*-propylene)-d$_8$polystyrene. These latter two copolymers were then self-assembled as d$_8$-polystyrene-core micelles in squalane after purification via a solvent switch using dichloromethane as a good solvent for both blocks.[11,12,32]

A gradual *reduction* in neutron scattering intensity was observed on heating these dispersions to 100-145 °C, suggesting copolymer chain exchange between the initial micelles driven by entropic mixing.[11] The extent (and rate) of chain mixing increased significantly at higher temperatures and the exchange kinetics could be fitted using a 'single chain exchange' model. Moreover, using longer core-forming polystyrene blocks led to a much slower rate of copolymer chain exchange.[11] Subsequent studies by the Minnesota team examined the effect of (i) higher copolymer concentrations,[12] (ii) varying the molecular weight distribution,[13] (iii) the behaviour of binary mixtures of diblock copolymers with differing core-forming block

DPs,[15] (iv) copolymer architecture (i.e. diblocks vs. triblocks),[16] and (v) addition of corona block in the form of free homopolymer.[17]

In this **Chapter** we explore whether copolymer chain exchange occurs between hydrogenous poly(lauryl methacrylate)$_{39}$-poly(methyl methacrylate)$_x$ [PLMA$_{39}$-PMMA$_x$] and the analogous core-deuterated [PLMA$_{39}$-d$_8$PMMA$_x$] spherical nanoparticles prepared directly in *n*-dodecane via RAFT PISA. First, the spherical nanoparticles were characterised by SAXS. Subsequently, TR-SANS was used to assess whether copolymer chain exchange occurs for this particular diblock copolymer system when varying (i) temperature and (ii) the DP of the core-forming PMMA block. Understanding the behaviour of such sterically-stabilised nanoparticles at elevated temperature is expected to provide useful insights regarding the evolution in copolymer morphology during PISA. More specifically, do nanoparticles grow solely via micelle fusion/fission events, or is the exchange of individual copolymer chains also likely to be involved? Such fundamental insights should enhance our understanding of the true nature of PISA and its progeny. Additionally, monomer solvation should be considered during RAFT PISA which should make both mechanisms more likely to occur, this parameter is not included in this study.

3.2. Experimental

3.2.1. Materials

Lauryl methacrylate and methyl methacrylate were purchased from Sigma-Aldrich (UK) and deuterated methyl methacrylate was purchased from Apollo Scientific (UK). Each monomer was passed through basic alumina to remove its inhibitor prior to use. Tert-Butylperoxy-2-ethylhexanoate (Trigonox 21S or T21s) initiator was supplied by AkzoNobel (The Netherlands). THF, *n*-dodecane, triethylamine, butylated hydroxytoluene, 2-propanol and 2,2-azobis(2-methylpropionitrile) (AIBN) were purchased from Sigma-Aldrich (UK). 4-Cyano-4-((2-phenylethanesulfonyl)thiocarbonylsulfanyl)pentanoic acid (PETTC) was prepared in-house according to a well-established protocol.[33] Both d$_{26}$-dodecane ($C_{12}D_{26}$) and d$_2$-dichloromethane (CD_2Cl_2) were obtained from Cambridge Isotope Laboratory (USA) while d-chloroform ($CDCl_3$) was purchased from VWR (UK).

3.2.2. Methods

3.2.2.1. PLMA Macro-CTA Synthesis via RAFT Solution Polymerisation

A near-monodisperse $PLMA_{39}$ macro-CTA was prepared via RAFT solution polymerisation of LMA (59.95 g, 235.6 mmol) at 70 °C in 62 g toluene using PETTC (2.00 g, 5.89 mmol; target DP = 40) and AIBN initiator (0.19 g, 1.18 mmol; PETTC/AIBN molar ratio = 5.0). This polymerisation was quenched after 4 h (76% conversion; obtained by ^{1}H NMR, see **Equation 3.1**) to avoid loss of RAFT chain-ends under monomer-starved conditions.

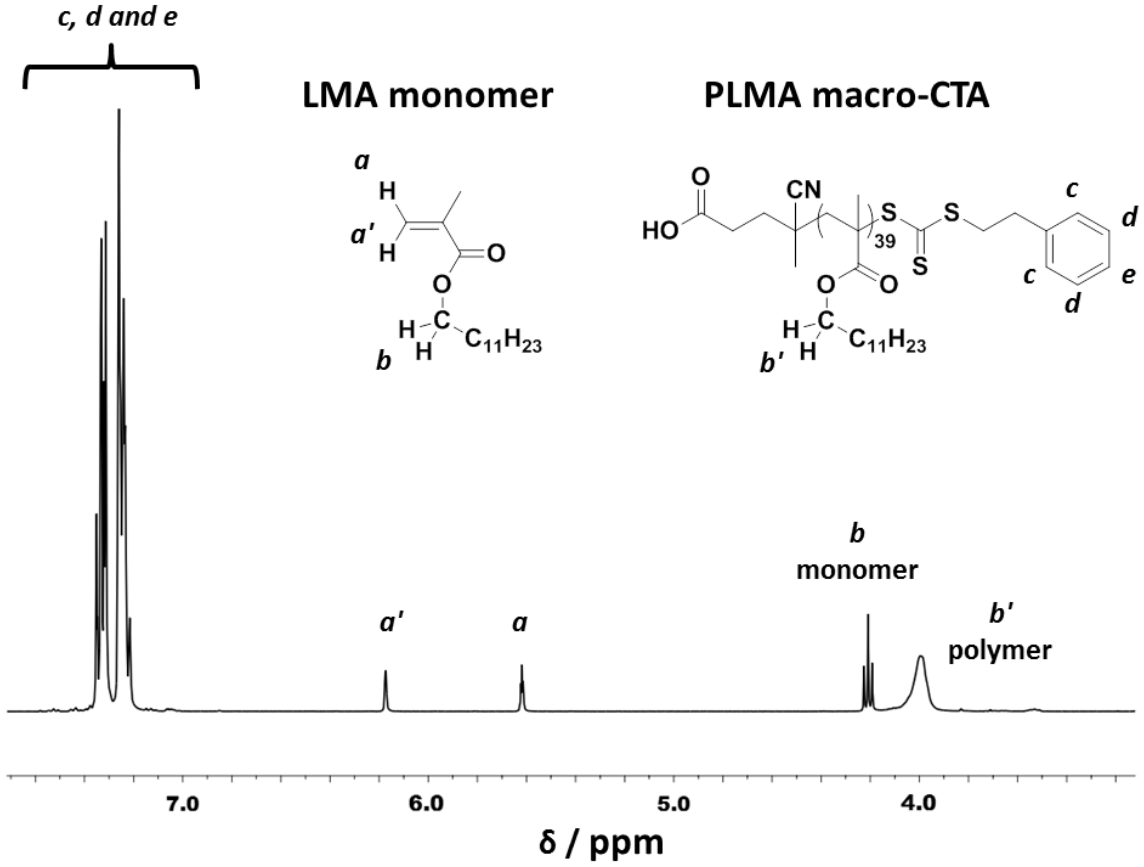

Figure 3.2. Representative proton NMR spectrum recorded in $CDCl_3$ for a sample of the reaction solution taken during the RAFT-mediated solution polymerisation of lauryl methacrylate. After a reaction time of 4 h, a monomer conversion of 76% was calculated using **Equation 3.1** by comparing the integrated monomer vinyl protons (*a* and *a*') with the integrated oxymethylene signals ($b_{monomer}$ and $b'_{polymer}$) assigned to LMA monomer and PLMA homopolymer.

A mean DP of 39 was determined via end-group analysis using proton NMR spectroscopy (CD_2Cl_2) by comparing the integrated aromatic PETTC signals at 7.18-7.38 ppm to those of the oxymethylene signals at 3.92–4.08 ppm assigned to the LMA repeat units (**Figure 3.2 and Equation 3.2**). THF GPC analysis indicated a M_n of 9 700 and an M_w/M_n of 1.12, which is consistent with previous studies of well-controlled RAFT polymerisations.[4,34,35]

$$\textbf{\textit{LMA conversion}}\ (\%) = \mathbf{1} - \frac{\boldsymbol{a} + \boldsymbol{a}'}{\boldsymbol{b}_{\mathbf{monomer}} + \boldsymbol{b}'_{\mathbf{polymer}}} \times \mathbf{100}\% \quad (\mathbf{3.1})$$

The mean DP of the PLMA precursor was determined via end-group analysis by analysing a proton NMR spectrum recorded for the purified homopolymer in CD_2Cl_2. In this case, the proton signal assigned to the aromatic end-group at 7.18-7.38 ppm was compared to that of the oxymethylene ($b'_{polymer}$) signal of the PLMA homopolymer at 3.92–4.08 ppm. (**Equation 3.2**).

$$\textbf{\textit{PLMA DP}} = \frac{(\boldsymbol{c} + \boldsymbol{d} + \boldsymbol{e}) \times \frac{\mathbf{2}}{\mathbf{5}}}{\boldsymbol{b}'_{\mathbf{polymer}}} \quad (\mathbf{3.2})$$

3.2.2.2. Synthesis of Hydrogenous $PLMA_{39}$-$PMMA_x$ and Core-Deuterated $PLMA_{39}$-d_8PMMA_x Diblock Copolymer Spheres via RAFT Dispersion Polymerisation

Methyl methacrylate (MMA; 0.19 g, 1.89 mmol) was used for chain extension of a $PLMA_{39}$ macro-CTA (0.30 g, 0.029 mmol; target DP = 60) in 1.96 g *n*-dodecane at 20% w/w solids, using a T21s initiator (23 µl of a 10% v/v solution, targeting a macro-CTA/initiator molar ratio of 3.0). This reaction mixture was heated to 90 °C for 16 h. A final MMA conversion of 92% was determined by proton NMR analysis of the crude reaction mixture diluted in $CDCl_3$

(the integrated monomer vinyl signals at 5.59 and 6.13 ppm were compared to the integrated pendent methoxy signal assigned to the MMA repeat units at 3.6 ppm) (**Figure 3.3 and Equation 3.3**).

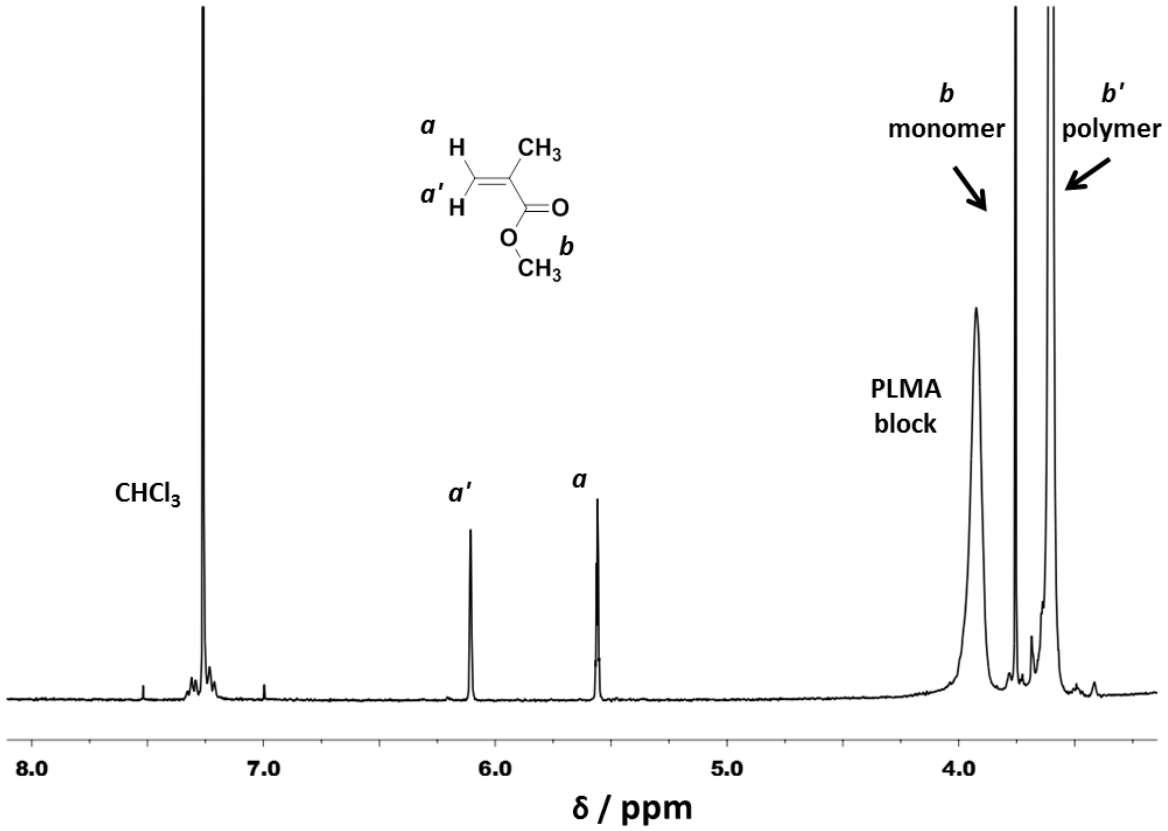

Figure 3.3. Representative proton NMR spectrum recorded for a crude sample of $PLMA_{39}$-$PMMA_{55}$ (after dilution with $CHCl_3$ to ensure nanoparticle dissolution). Monomer conversions were calculated according to **Equation 3.3** using the integrated monomer vinyl signals (*a* and *a*') and the methyl signals ($b_{monomer}$ and $b'_{polymer}$) assigned to the MMA and PMMA.

A PMMA DP of 100 was also targeted when using 0.31 g MMA (3.16 mmol) and 2.46 g *n*-dodecane and in this case the final MMA conversion was 94%. Core-deuterated nanoparticles were prepared via the same protocol by using d_8MMA instead of MMA. The densities for MMA, d_8MMA, PMMA and d_8PMMA are 0.936 g cm^{-3}, 1.011 g cm^{-3}, 1.188 g cm^{-3} and

1.255 g cm^{-3}, respectively (according to the supplier). Thus the difference between the monomer and polymer densities are 0.24 g cm^{-3} and 0.25 g cm^{-3} for the hydrogenous and deuterated blocks, which indicates almost identical volume contractions during the respective homopolymerisations of MMA and d_8MMA. Hence identical MMA and d_8MMA monomer volumes were used for these syntheses, which ensured comparable core volumes. However, small differences in the final monomer conversion led to minor differences in block volumes for the hydrogenous and deuterated core-forming PMMA blocks (**Table 3.1**).

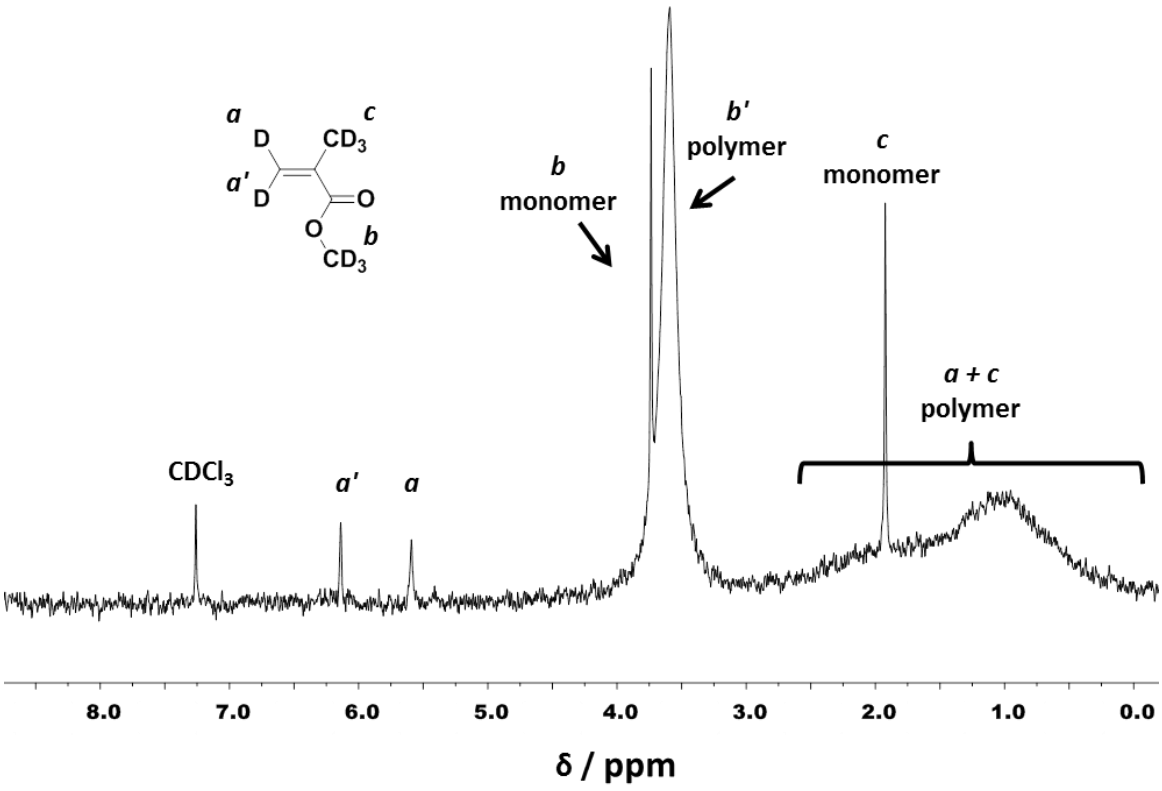

Figure 3.4. Representative deuterium NMR spectrum recorded for a sample of the crude reaction solution during the synthesis of $PLMA_{39}$-d_8PMMA_{57} (after dilution with $CHCl_3$ to ensure nanoparticle dissolution). Monomer conversions were calculated according to **Equation 3.3** by comparing the integrated monomer vinyl signals (*a* and *a*') with the integrated methoxy signals assigned to MMA and PMMA ($b_{monomer}$ and $b'_{polymer}$).

Final d_8MMA conversions of 95% and 96% were determined by analysing the crude reaction mixture using deuterium NMR spectroscopy (**Figure 3.4**); this approach indicated core-forming block DPs of 57 and 96, respectively. These values are close to those calculated for the corresponding hydrogenous PMMA blocks.

$$\boldsymbol{MMA\ or\ d_8MMA\ conversion}\ (\%) = \mathbf{1} - \frac{(\boldsymbol{a} + \boldsymbol{a'}) \times \mathbf{\frac{3}{2}}}{\boldsymbol{b}_{\mathbf{monomer}} + \boldsymbol{b'}_{\mathbf{polymer}}} \times \mathbf{100}\% \quad (\mathbf{3.3})$$

3.2.2.3. Copolymer Characterisation

THF GPC. Molecular weight distributions were assessed by gel permeation chromatography (GPC) using THF as an eluent. The GPC set-up comprised an Agilent 1260 Infinity series degasser and pump, two Agilent PLgel 5 μm Mixed-C columns in series and a refractive index detector. The mobile phase contained 2.0% v/v triethylamine and 0.05% w/w butylhydroxytoluene (BHT) and the flow rate was fixed at 1.0 ml min^{-1}. Samples were dissolved in THF containing 0.50% v/v toluene as a flow rate marker prior to GPC analysis. A series of ten near-monodisperse poly(methyl methacrylate) standards (M_p values ranging from 1 280 to 330 000 g mol^{-1}) were used for calibration.

NMR spectroscopy. Proton and deuterium NMR spectra were recorded in either $CDCl_3$, $CHCl_3$ or CD_2Cl_2 using a Bruker AVANCE III HD 400 or 500 MHz spectrometer. Spectra were analysed using TopSpin version 3.1 software. For the $PLMA_{39}$-$PMMA_x$ synthesis, the final MMA conversion was determined using proton NMR spectroscopy by dissolution of a small volume of the crude dispersion in $CDCl_3$ prior to analysis. Similarly, the final d_8MMA conversion obtained for the synthesis of the $PLMA_{39}$-d_8PMMA_x diblock copolymer was determined using deuterium NMR spectroscopy by diluting a small amount of the crude dispersion in $CHCl_3$. Prior to analysis, the spectrometer was locked using an NMR tube containing $CDCl_3$, which was then removed and replaced with an NMR tube containing a solution of $PLMA_{39}$-d_8PMMA_x dissolved in $CHCl_3$. Deuterium NMR spectra were obtained at 76.77 MHz using an unlocked spectrometer to record 128 scans at 8000 data points per

spectrum over an acquisition window of 1.5 kHz and using a relaxation delay time of 5 s. Copolymer dispersions were dissolved using $CHCl_3$, the $CDCl_3$ signal was set to 7.26 ppm, and the integrated d_8MMA vinyl signals at 5.59 and 6.14 ppm were compared to those assigned to the integrated methoxy signals of d_8MMA monomer and d_8PMMA polymer between 4.25 ppm and 2.79 ppm (see **Figure 3.4**).

Small-angle X-ray scattering (SAXS). Measurements were performed using a Bruker SAXS Nanostar instrument modified with a GeniX3D microfocus Cu Kα X-ray tube and motorized scatterless slits for the beam collimation (Xenocs, France), and equipped with a 2D HiSTAR multiwire gas detector (Siemens/Bruker; sample-to-detector distance = 1.46 m). Data were recorded over a q range of 0.009 $Å^{-1} < q < 0.17$ $Å^{-1}$. Data were collected using a glass capillary cell at 22 °C. Water and a glassy carbon standard were used for absolute intensity calibration.[36] SAXS measurements were conducted on 1.0% w/w dispersions of either $PLMA_{39}$-$PMMA_x$ or $PLMA_{39}$-d_8PMMA_x spheres in *n*-dodecane. Exposure times were 1800 s for the empty capillary and solvent background. Scattering data for the dilute copolymer dispersions were collected for 500 s, whereas data for the $PLMA_{39}$ macro-CTA solution were collected for 1800 s. Data were fitted using a well-known spherical micelle model[37-39] or Debye function[40] after normalization and background subtraction using the Irena package[41] for Igor Pro.

Small-angle neutron scattering (SANS). SANS studies were conducted using the Sans2d small-angle diffractometer at the ISIS Pulsed Neutron Source (STFC Rutherford Appleton Laboratory, Didcot, U.K.).[42] A simultaneous q range of 0.0045 – 0.7 $Å^{-1}$ was achieved utilising an incident wavelength range of 1.75 – 16.5 Å. The scattering vector q is defined as (**Equation 3.4**):

$$q = \frac{4\pi \sin\frac{\theta}{2}}{\lambda} \quad (3.4)$$

where θ is the scattered angle and λ is the incident neutron wavelength. The beam diameter was 8 mm. Each raw scattering data set was corrected for the detector efficiency, sample transmission and background scattering and then converted into scattering cross-section data ($\partial\Sigma/\partial\Omega$ vs. q) using the instrument-specific software.[43] These data were placed on an absolute scale (cm^{-1}) using the scattering from a standard sample (a solid blend of hydrogenous and perdeuterated polystyrene) in accordance with established protocols.[44] Raw data were afterwards sliced into 1 min time frames using instrument-specific software.[43]

Differential scanning calorimetry (DSC). Measurements were performed on a TA instruments TADSC25 discovery series instrument using aluminium Tzero pans with Tzero for PMMA GPC standards, and Tzero pans and Tzero hermetic lids for diblock copolymer powders. Calibrations were performed with an indium standard sample. $PLMA_{39}$-$PMMA_x$ (where x is 55 or 94) and $PLMA_{39}$-d_8PMMA_x (where x is 57 or 96) block copolymer powders were purified by precipitation each 20% w/w diblock copolymer dispersions into a 10-fold excess of 2-propanol. The diblock copolymers were isolated via filtration and dried *in vacuo* for 24 h. During a DSC run, diblock copolymer samples were heated to 200 °C for 5 min followed by cooling and equilibration at 40 °C for 5 min. Measurements were performed upon heating from 40 °C to 200 °C using a 10 °C per minute temperature ramp.

3.2.3. Small-Angle Scattering Models

SAS model for molecularly-dissolved $PLMA_{39}$ chains in *n*-dodecane

The SAXS pattern recorded for molecularly-dissolved $PLMA_{39}$ chains in *n*-dodecane was fitted using the Debye function[40] to determine the mean radius of gyration of the polymer coil (R_g):

$$\boldsymbol{F_c(q, R_g) = \frac{2\left[\exp\left(-q^2 {R_g}^2\right) - 1 + q^2 {R_g}^2\right]}{q^4 {R_g}^4}} \quad (\mathbf{3.5})$$

where $F_c(q, R_g)$ is the form factor for Gaussian chains.

SAS model for dilute $PLMA_{39}$–$PMMA_x$ and $PLMA_{39}$–d_8PMMA_x spheres

In general, the differential scattering cross-section per unit sample volume $\frac{d\Sigma}{d\Omega}(q)$ for a dispersion of particles can be expressed as:

$$\frac{d\Sigma}{d\Omega}(q) = NS_{SF}(q)\int_0^\infty \dots \int_0^\infty F(q, r_1, \dots, r_k)\Psi(r_1, \dots, r_k)dr_1 \dots dr_k \quad (3.6)$$

where $S_{SF}(q)$ is the structure factor. This factor describes variations of scattering from randomly arranged particles, which become more pronounced when considering either strongly interacting scattering objects or densely-packed concentrated dispersions. Since, only dilute dispersions are considered in this study, $S_{SF}(q) = 1$. $F(q, r_1, \dots, r_k)$ is a particle form factor expressed in terms of a set of k parameters , $\Psi(r_1, \dots, r_k)$ is the parameter distribution function and *N* is the particle number density per unit sample volume, which is generally expressed as:

$$N = \frac{\varphi}{\int_0^\infty \dots \int_0^\infty V(r_1, \dots, r_k)\,\Psi(r_1, \dots, r_k)dr_1 \dots dr_k} \quad (3.7)$$

where $V(r_1, \dots, r_k)$ is the particle volume and φ is the particle volume fraction in the dispersion. For spherical micelles it is sufficient to consider only polydispersity of the micelle core radius, defined as r_1, usually expressed as a Gaussian distribution:

$$\Psi(r_1) = \frac{1}{\sqrt{2\pi{\sigma_{Rs}}^2}}\exp\left(-\frac{(r_1 - R_s)^2}{2{\sigma_{Rs}}^2}\right) \quad (3.8)$$

where R_s is the mean micelle core radius and σ_{Rs} is its standard deviation. All other fitting parameters describing the micelle structural model could be considered monodisperse (their distribution functions correspond to Dirac's delta function).

The spherical micelle form factor (**Equation 3.6**) can be expressed as:[45]

$$\begin{aligned} F(q, r_1) = {} & {N_s}^2(r_1){\beta_s}^2{A_s}^2(q, r_1) + N_s(r_1){\beta_c}^2F_c(q, R_g) \\ & + N_s(r_1)[N_s(r_1) - 1]{\beta_c}^2{A_c}^2(q, r_1) \\ & + 2{N_s}^2(r_1)\beta_s\beta_cA_s(q, r_1)A_c(q, r_1) \end{aligned} \quad (3.9)$$

where $N_s(\boldsymbol{r_1})$ is the aggregation number (or total number of copolymer chains per spherical nanoparticle):

$$\boldsymbol{N_s(r_1) = (1 - x_{sol}) \frac{\frac{4}{3}\pi {r_1}^3}{V_s}} \quad (3.10)$$

where, x_{sol} is the fraction of solvent in the micelle core and V_s is the volume of a single core-forming block (**Table 3.1**).

β_s and β_c represent the total excess scattering of the core-forming block (PMMA or d_8PMMA) and the corona-forming block (PLMA), respectively. These values can be calculated by $\beta_s = V_s(\xi_s - \xi_{solv})$ and $\beta_c = V_c(\xi_c - \xi_{solv})$, where V_c is the volume of a single corona-forming block (**Table 3.1**); ξ_s, ξ_c and ξ_{solv} are the SLDs of the core, corona and solvent (see **Table 3.1** for the calculated neutron and X-ray SLDs of each component in the dispersion). Self-correlation term of the spherical core in **Equation 3.9** is expressed as:

$$\boldsymbol{A_s(q, r_1) = \Phi(qr_1) \exp\left(-\frac{q^2\sigma^2}{2}\right)} \quad (3.11)$$

where

$$\boldsymbol{\Phi(qr_1) = \frac{3[\sin(qr_1) - qr_1\cos(qr_1)]}{(qr_1)^3}} \quad (3.12)$$

A sigmoidal interface between the micelle core and corona was assumed for the micelle model (**Equation 3.11**). This is described by the exponent term with a width σ accounting for a decaying scattering length density at the membrane surface. This σ value was fixed at 0.22 nm during fitting. The self-correlation term for the corona block, $F_c(q)$, is given by the Debye function (**Equation 3.5**). The scattering amplitude of the corona self-term (**Equation 3.9**) was obtained from a normalized Fourier transform of the radial density distribution function of the coronal chains in the micelles:

$$\boldsymbol{A_c(q, r_1) = \frac{\int_{r_1}^{r_1+2s} \mu_c(r) \frac{\sin(qr)}{qr} r^2 dr}{\int_{r_1}^{r_1+2s} \mu_c(r) r^2 dr} \exp\left(-\frac{q^2\sigma^2}{2}\right)} \quad (3.13)$$

The radial profile, $\mu_c(r)$, is expressed by a linear combination of two cubic b splines, with two fitting parameters *s* and *a* corresponding to the width of the scattering length density corona profile and the function weight coefficient, respectively. This information can be found elsewhere,[46,47] as can the approximate integrated form of **Equation 3.13**.

According to **Equation 3.7** the number density per unit sample volume for the spherical micelles can be expressed as:

$$\boldsymbol{N = \frac{\varphi}{\int_0^\infty V(r_1)\Psi(r_1)dr_1}} \quad (\mathbf{3.14})$$

where, $V(r_1)$ is the total volume of copolymer in a spherical micelle $[V(r_1) = (V_s + V_c)N_s(r_1)]$.

SAS model parameters (copolymer block volumes and SLDs)

The volumes of each copolymer block, i.e. $PLMA_{39}$, $PMMA_x$ and d_8-$PMMA_x$, (**Table 3.1**) were calculated from:

$$\boldsymbol{V_b = DP \cdot v_m} \quad (\mathbf{3.15})$$

where DP is the degree of polymerization and v_m is the volume of the repeat unit in each block such that $v_m = \frac{M_{Mon}}{N_A \rho}$, where M_{Mon} is the molecular weight of the corresponding block repeat unit, N_A is Avogadro's number and ρ is the mass density of either the core-forming or corona-forming block.

Scattering length densities (SLD) for each component of the nanoparticle dispersion were calculated for neutrons and X-rays (**Table 3.1**) using:

$$\boldsymbol{\xi = \frac{\sum_{i=1}^{L} n_i b_i}{v_m}} \quad (\mathbf{3.16})$$

where L is the number of types of chemical elements in a compound, n_i is the number of atoms of the i^{th} chemical element (or one of its isotopes), b_i is the scattering length of the i^{th} chemical element nucleus (for neutrons) or atom (for X-rays, determined by its number of

electrons multiplied by scattering length of an electron), and v_m is the molecular volume of either a single monomer repeat unit or a solvent molecule.

Table 3.1. Summary of the volumes, densities and calculated X-ray and neutron SLDs for each methacrylic block and the various solvent compositions used in this study. Neutron SLDs at 150 °C were calculated using estimated mass densities, by assuming that the temperature dependence of the densities of each block is comparable to that reported for hydrogeneous poly(methyl methacrylate).[48] Neutron SLD of the solvent was calculated using literature densities at elevated temperatures.[49] The SLD of the dodecane mixtures was calculated based on the false assumption that the SLD has a linear relation with the used volume fractions,[50] but suitable for the purpose of this work to highlight copolymer chain exchange.

	Block volume / Å^3	**Density / g cm^3**	**X-ray SLD / × 10^{-6} Å^{-2}**	**Neutron SLD / × 10^{-6} Å^{-2} at 20 °C**	**Neutron SLD / × 10^{-6} Å^{-2} at 150 °C**
PLMA$_{39}$	17716	0.93	8.81	0.13	0.12
PMMA$_{55}$	7736	1.188	10.87	1.07	1.01
d$_8$PMMA$_{57}$	8216	1.255	10.64	6.87	6.49
PMMA$_{94}$	13209	1.188	10.87	1.07	1.01
d$_8$PMMA$_{96}$	14184	1.255	10.64	6.87	6.49
***n*-dodecane**	-	0.75	7.32	-0.46	-0.40
d$_{26}$-dodecane	-	0.864	-	6.71	5.97
38:% *n*-dodecane + 62% d$_{26}$-dodecane by volume	-	-	-	3.97	3.55

Scattering patterns were fitted using the spherical micelle model described in this section. The pre-determined block volumes and SLDs for each component were fixed for this model. Geometric parameters (i.e. the mean core radius, its standard deviation, and the R_g of the micelle corona) and the scale were allowed to vary until the best data fits were obtained.

3.2.3.4. SANS Sample Preparation

Prior to SANS analysis, equal volumes of 20% w/w hydrogenous and core-deuterated nanoparticle dispersions were combined and subsequently diluted to 1.0% w/w solids using a judicious mixture of *n*-dodecane and d_{26}-dodecane, such that the neutron scattering length density of this binary solvent mixture lies halfway between that of PMMA and d_8PMMA. If exchange of diblock copolymer chains between nanoparticles occurs on annealing such as binary mixture of dispersions, entropic mixing ensures that hybrid nanoparticle cores are obtained that comprise both hydrogenous and deuterated PMMA blocks. As a result, the core scattering length density should gradually become equal to that of the binary solvent mixture, which means that the neutron scattering intensity should be gradually reduced to a minimum value once copolymer chain exchange is complete.

The scattering length densities for PMMA and d_8PMMA and the corresponding desired composition for the *n*-dodecane/d_{26}-dodecane binary solvent mixture were calculated using **Equations 3.16** and **3.17**. Assuming ideal entropic mixing, the scattering length density of mixtures (P_{total}) can be calculated by multiplying the volume fraction (ϕ_i) of each component by its scattering length density (p_i) and taking the sum (**Equation 3.17**).

$$\boldsymbol{P_{total} = \sum \emptyset_i \times p_i} \quad (\mathbf{3.17})$$

A 1:1 mixed dispersion by volume was prepared by combining 0.30 ml of a 20% w/w dispersion of $PLMA_{39}$-$PMMA_x$ nanoparticles in *n*-dodecane with 0.30 ml of a 20% w/w dispersion of $PLMA_{39}$-d_8PMMA_x nanoparticles in the same solvent. The mean SLD of the mixed nanoparticle core was calculated and, based on this value, this mixed dispersion was diluted to 1.0% w/w to afford a final 38:62 v/v mixture of *n*-dodecane and d_{26}-dodecane. This binary solvent mixture was carefully selected so that its neutron SLD lay halfway between that of the original hydrogenous and deuterated PMMA cores. (**Table 3.2**).

Table 3.2. Summary of the sample preparation for mixtures of hydrogenous and semi-deuterated nanoparticle dispersions used in the TR-SANS experiments. Judicious mixtures of 20% w/w dispersions of fully hydrogenous and core-deuterated $PLMA_{39}$-$PMMA_x$ (where x is either 55 or 94 for the hydrogenous species and x is either 57 or 96 for the core-deuterated species) nanoparticles were combined in a 1:1 ratio by volume and thereafter diluted to 1.0% w/w using a binary mixture of *n*-dodecane and d_{26}-dodecane.

Composition	**Binary dispersion at 20% w/w / µl**	***n*-dodecane / µl**	**d_{26}-dodecane / µl**
Background	-	229	371
$PLMA_{39}$-$PMMA_{55}$ + $PLMA_{39}$-d_8PMMA_{57} 1:1 v/v ratio	47	186	367
$PLMA_{39}$-$PMMA_{94}$ + $PLMA_{39}$-d_8PMMA_{96} 1:1 v/v ratio	47	186	367

3.3. Results

3.3.1. Preparation of Hydrogenous and Core-deuterated PLMA-PMMA Spheres

Well-defined spherical diblock copolymer nanoparticles were prepared by a two-step PISA synthesis, see **Figure 3.5**. First, a $PLMA_{39}$ macro-CTA was prepared via RAFT solution polymerisation of LMA in toluene at 70 °C. Then this precursor was chain-extended via RAFT dispersion polymerisation of either deuterated or hydrogenous MMA at 20 % w/w solids in *n*-dodecane at 90 °C. At a certain critical PMMA DP, micellar nucleation occurs and the growing copolymer chains self-assemble to form spherical nanoparticles.

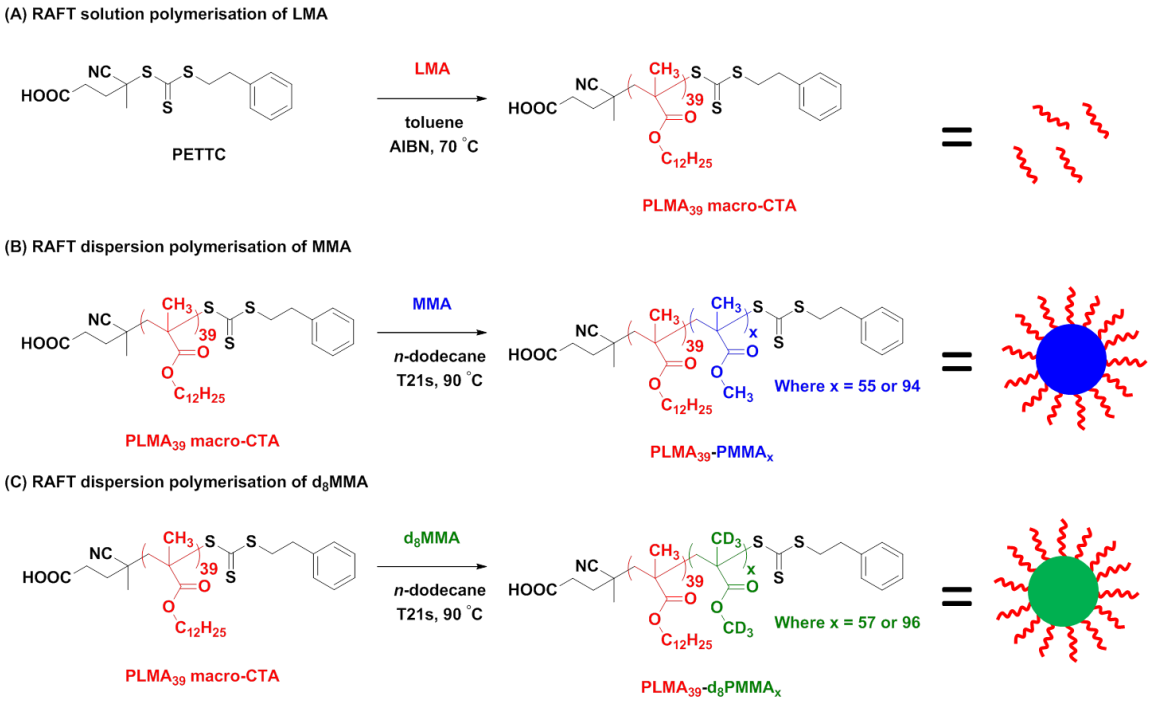

Figure 3.5. (A) $PLMA_{39}$ homopolymer was prepared via RAFT solution polymerisation of LMA in toluene at 70 °C. Subsequently, this precursor block was chain-extended with either (B) MMA or (C) d_8MMA in *n*-dodecane at 90 °C. This RAFT dispersion polymerisation protocol was used to prepare the following four types of sterically-stabilised spherical nanoparticles: $PLMA_{39}$-$PMMA_{55}$, $PLMA_{39}$-d_8PMMA_{57}, $PLMA_{39}$-$PMMA_{94}$ and $PLMA_{39}$-d_8PMMA_{96}.

Proton NMR spectroscopy studies indicated high MMA conversions (>92%) for both PISA syntheses involving hydrogenous MMA (see **Figure 3.3 and Equation 3.3**). Similarly high

conversions were obtained for the corresponding d_8PMMA syntheses using deuterium NMR spectroscopy (see **Figure 3.4 and Equation 3.3**). THF GPC analysis of the four $PLMA_{39}$-$PMMA_{55}$, $PLMA_{39}$-$PMMA_{94}$, $PLMA_{39}$-d_8PMMA_{57} and $PLMA_{39}$-d_8PMMA_{96} diblock copolymers confirmed high blocking efficiencies in each case, with a significant shift to lower retention times compared to the $PLMA_{39}$ precursor block (**Figure 3.6**). Moreover, almost identical molecular weight distributions were obtained for the all-hydrogenous and corresponding core-deuterated copolymers, suggesting good reproducibility for these PISA syntheses when using MMA and d_8MMA.

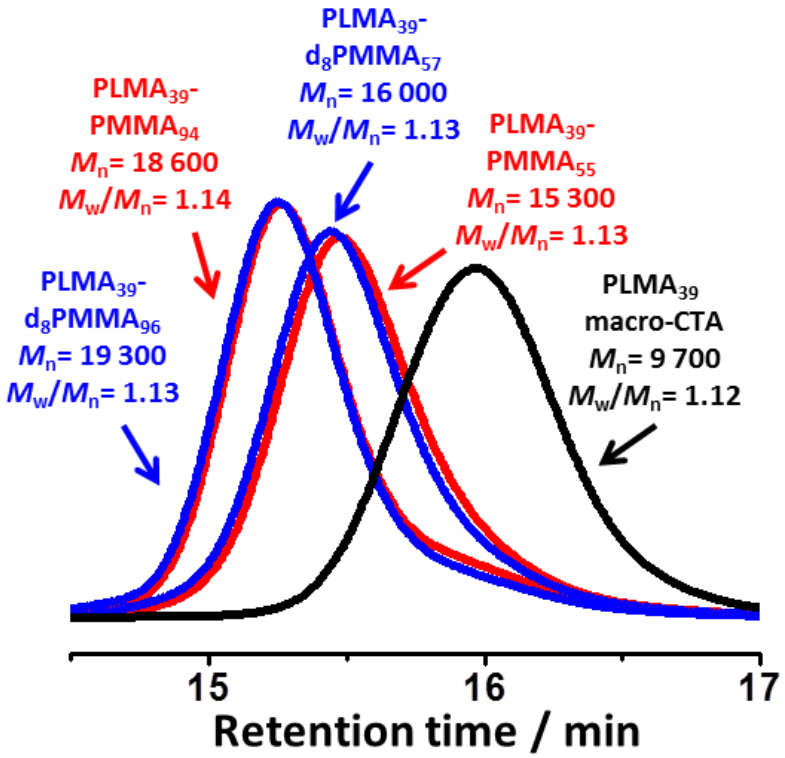

Figure 3.6. Area-normalised THF GPC traces recorded for $PLMA_{39}$ macro-CTA, $PLMA_{39}$-$PMMA_{55}$, $PLMA_{39}$-d_8PMMA_{57}, $PLMA_{39}$-$PMMA_{94}$ and $PLMA_{39}$-d_8PMMA_{96} using a refractive index detector (calibrated against a series of near-monodisperse poly(methyl methacrylate) standards. These data confirm high blocking efficiencies and almost identical molecular weight distributions for each pair of fully hydrogenous and core-deuterated diblock copolymers.

3.3.2. SAXS Studies of Dissolved $PLMA_{39}$ Chains

SAXS was used to characterise the dimensions of the molecularly-dissolved $PLMA_{39}$ precursor and the four types of diblock copolymer nanoparticles. First, a 1.0% w/w solution of the $PLMA_{39}$ precursor in *n*-dodecane was analysed to estimate the thickness of the corona block (**Figure 3.7**). The data were fitted using the Debye function[40] (see **Equation 3.5**). This analysis indicated a mean radius of gyration (R_g) of 1.91 nm. The Debye function[40] was considered to be an appropriate model for this homopolymer because little is known about the solvent-polymer interactions. This function assumes that *n*-dodecane is a theta solvent for this polymer, (i.e. neither good nor bad solvent). Additionally, the *n*-dodecane solvent is chemically similarly to its lauryl side-groups ($-C_{12}H_{25}$), which leads to relatively poor X-ray contrast. Thus, to a good first approximation most of the X-ray scattering should originate from the methacrylic backbone.

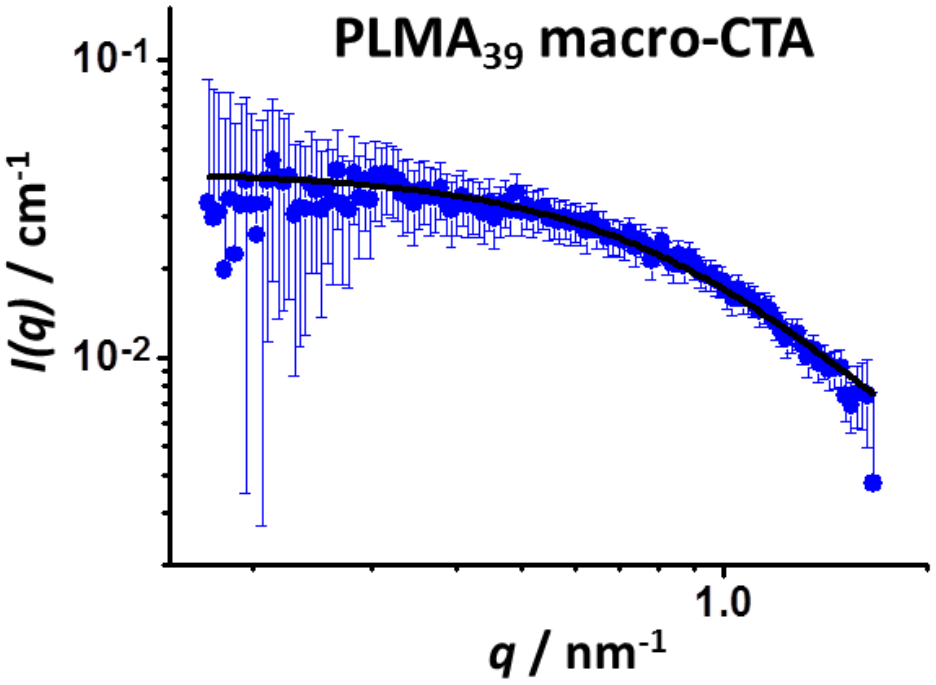

Figure 3.7. SAXS pattern recorded for a 1.0% w/w solution of the $PLMA_{39}$ precursor block dissolved in *n*-dodecane. The black line corresponds to the data fit obtained using the Debye function.[40] This analysis indicated a mean radius of gyration, R_g, of 1.91 nm.

3.3.3. Variable Temperature SAXS Studies on Hydrogenous and Core-Deuterated PLMA-PMMA Spheres

Hydrogenous $PLMA_{39}$-$PMMA_x$ and core-deuterated $PLMA_{39}$-d_8PMMA_x diblock copolymer dispersions were prepared at 20% w/w solids via PISA, and subsequently diluted with *n*-dodecane to afford 1.0 % w/w (0.7% v/v) dispersions prior to SAXS analysis (**Figure 3.8A**). Each of the four scattering patterns recorded for the hydrogenous and core-deuterated nanoparticles exhibited a zero gradient at low *q*, which is consistent with the expected spherical morphology.[30] Good fits to these scattering curves were obtained when utilising a well-known spherical micelle model[37,39,51,52] (see **Equations 3.6-3.13**). A mean R_g value of around 2.0 nm was determined for the $PLMA_{39}$ stabiliser chains at the surface of these nanoparticles, which is only slightly larger than the R_g value of 1.91 nm obtained by SAXS studies of the molecularly-dissolved $PLMA_{39}$ precursor (**Figure 3.7**). This small difference suggests a slightly perturbed (stretched) chain conformation. Apparent copolymer concentrations of around 0.5% v/v were obtained, which are slightly lower than the expected value of 0.7% v/v. Nanoparticle core diameters of around 11 and 14 nm were determined for core-forming block DPs of 55 and 94, respectively (see **Table 3.3**). Overall nanoparticle diameters (*D*) were calculated to be approximately 18.5 and 22.0 nm after combining the core radius (R_{core}) with the R_g obtained for the $PLMA_{39}$ coronal chains (using $D = 2R_{core} + 4R_g$). This approach indicated almost identical overall nanoparticle diameters when using either hydrogenous or deuterated MMA (**Table 3.4**).

These 1.0% w/w nanoparticle dispersions were then annealed to assess their thermal stability. Each dispersion was heated to 150 °C for 30 min, which corresponds to the maximum experimental time and temperature used in the TR-SANS experiments (see later). SAXS analysis of these annealed dispersions after returning to 20 °C afforded very similar scattering patterns to those obtained for the non-annealed dispersions. Fitting the SAXS patterns using a spherical micelle model produced comparable corona thicknesses and nanoparticle core diameters (see **Figure 3.8B and Tables 3.3 and 3.4**). This suggests excellent colloidal and thermal stability for these nanoparticle dispersions under the stated conditions.

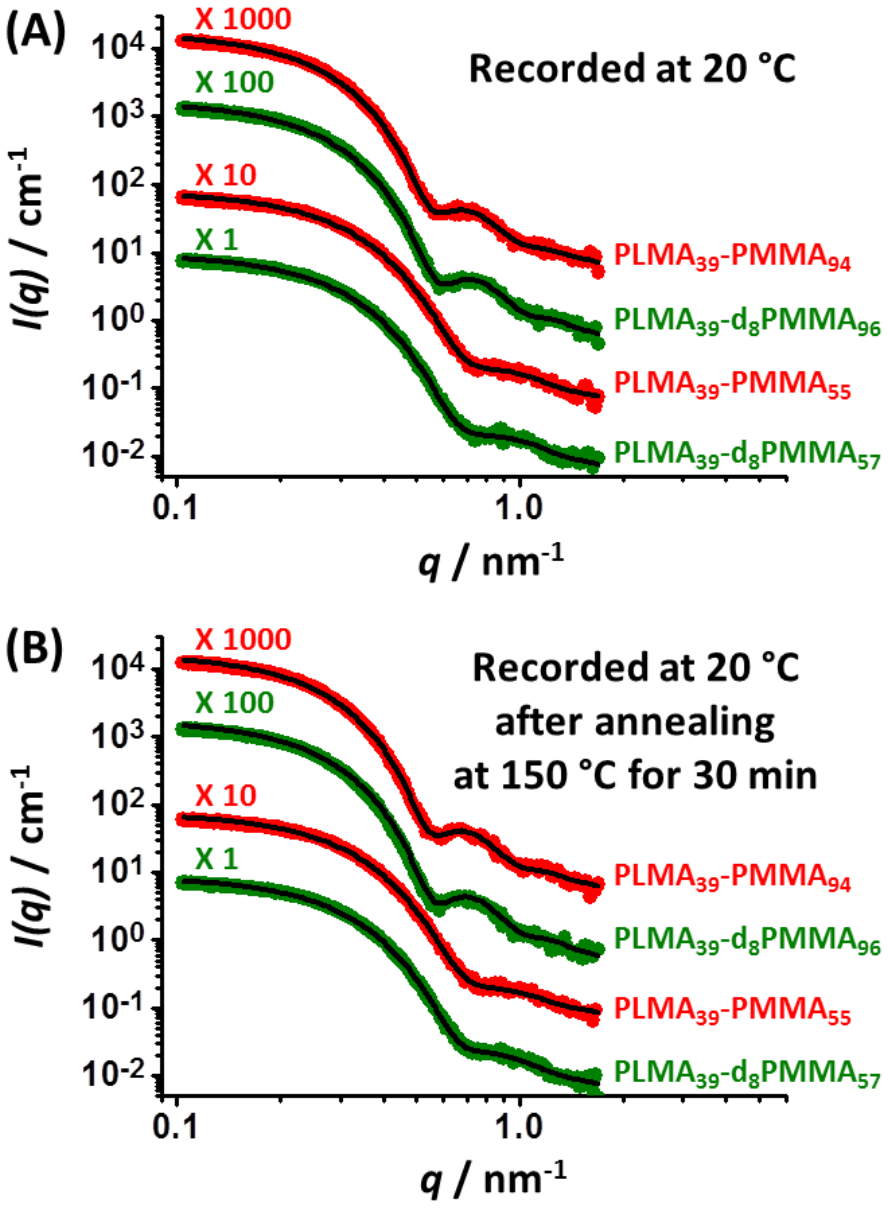

Figure 3.8. (A) SAXS patterns recorded at 22 °C for 1.0% w/w dispersions for each of the original four $PLMA_{39}$-$PMMA_x$ and $PLMA_{39}$-d_8PMMA_x diblock copolymer nanoparticles prepared via PISA (where x = 94 or 55 for $PMMA_x$ and 96 or 57 for d_8-$PMMA_x$). (B) SAXS patterns obtained at 20 °C for the same four diblock copolymer nanoparticles after heating to 150 °C for 30 min. SAXS patterns are multiplied by arbitrary factors for the sake of clarity. The solid lines are best fits to the data using a well-known spherical micelle model.[37-39]

Table 3.3. Summary of the input parameters used to fit the SAXS patterns recorded for 1.0% w/w (0.7% v/v) dispersions of $PLMA_{39}$-$PMMA_x$ and $PLMA_{39}$-d_8PMMA_x nanoparticles in *n*-dodecane (both as prepared and after heating to 150 °C for 30 min). Good data fits could be obtained without assuming any solvent to be present within the nanoparticle cores.

Copolymer ID	**Concentration / % v/v**	**Core radius (R_{core}) / nm**	**Shell radius (R_g) / nm**
$PLMA_{39}$-$PMMA_{55}$ (as prepared)	0.46	5.4 ± 0.6	2.0
$PLMA_{39}$-$PMMA_{55}$ (after heating to 150 °C for 30 min)	0.46	5.4 ± 0.6	2.0
$PLMA_{39}$-d_8PMMA_{57} (as prepared)	0.59	5.6 ± 0.5	2.0
$PLMA_{39}$-d_8PMMA_{57} (after heating to 150 °C for 30 min)	0.53	5.5 ± 0.6	2.0
$PLMA_{39}$-$PMMA_{94}$ (as prepared)	0.49	7.3 ± 0.7	2.0
$PLMA_{39}$-$PMMA_{94}$ (after heating to 150 °C for 30 min)	0.47	7.3 ± 0.7	2.0
$PLMA_{39}$-d_8PMMA_{96} (as prepared)	0.54	7.0 ± 0.6	2.0
$PLMA_{39}$-d_8PMMA_{96} (after heating to 150 °C for 30 min)	0.55	7.2 ± 0.6	2.0

Table 3.4. Summary of core and overall diameters for $PLMA_{39}$-$PMMA_x$ and $PLMA_{39}$-d_8PMMA_x nanoparticles determined by SAXS analysis before and after thermal annealing at 150 °C for 30 min.

Copolymer composition	Core diameter before heating / nm	Core diameter after heating / nm	Overall diameter before heating / nm	Overall diameter after heating / nm
$PLMA_{39}$-$PMMA_{55}$	10.8 ± 1.1	10.8 ± 1.2	18.9 ± 1.1	18.9 ± 1.2
$PLMA_{39}$-d_8PMMA_{57}	11.0 ± 1.0	10.9 ± 1.1	19.0 ± 1.0	19.0 ± 1.1
$PLMA_{39}$-$PMMA_{94}$	14.5 ± 1.4	14.7 ± 1.3	22.5 ± 1.4	22.6 ± 1.3
$PLMA_{39}$-d_8PMMA_{96}	13.9 ± 1.2	14.4 ± 1.2	21.9 ± 1.2	22.4 ± 1.2

SAXS analysis confirmed that almost identical nanoparticles of two different sizes were obtained via RAFT-mediated PISA using either hydrogeneous or deuterated MMA. Moreover, the nanoparticle dimensions are not affected by heating such dispersions to 150 °C for 30 min. The behaviour of these nanoparticles was studied at various temperatures using TR-SANS. According to the literature,[10-19,53] this technique can be used to examine if copolymer chain exchange occurs between such nanoparticles.

3.3.4. Examination of Copolymer Chain exchange Between Spherical PLMA-PMMA Spheres using TR-SANS

For a well-designed contrast match experiment, neutron scattering can readily discriminate between the hydrogenous and deuterated core-forming blocks. Prior to TR-SANS analysis, a 1:1 v/v binary mixture of $PLMA_{39}$-$PMMA_x$ and $PLMA_{39}$-d_8PMMA_x nanoparticles was made up and subsequently diluted to 1.0 % w/w using a judicious blend of *n*-dodecane and d_{26}-dodecane, such that the final solvent mixture contained 38% *n*-dodecane by volume (see **Equation 3.16 and 3.17 and Table 3.2**). This solvent composition was selected to ensure that its neutron SLD lies midway between those of the hydrogeneous and deuterated PMMA cores. This binary mixture of nanoparticles was heated to various temperatures during the

TR-SANS experiment to induce copolymer chain exchange. If copolymer chain exchange occurs between these two types of nanoparticles, then the SLD of the hybrid (mixed) nanoparticle cores should tend towards that of the binary solvent **(Figure 3.9)**. Thus, the neutron scattering intensity, *I(q)*, should be gradually reduced over time, since this parameter is approximately proportional to the *square* of the difference in the neutron SLD ($\Delta\rho^2$).[54]

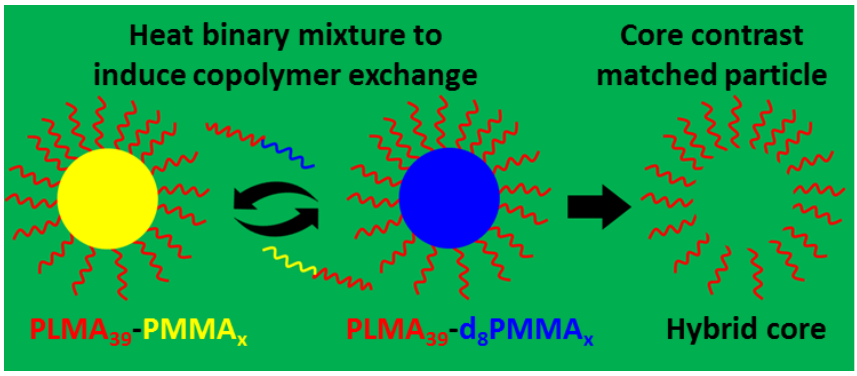

Figure 3.9. Schematic representation of a TR-SANS experiment in which copolymer chain exchange occurs between a binary mixture of spherical nanoparticles comprising hydrogenous and deuterated cores. As entropic mixing occurs, the neutron scattering intensity is reduced because the neutron SLD of the hybrid nanoparticle cores tends towards that of the binary solvent (which is a judicious mixture of 38% *n*-dodecane and 62% d_{26}-dodecane by volume).

Unfortunately, it is non-trivial to fit the SANS scattering patterns recorded for the individual $PLMA_{39}$-$PMMA_x$ and $PLMA_{39}$-d_8PMMA_x nanoparticles using the model employed for SAXS analysis. This is because there is a non-linear relationship between scattering intensity and solvent composition for long-chain hydrocarbons.[50] Additionally, the hydrogenous lauryl side-chains of the PLMA stabiliser block become more pronounced in the SANS scattering patterns owing to the additional contrast that is introduced by utilising a solvent mixture. This phenomenon particularly affects the scattering pattern at short lengths scales (i.e. high *q*). Therefore, theoretical SANS scattering patterns for both the initial binary mixture of nanoparticles and the final hybrid (mixed) nanoparticles were calculated using the experimental SAXS scattering patterns recorded for the spherical $PLMA_{39}$-$PMMA_x$ and $PLMA_{39}$-d_8PMMA_x nanoparticles (**Figure 3.8**). This was achieved by adjusting the neutron SLD for the core-forming block and solvent to the calculated values, while keeping all other parameters constant (**Figures 3.10A and 3.10B**).

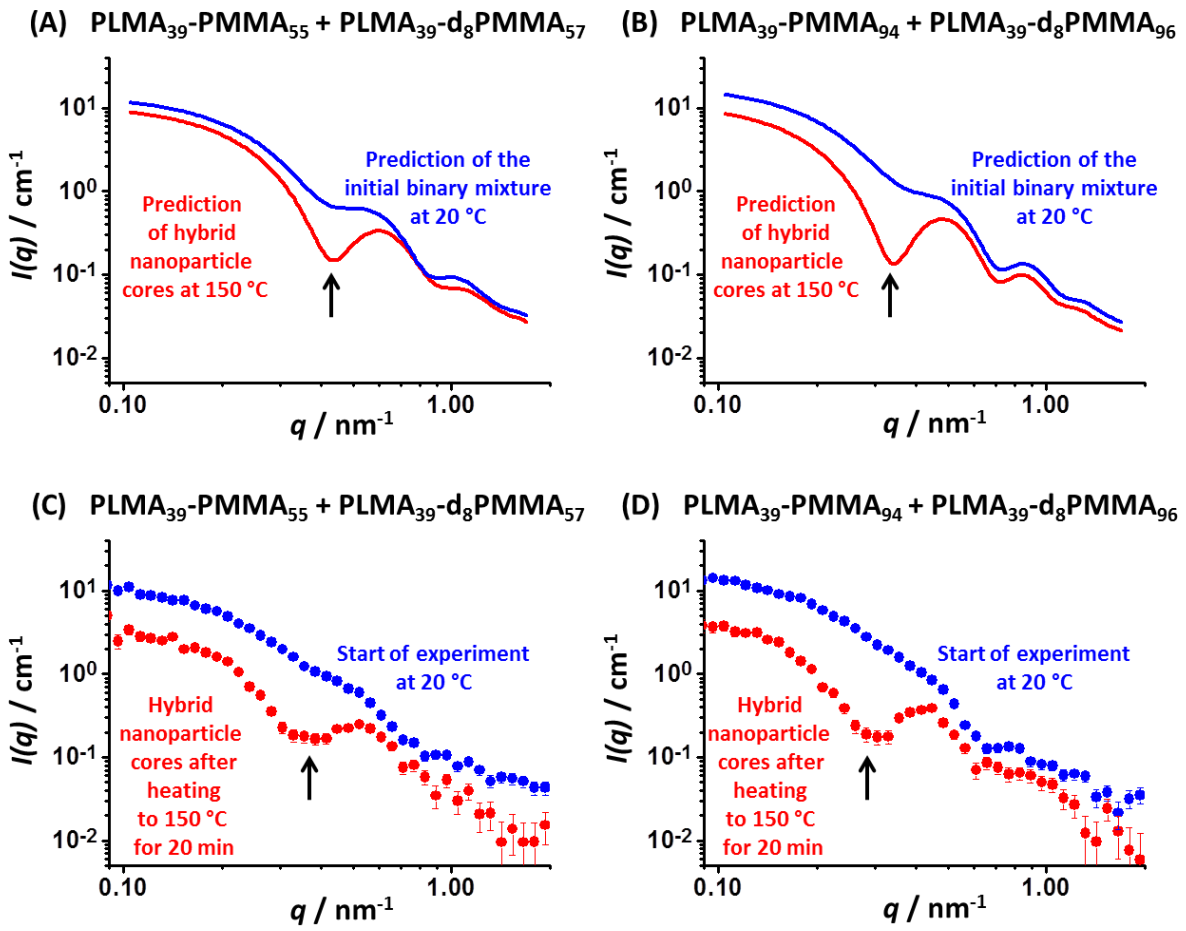

Figure 3.10. (A) Theoretical SANS pattern for a 1:1 binary mixture by volume of $PLMA_{39}$-$PMMA_{55}$ and $PLMA_{39}$-d_8PMMA_{57} nanoparticles calculated from their respective SAXS patterns. (B) Theoretical SANS pattern for a 1:1 binary mixture by volume of $PLMA_{39}$-PMM_{94} and $PLMA_{39}$-d_8PMMA_{96} nanoparticles calculated from their respective SAXS patterns. (C) Experimental SANS pattern recorded for a 1.0% w/w dispersion of a 1:1 binary mixture by volume of $PLMA_{39}$-$PMMA_{55}$ and $PLMA_{39}$-d_8PMMA_{57} nanoparticles at 150 °C, both at the beginning of the TR-SANS experiment and again after 20 min. (D) Experimental SANS pattern recorded for a 1.0% w/w dispersion of a 1:1 binary mixture by volume of $PLMA_{39}$-$PMMA_{94}$ and $PLMA_{39}$-d_8PMMA_{96} nanoparticles at 150 °C, both at the beginning of the TR-SANS experiment and again after 20 min. In both cases a pronounced minimum appears at intermediate *q* (indicated with the black arrows), which indicates that copolymer chain exchange occurs under these conditions.

The SANS scattering patterns calculated for the initial binary mixture for both the $PLMA_{39}$-$PMMA_{55}$ + $PLMA_{39}$-d_8PMMA_{57} nanoparticles and the $PLMA_{39}$-$PMMA_{94}$ + $PLMA_{39}$-d_8PMMA_{96} nanoparticles are shown as blue curves. As expected, the calculated SANS scattering patterns for the final hybrid (mixed) nanoparticles exhibited a significant reduction in scattering intensity, with a pronounced minimum appearing at intermediate *q* in each case. Experimental SANS data confirm these predictions: a progressive reduction in the overall neutron scattering intensity is observed over time (**Figures 3.10C and 3.10D**). At the start of the experiment, the blue scattering curves are relatively featureless in the absence of any copolymer exchange. However, as copolymer chain exchange occurs, a distinct minimum is observed at intermediate *q* owing to the lack of contrast between the neutron SLD of the solvent mixture and that of the hybrid nanoparticle cores. The same approach was previously utilised by Lodge *et al.*[11-13,15-17,19,53] and Lund and co-workers[14,18] when investigating copolymer chain exchange between diblock copolymer micelles prepared via the traditional post-polymerisation processing route (i.e. a solvent switch).

Heating the initial binary mixture of $PLMA_{39}$-$PMMA_x$ and $PLMA_{39}$-d_8PMMA_x nanoparticles causes a reduction in the total neutron scattering intensity. This is because the neutron SLD of the isotopically heterogeneous nanoparticle cores tends to that of the binary solvent mixture as a result of entropically-driven copolymer chain exchange, which leads to the formation of hybrid (mixed) nanoparticle cores. However, some residual scattering is still observed owing to the hydrogenous nature of the $PLMA_{39}$ stabiliser block. The extent of copolymer exchange can be determined using the invariant scalar form of the total scattering, *Q* (**Equation 3.18**). The invariant *(Q)* depends only on the concentration, volume fraction and neutron contrast and not on the nanoparticle structure.[55] Thus this parameter is well-suited for monitoring the redistribution of copolymer chains to form hybrid (mixed) nanoparticle cores since this leads to a progressive reduction in neutron contrast. This analytical approach differs from that reported in the literature[11], where changes in neutron scattering intensity at low angles were used to monitor the redistribution of copolymer chains.

$$\boldsymbol{Q} = \int_{\boldsymbol{q}_{\mathbf{min}}}^{\boldsymbol{q}_{\mathbf{max}}} \boldsymbol{I}(\boldsymbol{q}) \times \boldsymbol{q}^{\mathbf{2}} \times \boldsymbol{dq} \quad (\mathbf{3.18})$$

The invariant *(Q)* was calculated using **Equation 3.18** and plotted against time (**Figure 3.11**). Initially, each binary mixture of hydrogenous and core-deuterated nanoparticles was heated to 150 °C. These TR-SANS experiments revealed a striking difference between the 18.5 nm and 22.0 nm nanoparticles. For the smaller nanoparticles, fully mixed hybrid nanoparticle cores were formed within 3 min at this temperature, whereas the scattering intensity arising from the larger nanoparticles required 9 min to attain a constant (lower) value. Both binary mixtures of nanoparticles exhibited faster copolymer exchange rates at higher temperatures. Moreover, the exchange rate for the shorter copolymer chains is significantly faster than that for the longer copolymer chains. Clearly, the exchange kinetics are strongly dependent on the core-forming block DP. These findings are consistent with observations made by Bates and co-workers for PEP-PS micelles, whereby a longer core-forming PS block led to significantly slower exchange kinetics.[11-13,15]

Furthermore, it is clear that higher temperatures yield lower final *Q* values. A possible explanation for this phenomenon involves the formation of a progressively larger fraction of dissolved block copolymers at higher temperatures. Additionally, nanoparticle core solvation by hot solvent might also contribute to this effect. This is because the invariant is a measure of homogeneity within the nanoparticle dispersion and either process should produce a more homogeneous dispersion. Further studies are warranted to confirm this hypothesis. Experiments such as variable temperature ^{1}H NMR studies on nanoparticle dispersions are likely to be informative. Fielding et al. reported such NMR studies on PLMA-PBzMA worms in d_{26}-dodecane.[4] Distinct signals from the core-forming PBzMA block became visible on heating such a nanoparticle dispersion. This was interpreted in terms of surface plasticisation of the worm cores, which led to a morphological worm-to-sphere transition.

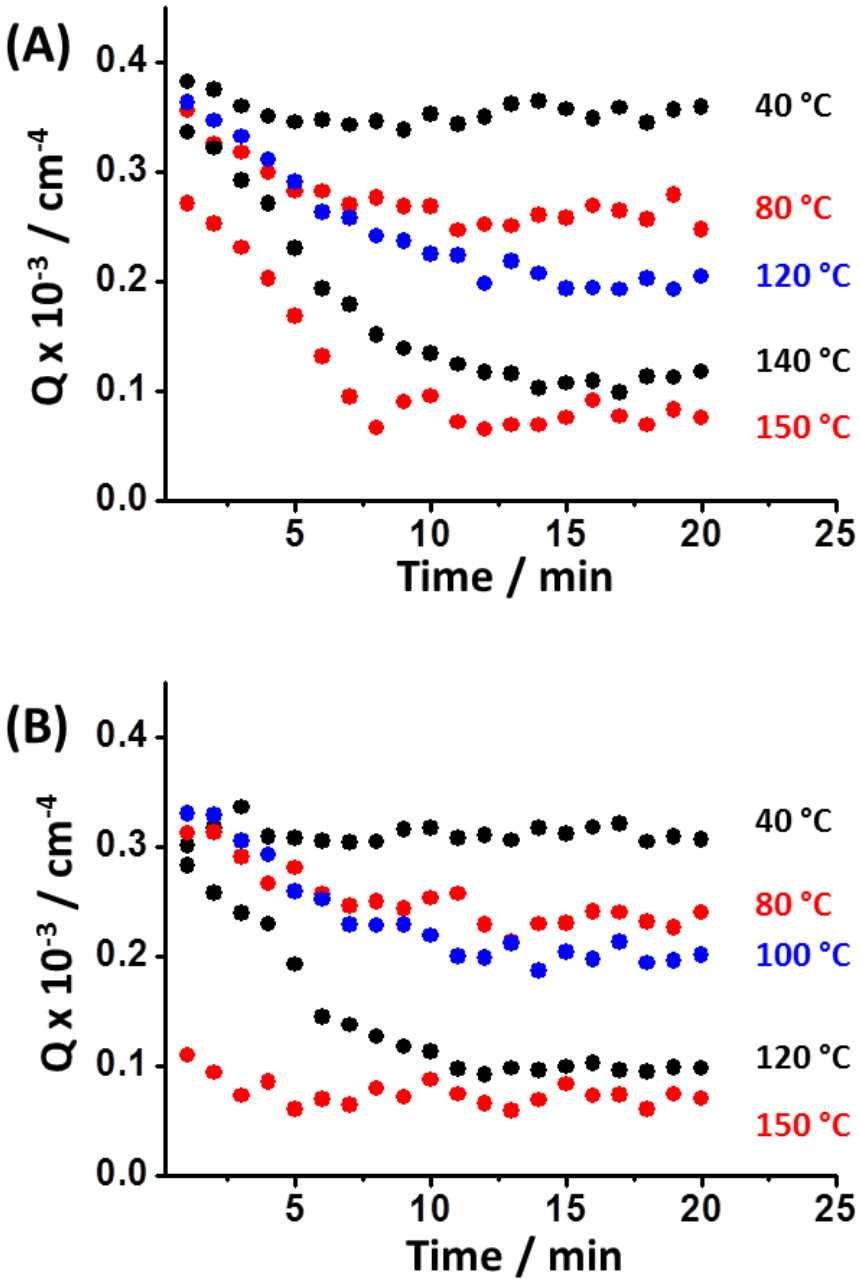

Figure 3.11. Heating binary mixtures of (A) $PLMA_{39}$-$PMMA_{94}$ and $PLMA_{39}$-d_8PMMA_{96} nanoparticles of around 22.0 nm diameter and (B) $PLMA_{39}$-$PMMA_{55}$ and $PLMA_{39}$-d_8PMMA_{57} nanoparticles of around 18.5 nm diameter causes a reduction in the scattering invariant *(Q)* during a TR-SANS experiment. The reduction in *Q* over time is the result of a reduction in neutron contrast for the nanoparticle cores owing to copolymer exchange. Higher temperatures result in faster rates of copolymer chain exchange between nanoparticles.

Minimal change in *Q* was observed at 40 °C, regardless of the nanoparticle diameter. This suggests that very slow (if any) copolymer exchange occurs at this temperature. This is understandable because these data were collected well below the T_g of the PMMA core-forming block, which is around 88 °C in the bulk (see **Figure 3.12**). This is significantly lower than the T_g for a $PMMA_{102}$ homopolymer which is around 120 °C (N.B. T_g values of around 127 °C were determined for PMMA homopolymers with higher DPs, see **Figure 3.13**.). One significant difference between these two species is the PLMA block in the former case, which might reduce the T_g of the PMMA block. Moreover, the T_g for the deuterated PMMA block appears to be 6 °C lower than that for the hydrogenous PMMA block. Interestingly, **Figure 3.11** shows that copolymer chain exchange can certainly occur below 80 °C, since a significant reduction in the scattering invariant (*Q*) is observed at this temperature.

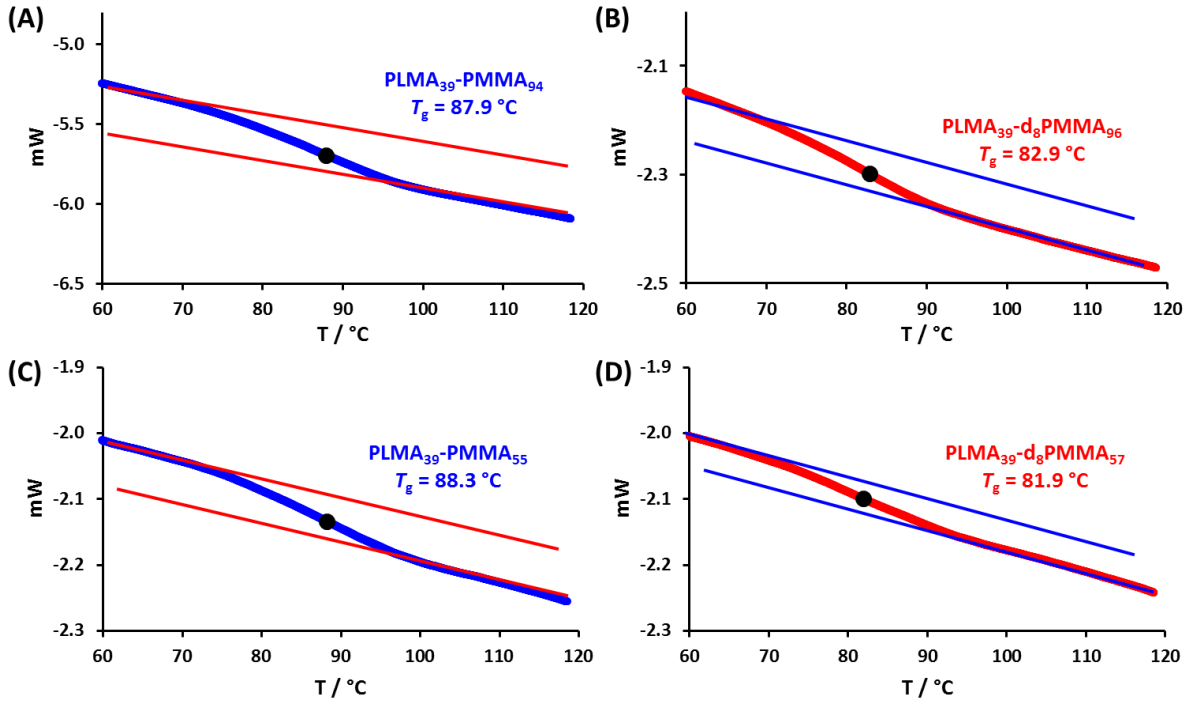

Figure 3.12. PMMA T_g determination via DSC for (A) $PLMA_{39}$-$PMMA_{94}$, (B) $PLMA_{39}$-d_8PMMA_{96}, (C) $PLMA_{39}$-$PMMA_{55}$ and (D) $PLMA_{39}$-d_8PMMA_{57}. Diblock copolymers were purified by precipitation of the 20% w/w nanoparticle dispersion into 2-propanol followed by filtration. T_g values for hydrogenous PMMA appear to be around 88 °C, while the semi-deuterated diblock copolymer exhibits a T_g of around 82 °C.

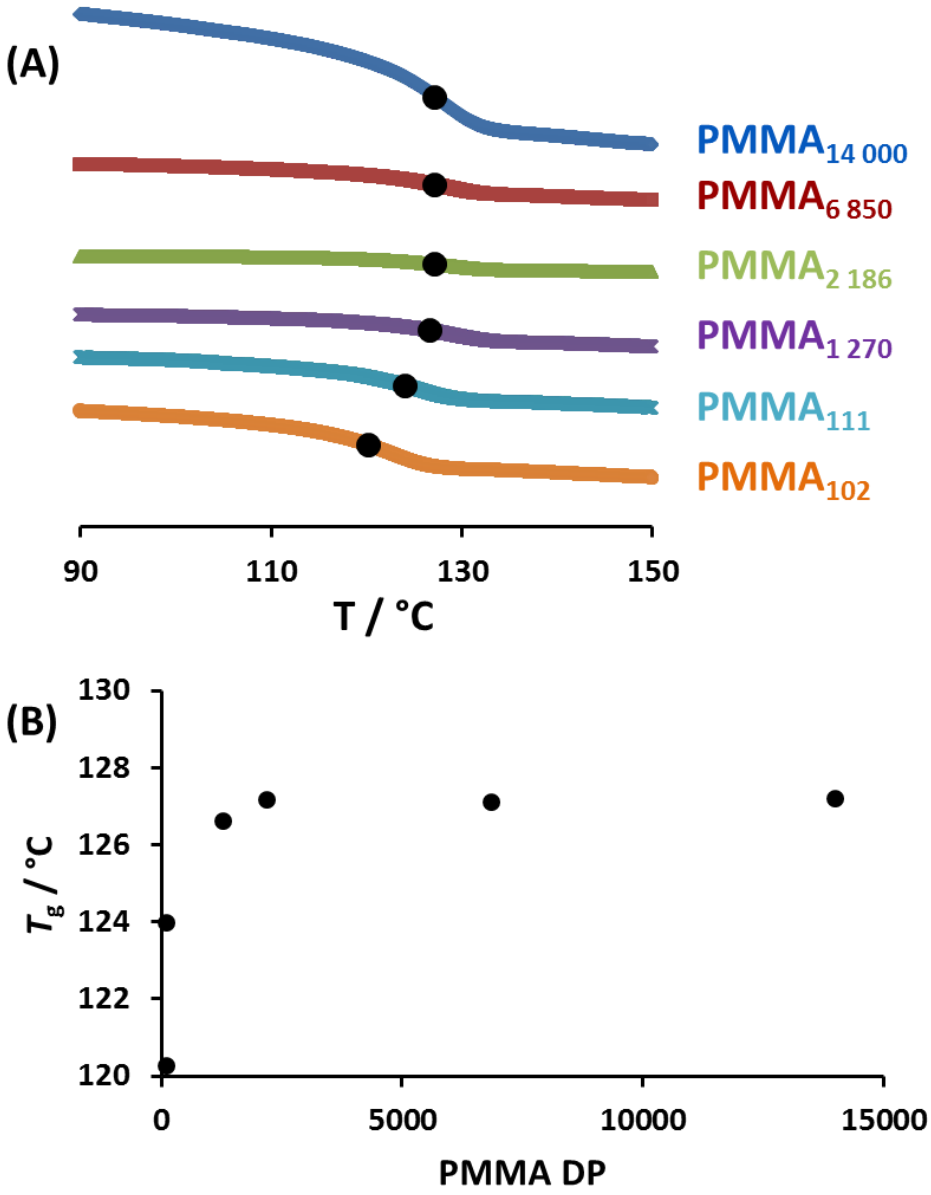

Figure 3.13. (A) T_g determination by DSC for a series of PMMA homopolymers with DPs ranging between 102 and 14 000. The black dot indicates the calculated T_g value. (B) T_g plotted against PMMA DP. Lower PMMA homopolymer DPs lead to lower T_g values; $PMMA_{14\,000}$ has a T_g of 127 °C whereas $PMMA_{102}$ has a T_g of 120 °C.

3.4. Discussion

All TR-SANS studies were performed using 1.0 % w/w nanoparticle dispersions. At such a low copolymer concentration, the micelle fusion/fission mechanism seems rather unlikely. Moreover, both Lodge and co-workers[11-13,15-17,19,53] and the Lund group[14,18] show that the chain expulsion/insertion mechanism is consistent with the experimental observations. It is worth considering the implications of these findings in the context of PISA syntheses.

The TR-SANS data reported herein indicate that there is exchange of copolymer chains between $PLMA_{39}$-$PMMA_x$ spheres prepared via PISA at 90 °C, which is the reaction temperature used for their synthesis. Based on the literature, it is reasonable to assume that this occurs via the chain expulsion/insertion mechanism. During PISA, the unreacted MMA monomer swells the nanoparticle cores, thus accelerating the rate of polymerisation[27,31] while also acting as a vital processing aid (or co-solvent) for the insoluble growing PMMA chains by enhancing their mobility. Thus it is very likely that the same copolymer exchange mechanism also operates immediately after the micellar nucleation event during PISA, when the insoluble PMMA blocks are relatively short and the nascent nanoparticles are highly monomer-swollen. However, the energy penalty required to remove a copolymer chain from such nanoparticles becomes much greater for longer core-forming blocks. Thus the chain expulsion/insertion mechanism should become increasingly unlikely as the core-forming chains grow longer and the solvating MMA monomer gradually becomes depleted. Furthermore, PISA syntheses conducted at low copolymer concentrations using relatively long stabiliser blocks typically yield kinetically-trapped spheres.[1,3,4,9,30] For such formulations, there is likely to be a gradual transition from ergodic (dynamic) spherical micelles to non-ergodic (frozen) micelles during the polymerisation, particularly when targeting relatively long core-forming blocks.

In contrast, the formation of highly anisotropic worms during PISA is believed to proceed via 1D fusion of multiple spheres, i.e. by a micelle fusion/fission mechanism.[4] This hypothesis is consistent with the observation that worms typically cannot be obtained at relatively low copolymer concentrations in PISA syntheses[1,2] because this mechanism becomes much less likely under such conditions. Moreover, worms are normally only obtained when targeting relatively short stabiliser blocks.[4] Again, this is understandable because weaker steric

stabilisation of the nascent spherical nanoparticles promotes their 1D fusion. Finally, the formation of worms (and vesicles) requires relatively long core-forming blocks to be targeted, for which the chain expulsion/insertion mechanism becomes much less likely.

According to Bates and co-workers[11-13,15-17,19,53] and Zinn et al.[14,18] the micelle fusion/fission mechanism is highly unlikely to be applicable to conventional diblock copolymer micelles (or nanoparticles). We agree with these findings but contend that the *monomer-swollen* nanoparticles that grow during PISA are much more likely to be able to undergo micelle fusion/fission than nanoparticles prepared via post-polymerisation processing in the absence of any monomer (or other co-solvent). This is because core-solvation could increase the mobility of the polymer blocks within the nanoparticle cores, making the particle more susceptible to such a process. Thus, this mechanism appears to be the most likely explanation for the formation of highly anisotropic worms during many PISA syntheses.[2-4,56]

In summary, both the chain expulsion/insertion mechanism and micelle fusion/fission mechanism are likely to play important roles during PISA, with their relative prevalence depending on the precise formulation. Finally, we note that using thermal initiators with differing decomposition temperatures (or utilising photo-initiation at ambient temperature) could substantially affect the rate of copolymer chain exchange during PISA, which may in turn influence the evolution in copolymer morphology.[57] Clearly, more research is warranted to examine the intriguing hypotheses outlined above.

3.5. Conclusions

Two pairs of hydrogenous $PLMA_{39}$-$PMMA_x$ and core-deuterated $PLMA_{39}$-d_8PMMA_x diblock copolymers (where x is 55 or 94 for the hydrogenated species, and 57 or 96 for the core-deuterated species) were synthesised in the form of sterically-stabilised nanoparticles via RAFT-mediated PISA in *n*-dodecane. NMR spectroscopy studies confirmed high monomer conversions were achieved in each case and GPC analysis indicated almost identical narrow molecular weight distributions ($M_w/M_n \leq 1.14$) for each pair. Binary mixtures of hydrogenous

and core-deuterated nanoparticles were analysed by TR-SANS at various temperatures to examine whether any copolymer chain exchange occurs. This technique provides compelling evidence for entropic mixing of the copolymer chains, with the rapid formation of more weakly scattering nanoparticles comprising hybrid (mixed) cores at 80 °C or above. The rate of copolymer chain exchange is strongly temperature-dependent, with higher temperatures leading to faster exchange. Moreover, significantly faster chain exchange kinetics were observed for the shorter PMMA block (DP = 55) compared to the longer PMMA block (DP = 94).

These results are fully consistent with those expected based on the pioneering studies by Bates, Lodge and co-workers. When considered in the context of RAFT-mediated PISA, these data suggest that the chain expulsion/insertion mechanism is highly likely for monomer-swollen nascent micelles but it should become much less important as the core-forming block DP increases (and also under monomer-starved conditions). However, a micelle fusion/fission mechanism remains the most logical explanation for the formation of worms from spheres during PISA, especially given that such anisotropic morphologies are typically not generated when performing PISA syntheses at relatively low copolymer concentration. It is perhaps worth emphasising here that the latter mechanism should be favored by (i) the use of a relatively short stabiliser block and (ii) the well-established monomer solvation of the growing core-forming blocks during PISA, which significantly increases their chain mobility.

3.6. References

(1) Lopez-Oliva, A. P.; Warren, N. J.; Rajkumar, A.; Mykhaylyk, O. O.; Derry, M. J.; Doncom, K. E. B.; Rymaruk, M. J.; Armes, S. P. Polydimethylsiloxane-Based Diblock Copolymer Nano-objects Prepared in Nonpolar Media via RAFT-Mediated Polymerization-Induced Self-Assembly, *Macromolecules*, **2015**, *48*, 3547-3555.

(2) Fielding, L. A.; Derry, M. J.; Ladmiral, V.; Rosselgong, J.; Rodrigues, A. M.; Ratcliffe, L. P. D.; Sugihara, S.; Armes, S. P. RAFT dispersion polymerization in non-polar solvents: facile production of block copolymer spheres, worms and vesicles in n-alkanes, *Chemical Science*, **2013**, *4*, 2081-2087.

(3) Blanazs, A.; Ryan, A. J.; Armes, S. P. Predictive Phase Diagrams for RAFT Aqueous Dispersion Polymerization: Effect of Block Copolymer Composition, Molecular Weight, and Copolymer Concentration, *Macromolecules*, **2012**, *45*, 5099-5107.

(4) Fielding, L. A.; Lane, J. A.; Derry, M. J.; Mykhaylyk, O. O.; Armes, S. P. Thermo-responsive Diblock Copolymer Worm Gels in Non-polar Solvents, *Journal of the American Chemical Society*, **2014**, *136*, 5790-5798.

(5) Tan, J.; Sun, H.; Yu, M.; Sumerlin, B. S.; Zhang, L. Photo-PISA: Shedding Light on Polymerization-Induced Self-Assembly, *ACS Macro Letters*, **2015**, *4*, 1249-1253.

(6) Pei, Y.; Thurairajah, L.; Sugita, O. R.; Lowe, A. B. RAFT Dispersion Polymerization in Nonpolar Media: Polymerization of 3-Phenylpropyl Methacrylate in n-Tetradecane with Poly(stearyl methacrylate) Homopolymers as Macro Chain Transfer Agents, *Macromolecules*, **2015**, *48*, 236-244.

(7) Pei, Y. W.; Dharsana, N. C.; Van Hensbergen, J. A.; Burford, R. P.; Roth, P. J.; Lowe, A. B. RAFT dispersion polymerization of 3-phenylpropyl methacrylate with poly 2-(dimethylamino)ethyl methacrylate macro-CTAs in ethanol and associated thermoreversible polymorphism, *Soft Matter*, **2014**, *10*, 5787-5796.

(8) Karagoz, B.; Boyer, C.; Davis, T. P. Simultaneous Polymerization-Induced Self-Assembly (PISA) and Guest Molecule Encapsulation, *Macromolecular Rapid Communications*, **2014**, *35*, 417-421.

(9) Derry, M. J.; Fielding, L. A.; Armes, S. P. Industrially-relevant polymerization-induced self-assembly formulations in non-polar solvents: RAFT dispersion polymerization of benzyl methacrylate, *Polymer Chemistry*, **2015**, *6*, 3054-3062.

(10) Lund, R.; Willner, L.; Richter, D.; Dormidontova, E. E. Equilibrium Chain Exchange Kinetics of Diblock Copolymer Micelles: Tuning and Logarithmic Relaxation, *Macromolecules*, **2006**, *39*, 4566-4575.

(11) Choi, S. H.; Lodge, T. P.; Bates, F. S. Mechanism of Molecular Exchange in Diblock Copolymer Micelles: Hypersensitivity to Core Chain Length, *Physical Review Letters*, **2010**, *104*, 047802.

(12) Choi, S.-H.; Bates, F. S.; Lodge, T. P. Molecular Exchange in Ordered Diblock Copolymer Micelles, *Macromolecules*, **2011**, *44*, 3594-3604.

(13) Lu, J.; Choi, S.; Bates, F. S.; Lodge, T. P. Molecular Exchange in Diblock Copolymer Micelles: Bimodal Distribution in Core-Block Molecular Weights, *ACS Macro Letters*, **2012**, *1*, 982-985.

(14) Zinn, T.; Willner, L.; Pipich, V.; Richter, D.; Lund, R. Effect of Core Crystallization and Conformational Entropy on the Molecular Exchange Kinetics of Polymeric Micelles, *ACS Macro Letters*, **2015**, *4*, 651-655.

(15) Lu, J.; Bates, F. S.; Lodge, T. P. Chain Exchange in Binary Copolymer Micelles at Equilibrium: Confirmation of the Independent Chain Hypothesis, *ACS Macro Letters*, **2013**, *2*, 451-455.

(16) Lu, J.; Bates, F. S.; Lodge, T. P. Remarkable Effect of Molecular Architecture on Chain Exchange in Triblock Copolymer Micelles, *Macromolecules*, **2015**, *48*, 2667-2676.

(17) Lu, J.; Bates, F. S.; Lodge, T. P. Addition of Corona Block Homopolymer Retards Chain Exchange in Solutions of Block Copolymer Micelles, *Macromolecules*, **2016**, *49*, 1405-1413.

(18) Zinn, T.; Willner, L.; Pipich, V.; Richter, D.; Lund, R. Molecular Exchange Kinetics of Micelles: Corona Chain Length Dependence, *ACS Macro Letters*, **2016**, *5*, 884-888.

(19) Ma, Y.; Lodge, T. P. Chain Exchange Kinetics in Diblock Copolymer Micelles in Ionic Liquids: The Role of χ, *Macromolecules*, **2016**, *49*, 9542-9552.

(20) Mueller, E.; Alsop, R. J.; Scotti, A.; Bleuel, M.; Rheinstadter, M. C.; Richtering, W.; Hoare, T. Dynamically Cross-Linked Self-Assembled Thermoresponsive Microgels with Homogeneous Internal Structures, *Langmuir*, **2018**, *34*, 1601-1612.

(21) Dormidontova, E. E. Micellization Kinetics in Block Copolymer Solutions: Scaling Model, *Macromolecules*, **1999**, *32*, 7630-7644.

(22) Halperin, A. On Micellar Exchange: The Role of the Insertion Penalty, *Macromolecules*, **2011**, *44*, 5072-5074.

(23) Halperin, A.; Alexander, S. Polymeric micelles: their relaxation kinetics, *Macromolecules*, **1989**, *22*, 2403-2412.

(24) Haliloğlu, T.; Bahar, I.; Erman, B.; Mattice, W. L. Mechanisms of the Exchange of Diblock Copolymers between Micelles at Dynamic Equilibrium, *Macromolecules*, **1996**, *29*, 4764-4771.

(25) Wang, Y.; Kausch, C. M.; Chun, M.; Quirk, R. P.; Mattice, W. L. Exchange of Chains between Micelles of Labeled Polystyrene-block-poly(oxyethylene) As Monitored by Nonradiative Singlet Energy Transfer, *Macromolecules*, **1995**, *28*, 904-911.

(26) Growney, D. J.; Mykhaylyk, O. O.; Armes, S. P. Micellization and Adsorption Behavior of a Near-Monodisperse Polystyrene-Based Diblock Copolymer in Nonpolar Media, *Langmuir*, **2014**, *30*, 6047-6056.

(27) Cornel, E. J.; van Meurs, S.; Smith, T.; O'Hora, P. S.; Armes, S. P. In Situ Spectroscopic Studies of Highly Transparent Nanoparticle Dispersions Enable Assessment of Trithiocarbonate Chain-End Fidelity during RAFT Dispersion Polymerization in Nonpolar Media, *Journal of the American Chemical Society*, **2018**, *140*, 12980-12988.

(28) Ratcliffe, L. P. D.; Blanazs, A.; Williams, C. N.; Brown, S. L.; Armes, S. P. RAFT polymerization of hydroxy-functional methacrylic monomers under heterogeneous conditions: effect of varying the core-forming block, *Polymer Chemistry*, **2014**, *5*, 3643-3655.

(29) Cunningham, V. J.; Alswieleh, A. M.; Thompson, K. L.; Williams, M.; Leggett, G. J.; Armes, S. P.; Musa, O. M. Poly(glycerol monomethacrylate)-Poly(benzyl methacrylate) Diblock Copolymer Nanoparticles via RAFT Emulsion Polymerization: Synthesis, Characterization, and Interfacial Activity, *Macromolecules*, **2014**, *47*, 5613-5623.

(30) Derry, M. J.; Fielding, L. A.; Warren, N. J.; Mable, C. J.; Smith, A. J.; Mykhaylyk, O. O.; Armes, S. P. In situ small-angle X-ray scattering studies of sterically-stabilized diblock copolymer nanoparticles formed during polymerization-induced self-assembly in non-polar media, *Chemical Science*, **2016**, *7*, 5078-5090.

(31) Blanazs, A.; Madsen, J.; Battaglia, G.; Ryan, A. J.; Armes, S. P. Mechanistic Insights for Block Copolymer Morphologies: How Do Worms Form Vesicles?, *Journal of the American Chemical Society*, **2011**, *133*, 16581-16587.

(32) Choi, S.-H.; Bates, F. S.; Lodge, T. P. Structure of Poly(styrene-b-ethylene-alt-propylene) Diblock Copolymer Micelles in Squalane, *The Journal of Physical Chemistry B*, **2009**, *113*, 13840-13848.

(33) Semsarilar, M.; Ladmiral, V.; Blanazs, A.; Armes, S. P. Anionic Polyelectrolyte-Stabilized Nanoparticles via RAFT Aqueous Dispersion Polymerization, *Langmuir*, **2012**, *28*, 914-922.

(34) Chiefari, J.; Chong, Y. K.; Ercole, F.; Krstina, J.; Jeffery, J.; Le, T. P. T.; Mayadunne, R. T. A.; Meijs, G. F.; Moad, C. L.; Moad, G.; Rizzardo, E.; Thang, S. H. Living free-radical polymerization by reversible addition-fragmentation chain transfer: The RAFT process, *Macromolecules*, **1998**, *31*, 5559-5562.

(35) Moad, G.; Rizzardo, E.; Thang, S. H. Toward living radical polymerization, *Accounts of Chemical Research*, **2008**, *41*, 1133-1142.

(36) Fan, L. X.; Degen, M.; Bendle, S.; Grupido, N.; Ilavsky, J. The Absolute Calibration of a Small-Angle Scattering Instrument with a Laboratory X-ray Source, **2010**, *247*, 012005.

(37) Pedersen, J. S.; Gerstenberg, M. C. Scattering Form Factor of Block Copolymer Micelles, *Macromolecules*, **1996**, *29*, 1363-1365.

(38) Pedersen, J. S.; Schurtenberger, P. Scattering Functions of Semiflexible Polymers with and without Excluded Volume Effects, *Macromolecules*, **1996**, *29*, 7602-7612.

(39) Pedersen, J. S. Form factors of block copolymer micelles with spherical, ellipsoidal and cylindrical cores, *Journal of Applied Crystallography*, **2000**, *33*, 637-640.

(40) Debye, P. Molecular-weight Determination by Light Scattering, *The Journal of Physical and Colloid Chemistry*, **1947**, *51*, 18-32.

(41) Ilavsky, J.; Jemian, P. R. Irena: tool suite for modeling and analysis of small-angle scattering, *Journal of Applied Crystallography*, **2009**, *42*, 347-353.

(42) www.isis.stfc.ac.uk (9 May 2019)

(43) www.mantidproject.org (9 May 2019)

(44) Wignall, G. D.; Bates, F. S. Absolute Calibration of Small-Angle Neutron-Scattering Data, *Journal of Applied Crystallography*, **1987**, *20*, 28-40.

(45) Pedersen, J. S. Form factors of block copolymer micelles with spherical, ellipsoidal and cylindrical cores, *Journal of Applied Crystallography*, **2000**, *33*, 637-640.

(46) Pedersen, J. S.; Gerstenberg, M. C. The structure of P85 Pluronic block copolymer micelles determined by small-angle neutron scattering, *Colloids and Surfaces a-Physicochemical and Engineering Aspects*, **2003**, *213*, 175-187.

(47) Pedersen, J. S.; Svaneborg, C.; Almdal, K.; Hamley, I. W.; Young, R. N. A small-angle neutron and X-ray contrast variation scattering study of the structure of block copolymer micelles: Corona shape and excluded volume interactions, *Macromolecules*, **2003**, *36*, 416-433.

(48) Mark, J.E. *Physical properties of polymers Handbook*; 2nd ed.; Springer, **2007**, p93.

(49) Caudwell, D. R.; Trusler, J. P. M.; Vesovic, V.; Wakeham, W. A. The Viscosity and Density of n-Dodecane and n-Octadecane at Pressures up to 200 MPa and Temperatures up to 473 K, *International Journal of Thermophysics*, **2004**, *25*, 1339-1352.

(50) Arleth, L.; Pedersen, J. S. Scattering vector dependence of the small-angle scattering from mixtures of hydrogenated and deuterated organic solvents, *Journal of Applied Crystallography*, **2000**, *33*, 650-652.

(51) Pedersen, J. S.; Svaneborg, C.; Almdal, K.; Hamley, I. W.; Young, R. N. A Small-Angle Neutron and X-ray Contrast Variation Scattering Study of the Structure of Block Copolymer Micelles: Corona Shape and Excluded Volume Interactions, *Macromolecules*, **2003**, *36*, 416-433.

(52) Pedersen, J. S.; Gerstenberg, M. C. The structure of P85 Pluronic block copolymer micelles determined by small-angle neutron scattering, *Colloids and Surfaces A: Physicochemical and Engineering Aspects*, **2003**, *213*, 175-187.

(53) Zhao, D.; Ma, Y.; Lodge, T. P. Exchange Kinetics for a Single Block Copolymer in Micelles of Two Different Sizes, *Macromolecules*, **2018**, *51*, 2312-2320.

(54) Grillo, I. In Soft Matter Characterization; Borsali, R., Pecora, R., Eds.; Springer Netherlands: Dordrecht, 2008, p 723-782.

(55) Durr, J.; Schempp, S.; Lamparter, P.; Bill, J.; Steeb, S.; Aldinger, F. X-ray and neutron small angle scattering with Si-C-N ceramics using isotopic substitution, *Solid State Ionics*, **1997**, *101*, 1041-1047.

(56) Blanazs, A.; Verber, R.; Mykhaylyk, O. O.; Ryan, A. J.; Heath, J. Z.; Douglas, C. W. I.; Armes, S. P. Sterilizable Gels from Thermoresponsive Block Copolymer Worms, *Journal of the American Chemical Society*, **2012**, *134*, 9741-9748.

(57) Blackman, L. D.; Doncom, K. E. B.; Gibson, M. I.; O'Reilly, R. K. Comparison of photo- and thermally initiated polymerization-induced self-assembly: a lack of end group fidelity drives the formation of higher order morphologies, *Polymer Chemistry*, **2017**, *8*, 2860-2871.

Chapter 4

Copolymer Exchange Between Binary Mixtures of PLMA-PBzMA Spherical Nanoparticles with Different Core Diameters

4.1. Introduction

In contrast to **Chapter 2**, where nanoparticle behaviour is assessed *during* their synthesis via RAFT PISA, this **Chapter** expands on the scope of the in **Chapter 3** discussed thermally-induced diblock copolymer chain exchange process between spherical nanoparticles. The behaviour of relatively small and large PLMA-PBzMA diblock copolymer spheres (with a relatively short and long core-forming PBzMA DP, respectively), and the possibility of copolymer exchange between these species are assessed in this **Chapter**.

It is known that heat treatment can cause block copolymer chain exchange between nanoparticles in non-polar media, as shown in **Chapter 3** and by Lodge and co-workers.[1-6] As stated previously in this Thesis, but nevertheless discussed here again (and expanded) for its importance to the work presented in this **Chapter**, two main mechanisms have been suggested for this phenomenon, (i) chain expulsion/insertion and (ii) micelle fusion/fission.[6-11] Theoretical studies by Halperin[8,9] and experimental observations made by both Lund and co-workers[12,13] and Lodge and co-workers[1-4,6,14-16] strongly suggest that the former mechanism is appropriate for diblock copolymer micelles (a.k.a. sterically-stabilised nanoparticles). However, Armes and co-workers have suggested that particle-particle fusion might play an important role during certain RAFT PISA synthesis. Indeed, such a mechanism seems to be the most likely explanation for the *in situ* self-assembly of sterically-stabilised diblock copolymer worms during RAFT PISA. This is because worms are more likely to be obtained at higher copolymer concentrations.[17-21] As discussed in **Chapter 3**, both the chain expulsion/insertion mechanism and micelle fusion/fission mechanism may well play important roles during nanoparticle preparation via RAFT PISA.

The micellar fusion/fission mechanism is believed to play an important role during the morphological transitions of nanoparticles. A good example is the *reversible* worm-to-sphere transition that occurs on heating PLMA-PBzMA copolymer worms in non-polar media.[21] Heating causes surface plasticisation of the core-forming PBzMA block, which leads to a subtle reduction in the packing parameter and results in worm fission to form spherical nanoparticles. The worm morphology is regenerated when the hot dispersion is cooled to

room temperature. However, regeneration only occurs at sufficiently high copolymer concentration, which is consistent with the micellar fusion/fission mechanism. Interestingly, this morphological transition is accompanied by physical (de)gelation. Diblock copolymer worms form a physical gel at room temperature, but a low-viscosity free-flowing dispersion of spheres is obtained on heating to above 50 °C. Originally, worm entanglements were believed to cause gelation at room temperature.[22] However, a recent study reports that percolation theory can explain worm gelation, which suggests that multiple worm-worm contacts may be sufficient to form a free-standing gel.[23]

In this **Chapter**, we examine copolymer exchange between a series of binary mixtures of spherical nanoparticles with differing mean diameters. Poly(lauryl methacrylate)-poly(benzyl methacrylate) ($PLMA_{39}$-$PBzMA_x$) nanoparticles were prepared via RAFT PISA in *n*-dodecane. The DP of the core-forming $PBzMA_x$ block was either 97 or 294; it is known that a higher core-forming block DP leads to larger spheres, provided that a sufficiently long stabiliser block DP is used to ensure that there is no evolution in copolymer morphology.[19] For these two diblock copolymers, spherical nanoparticles with core diameters of 21 ± 2 nm and of 48 ± 5 nm were obtained, as determined by SAXS analysis. The motivation of the research described in this **Chapter** is to further understand the behaviour of spherical nanoparticles at elevated temperatures in respect to the core-forming bock DP. Additionally, we want to answer the question if two separate species of diblock copolymer spheres can simultaneously be used in engine oils, or if their coexistence in a single dispersion is complicated by copolymer chain exchange.

4.2. Experimental

4.2.1 Materials

Lauryl methacrylate and benzyl methacrylate was purchased from Sigma Aldrich (UK) and passed through basic alumina prior to use. Tert-Butyl peroxy-2-ethylhexanoate (Trigonox 21S or T21s) initiator was supplied by AkzoNobel (The Netherlands). *n*-Dodecane, THF, triethylamine, butylated hydroxytoluene and 2,2-azobis(2-methylpropionitrile) (AIBN) were purchased from Sigma-Aldrich (UK). 4-Cyano-4-((2-phenylethanesulfonyl)thiocarbonylsulfanyl)pentanoic acid (PETTC) was prepared in-house according to a well-established protocol.[24] d_2-Dichloromethane (CD_2Cl_2) was obtained from Cambridge Isotope Laboratory (USA), while d-chloroform ($CDCl_3$) was purchased from VWR (UK).

4.2.2 Methods

4.2.2.1.Synthesis of Spherical $PLMA_{39}$-$PBzMA_x$ Diblock Copolymer Nanoparticles via RAFT Dispersion Polymerisation

A $PLMA_{39}$ macro-CTA was prepared as described in **Chapter 3.2.2.1**. Subsequently, benzyl methacrylate (BzMA; 0.33 ml 0.34 g, 1.95 mmol) was used for the chain extension of a $PLMA_{39}$ macro-CTA (0.20 g, 0.019 mmol; target DP = 100) in 2.17 g *n*-dodecane at 20% w/w solids, using T21s initiator (16 µl of a 10% v/v solution; macro-CTA/initiator molar ratio = 3.0). This reaction mixture was heated to 90 °C for 16 h and a final BzMA conversion of 97% was determined by ^{1}H NMR analysis of the crude reaction mixture diluted in $CDCl_3$ (to ensure dissolution of the diblock copolymer nanoparticles), see **Figure 4.1** and **Equation 4.1**. The integrated BzMA monomer vinyl signals at 5.59 and 6.17 ppm were compared to that of the integrated methoxy signal assigned to the polymerised BzMA repeat units at 4.77-5.00 ppm). A PBzMA DP of 300 was targeted at 20% w/w solids using $PLMA_{39}$ macro-CTA (0.10 g, 0.01 mmol), BzMA (0.50 ml, 0.52 g, 1.70 mmol) of BzMA, *n*-dodecane (2.46 g) and 8 µl of a 10% v/v solution of T21S. A final conversion of 98% was obtained, yielding a final PBzMA core-forming block DP of 294.

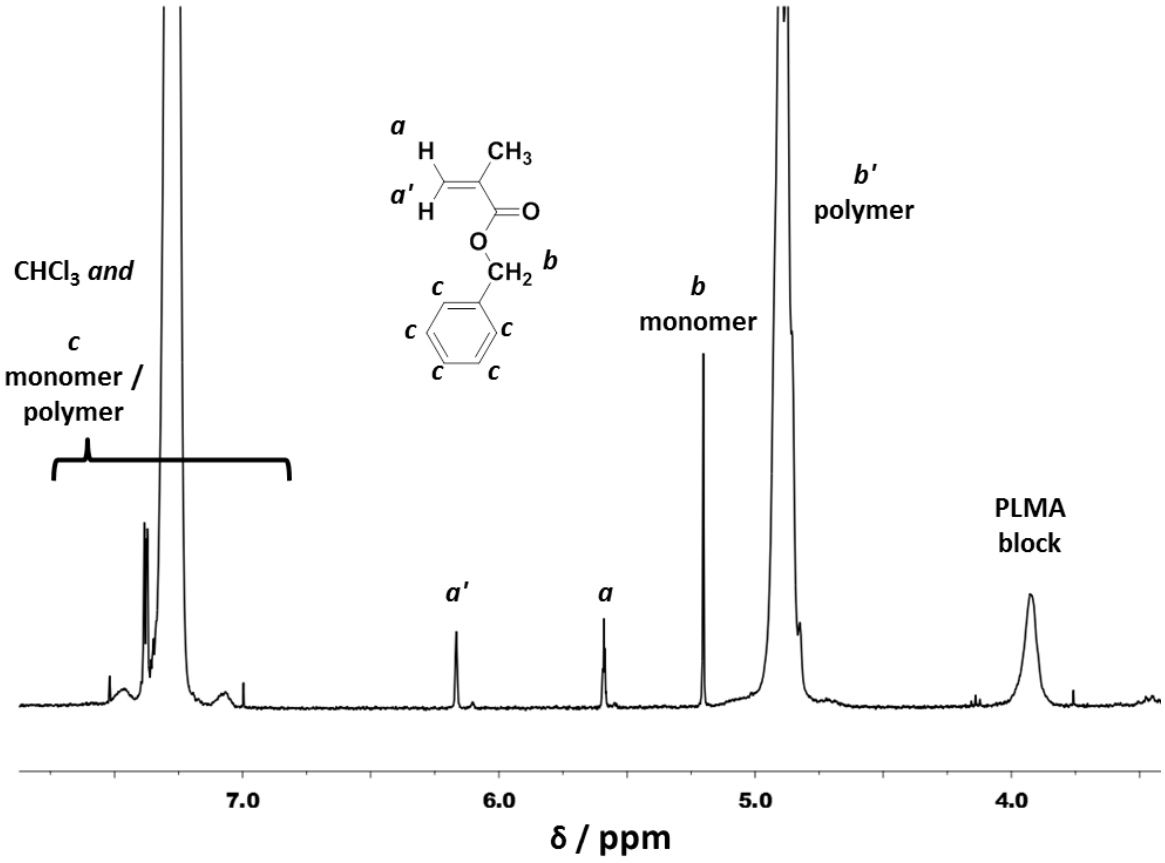

Figure 4.1. Representative proton NMR spectrum recorded for the crude reaction mixture of $PLMA_{39}$-$PBzMA_{294}$ nanoparticles, dissolved in $CDCl_3$ prior to analysis. Monomer conversions were calculated according to **Equation 4.1**, using the integrated monomer vinyl signals (*a* and *a'*) and the integrated monomer and polymer methyl signals (b_{monomer} and b'_{polymer}).

$$\textbf{BzMA conversion}\ (\%) = \mathbf{1} - \frac{\boldsymbol{a} + \boldsymbol{a}'}{\boldsymbol{b}_{\textbf{monomer}} + \boldsymbol{b}'_{\textbf{polymer}}} \times \mathbf{100}\% \quad (\mathbf{4.1})$$

4.2.2.2. Copolymer Characterisation

THF GPC. Molecular weight distributions were assessed by GPC using THF as an eluent. The instrument setup and calibration standards are described in **Chapter 3.2.2.3.**

NMR spectroscopy. Proton NMR spectra were recorded in $CDCl_3$ or CD_2Cl_2 using a Bruker

AV3HD-400 or 500 MHz spectrometer. Spectra were analysed using TopSpin version 3.1 software. For the $PLMA_{39}$-$PBzMA_x$ synthesis, the final BzMA monomer conversion was determined by dissolution of a small volume of the crude dispersion in $CDCl_3$ prior to analysis as described in **Section 4.2.2.1.**

Transmission Electron Microscopy (TEM). Images were obtained following a protocol as described in **Chapter 2.2.2.6**.

Small-angle X-ray scattering (SAXS). Experiments were performed at the ID02 beamline at the ESRF in Grenoble, France. A monochromatic X-ray beam (λ = 0.0995 nm) and a 2D SAXS detector (Rayonix MX-170HS) were used for these studies. A q range of 0.012–1.5 nm^{-1} was employed for measurements, where q to the modulus of the scattering vector (see **Equation 4.4**). For time-resolved measurements, a glass capillary of 2 mm thickness was inserted into a heating stage (HFSX350-CAP, Linkam Scientific Instruments, Tadworth, UK). X-ray scattering data were reduced (integration, normalisation, and background subtraction) using standard routines available at the ID02 beamline. The scattering intensity of water was used for absolute scale calibration of the X-ray scattering patterns. Data were fitted using either a well-known spherical micelle model[25-27] or the Debye function[28] for dissolved PLMA macro-CTA, after normalisation and background subtraction using the Irena package[29] for Igor Pro. These models are described in **Chapter 3.2.3.** for dissolved $PLMA_{39}$ chains and $PLMA_{39}$-$PMMA_x$ spheres. The same model was used for $PLMA_{39}$-$PBzMA_x$ spheres, block volumes and SLD of the components were calculated as described in **Chapter 3.2.3.** and summarised in **Table 4.1**. Satisfying fits to the Scattering data were achieved with fixed values for the block volumes and SLDs, all other variables (such as core radius, stabiliser R_g, polymer volume fraction etc.) were allowed to vary.

Table 4.1. Summary of mean block volumes, densities and X-ray SLDs used for SAXS modeling. Mean block volumes and SLDs were calculated by assuming that the thermal expansion coefficients of PLMA and PBzMA were equal to that reported by Fetters and co-workers for poly(*n*-butyl methacrylate) and polystyrene, respectively. Here, high molecular weight densities were assumed for PLMA and *both* PBzMA blocks.[30]

Polymer block	Temperature / °C	Block volume / Å^3	Density / g cm^{-3}	X-ray SLD (× 10^{-6}) / Å^{-2}
$PLMA_{39}$	20	17 716	0.930	8.809
	25	17 766	0.927	8.780
	50	18 021	0.914	8.657
	75	18 283	0.901	8.534
	100	18 553	0.888	8.411
	125	18 830	0.875	8.288
	150	19 117	0.862	8.165
$PBzMA_{294}$	20	72 965	1.179	10.67
	25	73 127	1.176	10.65
	50	73 951	1.163	10.53
	75	74 794	1.150	10.41
	100	75 656	1.137	10.29
	125	76 538	1.124	10.17
	150	77 441	1.111	10.06
$PBzMA_{97}$	20	24 073	1.179	10.67
	25	24 127	1.176	10.65
	50	24 399	1.163	10.53
	75	24 677	1.150	10.41
	100	24 961	1.137	10.29
	125	25 252	1.124	10.17
	150	25 550	1.111	10.06
n-Dodecane	20	-	0.570	7.320
	25	-	0.746	7.283
	50	-	0.727	7.098
	75	-	0.709	6.922
	100	-	0.690	6.737
	125	-	0.671	6.551
	150	-	0.651	6.356

4.3. Results and Discussion

4.3.1. Preparation of PLMA-PBzMA Spheres

Spherical $PLMA_{39}$-$PBzMA_x$ nanoparticles (where x is either 97 or 294) were prepared at 20% w/w using a well-established RAFT PISA protocol in non-polar media.[17,19,21,31] A $PLMA_{39}$ precursor (macro-CTA) was chain-extended with BzMA monomer and once a critical PBzMA core DP is attained, micellar nucleation occurs (**Figure 4.2**). Both polymerisations led to high BzMA monomer conversions (>97%) according to proton NMR analysis of the crude reaction mixtures (diluted in $CDCl_3$ to ensure nanoparticle dissolution) (**Figure 4.1**.) Higher target PBzMA core DPs lead to larger spherical particles when utilising a sufficiently long macro-CTA.[19] In this case, a PBzMA core DP of 97 led to spherical particles with a mean core diameter of 21 ± 2 nm. Similarly, a PBzMA core DP of 294 formed spheres with a mean core diameter of 48 ± 5 nm, according to SAXS analysis.

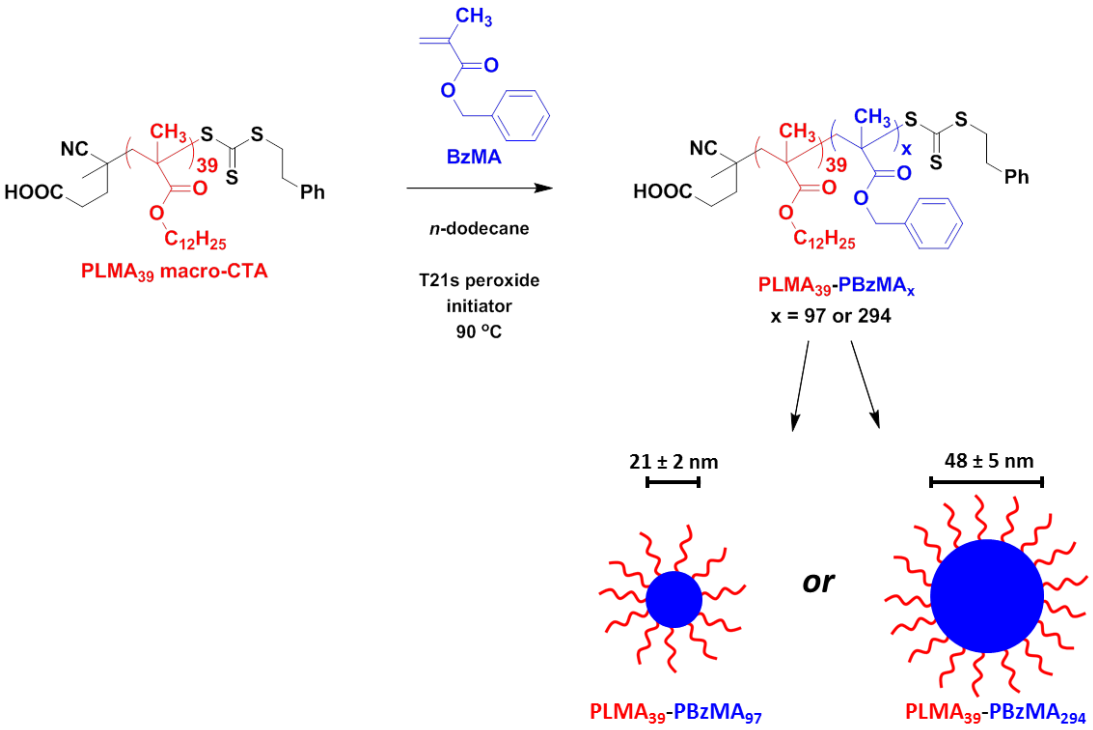

Figure 4.2. A $PLMA_{39}$ macro-CTA was chain-extended with BzMA monomer in *n*-dodecane via RAFT PISA to form sterically-stabilised spherical nanoparticles. SAXS analysis indicated that final PBzMA block DPs of 97 and 294 resulted in mean core diameters of 21± 2 nm and 48 ± 5 nm, respectively.

Block copolymer nanoparticles were dissolved in THF prior to GPC analysis for assessment of the molecular weight distribution and blocking efficiency for this PISA formulation (**Figure 4.3**). Unimodal molecular weight distributions were obtained ($M_w/M_n \leq 1.20$), indicating good living character for this RAFT PISA formulation. A clear shift to lower retention time for each of the two diblock copolymers compared to that for the initial $PLMA_{39}$ macro-CTA indicated high blocking efficiencies.

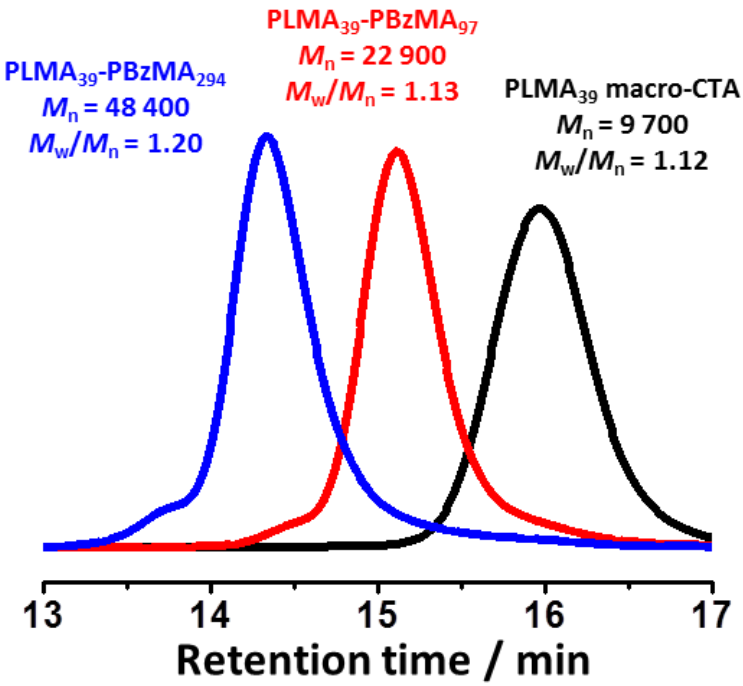

Figure 4.3. Area-normalised THF GPC traces recorded using a refractive index detector for a $PLMA_{39}$ macro-CTA, and corresponding $PLMA_{39}$-$PBzMA_{97}$ and $PLMA_{39}$-$PBzMA_{294}$ diblock copolymers. Unimodal molecular weight distributions were obtained, indicating good control over the RAFT dispersion polymerisation of BzMA. A clear shift towards lower retention times indicates high blocking efficiencies.

4.3.2. Variable temperature SAXS analysis on PLMA-PBzMA spheres

It is known that diblock copolymer chain exchange can occur between spherical nanoparticles in non-polar media (**Chapter 3**). This process is sensitive to both temperature and the core-forming block DP.[3,6] In this study, we assess chain exchange between spherical nanoparticles of differing diameters and core-forming block DPs. A prerequisite for thermally-induced

chain exchange at low copolymer concentration is expulsion of the core-forming block from the nanoparticle core. Moreover, the nanoparticle cores should become progressively more solvated with hot solvent on heating such dispersion. Such core solvation is likely to aid chain expulsion/insertion, making the thermally-activated redistribution of copolymer chains more likely. $PLMA_{39}$-$PBzMA_{97}$ and $PLMA_{39}$-$PBzMA_{294}$ spheres were diluted to 1.0% w/w with *n*-dodecane, and subsequently analysed by SAXS during a 25 °C-150 °C-25 °C thermal cycle (**Figure 4.4, and Tables 4.2 and 4.3**). Heating $PLMA_{39}$-$PBzMA_{97}$ spheres alone led to a progressive change in their scattering pattern, which returned to its original form after cooling from 150 °C to 25 °C. Such changes indicated significant nanoparticle core solvation and/or formation of a molecularly dissolved block copolymer fraction. In contrast, heating the larger $PLMA_{39}$-$PBzMA_{294}$ spheres up to 150 °C led to almost no change in their scattering pattern. This suggests that the larger spheres are more robust on heating, and their cores are much less plasticised by hot solvent than the smaller spheres, with no micelle dissociation occurring at 150 °C. Moreover, initial spherical particle diameters were recovered on cooling in both cases, indicating good thermoreversibility.

Scattering patterns were fit using a well-known spherical micelle model[25,27] (see **Chapter 3**). Satisfactory data fits could be achieved by assuming that the change in density of the corona and core-forming block were equal to that reported for poly(*n*-butyl methacrylate) and polystyrene respectively (see **Table 4.1**).[32] Such SAXS pattern fits indicated minimal change in the mean diameter for $PLMA_{39}$-$PBzMA_{97}$ and $PLMA_{39}$-$PBzMA_{294}$ spheres on heating to 150 °C. Both types of nanoparticles could be fitted by assuming no solvent was present in their cores at 25 °C (**Figure 4.4**). However, a broad peak is visible in the high q range (around $q = 0.8$ nm^{-1}), this feature is especially visible in the scattering patterns of the larger $PLMA_{39}$-$PBzMA_{294}$ spheres (scattering of smaller features from the $PLMA_{39}$-$PBzMA_{97}$ spheres might hide this broad peak in the scattering pattern of these species). Unfortunately, this feature could not be well-fitted using the spherical micelle model. We can speculate that this feature arises from the brush like nature of the PLMA stabiliser block (i.e. this peak might provide information about the distance between the stabiliser chains on the surface of the nanoparticle). More research is required to understand this feature of the scattering pattern; fortunately, the rest of the scattering pattern at lower q could be well-fitted to gain insights into the spherical particle core-radius.

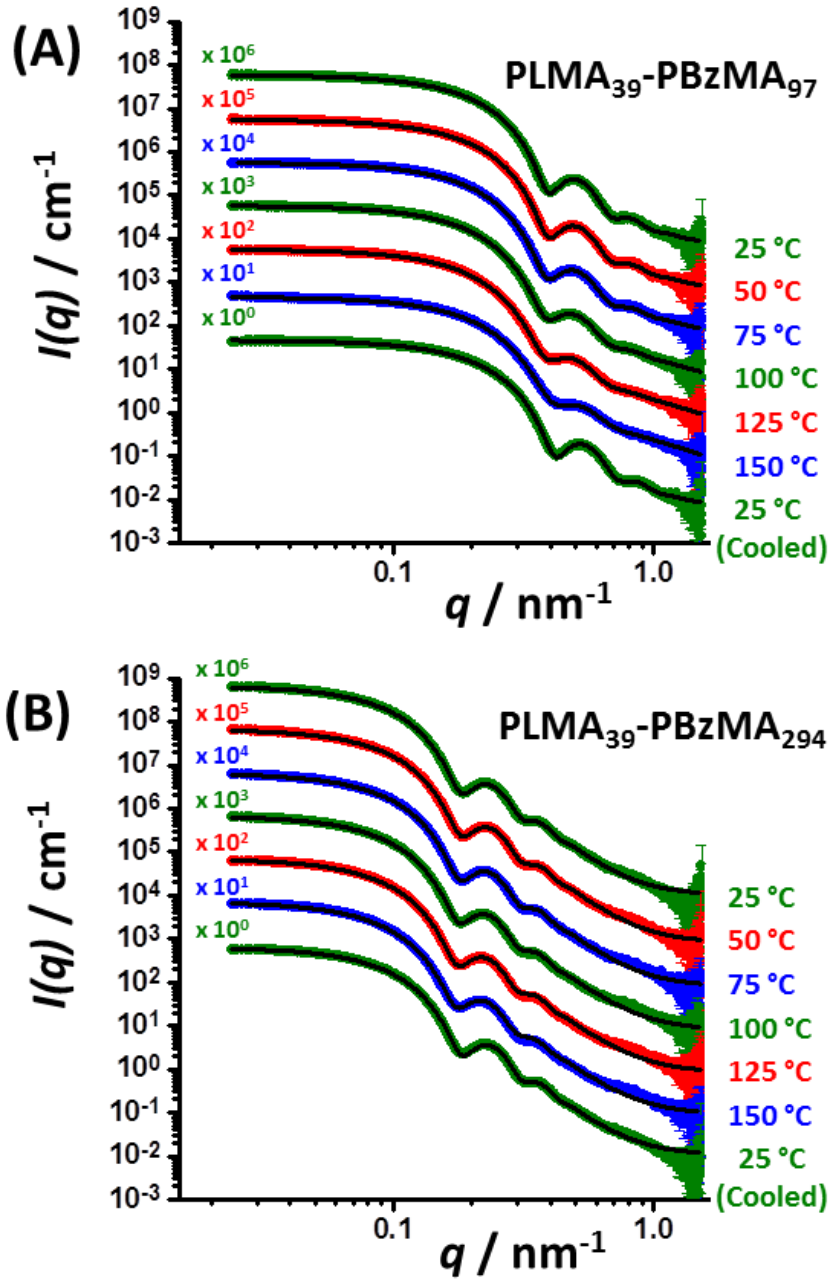

Figure 4.4. SAXS scattering patterns of (A) $PLMA_{39}$-$PBzMA_{97}$ and (B) $PLMA_{39}$-$PBzMA_{294}$ spheres recorded at various temperatures. Heating the latter nanoparticles up to 150 °C causes minimal change in their scattering pattern. Differences between the scattering patterns recorded at 25 °C and 150 °C for the smaller $PLMA_{39}$-$PBzMA_{97}$ spheres indicate significant core solvation and/or molecularly dissolved block copolymer formation. Annealed dispersions were cooled to 25 °C before collecting the final scattering pattern. Black traces indicate data fits obtained using a well-known spherical micelle model[25,27].

Table 4.2. SAXS data fits recorded for $PLMA_{39}$-$PBzMA_{97}$ spherical nanoparticles at various temperatures from 25 °C to 150 °C. $PLMA_{39}$ and $PBzMA_{97}$ core volumes were calculated for each temperature by assuming that the thermal expansion coefficients of PLMA and PBzMA were equal to that reported by Fetters and co-workers for poly(*n*-butyl methacrylate) and polystyrene, respectively.[30]

Temperature / °C	Concentration % v/v	Core diameter / nm	Shell R_g / nm	Core solvation / %	Overall diameter / nm
25[a]	0.69	21.1 ± 1.7	2.0	0	29.0
50	0.60	21.2 ± 1.7	2.0	14	29.2
75	0.57	21.4 ± 1.9	2.0	29	29.4
100	0.55	21.5 ± 2.1	2.0	43	29.5
125	0.53	21.5 ± 2.3	1.9	54	29.3
150	0.45	20.4 ± 2.4	2.0	63	28.2
25[b]	0.60	19.9 ± 1.6	2.0	0	27.9

[a]As prepared via RAFT PISA.
[b]After cooling from 150 °C to 25 °C.

Table 4.3. SAXS data fits recorded for $PLMA_{39}$-$PBzMA_{294}$ spherical nanoparticles at various temperatures from 25 °C to 150 °C. $PLMA_{39}$ and $PBzMA_{294}$ core volumes were calculated for each temperature as described in **Table 4.2**.[30]

Temperature / °C	Concentration % v/v	Core diameter / nm	Shell R_g / nm	Core solvation / %	Overall diameter / nm
25[a]	0.78	48.1 ± 4.9	2.0	0	56.1
50	0.75	48.1 ± 4.9	2.0	0	56.1
75	0.68	48.6 ± 5.0	2.0	0	56.6
100	0.66	49.1 ± 5.1	2.0	0	57.1
125	0.64	49.6 ± 5.2	2.0	0	57.6
150	0.60	50.1 ± 5.4	2.0	0	58.1
25[b]	0.76	48.0 ± 4.8	1.9	0	55.8

[a]As prepared via RAFT PISA.
[b]After cooling from 150 °C to 25 °C.

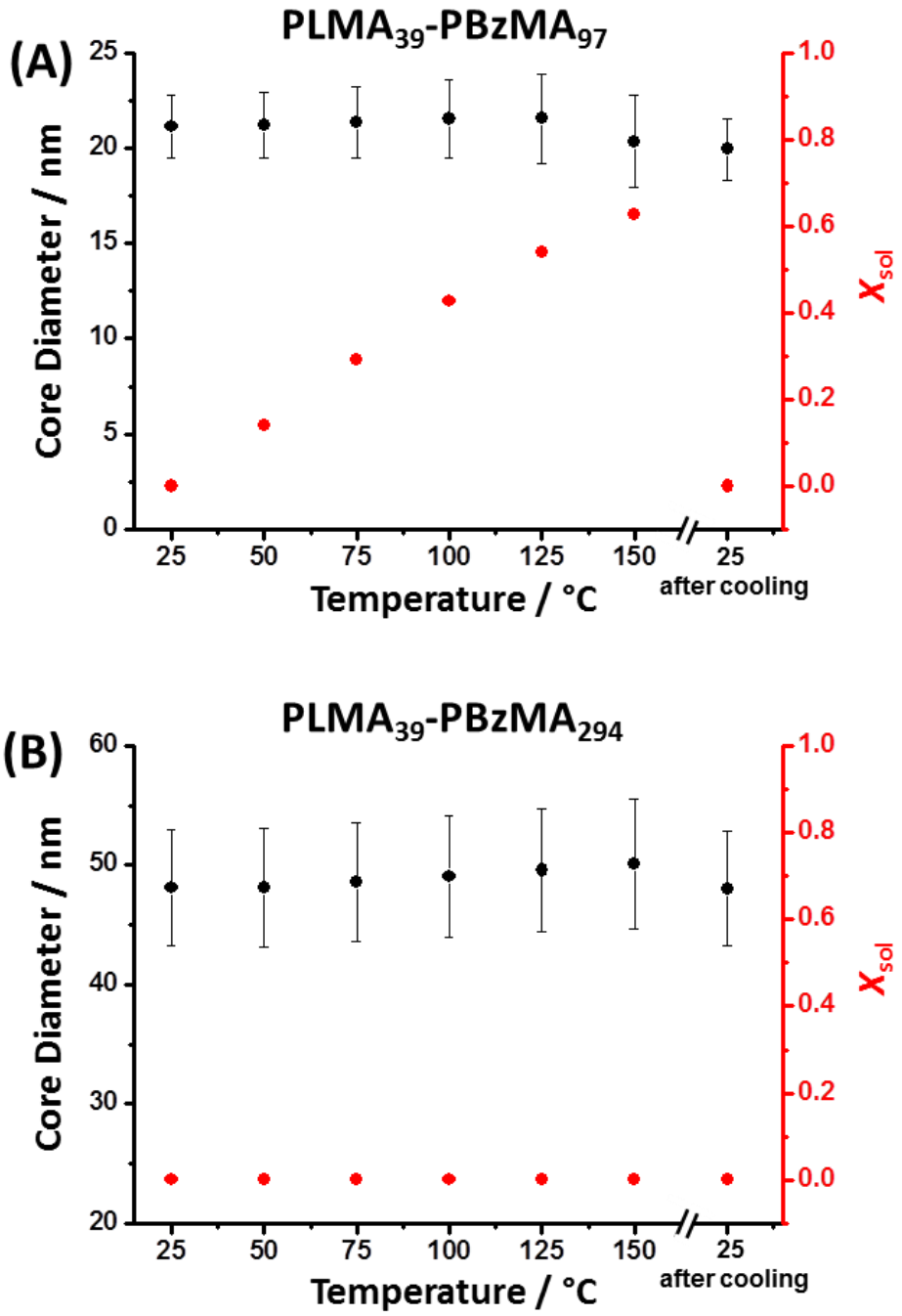

Figure 4.5. Core diameters and solvent volume fraction (X_{sol}) in the nanoparticle cores obtained by variable temperature SAXS analysis for (a) $PLMA_{39}$-$PBzMA_{97}$ and (b) $PLMA_{39}$-$PBzMA_{294}$. The spherical core diameter remains constant for both nanoparticles when heated. However, progressively higher X_{sol} values are observed on heating for $PLMA_{39}$-$PBzMA_{97}$. On cooling to 25 C, the original X_{sol} value is obtained. In contrast, the $PLMA_{39}$-$PBzMA_{294}$ exhibit no discernible change in X_{sol} on heating to 150 °C.

As expected, SAXS analysis indicated progressive core solvation on heating the smaller spheres (**Figure 4.5**). However, this was not observed for the larger $PLMA_{39}$-$PBzMA_{294}$ spheres at 150 °C. Returning the $PLMA_{39}$-$PBzMA_{97}$ spheres to 25 °C led to complete desolvation of the core-forming chains. The continued existence of similar-sized nanoparticles at 150 °C, despite significant core solvation, implies a reduction in aggregation number (N_{agg}). This parameter was calculated using **Equation 4.2**. Here, X_{sol} is the volume fraction of solvent within the nanoparticle core and V_m is the volume occupied by an individual PBzMA block.

$$N_{agg} = \frac{\frac{4}{3}\pi R^3 \times (1 - X_{sol})}{V_m} \quad (4.2)$$

The calculated N_{agg} values were plotted against temperature for both $PLMA_{39}$-$PBzMA_{97}$ and $PLMA_{39}$-$PBzMA_{294}$ spheres (**Figure 4.6**). A significant reduction in N_{agg} from 204 to 65 was observed for the $PLMA_{39}$-$PBzMA_{97}$ spheres on heating to 150 °C. Returning to 25 °C produced spheres with a slightly lower N_{agg} than the original nanoparticles. In contrast, the larger $PLMA_{39}$-$PBzMA_{294}$ spheres exhibited a modest increase in N_{agg} at 150 °C. However, this might be an artefact owing to thermal expansion. Nanoparticle core and corona volumes at each temperatures were calculated assuming that the change in mass density is equal to that reported for polystyrene and poly(*n*-butyl methacrylate) respectively (**Table 4.1**), ideally the thermal expansion of these components should be measured (for example by variable temperature helium pycnometry) to avoid such artefacts.[32] In principle, N_{agg} should be reduced on heating owing to a formation of a fraction of molecularly dissolved chains at higher temperatures.[33] Therefore, it is likely that the N_{agg} actually remains constant for the $PLMA_{39}$-$PBzMA_{294}$ spheres when heated to 150 °C. These results suggest that the smaller $PLMA_{39}$-$PBzMA_{97}$ spheres undergo micelle disassociation to form molecularly dissolved chains, whereas the larger $PLMA_{39}$-$PBzMA_{294}$ spheres do not when heated to 150 °C. Moreover, to support this micellar disassociation process, we can see that the polymer volume fraction reduces upon heating (**Table 4.2 and 4.3**). This indicates that the fraction of aggregated polymer chains (into spherical nanoparticles) decreases, and that a fraction of

molecular dissolved chains gradually appears increases with temperature. As expected, this decrease in polymer volume fraction is more prominent for the smaller $PLMA_{39}$-$PBzMA_{97}$ spheres than the block copolymer spheres with the longer core-forming block. However, we should note that the original volume fraction is not achieved after returning to 25 °C. This is especially prominent for the smaller spheres. This indicates that there might still be a fraction of molecular dissolved block copolymer chains present. It would be likely that the particles return to their original dimensions over time; more research is required to investigate this. Interestingly, these observations agree with the strong DP dependence for the chain expulsion/insertion mechanism, as reported by Lodge and co-workers for PEP-PS block copolymers in squalane,[3,6] and the TR-SANS studies of copolymer chain exchange between PLMA-PMMA spherical nanoparticles described in **Chapter 3**.

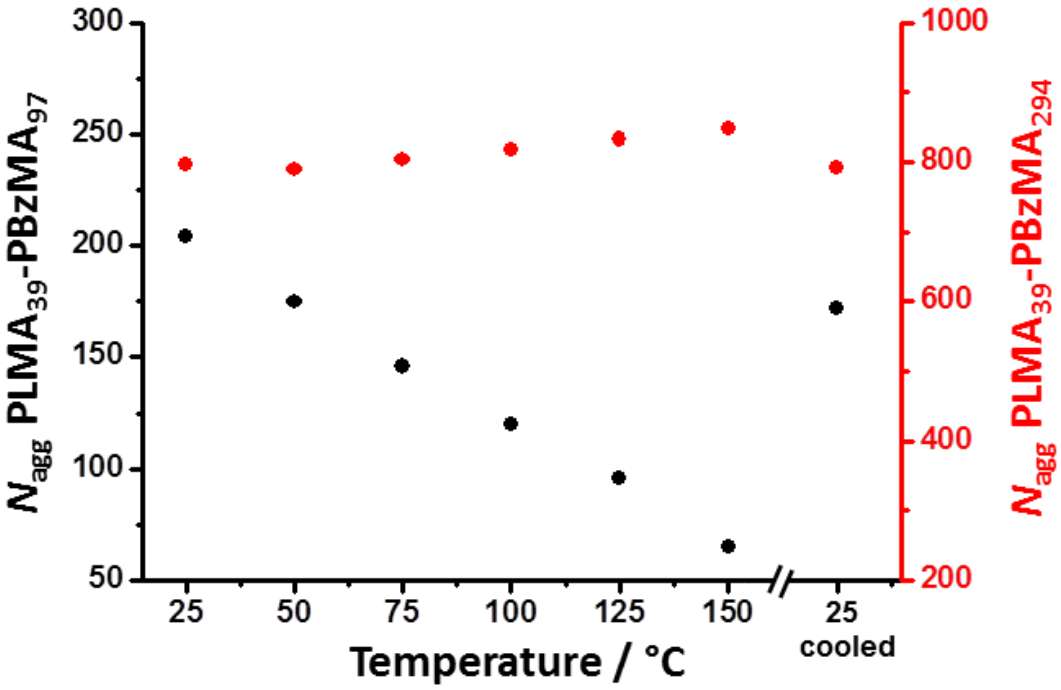

Figure 4.6. Temperature dependence of aggregation number (N_{agg}) determined by SAXS analysis at various temperatures for 1.0% w/w dispersions of (black) $PLMA_{39}$-$PBzMA_{97}$ and (red) $PLMA_{39}$-$PBzMA_{294}$ spheres. The former spheres exhibit a significant reduction in N_{agg} on heating while the latter exhibit minimal change in this parameter.

4.3.2. Particle-particle fusion of $PLMA_{39}$-$PBzMA_{97}$ and $PLMA_{39}$-$PBzMA_{294}$ spheres

A 1:1 v/v binary mixture of $PLMA_{39}$-$PBzMA_{97}$ and $PLMA_{39}$-$PBzMA_{294}$ spheres was heated to 150 °C for 1 h at 1.0 % w/w to examine the possibility of thermally-activated exchange of copolymer chains between such nanoparticles. TEM analysis confirmed a well-defined spherical morphology for the initial individual nanoparticles prior to heating. The binary dispersion exhibited two nanoparticle populations prior to thermal annealing. Interestingly, TEM analysis of this binary mixture after heating to 150 °C for 1 h indicated a single population of spherical nanoparticles exhibiting an intermediate mean particle diameter (**Figure 4.7**).

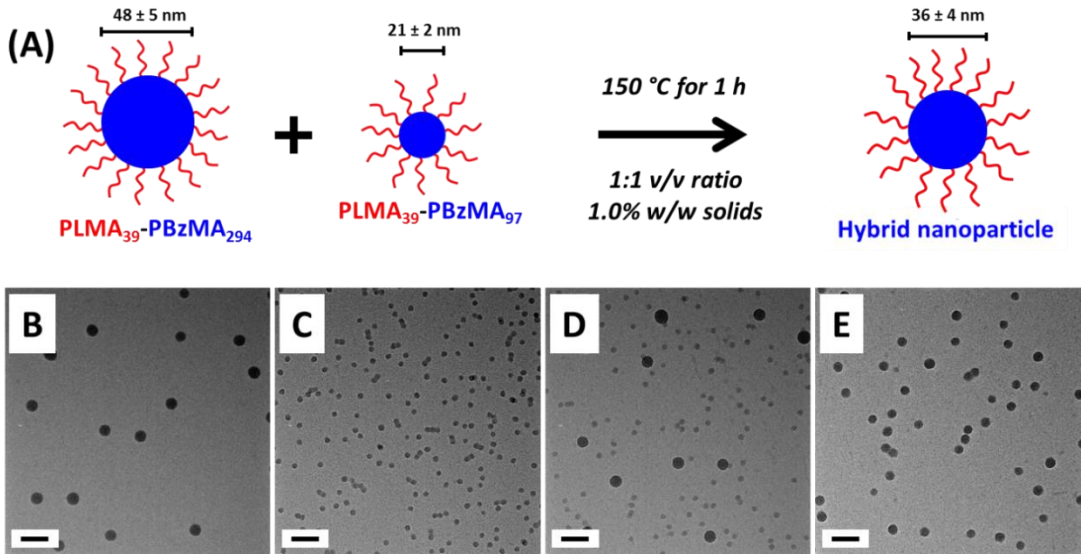

Figure 4.7. (A) Schematic representation of the formation of hybrid nanoparticles by heating a binary mixture of $PLMA_{39}$-$PBzMA_{294}$ spheres (SAXS core-diameters of 48 ± 5 nm) and $PLMA_{39}$-$PBzMA_{97}$ spheres (SAXS core diameter 21 ± 2 nm) in a 1:1 v/v ratio at 1.0% w/w to 150 °C for 1 h. The final hybrid nanoparticles have an intermediate SAXS core diameter of 36 ± 4 nm. (Bottom) TEM images of (B) $PLMA_{39}$-$PBzMA_{294}$ spheres, (C) $PLMA_{39}$-$PBzMA_{97}$ spheres, (D) 1:1 v/v mixture of the former two spherical nanoparticles before heating, two distinct populations of spherical nanoparticles are visible within this dispersions, (E) the final hybrid spherical nanoparticles formed by entropic mixing after heating to 150 °C for 1 h. All scale bars correspond to 100 nm.

TEM studies were further supported by SAXS analysis. SAXS patterns recorded for the two initial dispersions, their 1:1 v/v binary mixture and the final hybrid nanoparticles exhibit zero gradients in the low *q* region (**Figure 4.8**). This suggests a spherical morphology for each of the initial dispersions and also the newly-formed *hybrid* nanoparticles. Fitting the SAXS scattering patterns for the two initial dispersions to a well-known spherical micelle model[25,27] (see **Chapter 3**) indicated mean core diameters of 21 ± 2 nm and 48 ± 4.9 nm for the initial $PLMA_{39}$-$PBzMA_{94}$ and $PLMA_{39}$-$PBzMA_{297}$ nanoparticles, respectively. The SAXS scattering pattern recorded for the initial binary dispersion could be well-fitted using the two predetermined particle size distributions by simply varying the nanoparticle volume fractions (**Table 4.4**).

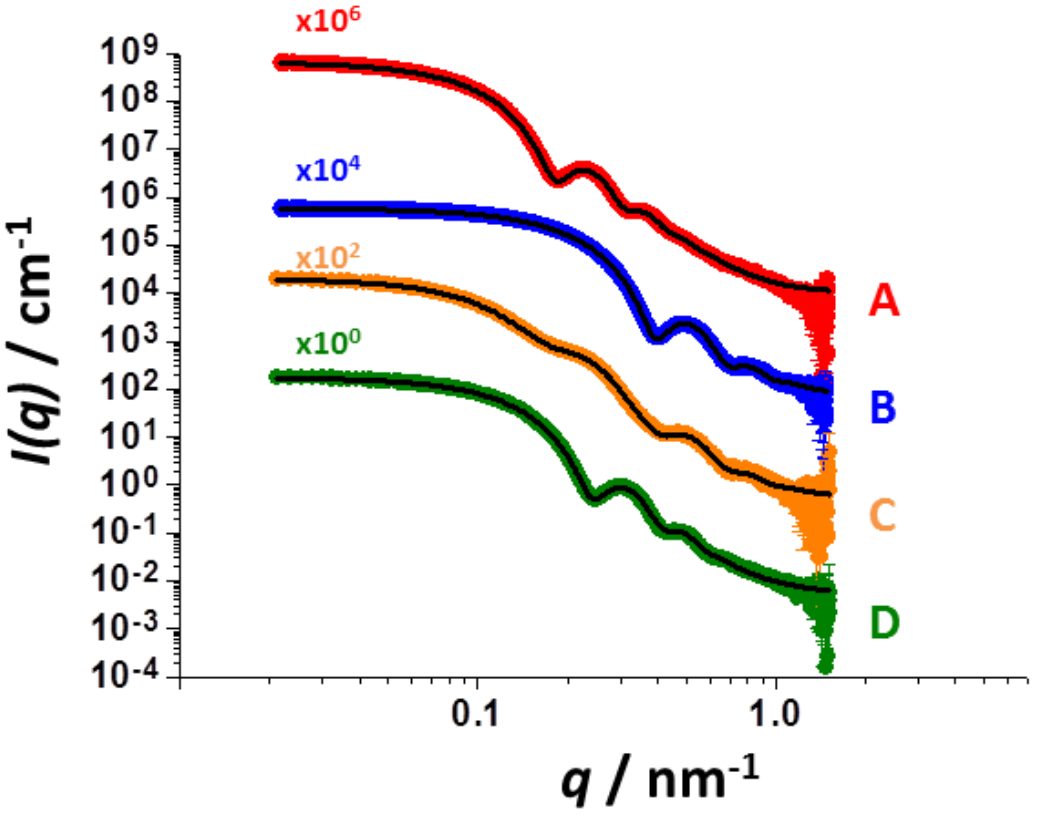

Figure 4.8. SAXS patterns recorded at 22 °C for 1.0 % w/w dispersions of: (A) $PLMA_{39}$-$PBzMA_{294}$ and (B) $PLMA_{39}$-$PBzMA_{97}$ spherical nanoparticles, (C) a binary mixture (1:1 v/v ratio) of these two dispersions before thermal annealing and (D) the hybrid nanoparticles formed after thermal annealing at 150 °C for 1 h. Black traces indicate fits to the data obtained using a well-known spherical micelle model[25,27].

TEM studies confirmed that annealing the binary dispersion at 150 °C for 1 h produced spherical nanoparticles of intermediate size. SAXS analysis clearly supports this finding, as the local minimum in the scattering curve falls between that of the two minima observed for the initial spherical nanoparticles. The SAXS scattering pattern obtained for these hybrid nanoparticles was fitted using a well-known spherical micelle model with a mean PBzMA core volume calculated from the known proportions of the two nanoparticle populations (**Table 4.4**). Assuming full entropic mixing, this fit to the data gave a mean *hybrid* core diameter of 36 ± 3 nm, which is intermediate between that of the two initial PLMA-PBzMA nanoparticle core diameters.

Table 4.4. Summary of SAXS fitting parameters for the initial $PLMA_{39}$-$PBzMA_{97}$ and $PLMA_{39}$-$PBzMA_{294}$ dispersions at 25 °C, a 1:1 v/v binary dispersion of these two types of nanoparticles before annealing and the hybrid nanoparticles formed after annealing this binary mixture at 150 °C for 1 h. The latter two entries were both analysed at 20 °C.

Formulation	**PBzMA block volume / Å^3**	**Concentration / % v/v**	**$PBzMA_x$ core diameter / nm**	**$PLMA_{39}$ shell R_g / nm**
$PLMA_{39}$-$PBzMA_{294}$	73 127	0.77	48.1 ± 4.9	2.0
$PLMA_{39}$-$PBzMA_{97}$	24 127	0.69	21.1 ± 1.7	2.0
Binary mixture (1:1 v/v ratio)	72 965 + 24 073	0.22 + 0.22	48.1 ± 4.9 + 21.1 ± 1.7	2.0
Hybrid nanoparticles	51 718	0.48	36 ± 3	1.93

*All data were fitted assuming no solvent is present in the nanoparticle cores and using a fixed $PLMA_{39}$ block volume of 17716 Å^3.

4.3.3. TR-SAXS Studies on PLMA-PBzMA Particle Fusion

Given the relatively low copolymer concentrations, it seems likely that these hybrid nanoparticles are formed via the chain expulsion/insertion mechanism, rather than by the micelle fusion/fission mechanism. This hypothesis is supported by experimental studies by Lodge and co-workers[3,6] and theoretical studies by Halperin[8,9]. The formation of such hybrid nanoparticles at elevated temperatures is driven by entropic mixing. Moreover, the SAXS observations of core solvation and a significant reduction in N_{agg} on heating $PLMA_{39}$-$PBzMA_{97}$ spheres strongly suggests the likelihood of thermally-induced copolymer chain exchange between these smaller nanoparticles. However, chain expulsion is likely to be much more demanding for the larger $PLMA_{39}$-$PBzMA_{294}$ spheres, because minimal core solvation and no reduction in N_{agg} were observed on heating in this case. To explore the particle-particle fusion mechanism, time-resolved SAXS (TR-SAXS) was performed while heating a 1:1 v/v binary mixture of a 1.0% w/w dispersion of $PLMA_{39}$-$PBzMA_{97}$ and $PLMA_{39}$-$PBzMA_{294}$ spheres up to 150 °C (**Figures 4.9 and 4.10**).

The initial scattering pattern of the binary mixture was collected at 20 °C, with two distinct minima representing the bimodality of this mixed dispersion (**Figure 4.9**). After heating to 150 °C at 30 °C min^{-1}, the first scattering pattern recorded at this temperature also exhibited these two minima. However, maintaining this dilute binary dispersion at 150 °C led to an increase in the low q gradient. This slope changed from zero to -0.69 within 5 min. Thereafter, the initial zero gradient was observed. This indicates that the fusion mechanism involves weakly anisotropic intermediate morphologies. Moreover, the intensity at low q (q = 0.019 nm^{-1}) (**Figure 4.9B**) increases within the first 7 min. This indicates that the formed anisotropic intermediate morphology have a larger volume than the initial spheres. This is because intensity at low q depends on the volume of the scattering objects, the concentration and the scattering contrast; the latter two parameters are likely to remain approximately constant in this case. A gradual reduction in intensity at low q is observed after 7 min. This suggests that the volume of the scattering objects gradually reduce over time.

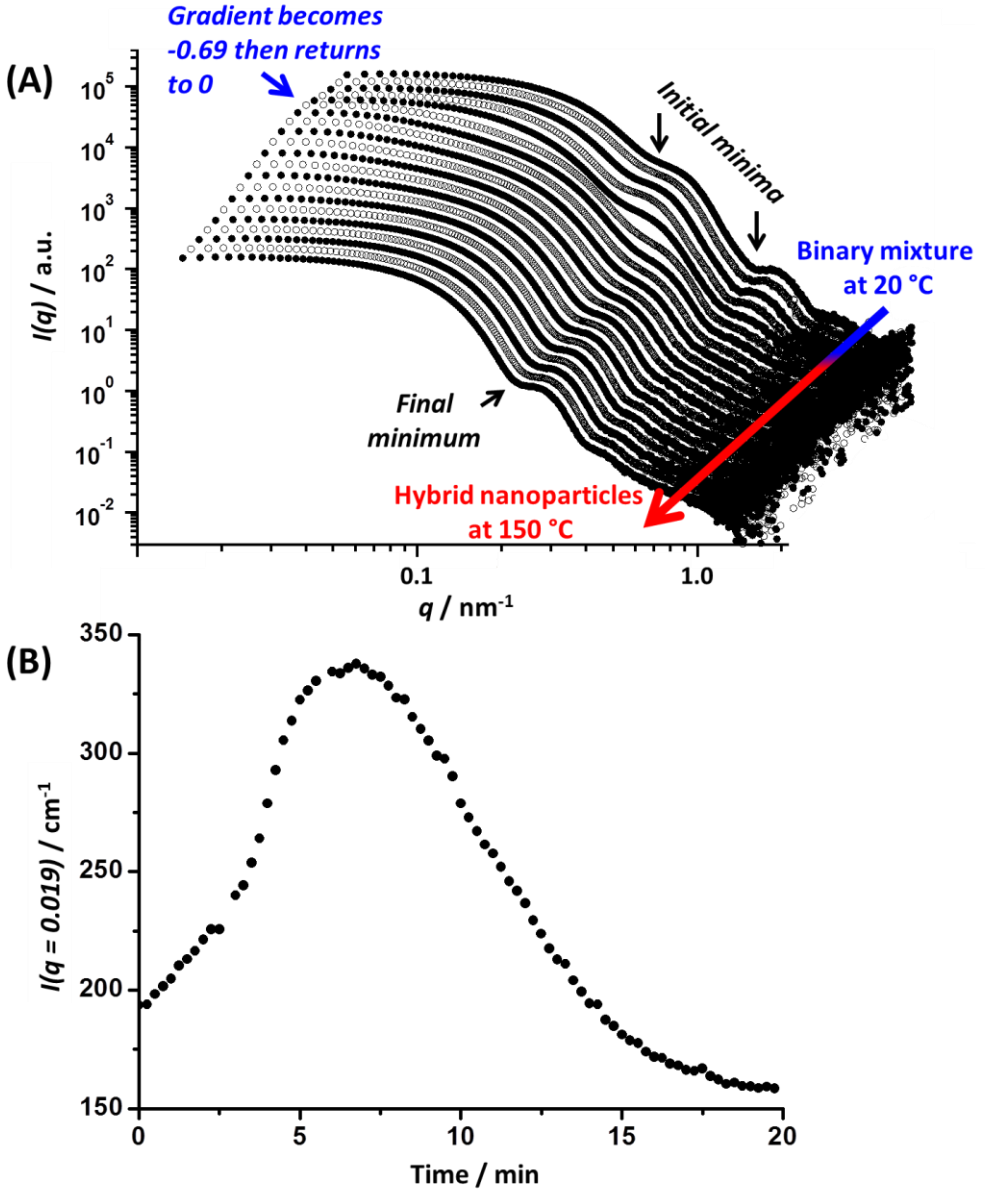

Figure 4.9. (A) TR-SAXS patterns recorded on heating a 1.0% w/w nanoparticle dispersion comprising a 1:1 v/v binary mixture of $PLMA_{39}$-$PBzMA_{97}$ and $PLMA_{39}$-$PBzMA_{294}$ spheres up to 150 °C at a heating rate of 30 °C min^{-1}. Two distinct intensity minima corresponding to first minimum of big ($PLMA_{39}$-$PBzMA_{294}$) and small ($PLMA_{39}$-$PBzMA_{97}$) spherical particles are discernible in the initial pattern recorded for this binary mixture at 20 °C. In contrast, the final scattering pattern, obtained after annealing for 20 min at 150 °C, shows two minima corresponding to a *single* population of spherical nanoparticles (q_1R = 4.49 and q_2R = 7.73, where R = 36 nm). (B) Scattering intensity at low q (q = 0.019 nm^{-1}) during the time-resolved scattering experiment at 150 °C.

This final scattering pattern acquired after 20 min at 150 °C exhibited just a single minimum. Cooling of this dispersion back to 20 °C produced two minima which corresponds to a *single* population of spherical nanoparticles (q_1R = 4.49 and q_2R = 7.73, where R = 36 nm) (**Figure 4.10**). This suggests near-monodisperse spheres are formed at this temperature.

The final scattering intensity, obtained after 20 min at 150 °C, is lower than the initial value (**Figure 4.9**). It is likely that the higher intensities at the start of the particle fusion process are caused by the larger spheres in the binary mixture, which would naturally scatter more, than the final hybrid nanoparticles of intermediate size.

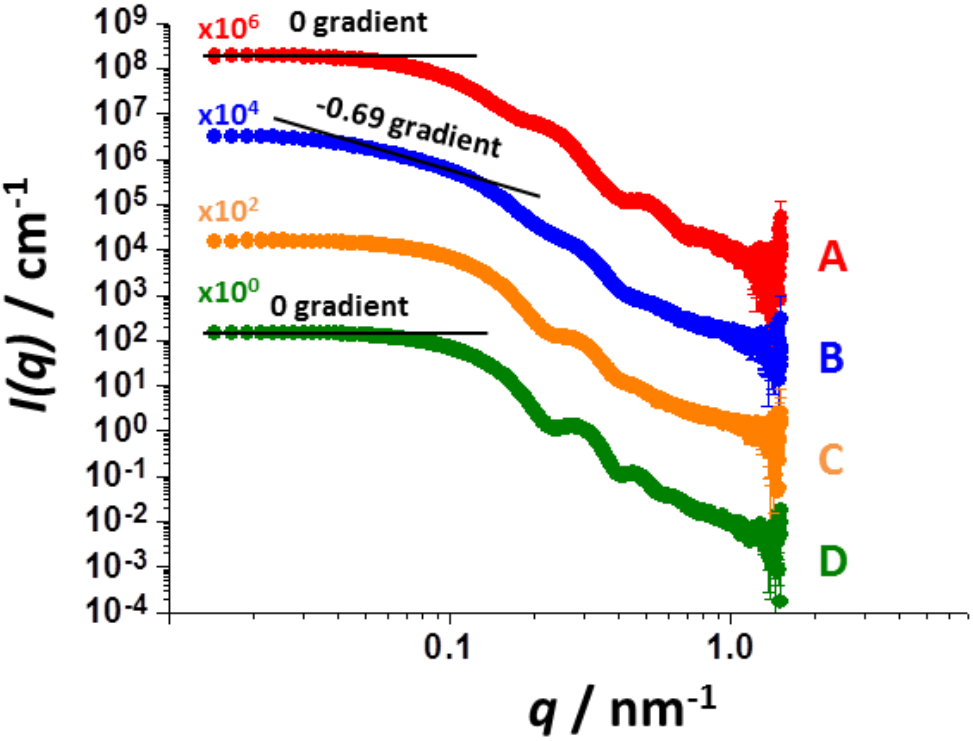

Figure 4.10. Individual SAXS patterns obtained during time-resolved SAXS experiments in which an equivolume binary mixture of $PLMA_{39}$-$PBzMA_{97}$ and $PLMA_{39}$-$PBzMA_{294}$ spheres was thermally annealed at 150 °C to form hybrid nanoparticles of intermediate diameters. (A) Initial binary mixture at 20 °C, (B) anisotropic intermediate transient morphology after 5 min at 150 °C, (C) hybrid spherical particles obtained after 20 min at 150 °C and (D) the final hybrid spherical nanoparticles obtained after cooling to 20 °C.

The progressive increase in scattering intensity and gradient at low *q* during thermal annealing suggests the formation of weakly anisotropic *intermediate* species with a larger volume than the initial spheres. Moreover, this implies that the change in morphology does not simply result from expulsion/insertion of $PLMA_{39}$-$PBzMA_{97}$ and $PLMA_{39}$-$PBzMA_{294}$ chains between the small and large nanoparticles. This is because such a mechanism is likely to simply increase the smaller nanoparticle diameter and reduce the larger species; it is certainly difficult to see why it should result in *anisotropic* intermediate morphologies. Given that core solvation and aggregation number strongly depend on the DP of the core-forming block, it is more likely that the shorter $PLMA_{39}$-$PBzMA_{97}$ chains are more likely to be redistributed in the binary mixed dispersion (i.e. there should be copolymer exchange between small nanoparticles, and from small to large nanoparticles). However, this is much less likely to occur for the longer $PLMA_{39}$-$PBzMA_{294}$ chains. Therefore it is likely that the anisotropic *intermediate* species are formed by the migration of $PLMA_{39}$-$PBzMA_{97}$ chains from small spheres to the large $PLMA_{39}$-$PBzMA_{294}$ nanoparticles. An alternative mechanism for the redistribution of polymer chains is the micelle fusion/fission mechanism. Based on these results we cannot exclude this pathway; however, considering that the literature[8,9] suggests that this mechanism is more demanding than chain expulsion/insertion, and because of the low concentration (1.0% w/w) it seems likely that migration of chains is the dominant mechanism for this process. However, such a mechanism does not explain the final intermediate spherical particle diameter: Migration of $PLMA_{39}$-$PBzMA_{97}$ chains to the larger $PLMA_{39}$-$PBzMA_{294}$ spheres should simply cause their N_{agg} and mean diameter to increase. Therefore, these results suggest that the shorter copolymer chains act like a surfactant and displace some of the copolymer chains from the $PLMA_{39}$-$PBzMA_{294}$ spheres. The latter undergo particle dissociation once a critical fraction of $PLMA_{39}$-$PBzMA_{97}$ chains have displaced the longer chains. Similar observations have been reported for the treatment of aqueous vesicle dispersions with surfactant. Indeed, it is well-known that surfactants can destabilise such diblock copolymer nano-objects.[34]

4.3.4. Effect of Mixing Ratio on Particle-Particle Fusion

In attempts to reproduce the anisotropic *intermediate* morphology as a kinetically stable nanoparticle and to gain more insight into the particle fusion mechanism; varying amounts of small $PLMA_{39}$-$PBzMA_{97}$ spheres were fused with large $PLMA_{39}$-$PBzMA_{294}$ spheres at 150 °C for 1 h. Such dispersions were prepared at several volumetric ratios at 20% w/w solids, diluted to 1.0 % w/w solids with *n*-dodecane and heated up to 150 °C for 1 h. $PLMA_{39}$-$PBzMA_{97}$ volume fractions from 0.05 to 0.50 were examined to simulate the particle fusion process. TEM analysis of these annealed dispersions revealed formation of the expected weakly anisotropic nanoparticles when using $PLMA_{39}$-$PBzMA_{97}$ volume fractions of between 0.20 and 0.35 (**Figure 4.11**). These species have, as predicted using *in situ* SAXS (**Figure 4.9**), an anisotropic dimer-like character and a larger in volume than the original spheres. Moreover, one might even speculate about the formation of a trimer like structures at 0.30 v/v.

Further insight the formation of these kinetically stable *hybrid* nanoparticles was obtained by SAXS analysis (see **Figure 4.12 and Table 4.5**). Scattering patterns for these annealed dispersions were recorded at 1.0 % w/w solids. This relatively low concentration ensures that the structure factor is simply equal to unity, and an approximate zero gradient at low *q* indicates a spherical morphology in most cases. Moreover, a low *q* gradient of -1 is characteristic of anisotropic morphologies, such as rods or worms. A slight upturn in gradient was observed for the 0.25, 0.30 and 0.35 v/v samples, here a fit to a spherical micelle model was not achieved. These observations correspond with the TEM analysis where anisotropic morphologies were observed at these fractions.

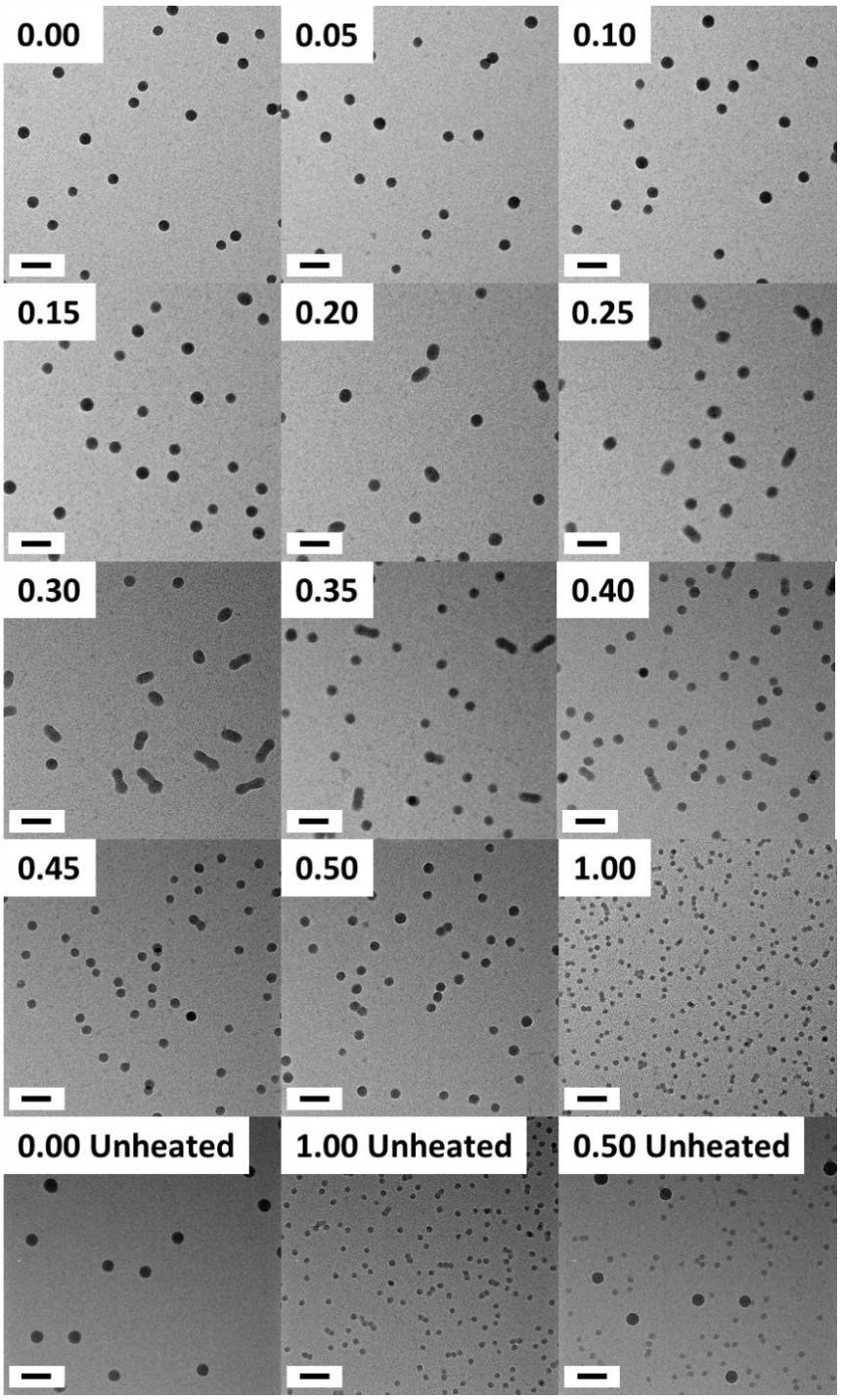

Figure 4.11. TEM images recorded for binary mixtures of $PLMA_{39}$-$PBzMA_{97}$ and $PLMA_{39}$-$PBzMA_{294}$ spheres before and after fusion. These binary dispersions were 1.0% w/w solids and heated to 150 °C for 1 h. Caption labels denote the volume fraction of the smaller $PLMA_{39}$-$PBzMA_{97}$ spheres used in these experiments. TEM images for the initial unheated nanoparticles (both separately and after 1:1 mixing) are also shown for reference. All scale bars correspond to 100 nm.

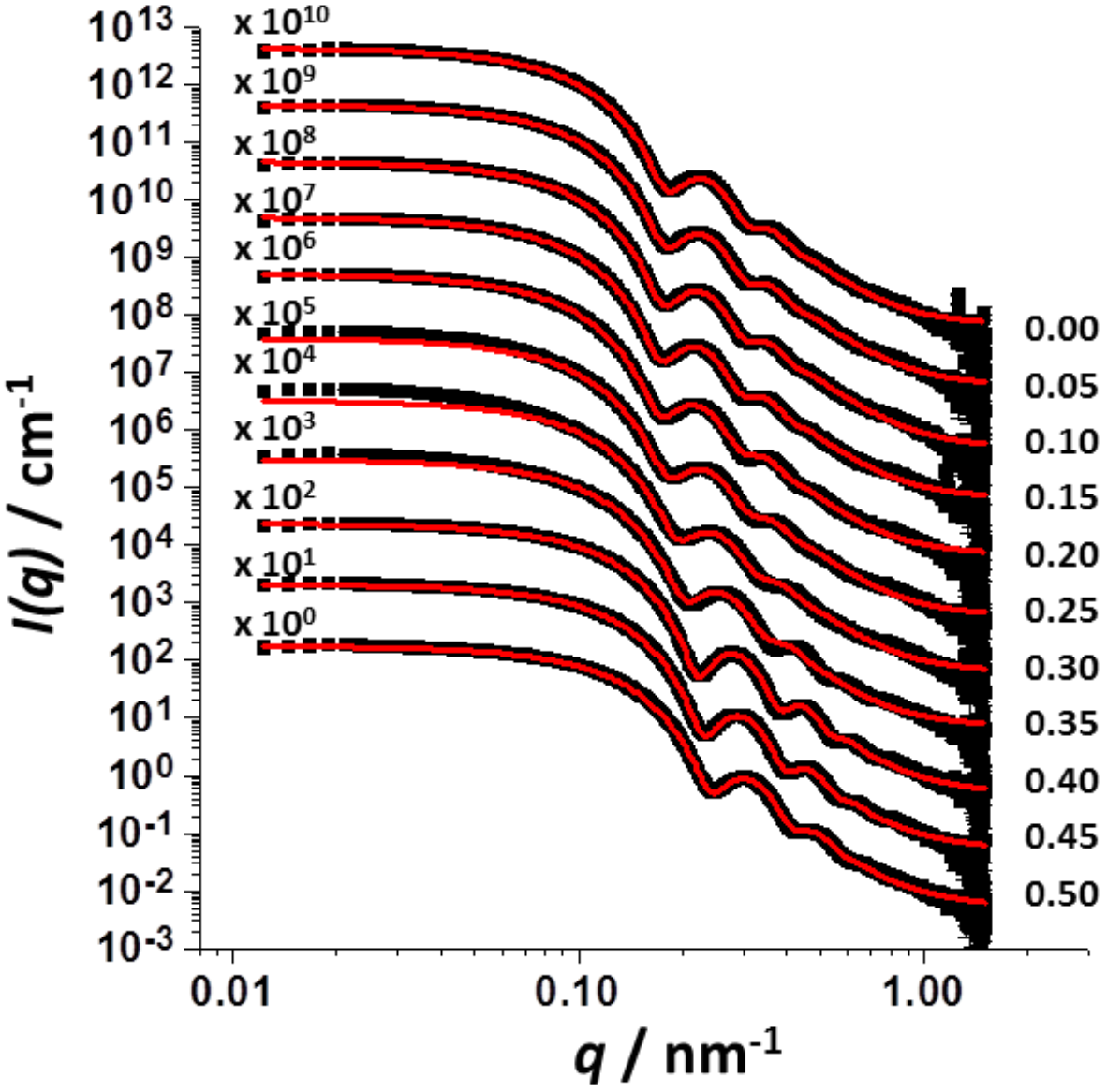

Figure 4.12. SAXS scattering patterns recorded for binary mixtures of $PLMA_{39}$-$PBzMA_{97}$ and $PLMA_{39}$-$PBzMA_{294}$ spheres after thermal annealing. These binary dispersions were diluted to 1.0% w/w solids and heated to 150 °C for 1 h. Caption labels denote the volume fraction of the smaller $PLMA_{39}$-$PBzMA_{97}$ spheres used in these experiments. Red lines represent the best fit obtained a spherical micelle model.

Table 4.5. Summary of SAXS fitting parameters obtained for $PLMA_{39}$-$PBzMA_{97}$ and $PLMA_{39}$-$PBzMA_{294}$ dispersions and the hybrid nanoparticles formed by annealing such binary mixtures at 150 °C for 1h. Core block volumes were calculated from the initial core volumes and nanoparticle mixing ratios assuming full entropic mixing. All data were fitted by assuming no solvent in the nanoparticle cores and a fixed $PLMA_{39}$ block volume of 17716 $Å^3$.

$PBzMAB_{97}$ / $PBzMA_{294}$ Volume ratio	**Average core-forming block volume / $Å^3$**	**Concentration / % v/v**	**$PBzMA_x$ core diameter / nm**	**$PLMA_{39}$ Shell R_g / nm**
0 / 100	72222	0.51	48 ± 5	1.96
5 / 95	70413	0.54	49 ± 5	1.95
10 / 90	68556	0.53	49 ± 5	1.95
15 / 85	66649	0.56	50 ± 5	1.96
20 / 80	64691	0.56	50 ± 5	1.99
25 / 75	62678	0.50	48 ± 5	1.96
30 / 70	60609	0.47	45 ± 5	1.98
35 / 65	58481	0.52	34 ± 5	1.98
40 / 60	56291	0.51	39 ± 3	1.98
45 / 55	54038	0.50	38 ± 3	1.97
50 / 50	51718	0.48	36 ± 3	1.93

Nanoparticle core diameters for the initial $PLMA_{39}$-$PBzMA_{97}$ and $PLMA_{39}$-$PBzMA_{294}$ spheres and binary mixtures thereof were obtained by fitting the corresponding SAXS scattering patterns to a well-known spherical micelle model[25,27] (see **Chapter 3**). The core-forming PBzMA block volume is an important input parameter for this model. This value was calculated for both $PLMA_{39}$-$PBzMA_{294}$ and $PLMA_{39}$-$PBzMA_{94}$ from their core-forming block DPs. However, the newly-formed *hybrid* nanoparticles consist of a pair of two block copolymer species with two distinct molecular weight distributions. Therefore, an average copolymer chain volume was calculated based on the total core-forming block volume, taking into account the relative proportions of the two components. A statistical distribution of copolymer chains between hybrid nanoparticles was assumed for the annealed dispersion.

Satisfactory fits to the SAXS patterns recorded for the initial binary dispersion and the newly-formed hybrid nanoparticles were obtained using this approach.

These data fits to the scattering patterns show that, in most cases, the hybrid nanoparticles are relatively monodisperse, with standard deviations of around 10% obtained for the nanoparticle cores. Furthermore, a radius of gyration of around 1.99 nm was obtained for the $PLMA_{39}$ stabiliser chains at the nanoparticle surface, small deviation might be within experimental error. This value is comparable to that obtained for the molecularly-dissolved $PLMA_{39}$ macro-CTA in *n*-dodecane (1.91 nm; see **Chapter 3**), and also to that obtained for $PLMA_{39}$ stabiliser chains at the surface of hydrogenous and core-deuterated $PLMA_{39}$-$PMMA_x$ spherical nanoparticles (see **Chapter 3**). A copolymer volume fraction of around 0.5% v/v was obtained for each dispersion, which is close to the expected 0.7 % v/v value (1.0% w/w). This lower volume fraction may indicate incomplete monomer conversion which would lead to a lower polymer concentration, or aggregation since this is not accounted for in the used spherical micelle model Sedimentation could also explain the lower volume fractions. However, this is rather unlikely since no sediment was observed, even for the 20% w/w dispersions (as prepared via RAFT PISA) over a period of 3 months (moreover, 1% w/w samples were well-mingled before SAXS analysis).

Fitting the scattering data to the spherical micelle model gave the volume-average core diameter for the hybrid nanoparticles. For the hybrid nanoparticles formed from a 1:1 v/v binary dispersion, this value lies between that of the two initial core diameters. However, binary mixtures using 0.05 to 0.20 $PLMA_{39}$-$PBzMA_{97}$ spheres produced larger mean core diameters after thermal annealing, which is in accordance with TEM analysis. These data indicate that the particle-particle fusion mechanism from a binary mixture of spheres with differing particle diameters to monodisperse hybrid nanoparticles of *intermediate* size utilises the migration of short $PLMA_{39}$-$PBzMA_{97}$ chains to $PLMA_{39}$-$PBzMA_{294}$ nanoparticles. This is likely to form *intermediate* anisotropic nanoparticles, which then breaks up to form spheres with intermediate mean diameters (see **Figure 4.13** and **Figure 4.14**). Finally, we like to speculate that temperature would affect the particle-particle fusion process. It is very likely that the larger $PLMA_{39}$-$PBzMA_{294}$ nanoparticles become more likely to undergo chain exchange at higher temperatures. This might significantly alter the annealed hybrid morphology.

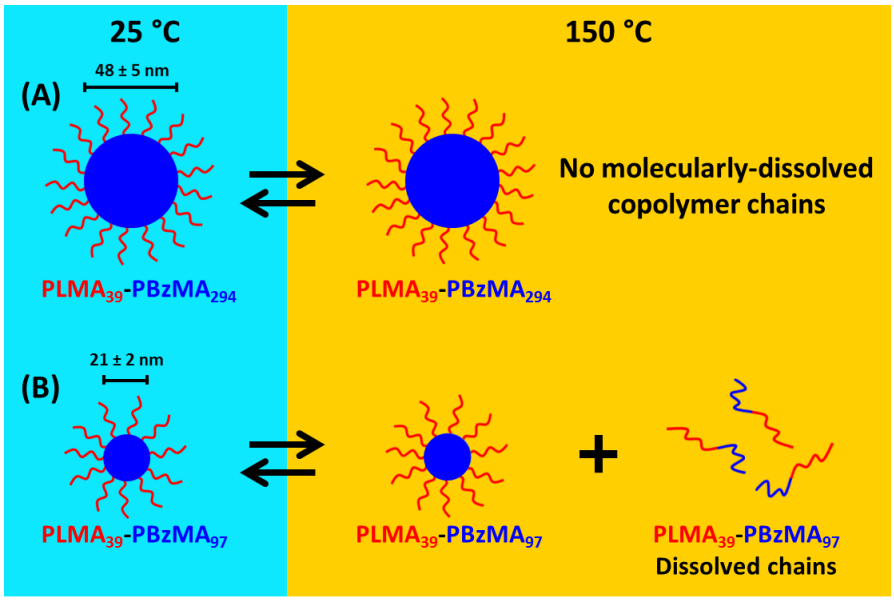

Figure4.13. Schematic representation of the respective behavior of (A) $PLMA_{39}$-$PBzMA_{294}$ and (B) $PLMA_{39}$-$PBzMA_{97}$ spherical nanoparticles at 25 °C and on heating up to 150 °C. The latter nanoparticles dissociate to form molecularly-dissolved copolymer chains at 150 °C. In contrast, the larger $PLMA_{39}$-$PBzMA_{294}$ spheres do not undergo (partial) dissociation at this temperature.

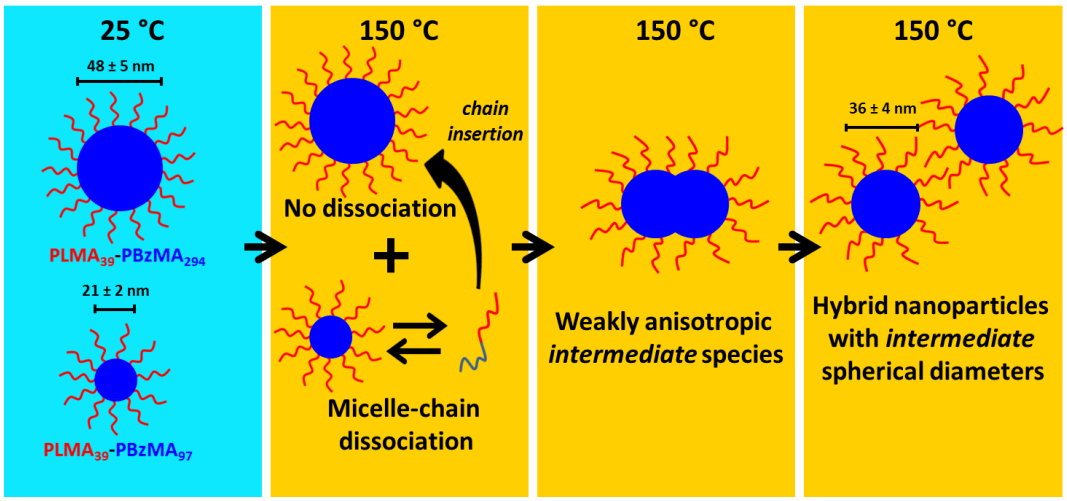

Figure 4.14. Schematic representation of particle-particle fusion between $PLMA_{39}$-$PBzMA_{294}$ and $PLMA_{39}$-$PBzMA_{97}$ spheres. The latter nanoparticle produces $PLMA_{39}$-$PBzMA_{97}$ chains on heating, which subsequently insert into the larger $PLMA_{39}$-$PBzMA_{294}$ spheres, leading to weakly anisotropic nano-objects. These intermediate anisotropic nano-objects break up into spherical *hybrid* nanoparticles, comprising intermediate mean diameters to that of the original two spherical nanoparticles.

4.4. Conclusions

RAFT PISA was used for the preparation of sterically-stabilised $PLMA_{39}$-$PBzMA_{97}$ and $PLMA_{39}$-$PBzMA_{294}$ diblock copolymer spheres in *n*-dodecane, with mean core diameters of 21 ± 2 nm and 48 ± 4.9 nm, respectively. The nanoparticles proved to be stable on heating to 150 °C for 1 h, as judged by SAXS analysis after cooling to 20 °C: almost identical core diameters were obtained before and after thermal annealing. Variable temperature SAXS analysis of these dilute dispersions indicated core solvation and a significant reduction in aggregation number for the smaller $PLMA_{39}$-$PBzMA_{97}$ spheres. In contrast, no changes were observed for the larger $PLMA_{39}$-$PBzMA_{294}$ diblock copolymer spheres. Annealing binary mixtures of these two dispersions in a 1:1 v/v ratio at 1.0 % w/w led to particle-particle fusion, forming nanoparticle cores with intermediate diameters. TR-SAXS analysis of this fusion process revealed an upturn in gradient at low *q*. This suggests that fusion proceeds via weakly anisotropic intermediate species.

More insights into the particle-particle fusion mechanism were obtained by annealing binary mixtures with various ratios between $PLMA_{39}$-$PBzMA_{97}$ and $PLMA_{39}$-$PBzMA_{294}$ spheres. Using $PLMA_{39}$-$PBzMA_{97}$ volume fractions of 0.25, 0.30 and 0.35 v/v yielded sterically stabilised anisotropic morphologies, as judged by TEM and SAXS. However, using volume fractions of 0.40 to 0.50 produced spherical nanoparticles of intermediate size. Interestingly, using volume fractions between 0.05 and 0.20 v/v yielded spherical nanoparticles with larger mean particle diameters than the original $PLMA_{39}$-$PBzMA_{294}$ spheres. These observations indicate that the particle-particle fusion mechanism between $PLMA_{39}$-$PBzMA_{97}$ and $PLMA_{39}$-$PBzMA_{294}$ spheres utilises the migration of $PLMA_{39}$-$PBzMA_{97}$ chains to the larger $PLMA_{39}$-$PBzMA_{294}$ spheres. This would form weakly anisotropic *intermediate* species, which then break up to form spheres of intermediately size.

4.5. References

(1) Lu, J.; Bates, F. S.; Lodge, T. P. Addition of Corona Block Homopolymer Retards Chain Exchange in Solutions of Block Copolymer Micelles, *Macromolecules*, **2016**, *49*, 1405-1413.

(2) Lu, J.; Bates, F. S.; Lodge, T. P. Remarkable Effect of Molecular Architecture on Chain Exchange in Triblock Copolymer Micelles, *Macromolecules*, **2015**, *48*, 2667-2676.

(3) Lu, J.; Bates, F. S.; Lodge, T. P. Chain Exchange in Binary Copolymer Micelles at Equilibrium: Confirmation of the Independent Chain Hypothesis, *ACS Macro Letters*, **2013**, *2*, 451-455.

(4) Lu, J.; Choi, S.; Bates, F. S.; Lodge, T. P. Molecular Exchange in Diblock Copolymer Micelles: Bimodal Distribution in Core-Block Molecular Weights, *ACS Macro Letters*, **2012**, *1*, 982-985.

(5) Choi, S.-H.; Bates, F. S.; Lodge, T. P. Molecular Exchange in Ordered Diblock Copolymer Micelles, *Macromolecules*, **2011**, *44*, 3594-3604.

(6) Choi, S. H.; Lodge, T. P.; Bates, F. S. Mechanism of Molecular Exchange in Diblock Copolymer Micelles: Hypersensitivity to Core Chain Length, *Physical Review Letters*, **2010**, *104*, 047802.

(7) Dormidontova, E. E. Micellization Kinetics in Block Copolymer Solutions: Scaling Model, *Macromolecules*, **1999**, *32*, 7630-7644.

(8) Halperin, A. On Micellar Exchange: The Role of the Insertion Penalty, *Macromolecules*, **2011**, *44*, 5072-5074.

(9) Halperin, A.; Alexander, S. Polymeric micelles: their relaxation kinetics, *Macromolecules*, **1989**, *22*, 2403-2412.

(10) Haliloğlu, T.; Bahar, I.; Erman, B.; Mattice, W. L. Mechanisms of the Exchange of Diblock Copolymers between Micelles at Dynamic Equilibrium, *Macromolecules*, **1996**, *29*, 4764-4771.

(11) Wang, Y.; Kausch, C. M.; Chun, M.; Quirk, R. P.; Mattice, W. L. Exchange of Chains between Micelles of Labeled Polystyrene-block-poly(oxyethylene) As Monitored by Nonradiative Singlet Energy Transfer, *Macromolecules*, **1995**, *28*, 904-911.

(12) Zinn, T.; Willner, L.; Pipich, V.; Richter, D.; Lund, R. Molecular Exchange Kinetics of Micelles: Corona Chain Length Dependence, *ACS Macro Letters*, **2016**, *5*, 884-888.

(13) Zinn, T.; Willner, L.; Pipich, V.; Richter, D.; Lund, R. Effect of Core Crystallization and Conformational Entropy on the Molecular Exchange Kinetics of Polymeric Micelles, *ACS Macro Letters*, **2015**, *4*, 651-655.

(14) Ma, Y.; Lodge, T. P. Chain Exchange Kinetics in Diblock Copolymer Micelles in Ionic Liquids: The Role of χ, *Macromolecules*, **2016**, *49*, 9542-9552.

(15) Ma, Y.; Lodge, T. P. Poly(methyl methacrylate)-block-poly(n-butyl methacrylate) Diblock Copolymer Micelles in an Ionic Liquid: Scaling of Core and Corona Size with Core Block Length, *Macromolecules*, **2016**, *49*, 3639-3646.

(16) Mansour, A. S.; Johnson, L. F.; Lodge, T. P.; Bates, F. S. Thermodynamic Characteristics of Poly(cyclohexylethylene-b-ethylene-co-ethylethylene) Block Copolymers, *Journal of Polymer Science Part B-Polymer Physics*, **2010**, *48*, 566-574.

(17) Derry, M. J.; Fielding, L. A.; Armes, S. P. Industrially-relevant polymerization-induced self-assembly formulations in non-polar solvents: RAFT dispersion polymerization of benzyl methacrylate, *Polymer Chemistry*, **2015**, *6*, 3054-3062.

(18) Blanazs, A.; Ryan, A. J.; Armes, S. P. Predictive Phase Diagrams for RAFT Aqueous Dispersion Polymerization: Effect of Block Copolymer Composition, Molecular Weight, and Copolymer Concentration, *Macromolecules*, **2012**, *45*, 5099-5107.

(19) Fielding, L. A.; Derry, M. J.; Ladmiral, V.; Rosselgong, J.; Rodrigues, A. M.; Ratcliffe, L. P. D.; Sugihara, S.; Armes, S. P. RAFT dispersion polymerization in non-polar solvents: facile production of block copolymer spheres, worms and vesicles in n-alkanes, *Chemical Science*, **2013**, *4*, 2081-2087.

(20) Lopez-Oliva, A. P.; Warren, N. J.; Rajkumar, A.; Mykhaylyk, O. O.; Derry, M. J.; Doncom, K. E. B.; Rymaruk, M. J.; Armes, S. P. Polydimethylsiloxane-Based Diblock Copolymer Nano-objects Prepared in Nonpolar Media via RAFT-Mediated Polymerization-Induced Self-Assembly, *Macromolecules*, **2015**, *48*, 3547-3555.

(21) Fielding, L. A.; Lane, J. A.; Derry, M. J.; Mykhaylyk, O. O.; Armes, S. P. Thermo-responsive Diblock Copolymer Worm Gels in Non-polar Solvents, *Journal of the American Chemical Society*, **2014**, *136*, 5790-5798.

(22) Blanazs, A.; Verber, R.; Mykhaylyk, O. O.; Ryan, A. J.; Heath, J. Z.; Douglas, C. W. I.; Armes, S. P. Sterilizable Gels from Thermoresponsive Block Copolymer Worms, *Journal of the American Chemical Society*, **2012**, *134*, 9741-9748.

(23) Lovett, J. R.; Derry, M. J.; Yang, P.; Hatton, F. L.; Warren, N. J.; Fowler, Patrick W.; Armes, S. P. Can percolation theory explain the gelation behavior of diblock copolymer worms?, *Chemical Science*, **2018**, *9*, 7138-7144.

(24) Semsarilar, M.; Ladmiral, V.; Blanazs, A.; Armes, S. P. Anionic Polyelectrolyte-Stabilized Nanoparticles via RAFT Aqueous Dispersion Polymerization, *Langmuir*, **2012**, *28*, 914-922.

(25) Pedersen, J. S.; Gerstenberg, M. C. Scattering Form Factor of Block Copolymer Micelles, *Macromolecules*, **1996**, *29*, 1363-1365.

(26) Pedersen, J. S.; Schurtenberger, P. Scattering Functions of Semiflexible Polymers with and without Excluded Volume Effects, *Macromolecules*, **1996**, *29*, 7602-7612.

(27) Pedersen, J. S. Form factors of block copolymer micelles with spherical, ellipsoidal and cylindrical cores, *Journal of Applied Crystallography*, **2000**, *33*, 637-640.

(28) Debye, P. Molecular-weight Determination by Light Scattering, *The Journal of Physical and Colloid Chemistry*, **1947**, *51*, 18-32.

(29) Ilavsky, J.; Jemian, P. R. Irena: tool suite for modeling and analysis of small-angle scattering, *Journal of Applied Crystallography*, **2009**, *42*, 347-353.

(30) Fetters, L. J.; Lohsey, D. J.; Colby, H. Physical Properties of Polymers Handbook; 2 ed.; Mark, J. E., Ed.; Springer New York: 2007, p 447-454.

(31) Rymaruk, M. J.; Thompson, K. L.; Derry, M. J.; Warren, N. J.; Ratcliffe, L. P. D.; Williams, C. N.; Brown, S. L.; Armes, S. P. Bespoke contrast-matched diblock copolymer nanoparticles enable the rational design of highly transparent Pickering double emulsions, *Nanoscale*, **2016**, *8*, 14497-14506.

(32) Mark, J.E. *Physical properties of polymers Handbook*; 2nd ed.; Springer, **2007**, p93.

(33) Li, X.; Cooksey, T. J.; Kidd, B. E.; Robertson, M. L.; Madsen, L. A. Mapping Coexistence Phase Diagrams of Block Copolymer Micelles and Free Unimer Chains, *Macromolecules*, **2018**, *51*, 8127-8135.

(34) Chambon, P.; Blanazs, A.; Battaglia, G.; Armes, S. P. How Does Cross-Linking Affect the Stability of Block Copolymer Vesicles in the Presence of Surfactant?, *Langmuir*, **2012**, *28*, 1196-1205.

Chapter 5

Conclusions and Future Work

5.1 Conclusions and Future Work

This Thesis reports the efficient preparation of various types of diblock copolymer nanoparticles via RAFT-mediated PISA in non-polar media. Four types of spherical nanoparticles were synthesised in either *n*-dodecane or *n*-tetradecane by chain-extending either a poly(stearyl methacrylate) (PSMA) macro-CTA with 2,2,2-trifluoroethyl methacrylate (TFEMA); or chain extending a poly(lauryl methacrylate) (PLMA) macro-CTA with methyl methacrylate (MMA), deuterated methyl methacrylate (d_8-MMA) or benzyl methacrylate (BzMA). Derry reported that such diblock copolymer nanoparticles (PLMA-PBzMA spheres) can be used as friction modifiers in automotive engine oils.[1] However, further research is warranted to understand the behaviour of these nanoparticles for such commercial applications. The above mentioned formulations were selected for this study to investigate the preparation method of diblock copolymer nanoparticles in non-polar media *in situ*, or to assess spherical nanoparticle behaviour at elevated temperatures. Indeed, each core-forming block was selected for specific properties to make them suitable for in-depth characterisation studies.

PTFEMA is a semi-fluorinated polymer with a relatively low refractive index (RI = 1.41). This enables the preparation of highly transparent dispersions by selection of an appropriate *n*-alkane solvent with a similar refractive index. Moreover, this semi-fluorinated monomer enables ^{19}F NMR studies. MMA is an industrially-relevant low-cost monomer. It enables convenient preparation of fully hydrogenous and core-deuterated PLMA-PMMA spheres. Binary dispersions of such nanoparticles enable time-resolved small-angle neutron scattering (TR-SANS) experiments to be conducted under contrast-matched conditions. This method was used in this Thesis to examine diblock copolymer chain exchange between spherical nanoparticles.

PSMA-PTFEMA spheres were prepared via RAFT PISA in either *n*-dodecane or *n*-tetradecane. These dispersions proved to be highly transparent at 30 °C and 70 °C, respectively. This isorefractivity enabled *in situ* visible absorption spectroscopy studies to be conducted during PISA. This approach was used to determine the stability of trithiocarbonate RAFT chain-ends under monomer-starved conditions. Much to our surprise, these studies indicated excellent RAFT chain-end stability for at least 2 h at 70 °C after a high TFEMA conversion (98%) had been achieved. Moreover, the polymerisation kinetics for this isorefractive RAFT dispersion polymerisation could be conveniently monitored by

dilatometry. Furthermore, RAFT chain-ends could be fully removed from the nanoparticle cores simply by treatment with excess thermal initiator at 70 °C. In summary, this RAFT PISA formulation possesses ideal characteristics: the trithiocarbonate chain-ends remain stable during the RAFT polymerisation for optimal control but can be readily removed thereafter. This is potentially important for certain applications because RAFT end-groups are malodorous, highly coloured and potentially toxic. Clearly, it would be interesting to extend the *in situ* visible absorption spectroscopy studies to include dithiobenzoate-based RAFT agents in addition to the trithiocarbonate RAFT agent examined in this Thesis. Such studies should take into account the more intense absorbance (greater molar extinction coefficient) observed for the former reagent, which may require more dilute reaction conditions. Furthermore, it would be interesting to explore the feasibility of preparing isorefractive worms and vesicles using more asymmetric PSMA-PTFEMA block copolymers via RAFT PISA. These particles might provide fundamental insights into temperature-induced worm-to-sphere and vesicle-to-worm morphological transitions using tracer diffusion experiments.[2-4] PLMA-PMMA nanoparticles prepared in mineral oil (RI ~1.47 at 20 °C)[5] are also relatively transparent. This PISA formulation is industrially relevant for the production of lubricating nanoparticles directly in automotive engine oils.[6] In principle, such nanoparticles should significantly reduce friction between metal surfaces, particularly in the boundary lubrication regime.[7] Indeed, extensive engine tests have been performed on PLMA-PMMA nanoparticles by the industrial sponsor of this project (Lubrizol).[8,9]

Given this commercial interest, it should be worth exploring whether *in situ* visible absorption spectroscopy studies can also be performed during the RAFT dispersion polymerisation of MMA using a PLMA precursor block. In principle, judicious choice of the base oil (Group I, II or III) and optimisation of the polymerisation temperature might enable sufficiently transparent dispersions to be obtained. Even if this cannot be achieved, *in situ* spectroscopic studies should be useful for the first stage of one-pot syntheses of PLMA-PMMA nanoparticles. This would enable the optimal time of addition of the MMA to be identified during the RAFT solution polymerisation of LMA.[6] In this case, isorefractivity is not required because no nanoparticles are present at this stage of the synthesis. Knowing precisely when to add the MMA should lead to optimal blocking efficiencies for such one-pot protocols. In this context, it is perhaps noteworthy that it should be possible to monitor a shoulder on the visible absorption band, rather than the absorbance at the maximum

wavelength. This would enable polymerisations to be followed even when using relatively high monomer concentrations without leading to deviations from the Beer-Lambert law.

The highly transparent PSMA-PTFEMA formulation developed in this Thesis has provided useful new insights into the true nature of RAFT-mediated PISA by minimising visible light scattering. As an alternative to matching the nanoparticle refractive index, the neutron SLD of the nanoparticle cores can be matched to that of the solvent. This approach was utilised to monitor copolymer chain exchange between nanoparticles using TR-SANS. Higher temperatures and shorter core-forming PMMA blocks resulted in faster copolymer chain exchange rates. The thermally-activated redistribution of diblock copolymer chains between nanoparticles suggests the presence of a molecularly dissolved block copolymer fraction within the dispersion at elevated temperatures. In principle, these soluble chains might significantly alter the nanoparticle lubrication performance. However, copolymer chain mobility can be eliminated by crosslinking the nanoparticle cores. Further research is required to establish the effect of core-crosslinking on nanoparticle lubrication efficiency.

Copolymer exchange occurred at 80 °C, which is below the reaction temperature of the RAFT PISA synthesis of the PLMA-PMMA nanoparticles (and below the T_g of the core-forming PMMA block). These results are important in terms of understanding the PISA mechanism, which is likely to proceed by a copolymer chain expulsion/insertion mechanism.[10,11] This suggests that copolymer chains can redistribute between nanoparticles during PISA. However, the rate of copolymer chain exchange strongly depends on the core-forming block DP, which implies that copolymer chain exchange should become progressively less likely as RAFT PISA proceeds. Hence, the micelle fusion/fission mechanism may become more favourable in the latter stages of the polymerisation. This is consistent with the morphological evolution from spheres to worms to vesicles that is observed for certain RAFT PISA formulations.[12] The effect of monomer core solvation on diblock copolymer chain exchange should be assessed in the future to gain more insight into the RAFT PISA mechanism.

Copolymer chain redistribution was also observed for PLMA-PBzMA spheres. This was confirmed using a binary mixture of such nanoparticles. Two distinct particle diameters were prepared by adjusting the PBzMA nanoparticle core DP; longer core DPs led to larger spheres. A binary mixture of $PLMA_{39}$-$PBzMA_{97}$ and $PLMA_{39}$-$PBzMA_{294}$ nanoparticles was heated to 150 °C for 1 h. This produced near-monodisperse *hybrid* spheres with an

intermediate particle diameter. Variable temperature SAXS and TR-SAXS provided valuable insights regarding the nanoparticle fusion mechanism. The copolymer chain mobility is strongly dependent on the core-forming block DP (as observed in **Chapter 3** for PLMA-PMMA spheres). We hypothesise that the shorter copolymer chains originating from the smaller nanoparticles aid the dissociation of the larger spherical particles. It may be worth exploring fusion between vesicular and spherical nanoparticles. It seems likely that this might result in the formation of worms, which might form a free-standing gel. Usually, this phase is difficult to access as it usually occupies a narrow region of the phase diagram.[13]

The ability of diblock copolymer chains to redistribute between nanoparticles suggests new post-synthetic routes to access *hybrid* nanoparticles by simply heating binary mixtures of chemically distinct nanoparticles such as PLMA-PMMA and PLMA-PBzMA. If successful, this entropic mixing approach would produce new nanoparticles that cannot be prepared directly via PISA. Moreover, this would allow the preparation of cheaper nanoparticles with ideally the same performance (considering that MMA is less expensive then BzMA). Furthermore, efficient nanoparticle crosslinking could be achieved by thermally-induced copolymer chain exchange of block copolymers with complementary reactivity. For example, using core-forming blocks such as poly(glycidyl methacrylate) and poly(2-hydroxypropyl methacrylate) should enable the preparation of core cross-linked nanoparticles without using a small molecule cross-linker.

5.2 References

(1) Derry, M. J.; Armes, S. P. Thesis title: Polymerisation-induced self-assembly in non-polar media, University of Sheffield: Department of Chemistry, March **2016**

(2) Goodwin, J. W.; Ottewill, R. H.; Parentich, A. Optical examination of structured colloidal dispersions, *The Journal of Physical Chemistry*, **1980**, *84*, 1580-1586.

(3) Kopswerkhoven, M. M.; Fijnaut, H. M. Dynamic behaviour of silica dispersions studied near the optical matching point, *Journal of Chemical Physics*, **1982**, *77*, 2242-2253.

(4) Kopswerkhoven, M. M.; Pathmamanoharan, C.; Vrij, A.; Fijnaut, H. M. concentration-dependence of the self-diffusion coefficient of hard, spherical-particles measured with photon-correlation spectroscopy, *Journal of Chemical Physics*, **1982**, *77*, 5913-5922.

(5) https://www.sigmaaldrich.com (Accessed on 19-03-2019)

(6) Derry, M. J.; Fielding, L. A.; Armes, S. P. Industrially-relevant polymerization-induced self-assembly formulations in non-polar solvents: RAFT dispersion polymerization of benzyl methacrylate, *Polymer Chemistry*, **2015**, *6*, 3054-3062.

(7) Zheng, R.; Liu, G.; Devlin, M.; Hux, K.; Jao, T.-C. Friction Reduction of Lubricant Base Oil by Micelles and Crosslinked Micelles of Block Copolymers, *Tribology Transactions*, **2010**, *53*, 97-107.

(8) Vincent P.R.; Smith T. R.; Patterson R.A.; Pashkovski, E. Lubrication composition for and method of lubricating an internal combustion engine, **2019** (filed 03-01-**2019**) , Patent number WO 2019/005738 A1

(9) Smith T. R.; O'Hora, P.S.; Pashkovski, E; Sampler E.P.; Patterson R.A.; Trickett, K. Lubricating composition containing a self-assembling polymethacrylate block copolymer and an ethylene-α-olefin copolymer, **2019** (filed 03-01-2019), Patent number WO 2019/005680 A1

(10) Lu, J.; Bates, F. S.; Lodge, T. P. Chain Exchange in Binary Copolymer Micelles at Equilibrium: Confirmation of the Independent Chain Hypothesis, *Acs Macro Letters*, **2013**, *2*, 451-455.

(11) Choi, S. H.; Lodge, T. P.; Bates, F. S. Mechanism of Molecular Exchange in Diblock Copolymer Micelles: Hypersensitivity to Core Chain Length, *Physical Review Letters*, **2010**, *104*, 047802

(12) Fielding, L. A.; Derry, M. J.; Ladmiral, V.; Rosselgong, J.; Rodrigues, A. M.; Ratcliffe, L. P. D.; Sugihara, S.; Armes, S. P. RAFT dispersion polymerization in non-polar solvents: facile production of block copolymer spheres, worms and vesicles in n-alkanes, *Chemical Science*, **2013**, *4*, 2081-2087.

(13) Lopez-Oliva, A. P.; Warren, N. J.; Rajkumar, A.; Mykhaylyk, O. O.; Derry, M. J.; Doncom, K. E. B.; Rymaruk, M. J.; Armes, S. P. Polydimethylsiloxane-Based Diblock Copolymer Nano-objects Prepared in Nonpolar Media via RAFT-Mediated Polymerization-Induced Self-Assembly, *Macromolecules*, **2015**, *48*, 3547-3555.